BERGISCHE UNIVERSITÄT WUPPERTAL

Search for Partners of the Top Quark with the ATLAS Experiment

Dissertation

Jan Küchler

Für Daniela

Contents

Introduction

Particle physics studies the nature of fundamental particles and their interactions. The Standard Model of particle physics is the foundation of the theoretical description of these processes. With the discovery of the Higgs boson at the Large Hadron Collider by the ATLAS and CMS experiments this theory is completed. Nonetheless, there are numerous motivations for an extension of the Standard Model. These are led by cosmological observations such as the abundance of dark matter or the observed asymmetry between matter and anti-matter, but also by theoretical shortcomings of the Standard Model such as the hierarchy problem. The latter part describes the dependence of the Higgs boson mass on radiative corrections and the unnatural fine-tuning needed to cancel the influence of the Plank mass scale.

The radiative corrections to the Higgs boson mass are dominated by the contributions of the top quark, which is the heaviest known fundamental particle. Many theories beyond the Standard Model thus include a partner of the top quark, a particle with similar characteristics and couplings. One such theory is Supersymmetry. Here, the existing space-time symmetries are extended by a symmetry relation between fermions and bosons. Each Standard Model particle is assigned a supersymmetric partner, leading to the natural prediction of a top quark partner. These supersymmetric particles have the same couplings as their Standard Model counterparts, but differ in their spin.

While Supersymmetry is a general theory with many free parameters, generic models include the prediction of a light top squark at the electroweak scale, the scalar superpartner of the top quark. This dissertation describes a search for a simplified model of Supersymmetry, which assumes only one light superparticle in addition to the top squark. The light particle is called neutralino, and is stable and weakly interacting, building a candidate for a particle description of dark matter. The top squark is assumed to be produced in pairs, and to then decay into the top quark and the neutralino. The search targets final states akin to the Standard Model production of top quark pairs, but with additional missing transverse momentum due to the undetectable neutralinos.

Alternative models of new physics include so-called vector-like top quarks, fermions for which the left- and right-handed components transform equally under weak interactions. They can decay via flavour-changing neutral currents, for example into a top quark and a Z boson. The pair production of vector-like top quarks with a subsequent decay of the Z bosons into neutrinos gives rise to a similar final state as in the search for supersymmetric top quark partners. A search for this final state is presented in this dissertation.

Depending on the signal model, different observables are used to enhance the signal expectation. In general, the presence of a hadronically decaying, high momentum top quark leads to the distinct signature of three close-by jets in the detector, of which the combined mass is that of the top quark. The searches employ techniques to reconstruct this decay in order to identify the top quark decay and reduce the background. The search strategy is based on a selection which maximises the expected significance of the signal by setting high thresholds on kinematic observables. The expected Standard Model background in these signal regions is estimated based on simulation, with the overall normalisation determined in background enriched selections. These background control regions are close to the signal region, but differ in one or more key selection requirements in order to achieve a high purity of the targeted background. The statistical interpretation of the results employs profile-likelihood estimates, building on simultaneous likelihood fits to the observed events in the signal and the control regions.

The analyses are based on pp collision data collected by the ATLAS experiment during the beginning of the LHC Run 2 in 2015 and 2016, corresponding to an integrated luminosity of $36.1\,\text{fb}^{-1}$. The aim of the analyses is to extend the sensitivity for top quark partners towards the TeV scale, and, in absence of a signal, to derive limits on model parameters.

The author has contributed to the following publications by the ATLAS collaboration. The contributions to the latter two publications are discussed in detail in this dissertation:

- ATLAS Collaboration, *Charged-particle distributions in $\sqrt{s}$ = 13 TeV pp interactions measured with the ATLAS detector at the LHC*, Phys. Lett. B **758** (2016) p. 67, arXiv: 1602.01633 [hep-ex]

- ATLAS Collaboration, *Search for top squarks in final states with one isolated lepton, jets, and missing transverse momentum in $\sqrt{s}$ = 13 TeV pp collisions with the ATLAS detector*, Phys. Rev. D **94** (2016) p. 052009, arXiv: 1606.03903 [hep-ex]

- ATLAS Collaboration, *Search for pair production of vector-like top quarks in events with one lepton, jets, and missing transverse momentum in $\sqrt{s}$ = 13 TeV pp collisions with the ATLAS detector*, JHEP **08** (2017) p. 052, arXiv: 1705.10751 [hep-ex]

- ATLAS Collaboration, *Search for top-squark pair production in final states with one lepton, jets, and missing transverse momentum using 36 fb^{-1} of $\sqrt{s}$ = 13 TeV pp collision data with the ATLAS detector*, JHEP **06** (2018) p. 108, arXiv: 1711.11520 [hep-ex]

In addition, the author contributed to the update of a *b*-tagging algorithm specialised to dense environments (see Appendix A), as well as to performance studies of the tracking with the upgraded inner detector, as documented in

- ATLAS Collaboration, *Track Reconstruction Performance of the ATLAS Inner Detector at $\sqrt{s}$ = 13 TeV*, ATL-PHYS-PUB-2015-018, 2015, URL: https://cds.cern.ch/record/2037683.

Theory of particle physics
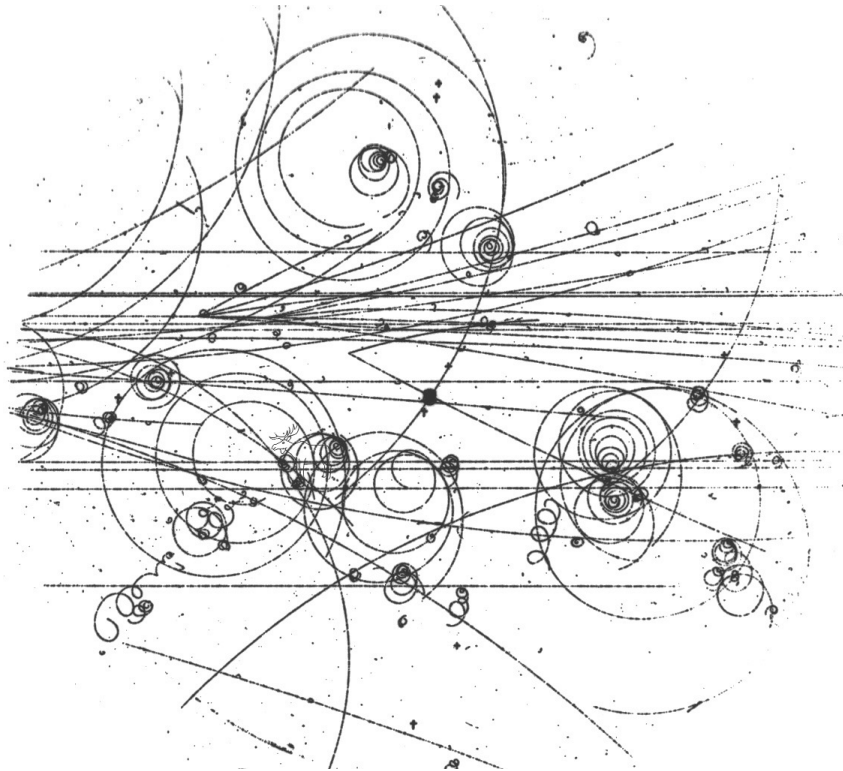
Chapter 1 The Standard Model

The Standard Model of Particle Physics (SM) is a quantum field theory that, since its development in the 1960's, provides a successful and precise description of the fundamental particles and their interactions [6–9]. Its latest confirmation has been the discovery of the Higgs boson by the ATLAS and CMS collaborations [10, 11].

This chapter gives an overview of the particles in the SM and its mathematical formulation. A selection of the multitude of experiments validating the theory and its consistency is shown, but also the need for theories beyond the SM is motivated.

1.1   Particles in the Standard Model

Elementary particles are classified according to their spin and encompass fermions, particles with half-integer spin, and bosons with integer spin. The SM consists of three kinds of particles, the fermionic leptons and quarks, as well as the bosons, which mediate interactions between the particles. Leptons and quarks are spin-$1/2$ fermions and are grouped in three generations of particles. The particles of the first generation are stable and form the constituents of ordinary matter. In contrast, the particles of the higher generations are generally unstable and decay into lighter particles, with the exception of the neutrinos. The higher generation fermions have identical properties to their first generation counterparts, apart from the higher masses. Table 1.1 gives an overview of the SM fermions and their charges and masses. Each fermion has an antiparticle, a particle with identical mass but opposite quantum numbers, e.g. electrical charge.

Table 1.1: Overview of the leptons and quarks in the Standard Model, with their electrical charge and masses [12]. The neutrino mass limit originates from the 95 % CL upper limit on the sum of all neutrino masses.

Generation	Leptons			Quarks		
	Name	Charge	Mass	Name	Charge	Mass
I	electron (e)	-1	511 keV	up (u)	$+2/3$	2.2 MeV
	e neutrino (ν_e)	0	< 0.23 eV	down (d)	$-1/3$	4.7 MeV
II	muon (μ)	-1	106 MeV	charm (c)	$+2/3$	1.28 GeV
	μ neutrino (ν_μ)	0	< 0.23 eV	strange (s)	$-1/3$	96 MeV
III	tau (τ)	-1	1.78 GeV	top (t)	$+2/3$	173.1 GeV
	τ neutrino (ν_τ)	0	< 0.23 eV	bottom (b)	$-1/3$	4.18 GeV

Table 1.2: Overview of the gauge bosons in the Standard Model, with their masses, interactions and electrical charge [12].

Particle	Mass	Interaction	Charge
Photon (γ)	0 GeV	electromagnetic	0
Gluon (g)	0 GeV	strong	0
W boson	80.4 GeV	weak	± 1
Z boson	91.2 GeV	weak	0

In addition to the electrical charge, quarks carry one of three different colour charges. Only colour-neutral combinations of particles have so far been observed directly, which means either combinations of three quarks with each colour once, or a combination of one colour and the corresponding anti-colour. This phenomenon is called confinement, and the colour neutral, bound particles are called hadrons.

Interactions between the fundamental particles are mediated by gauge bosons, as listed in Table 1.2. The electromagnetic interaction is mediated by the photon, which is a spin-1 massless particle. The fundamental symmetry group of the electromagnetic force is the $U(1)_{\text{EM}}$ group. The photon couples to the electric charge of a particle. As the photon is not charged, it does not exhibit self-coupling. The range of the electromagnetic interaction is infinite, as the photon is massless.

The weak force is mediated by the charged W bosons and the neutral Z boson, with $SU(2)_L$ as the fundamental symmetry group. It acts on all elementary fermions, coupling to the weak isospin of a particle. It is the only interaction neutrinos participate in. Neutrinos and up-type quarks carry a weak isospin of $^1/_2$, while the charged leptons and down-type quarks have a value of $-^1/_2$. The weak gauge bosons are massive, resulting in the apparent weakness of their couplings and the limited range of the interaction.

The strong force acts on the colour charge and thus only affects the quarks and its mediator particle, the gluon. The gluon is massless and electrically neutral, but is in one of eight different colour states. The symmetry group of the strong force is the $SU(3)_C$ group.

1.2   Mathematical formulation

The mathematical formulation of the Standard Model relies on the Lagrangian density $\mathcal{L}$, which is formulated in terms of the fundamental fields of the theory [13, 14]. The derivation of the theory is based on the invariance of the Lagrangian density under the gauge group

$$U(1)_Y \otimes SU(2)_L \otimes SU(3)_C \,, \tag{1.1}$$

where $U(1)_Y \otimes SU(2)_L$ is the symmetry group of the unified electroweak interaction, with Y indicating the hypercharge and L the left-handed nature of the weak interaction, and $SU(3)_C$ is the symmetry group of the strong interaction.

The fermions, i.e. the leptons and quarks, are described by the Dirac equation, for which the Lagrangian is

$$\mathcal{L} = \bar{\psi} \left(i \gamma^\mu \partial_\mu - m \right) \psi \,. \tag{1.2}$$

Here, ψ is the fermion field, γ^μ are the Dirac matrices and m is the mass of the fermion.

The existence of the vector bosons, as well as their interactions with the fermions, can be explained by requiring local gauge invariance under the aforementioned symmetry groups. The gauge invariance can be satisfied by the so-called minimal substitution. For this, the partial derivative ∂_μ is changed to

$$D_\mu = \partial_\mu - ig A_\mu^a t^a \,. \tag{1.3}$$

In this, g is a coupling strength, and t^a stands for the generators of the underlying symmetry group with the associated gauge field A. The kinematic behaviour of the gauge bosons is described by

$$\mathcal{L} = -\frac{1}{4} F_{\mu\nu}^a F^{a\mu\nu} \,, \text{ with} \tag{1.4}$$

$$F_{\mu\nu}^a = \partial_\mu A_\nu^a - \partial_\nu A_\mu^a + g f^{abc} A_\mu^b A_\nu^c \,, \tag{1.5}$$

with the vector boson field A, the coupling strength g and the structure constant f^{abc} of the underlying gauge symmetry. The generators t^a and the structure constants are related via the commutation relation $[t^a, t^b] = i f^{abc} t^c$.

The change of the derivative introduces a description of the interaction between fermions and the gauge bosons, with terms like

$$- g \bar{\psi} \gamma^\mu A_\mu^a t^a \psi \,, \tag{1.6}$$

as well as self-interaction terms for the vector bosons, as long as the structure constants f^{abc} are not zero.

1.3 Electroweak interactions

The electromagnetic and weak interactions of the Standard Model are described by a unified, electroweak theory. This includes the flavour-conserving, neutral interactions mediated by the photon and the Z boson, as well as the flavour-changing, charged interactions via the $W^\pm$ bosons. The latter interactions are maximally parity violating and only couple to left-handed fermions. The two components of a fermion field can be expressed as

$$\psi_{L/R} = \frac{1}{2} \left(1 \mp \gamma^5 \right) \psi \,, \tag{1.7}$$

where $\gamma^5 = i \gamma^0 \gamma^1 \gamma^2 \gamma^3$ is the product of the Dirac matrices.

The description of the electroweak interactions relies on the gauge invariance of the Lagrangian under the $U(1)_Y \times SU(2)_L$ group and the introduction of the gauge bosons B and W^i ($i = 1-3$). The coupling constants related to the two groups are independent and called g' and g.

The conserved quantum number corresponding to the $U(1)_Y$ symmetry is the hypercharge Y. Although the electromagnetic interaction can also be described by a $U(1)$ symmetry, the B field does not correspond directly to the photon. Formally, the structure constant of the $U(1)_Y$ group is zero, showing that no self-interaction of the gauge field exists.

The $SU(2)_L$ symmetry group, where the L subscript stands for the coupling to left-handed fermions, has the generators

$$t^i = \frac{\sigma^i}{2}, \ (i = 1-3) \,, \tag{1.8}$$

where the σ^i stands for the Pauli matrices. The corresponding structure constant is the totally anti-symmetric tensor ε^{ijk}.

Left-handed fermions transform as doublets under the $SU(2)_L$ interaction, while right-handed fermions transform as singlets:

$$f_L = \begin{pmatrix} u_L \\ d_L \end{pmatrix}, \begin{pmatrix} \nu_L \\ \ell_L \end{pmatrix}, \tag{1.9}$$

$$f_R = u_R, d_R, \ell_R, \tag{1.10}$$

for each of the three generations. Here, u stands for up-type quarks, d for down-type quarks, ℓ for the charged leptons and ν for the neutrinos. As neutrinos only interact via the weak interaction, right-handed neutrinos are not included in the Standard Model.

In the Lagrangian, the interaction terms according to Equation (1.6) for the weak interaction give

$$-g\bar{\psi}\gamma^\mu \frac{\sigma^i}{2} W^i_\mu \psi = -\frac{g}{2}\bar{\psi}\gamma^\mu \begin{pmatrix} W^3_\mu & W^1_\mu - iW^2_\mu \\ W^1_\mu + iW^2_\mu & W^3_\mu \end{pmatrix} \psi. \tag{1.11}$$

It is customary to write the off-diagonal entries of the W field matrix as

$$W^\pm = (W^1 \mp iW^2)/\sqrt{2}, \tag{1.12}$$

which define expressions for the observed $W^\pm$ bosons. As required, the coupling is flavour-changing, as it connects up- and down-type elements of left-handed fermion doublets in the interaction terms. It also describes the observed universality of the flavour-changing coupling for quarks and leptons, as only one coupling parameter g is involved.

For the quarks, the flavour eigenstates do not correspond directly to their mass eigenstates, but are linear combinations instead. The unitary Cabibbo-Kobayashi-Maskawa (CKM) matrix gives the appropriate combination factors.

The observed neutral and electromagnetic interactions can be described by taking linear combinations of the neutral fields W^3 and B, called Z and A,

$$\begin{pmatrix} Z_\mu \\ A_\mu \end{pmatrix} = \begin{pmatrix} \cos\theta_W & -\sin\theta_W \\ \sin\theta_W & \cos\theta_W \end{pmatrix} \begin{pmatrix} W^3_\mu \\ B_\mu \end{pmatrix}. \tag{1.13}$$

The field A represents the photon and couples with a constant of $g\sin\theta_W = g'\cos\theta_W = e$. Being a mixture of the W^3 and the B fields enables equal interactions with both left- and right-handed fermions, as required for the description of the photon. The coupling of the neutral weak interaction, mediated by the Z boson, is $e/(\sin\theta_W \cos\theta_W)$. The hypercharge Y of the $U(1)_Y$ symmetry and the weak isospin t^3 can be related to the electric charge of a particle according to the Gell-Mann Nishijima relation,

$$Q = t^3 + Y. \tag{1.14}$$

While the observed fermions as well as the W and Z bosons are massive, the introduction of explicit mass terms in the Lagrangian would break the $SU(2)$ symmetry. This is solved by the Higgs mechanism.

1.3.1 Higgs mechanism

In the Higgs mechanism, an additional $SU(2)$ doublet of complex, scalar fields is introduced, which together with its potential leads to a spontaneous breaking of the $U(1)_Y \times SU(2)_L$ symmetry of the
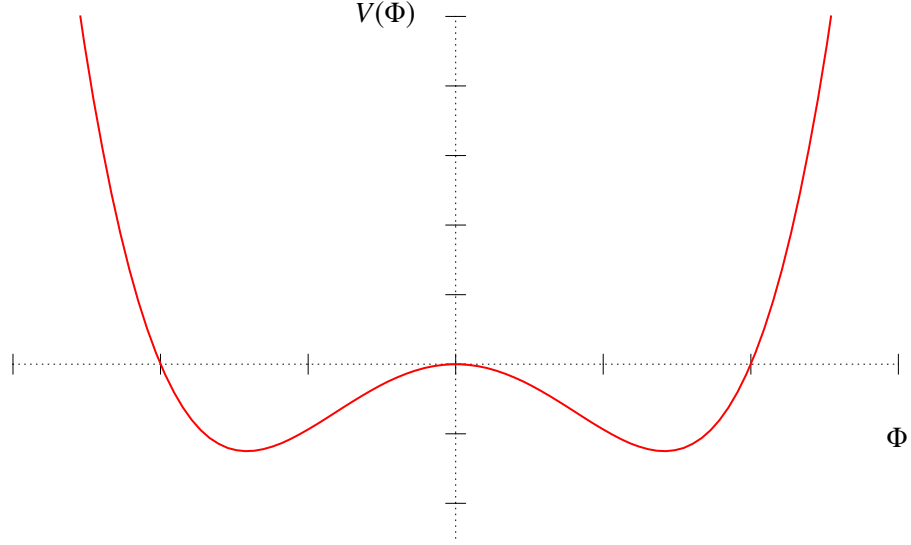
Figure 1.1: Sketch of the "mexican hat" Higgs potential in one dimension.

unified electroweak interaction into the observed $U(1)_{\text{EM}}$ symmetry. The doublet contains fields of positive and neutral charge,

$$\Phi = \begin{pmatrix} \phi+ \\ \phi^0 \end{pmatrix} . \tag{1.15}$$

The Lagrangian of the scalar field is

$$\mathcal{L} = \left(D_\mu \Phi\right)^\dagger \left(D^\mu \Phi\right) - \mu^2 \Phi^\dagger \Phi - \lambda \cdot (\Phi^\dagger \Phi)^2 , \tag{1.16}$$

where the first term describes the kinematic properties of the field and includes interaction terms with the gauge bosons, and the latter terms are the potential of the new field. Figure 1.1 shows a sketch of the potential, for which the parameters are chosen to be $\mu^2 < 0$ and $\lambda > 0$, leading to a minimum at

$$\Phi^\dagger \Phi = -\frac{\mu^2}{2\lambda} = \frac{v^2}{2} . \tag{1.17}$$

The field thus acquires a non-zero vacuum expectation value, defined as $\langle 0|\Phi|0\rangle = v/\sqrt{2}$. In the space of the four field degrees of freedom, the minimum is degenerate in three directions.

The vacuum expectation value is not invariant under $U(1)_Y \times SU(2)_L$ transformations and there is no unique minimum of the potential. The spontaneous breaking of the symmetry into the $U(1)_{\text{EM}}$ leads to three massless scalar particles, following the Goldstone theorem [15, 16]. These scalars appear as longitudinal polarisations of the gauge bosons in the theory, which in turn acquire mass. The neutral Higgs field is chosen to have the vacuum expectation value, $\Phi = (0 \; v)^{\text{T}}$. The kinetic term of the scalar field Lagrangian in Equation (1.16) then includes

$$\left\| \left(-ig\frac{\sigma^i}{2} W_\mu^i - i\frac{g'}{2} B_\mu \right) \begin{pmatrix} 0 \\ v \end{pmatrix} \right\|^2 \tag{1.18}$$

$$= \frac{1}{8} v^2 g^2 \left((W_\mu^1)^2 + (W_\mu^2)^2 \right) + \frac{1}{8} v^2 (g' B_\mu - g W_\mu^3)^2 . \tag{1.19}$$

With the transformation of $W^{1,2}$ into $W^{\pm}$ (see Equation (1.12)), the first term can be written as

$$\left(\frac{gv}{2}\right)^2 W_{\mu}^+ W^{-\mu} \ . \tag{1.20}$$

Thus, the mass of the charged W boson follows to $m_W = gv/2$.

The second term of Equation (1.19) can be identified with the mass term of the Z boson field as in Equation (1.13):

$$Z_{\mu} = \frac{1}{\sqrt{g^2 + g'^2}}(gW_{\mu}^3 - g'B_{\mu}) \ , \tag{1.21}$$

$$m_Z = \sqrt{g^2 + g'^2}\frac{v}{2} \ . \tag{1.22}$$

The remaining eigenstate, orthogonal to the Z field, is massless and represents the photon field,

$$A_{\mu} = \frac{1}{\sqrt{g^2 + g'^2}}(gW_{\mu}^3 + g'B_{\mu}) \ . \tag{1.23}$$

Mass terms for fermions can be added to the theory by Yukawa interactions with the Higgs doublet:

$$\mathcal{L} = y_f \left(\bar{f}_L \Phi f_R + \bar{f}_R \bar{\Phi} f_L\right) \ , \tag{1.24}$$

where y_f is the Yukawa coupling of the fermion f to the Higgs field. Such Yukawa terms are $SU(2)_L$ singlets and therefore do not break the gauge symmetry. The tree-level mass term for the fermion then follows to $m_f = y_f v/\sqrt{2}$. Since y_f is a free parameter in the theory, this procedure does not predict the fermion masses.

Additionally, the Higgs mechanism predicts a massive, scalar boson. The field can be expanded as a perturbation around the vacuum expectation value:

$$\Phi(x) = \frac{1}{\sqrt{2}} \begin{pmatrix} 0 \\ v + H(x) \end{pmatrix} \ . \tag{1.25}$$

Here $H(x)$ stands for fluctuations along the direction perpendicular to the direction of constant, minimal potential and represents the aforementioned boson. The mass of the boson follows from the potential term in Equation (1.16), $m_H = \sqrt{2\lambda}v$. As λ is a free parameter, the mass is not predicted by the theory. Interactions of the Higgs boson with the gauge bosons, as well as with fermions, follow from the same terms as the tree-level mass predictions when including the perturbation as in Equation (1.25). This structure explains that the coupling strength depends on the mass of the particles interacting with the Higgs boson.

1.4   Strong interactions

The strong interactions of quarks and gluons is described by the theory of Quantum Chromodynamics (QCD). Experimentally, no free quarks or gluons are observed, but experimental setups like deep inelastic scattering experiments confirm that hadrons are bound states of smaller particles, called partons. The description of QCD relies on a quantum number called colour, which labels three different states a quark can be in. The underlying symmetry of QCD is $SU(3)_C$, which represents rotations in the colour space.

The Lagrangian density for QCD is given by

$$\mathcal{L} = \sum_q \bar{\psi}_q \left(i\gamma^\mu D_\mu - m_q \right) \psi_q - \frac{1}{4} G^a_{\mu\nu} G^{a\mu\nu} \,, \text{ with} \tag{1.26}$$

$$D_\mu = \partial_\mu - i g_S t^a G^a_\mu \,, \tag{1.27}$$

$$G^a_{\mu\nu} = \partial_\mu G^a_\nu - \partial_\nu G^a_\mu - g_S f^{abc} G^b_\mu G^c_\nu \,. \tag{1.28}$$

The ψ_q stand for the fermionic quark fields, for all quark flavours q with masses m_q, and the G^a_μ represent the gluons, with $a = 1-8$. The covariant derivative contains the generators of the $SU(3)_C$, t^a, and the definition of $G^a_{\mu\nu}$ includes the structure constant of the symmetry group, f^{abc}. Quarks are in the fundamental representation of the $SU(3)_C$, representing the fact that there are three different colour states, while gluons transform according to the adjoint representation, describing the eight different gluon states. The g_S is the coupling constant of the strong force, which is conventionally expressed as $\alpha_S = g_S^2/4\pi$.

Since the structure constant of the $SU(3)_C$ is not zero, the theory describes self-interactions between the gluons. This leads to a strong energy dependence of the coupling α_S, which in leading-order can be expressed as

$$\alpha_S(Q^2) = \frac{\alpha_S(\mu^2)}{1 + \beta_0 \, \alpha_S(\mu^2) \ln \left(Q^2/\mu^2 \right)} \,, \text{ with} \tag{1.29}$$

$$\beta_0 = \frac{33 - 2n_f}{12\pi} \,. \tag{1.30}$$

Here, $\alpha_S(\mu^2)$ is the value of the strong coupling at a reference scale μ^2, and the factor n_f in the expression for β_0 is the number of quark flavours with $m_q < Q$.

At low energies, the value of α_S increases, even to a point where perturbative expansions in the coupling are no longer possible. This describes the observed confinement of quarks and gluons. When coloured particles separate from each other, the potential energy increases and it becomes energetically favourable to create quark–anti-quark pairs from the vacuum. Only colour-singlet states, either combinations of a colour and the same anti-colour, or of all three colours, are possible.

On the other hand, at high energies the coupling is reduced. This effect is called asymptotic freedom, as $\alpha_S \to 0$ for $Q \to \infty$, and describes the interactions of quasi-free quarks and gluons in high energy experiments.

1.5 Validation of the Standard Model

Since its creation, the Standard Model has been proven to be a reliable and precise description of particle physics phenomena. Although it has several free parameters, like the particle masses and the coupling constants of the three forces, the theory is found to be internally consistent. The GFITTER collaboration [17] has fitted the fundamental parameters of the SM to a variety of precision measurements. Figure 1.2 shows the deviations of the fit results, which are in good agreement with the measurements. None of the deviations exceeds three standard deviations. This shows that the measurements can be explained simultaneously in the theory.

Individual predictions of the theory, like event cross-sections, are validated in a magnitude of different measurements. Figure 1.3 shows selected results by the ATLAS collaboration as a function of the centre-of-mass energy. The measured cross-sections agree with the Standard Model predictions over close to 10 orders of magnitude, in a wide range of production modes.
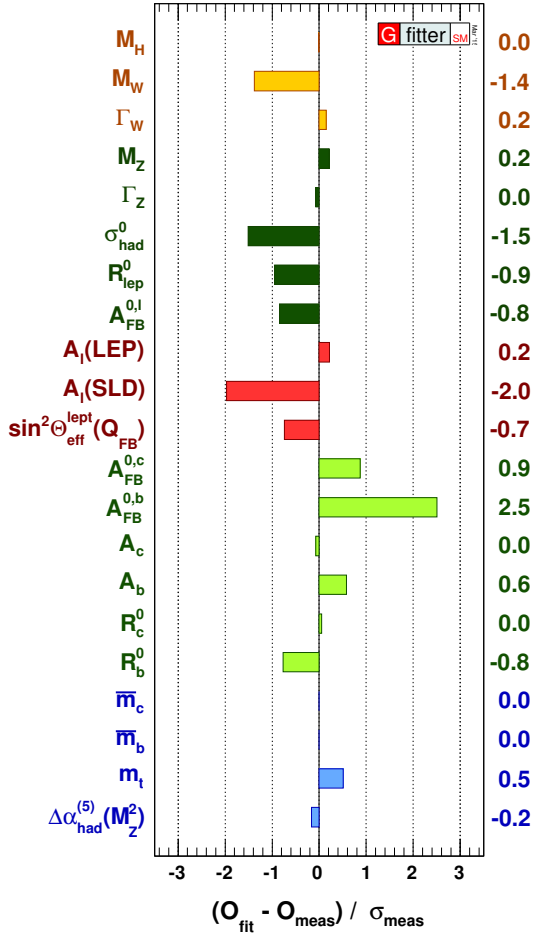
Figure 1.2: Differences of the results of the electroweak fit to the SM to the measurements, normalised to the measurement uncertainties [17].
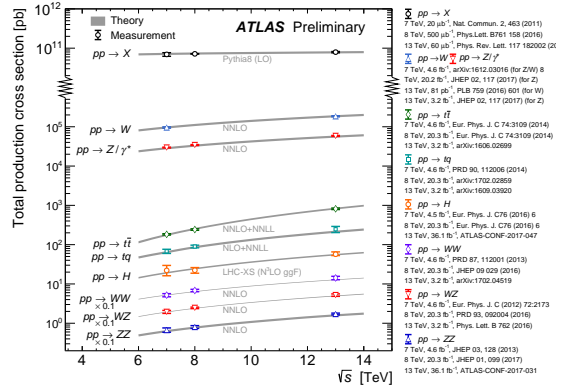
Figure 1.3: Summary of total production cross-section measurements as a function of centre-of-mass energy for selected processes. [18].
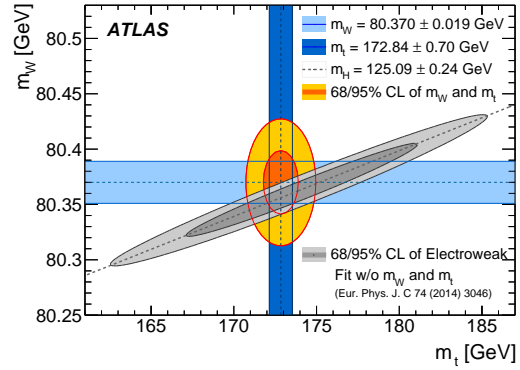
Figure 1.4: Comparison of the measurement and the indirect determination of the top quark mass and the W boson mass [19].

Due to radiative corrections, masses of particles can influence predictions, such as cross-sections or decay rates, even if they are not directly involved in the process. This allows to estimate the top quark mass from corrections to the W boson mass and the $Z \to b\bar{b}$ decay branching ratio, as well as the Higgs boson mass from electroweak precision measurements. Figure 1.4 alternatively shows recent measurement results for the top quark mass and the W boson mass, compared to the prediction based on such indirect effects. As can be seen, both the direct and the indirect measurements agree well, confirming the underlying theory for the indirect effects.

The discovery of the Higgs boson verifies the last prediction of the Standard Model. Measurements of the production cross-section of the Higgs boson are in good agreement with the Standard Model prediction [20]. Figure 1.5 additionally shows the results of a fit to scale factors for the Higgs coupling to fermions and vector bosons, based on ATLAS measurements in Run 1 of the LHC. The combination of the measurements in all decay modes is in agreement with the Standard Model.

This selection of precision measurements shows that the Standard Model is able to consistently and precisely describe most particle physics phenomena.
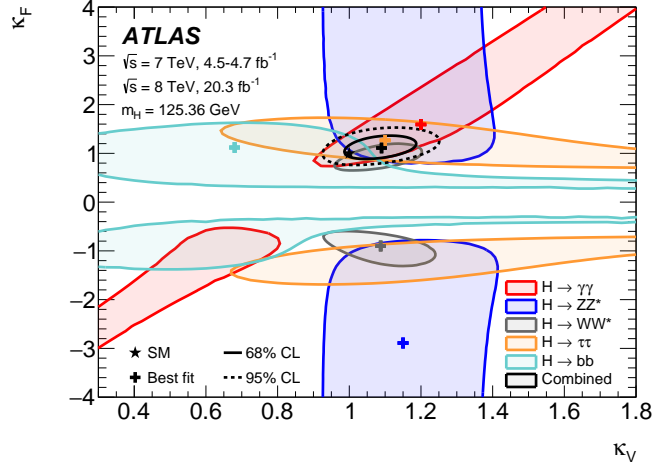
Figure 1.5: Results of the two-dimensional fit to the Higgs boson coupling-strength scale factors κ_F for fermions and κ_V for vector bosons [20].

1.6 Open questions in the Standard Model

Notwithstanding the success of the Standard Model, a number of experimental effects cannot be accommodated in the theory. Additionally, theoretical considerations point towards shortcomings of the theory and add to the motivation for a more complete theory, of which the SM is the low energy realisation.

Cosmological observations, such as the rotation curves of galaxies and galaxy clusters [21], as well as gravitational lensing and other effects, confirm the existence of non-luminous matter in the universe. This so-called dark matter does not interact electromagnetically, but can be seen due to gravitational effects. Measurements of the cosmic microwave background show that dark matter is about five times as abundant in the universe as ordinary matter [22]. The SM contains no particle that can explain the abundance of dark matter [12].

One of the few particle physics phenomena not described by the SM is neutrino oscillations [23], which require the neutrinos to have non-zero mass. The SM does not contain mass terms for the neutrinos, and no right-handed neutrino is included in the theory.

A second cosmological effect not explained by the SM is the low abundance of anti-matter in the universe compared to matter. Although the SM contains CP violating effects in the CKM matrix [24], the effect is not large enough to explain the observed asymmetry.

In addition to these non-described experimental observations, several theoretical considerations motivate additions to the SM. The SM has 19 free parameters when including a potential CP-violating QCD effect for which measurements are consistent with zero, but not considering neutrino masses. This large number of parameters itself is reason to suggest that the SM is only an effective theory based on a more complete theory with fewer free parameters. Furthermore, the mass parameters span six orders of magnitude, from the electron mass at 511 keV to the top quark mass at about 173 GeV. While this is no fundamental problem to the theory, it is seen as unnatural, as the SM does not offer any explanation for these differences.

The effects of gravity are not described by the SM. At the Planck Scale, $M_P \sim 10^{19}$ GeV, quantum gravitational effects become the same size as the other interactions and the SM in its current form breaks down. Strongly intervened with the large difference between the scale of gravity
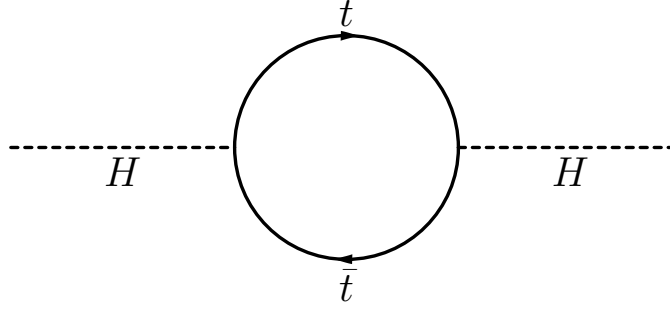
Figure 1.6: Example of a one-loop correction to the Higgs mass.

and that of the electroweak interactions is the hierarchy problem. Assuming that no physics beyond the SM occurs before the Planck scale, the Higgs boson receives large radiative corrections to the mass term. Unlike for fermions and gauge bosons, no symmetry protects the mass of fundamental scalar particles against such corrections.

The Higgs boson mass can be written as

$$m_H^2 = m_{H,0}^2 + \Delta m_H^2 \,, \tag{1.31}$$

where $m_{H,0}$ is the bare mass and Δm_H^2 is the radiative correction term. The contribution of the top quark to this term is shown in Figure 1.6. The value of this diagram is given by

$$\Delta m_H^2 = -\frac{y_t^2}{16\pi^2} \left(2\Lambda^2 + O\left(m_t^2 \ln \frac{\Lambda}{m_t} \right) \right) \,. \tag{1.32}$$

Here $y_t = \sqrt{2}m_t/v = 0.996 \pm 0.003$ is the top quark Yukawa coupling and Λ is the momentum cut-off for the top quark loop. The Higgs mass correction contains a quadratic dependence on the cut-off scale Λ. Assuming that the SM is valid up to the Planck scale, this correction is in the same order of magnitude. In order to receive the observed Higgs boson mass of 125 GeV, the bare mass would also need to be in the order of 10^{17} GeV to nearly cancel the contributions of the loop corrections. While this is certainly possible, the precision needed for this cancellation is regarded as highly unnatural and fine-tuned. Different mechanisms have been proposed which explain in a natural way the lightness of the Higgs boson mass.

Chapter 2 Vector-like quarks

The fine-tuning of the Higgs mass is mostly driven by the large top quark Yukawa coupling, which is directly proportional to the radiative corrections (see Equation (1.32)). Many theories beyond the Standard Model aim to explain the mass of the Higgs boson naturally. They therefore include a partner for the top quark, i.e., a particle with similar quantum numbers. The effects of this partner cancel out the top quark contributions to the radiative corrections.

A chiral fourth generation of quarks, or models including just a heavier, chiral copy of the top quark, are excluded by the measurements of the Higgs boson cross-section and decay branching ratios [25]. An alternative extension is the addition of so-called *vector-like* top quarks (VLTs), which are heavy, coloured, spin-$1/2$ fermions with the same electroweak couplings for the left- and right-handed components [26]. For these particles, a mass term such as

$$\mathcal{L} = m_T \bar{T} T \tag{2.1}$$

would not break the local $SU(2)_L$ invariance of the Lagrangian and is independent of the Higgs mechanism. The coupling of the vector-like top quark to the Higgs boson in loop-induced processes such as $gg \rightarrow H$ or $H \rightarrow \gamma\gamma$ is suppressed by the mass of the vector-like top quark. Due to mixing with the top quark, they can contribute to the radiative corrections to the Higgs mass, in processes such as those sketched in Figure 2.1. These contributions can resolve the quadratic divergences and solve the problem of fine-tuning.

Vector-like quarks (VLQs) are part of several models extending the SM. In "little Higgs" models [27, 28], the Higgs boson is a pseudo-Nambu-Goldstone boson from a spontaneously broken symmetry, explaining its lightness. Similarly, in composite Higgs models [29], the Higgs boson is a composite particle and thus protected from the strongly divergent radiative corrections. Both types of models include vector-like quarks, often with masses $O(1\text{ TeV})$. Vector-like quarks also appear in theories of gauge-coupling unification based on the E_6 symmetry group [30].
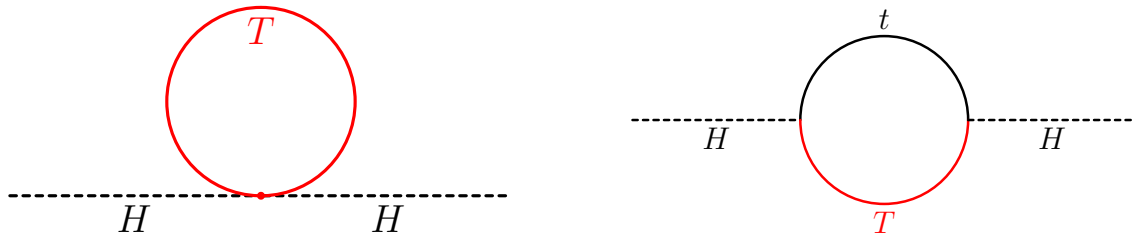
Figure 2.1: Radiative corrections to the Higgs mass involving a vector-like T quark.

Table 2.1: Vector-like quark $SU(2)_L$ multiplets with their hypercharges and charges.

Multiplet	Hypercharge	Charge
Singlets		
T	$+2/3$	$+2/3$
B	$-1/3$	$-1/3$
Doublets		
(X, T)	$+7/6$	$+5/3, \ +2/3$
(T, B)	$+1/6$	$+2/3, \ -1/3$
(B, Y)	$-5/6$	$-1/3, \ -4/3$
Triplets		
(X, T, B)	$+2/3$	$+5/3, \ +2/3, \ -1/3$
(T, B, Y)	$-1/3$	$+2/3, \ -1/3, \ -4/3$

In general, vector-like quarks can appear as singlets, doublets or triplets under $SU(2)_L$. Table 2.1 gives an overview of the possible multiplets of vector-like X, T, B and Y quarks, their charges and hypercharges.

2.1 Phenomenology

Vector-like quarks can mix with their SM counterparts, given the same quantum numbers, e.g. all up-like quarks including a vector-like T quark could mix. These generalised CKM-like mixing effects are suppressed by a factor of m_q/m_Q, where m_q is the mass of the SM quark and m_Q that of the VLQ. Together with constraints from precision measurements, it is therefore generally assumed that only the third-generation quarks mix with their vector-like counterparts.

At the LHC, vector-like quarks can be produced in pairs via the strong interaction, or singly via electroweak couplings. The pair production cross-section only depends on the strong coupling constant α_S and the mass of the VLQ. Figure 2.2 gives a representative diagram of the production
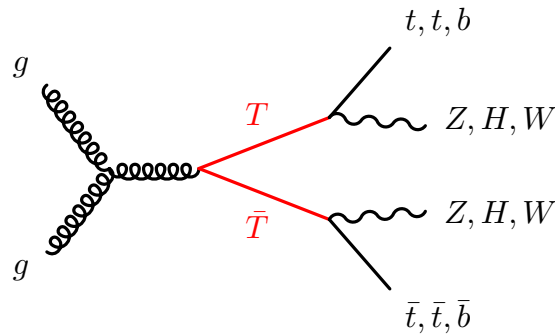
Figure 2.2: Example diagram for the production and decay of a vector-like top quark pair.
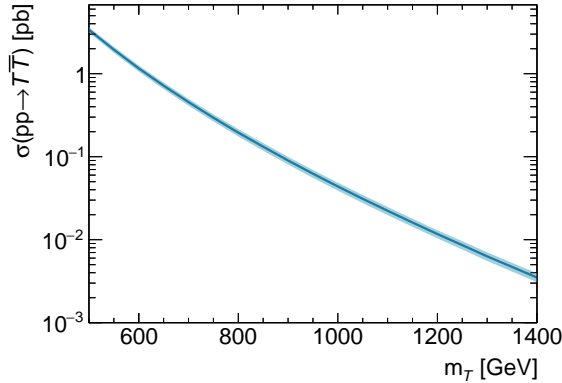
Figure 2.3: Production cross-section at next-to-next-to-leading order (NNLO) with next-to-next-to-leading logarithmic (NNLL) corrections for pairs of vector-like quarks [31–36]. The width of the curve represents the uncertainties due to the choice of factorisation and renormalisation scales, as well as the PDF uncertainty.

and the decay of a vector-like top quark pair. The cross-section in dependence of the VLQ mass is shown in Figure 2.3. The single production cross-section can surpass the pair production cross-section for vector-like quarks above a mass of about 1 TeV, but depends on the coupling of the VLQ to W and Z bosons.

The decays of vector-like quarks in general depend on the multiplet realisation. They can decay via flavour-changing neutral currents, breaking the Glashow-Iliopoulos-Maiani mechanism [37] due to their vector-like nature. Given the aforementioned mixing with third-generation quarks, vector-like quarks decay via the following processes [38]:

$$T \rightarrow Wb, Zt, Ht \, ,$$
$$B \rightarrow Wt, Zb, Hb \, ,$$
$$X \rightarrow Wt \, ,$$
$$Y \rightarrow Wb \, .$$

For $SU(2)_L$ singlets, all the mentioned decay modes are possible. For doublets and triplets, only small mass differences $O(1\,\text{GeV})$ between the VLQs are expected [26]. This makes cascade decays, such as $T \rightarrow WB$ impossible. For a (T, B) doublet, the decay modes depend on the generalised CKM matrix elements V_{Tb} and V_{tB}, i.e. on the mixing with the third generation quarks. For $V_{Tb} \simeq V_{tB}$ the same decays are possible as for the singlets. As in contrast to the singlet model, here only the right-handed component of (T, B) couples to the SM quarks, the polarisation of the quark in the decay differs. When instead $V_{Tb} \ll V_{tB}$, then the decays $T \rightarrow Wb$ and $B \rightarrow Zb, Hb$ are suppressed. This case is assumed to be natural, as it implies that the vector-like top quark mixes more strongly with the top quark, than the vector-like bottom quark with the bottom quark. In the case of a (X, T) doublet, the vector-like top quark has the same decay modes.

The focus of the analysis presented in this dissertation lies on the pair production of vector-like top quarks, with the $T \rightarrow Zt$ decay mode with one invisibly decaying Z boson as the target. The analysis thus selects final states similar to $t\bar{t}$ with additional missing transverse momentum. The branching ratios of the decay for the singlet model and for the doublet model with $V_{Tb} \ll V_{tB}$ are shown in Figure 2.4. For high T quark masses they converge to $\mathcal{B}(T \rightarrow Wb) \simeq 50\%$ and
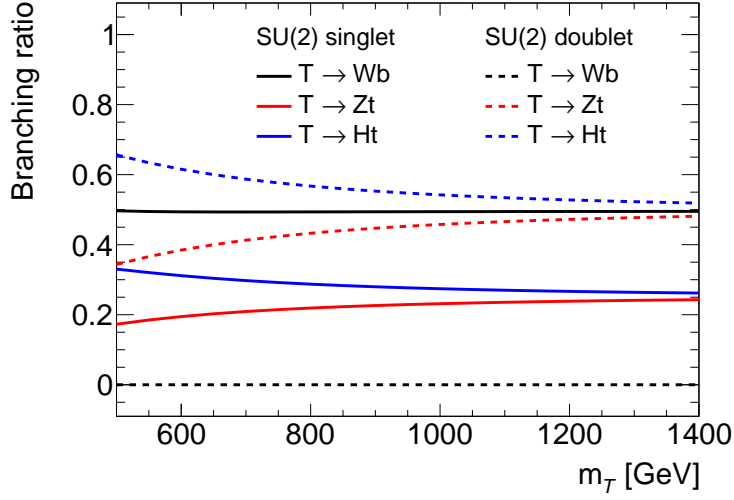
Figure 2.4: Branching ratios of the vector-like top quark decay for a $SU(2)_L$ singlet and for the $SU(2)_L$ doublet model, in case that $V_{Tb} \ll V_{tB}$ [38, 39].
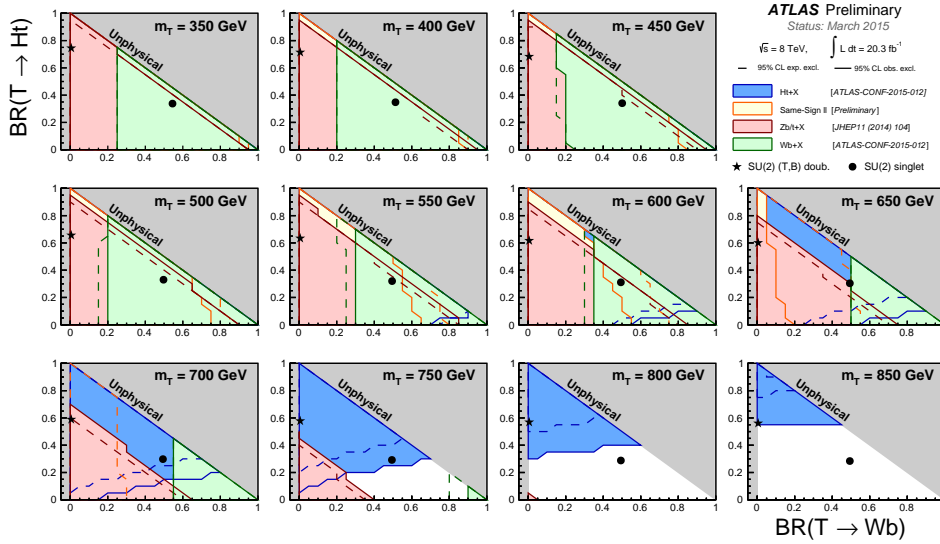
Figure 2.5: 95% confidence level (CL) excluded regions in the plane of $\mathcal{B}(T \rightarrow Wb)$ and $\mathcal{B}(T \rightarrow Ht)$ for various vector-like top quark masses [50]. The branching ratios sum to 100%, and $\mathcal{B}(T \rightarrow Zt) = 100\%$ in the lower left corner of each panel.

$\mathcal{B}(T \rightarrow Zt, Ht) \simeq 25\%$ for the T singlet, and to $\mathcal{B}(T \rightarrow Zt, Ht) \simeq 50\%$ and $\mathcal{B}(T \rightarrow Wb) = 0\%$ for the doublet model.

Previous searches targeting the pair production of vector-like quarks have been performed by the ATLAS and CMS collaborations at a centre-of-mass energy of $\sqrt{s} = 8$ TeV [40–47] and with the initial dataset for $\sqrt{s} = 13$ TeV [2, 48, 49]. Depending on the charge and the decay branching ratios, lower limits have been set on the VLQ mass in the range of 500 GeV to 1000 GeV. Figure 2.5 shows a summary of the ATLAS results at $\sqrt{s} = 8$ TeV.

Chapter 3 Supersymmetry

S upersymmetry is a possible extension of the space-time symmetries [51–53] and extends the Standard Model of particles physics. This chapter gives an overview of supersymmetry (SUSY) and the Minimal Supersymmetric Standard Model (MSSM), as well as details of the phenomenology of models with light top squarks. A detailed overview can be found in Ref. [54].

3.1 Introduction

A supersymmetry transformation relates fermionic and bosonic states. The symmetry generator Q is an anti-commuting spinor, defined as

$$Q \, |\text{fermion}\rangle = |\text{boson}\rangle \,, \qquad Q \, |\text{boson}\rangle = |\text{fermion}\rangle \,. \tag{3.1}$$

The hermitian conjugate of Q, $Q^\dagger$, is also a symmetry generator. Together with the four-momentum generator P^μ of space-time translations, these operators fulfil

$$\{Q, Q^\dagger\} = P^\mu \,, \tag{3.2}$$

$$\{Q, Q\} = \{Q^\dagger, Q^\dagger\} = 0 \,, \tag{3.3}$$

$$[P^\mu, Q] = [P^\mu, Q^\dagger] = 0 \,. \tag{3.4}$$

Irreducible representations of supersymmetry are called supermultiplets, which contain both fermionic and bosonic states. Following from the commutation relations, the number of fermion and boson degrees of freedom in one supermultiplet is always equal. As Q commutes with P^μ and therefore also P^2, it follows that all particles in a supermultiplet have exactly the same mass. The same applies to the gauge quantum numbers; all members of a supermultiplet have the same electric charge, weak isospin and colour.

Two types of irreducible supermultiplets exist. A *chiral* supermultiplet contains a single Weyl fermion with two spin helicity states as well as a complex scalar field. A *vector* or *gauge*

Table 3.1: Gauge supermultiplets in the MSSM.

Names	Spin $1/2$	Spin 1	$SU(3)_C, SU(2)_L, U(1)_Y$
gluino, gluon	$\tilde{g}$	g	8, 1, 0
winos, W bosons	$\widetilde{W}^\pm, \widetilde{W}^3$	$W^\pm, W^3$	1, 3, 0
bino, B boson	$\widetilde{B}$	B	1, 1, 0

Table 3.2: Chiral supermultiplets in the MSSM. Spin-0 fields are complex scalar fields, and spin-$1/2$ fields are left-handed, two-component Weyl fermions.

Names	Spin 0	Spin $1/2$	$SU(3)_C, SU(2)_L, U(1)_Y$
squarks, quarks	$(\tilde{u}_L \ \tilde{d}_L)$	$(u_L \ d_L)$	3, 2, $1/6$
($\times 3$ families)	$\tilde{u}_R^*$	$u_R^\dagger$	$\bar{3}$, 1, $-2/3$
	$\tilde{d}_R^*$	$d_R^\dagger$	$\bar{3}$, 1, $1/3$
sleptons, leptons	$(\tilde{\nu} \ \tilde{e}_L)$	$(\nu \ e_L)$	1, 2, $-1/2$
($\times 3$ families)	$\tilde{e}_R^*$	$e_R^\dagger$	1, 1, 1
Higgs, higgsinos	$(H_u^+ \ H_u^0)$	$(\widetilde{H}_u^+ \ \widetilde{H}_u^0)$	1, 2, $1/2$
	$(H_d^0 \ H_d^-)$	$(\widetilde{H}_d^0 \ \widetilde{H}_d^-)$	1, 2, $-1/2$

supermultiplet consists of a massless spin-1 boson and a massless Weyl fermion. When including gravity, a third type of supermultiplet containing the spin-2 graviton and its spin-$3/2$ superpartner is introduced.

The SM gauge bosons are parts of gauge supermultiplets, and their superpartners are called *gauginos*. A list of the gauge supermultiplets is given in Table 3.1. Both the gauge bosons and the gauginos transform under the adjoint representations of the gauge groups, with equal transformations for left- and right-handed components. The SM fermions therefore have to appear in chiral supermultiplets, for which the left- and right-handed couplings can differ. Their spin-0 partners are called *squarks* and *sleptons* (with the leading 's' abbreviating "scalar"). The Higgs boson is part of a chiral supermultiplet, together with the fermionic higgsino. In order to prevent a gauge anomaly, a supersymmetric SM needs two Higgs supermultiplets of hypercharges $Y = \pm 1/2$. The scalar Higgs fields mix and form mass eigenstates, of which the lightest corresponds to the Standard Model Higgs boson. Table 3.2 lists the chiral supermultiplets in the minimal supersymmetric extension of the SM.

If realised in nature, supersymmetry is necessarily broken. No scalar electron partner with a mass of $m_{\tilde{e}} = 511$ keV has been observed, nor any of the partners of the other light SM particles. Typical models assume *soft* SUSY breaking, i.e. only include mass terms and coupling parameters with positive mass dimension in SUSY-breaking terms. This form of SUSY-breaking preserves dimensionless couplings in the theory. While typically spontaneous symmetry breaking is assumed, the SUSY-breaking mechanism can be parametrised as additional terms in the effective Lagrangian density of the theory. This has the advantage of being unrestricted on the specific breaking model.

3.2 Phenomenology of the MSSM

The Minimal Supersymmetric Standard Model contains the minimal set of supermultiplets to describe all SM physics. In general, it includes 105 independent, free parameters in addition to the SM parameters, which are mostly in the SUSY breaking terms of the Lagrangian. Many of these parameters, which can be expressed as masses, phases and mixing angles, are strongly constrained by precision measurements of flavour physics and CP violation.

In the breaking of electroweak symmetry in the MSSM, both Higgs fields, H_u^0 and H_d^0, acquire vacuum expectation values, which sum up to the value known in the SM, $v_u^2 + v_d^2 = v^2$. The
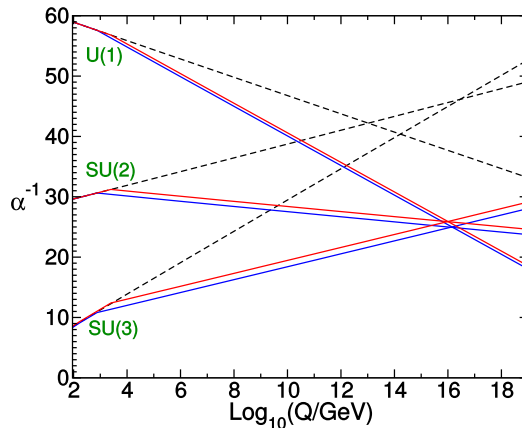
Figure 3.1: Evolution of the inverse coupling constants with energy in the SM (dashed lines) and in the MSSM (solid lines) for two common sparticle masses of 750 GeV (blue) and 2.5 TeV (red) [54].

ratio of the values is expressed as $\tan \beta = v_u/v_d$. Further parameters in the MSSM which are not strongly constrained by precision measurements are the higgsino mass parameter μ, as well as the gaugino mass parameters M_1, M_2 and M_3. Intrinsically, all undiscovered particles in the MSSM can have additional mass terms in the Lagrangian, making them naturally heavier than the particles discovered so far.

The parameters in the MSSM are subject to energy dependent evolution, just as in the SM. The evolution of the coupling constants is modified with respect to the SM, due to the presence of additional particles, which allows a unification of the couplings at high scales. Figure 3.1 shows the energy dependence of the inverse coupling constants α_i^{-1}. In the MSSM, the couplings unify at a scale of $M_U \sim 1.5 \times 10^{16}$ GeV.

3.2.1 *R*-parity

Generic soft SUSY breaking Lagrangians can include baryon and lepton number violating terms. Unsuppressed values of these couplings lead to rapid proton decay, which is incompatible with experimental results. In order to explain the strong suppression of these effects, an additional symmetry is included in the definition of the MSSM. The so-called *R*-parity is a multiplicative, conserved quantum number, defined as

$$P_R = (-1)^{3(B-L)+2s} \,, \tag{3.5}$$

where B and L are the baryon and lepton-numbers of the particle, and s is its spin.

R-parity is a discrete symmetry, and therefore commutes with the SUSY generator Q, even though SM and supersymmetric particles have different values of P_R. All SM particles as well as the additional Higgs bosons have even *R*-parity, while squarks, sleptons, gauginos and higgsinos have odd *R*-parity.

The consequence for the phenomenology of the MSSM is that sparticles can only be produced in even numbers. The lightest *R*-parity odd particle has to be stable, as it cannot decay into only SM particles. It is referred to as "lightest supersymmetric particle" (LSP). It is usually assumed to be only weakly interacting and is a candidate for a dark matter particle. All sparticles decay into a final state with an odd number of LSPs.

3.2.2 Mass mixing in the MSSM

After electroweak symmetry breaking, three of the eight scalar degrees of freedom in the Higgs sector of the MSSM become the longitudinal modes of the known, massive, weak bosons. The remaining five fields mix into five mass eigenstates. This results in two CP-even, neutral scalar bosons, h^0 and H^0, one CP-odd neutral scalar A^0 and two charged scalars $H^\pm$. The relations to the gauge eigenstates can be expressed via a mixing angle α and the ratio of the vacuum expectation values, $\tan\beta$. At tree-level, the mass of the lightest scalar boson is bound by the mass of the Z boson,

$$m_{h^0} < m_Z |\cos(2\beta)| \,. \tag{3.6}$$

Radiative corrections, such as given in Equations (1.32) and (3.9), can strongly influence this bound. The observed mass of 125 GeV then agrees with the upper bound of $m_{h^0} \lesssim 135$ GeV, which depends logarithmically on the mass of the top squark [54].

The gauginos of the electroweak bosons, as well as the higgsinos, mix due to the effects of electroweak symmetry breaking. The four neutral mass eigenstates are mixtures of $\widetilde{H}_u^0$, $\widetilde{H}_d^0$, $\widetilde{B}$ and $\widetilde{W}^3$, and are called *neutralinos*, $\tilde{\chi}_i^0$ with $i = 1 - 4$. The superpartners of the charged bosons, $\widetilde{H}^\pm$ and $\widetilde{W}^\pm$, mix into the two *charginos*, $\tilde{\chi}_i^\pm$ with $i = 1, 2$. The neutralino masses depend on the parameters M_1, M_2, μ and $\tan\beta$. Parametrised with the gauge couplings and the vacuum expectation values, the mixing is

$$\begin{pmatrix} \tilde{\chi}_1^0 \\ \tilde{\chi}_2^0 \\ \tilde{\chi}_3^0 \\ \tilde{\chi}_4^0 \end{pmatrix} = \begin{pmatrix} M_1 & 0 & -g'v_d/\sqrt{2} & g'v_u/\sqrt{2} \\ 0 & M_2 & gv_d/\sqrt{2} & -gv_u/\sqrt{2} \\ -g'v_d/\sqrt{2} & gv_d/\sqrt{2} & 0 & -\mu \\ g'v_u/\sqrt{2} & -gv_u/\sqrt{2} & -\mu & 0 \end{pmatrix} \begin{pmatrix} \widetilde{B} \\ \widetilde{W}^3 \\ \widetilde{H}_d^0 \\ \widetilde{H}_u^0 \end{pmatrix} \,. \tag{3.7}$$

Under the common assumption that $m_Z \ll |\mu|, M_1, M_2$, only small mixing effects are expected for the neutralinos, resulting in almost pure mass eigenstates. Many models predict that the lightest neutralino state is mostly "bino-like". In models with a unification of the gauge couplings, it follows that $M_2 \simeq 2 \times M_1$ and thus the mass of the second neutralino is close to twice as large as that of the first. Under the same assumptions, the chargino mixing is also small, and the mass of the lighter chargino is almost the same as that of the second neutralino.

As the squarks are scalar fields, they can mix and form six mass eigenstates for each of the left- and right-handed up-type and down-type squarks. The handedness of a squark refers to that of its fermionic partner. Assuming no additional sources of CP violation in the MSSM, the mixing in the first and second generation is small and only the third generation squarks can have very different masses because of the larger Yukawa-couplings.

The top squark mixing matrix can be expressed via a mixing angle $\theta_{\tilde{t}}$,

$$\begin{pmatrix} \tilde{t}_1 \\ \tilde{t}_2 \end{pmatrix} = \begin{pmatrix} \cos\theta_{\tilde{t}} & -\sin\theta_{\tilde{t}} \\ \sin\theta_{\tilde{t}} & \cos\theta_{\tilde{t}} \end{pmatrix} \begin{pmatrix} \tilde{t}_L \\ \tilde{t}_R \end{pmatrix} \,. \tag{3.8}$$

The two stop mass eigenstates are called $\tilde{t}_1$ and $\tilde{t}_2$ with $m_{\tilde{t}_1} < m_{\tilde{t}_2}$. Due to renormalisation-group effects, the top squarks are usually expected to be lighter than the other squarks. Typically the mixing effects are small and the lighter mass eigenstate $\tilde{t}_1$ is mainly composed of the partner of the right-handed top quark, $\tilde{t}_R$.

3.2.3 Higgs boson mass in the MSSM

Exact supersymmetry protects the masses of scalar fields from quadratic corrections as in the hierarchy problem (see Section 1.6). It relates the masses of scalar fields to that of their fermionic superpartners, which receive at most logarithmic corrections in higher orders. Even if supersymmetry is broken below a certain scale Λ, the additional particles contribute to the radiative corrections and can exhibit a cancellation effect. The contributions for a scalar S to the squared Higgs mass corrections is

$$\Delta m_H^2 = \frac{|y_S|^2}{16\pi^2} \left[2\Lambda^2 + O\left(m_S^2 \ln\left(\frac{\Lambda}{m_S} \right) \right) \right] \; . \tag{3.9}$$

Compared to the contributions of a fermion (see Equation (1.32)), this differs by the absolute sign. Figure 3.2 shows an example diagram for such corrections. When each fermion is accompanied by a scalar partner, the individual contributions cancel. Assuming a small mass difference $|m_S^2 - m_f^2|$ and equal couplings $y_S^2 = y_f^2$, the residual correction is then

$$\Delta m_H^2 = \frac{|y_f|^2}{16\pi^2} \left| m_S^2 - m_f^2 \right| \ln\left(\frac{\Lambda}{m_S} \right) + \cdots , \tag{3.10}$$

and requires a much smaller cancellation with the bare mass than the initial contributions. Supersymmetry ensures that each fermion has such a scalar partner. In soft Supersymmetry breaking scenarios, the couplings remain equal.
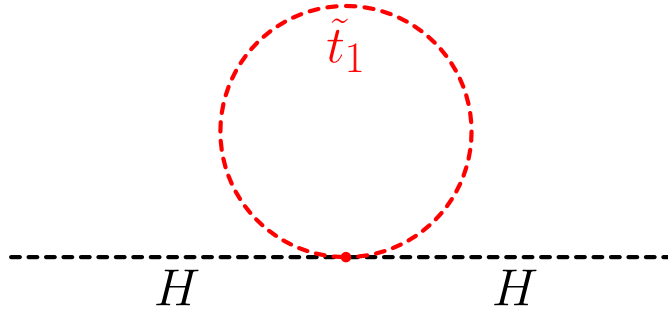
Figure 3.2: Example of a scalar one-loop correction to the Higgs mass.

3.3 Models with light top squarks

The analysis discussed in this dissertation targets signals with a light top squark (stop) at the electroweak scale. Because of the large top quark Yukawa coupling, the mass difference between the top squark and the top quark drives the residual corrections to the Higgs mass and therefore the question of fine-tuning. Thus, a small mass difference is preferred in natural models [55].

In general, the MSSM has 105 free parameters. In order to reduce the model dependence, simplified models [56, 57] are used, in which only a few supersymmetric particles are light, and all others are assumed to be decoupled. An alternative approach is the phenomenological MSSM (pMSSM) [58, 59], which is a subset of the MSSM tuned to fulfil phenomenological considerations. The pMSSM is parametrised by 19 values, specified at the electroweak scale, which are derived from the MSSM parameters by imposing constraints on additional sources of CP violation and flavour-changing neutral currents, as well as assuming universality of the first and second generation.
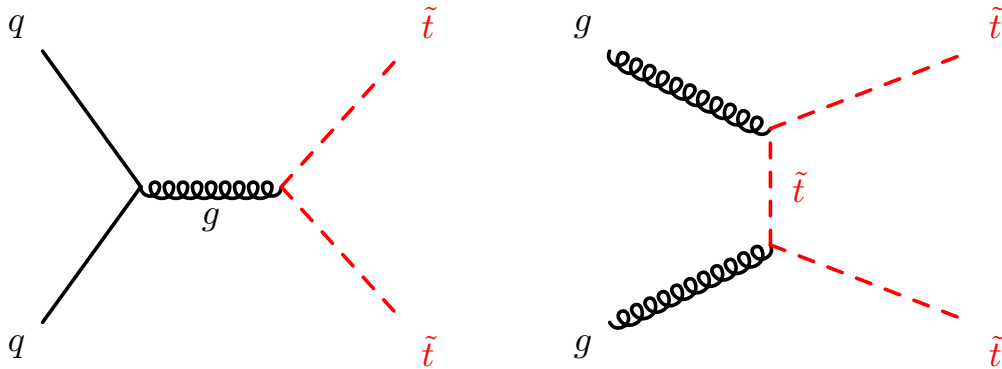
Figure 3.3: Example diagrams for the pair production of top squarks from quark–anti-quark annihilation and gluon fusion.

In general, the production of top squark pairs can, at leading order, occur via quark–anti-quark annihilation or gluon fusion. Figure 3.3 gives example diagrams for these processes. The production cross-section depends only on the strong coupling constant α_S and the mass of the top squark. Figure 3.4 shows the production cross-section as a function of the top squark mass, calculated at next-to-leading order (NLO) accuracy including the resummation of soft gluon emission at the next-to-leading logarithmic accuracy (NLL) [60].

Three models are considered in the analysis, differing by the choice of the LSP: A pure bino LSP, a higgsino LSP and a mixed bino/higgsino LSP model. Details on the motivation of these models as well as their phenomenology are given below.
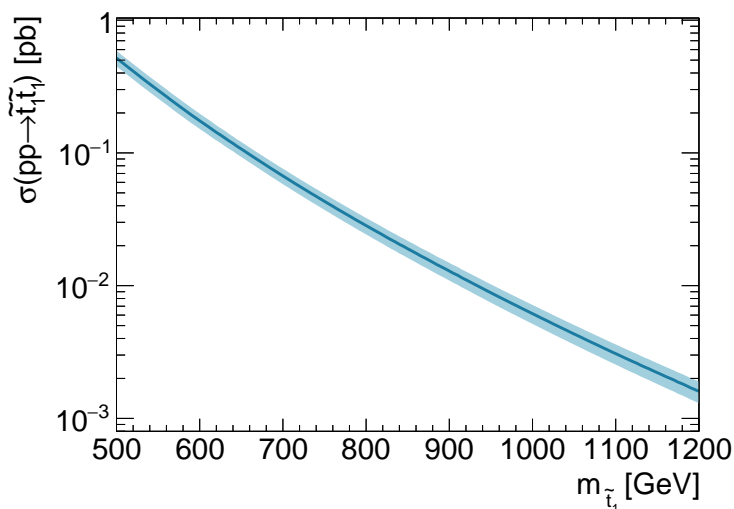
Figure 3.4: NLO+NLL cross-section for the pair production of top squarks [60]. The width of the line gives the uncertainty due to scale and PDF choices.

3.3.1 Bino LSP model

The main model considered in the analysis assumes a pure bino LSP. Only the top squark and the lightest neutralino are assumed to be light and all other sparticles are decoupled. The stop mixing angle is set to $\theta_{\tilde{t}} = 56°$, resulting in a top squark mass eigenstate with a right-handed component of about $\sin^2(\theta_{\tilde{t}}) \simeq 70\%$. This corresponds to the assumption that $|\mu|, M_2 \gg M_1 \gg m_Z$. The signal is modelled in terms of a simplified model, assuming that only the top squark and the neutralino exist.

The top squark decays into a top quark and the neutralino with a branching ratio of 100%, $\tilde{t}_1 \rightarrow t + \tilde{\chi}_1^0$, with the vertex sketched in Figure 3.5. Given that the coupling depends on the hypercharge, it is favoured even when other weak decay modes would exist, due to the large value of Y for the right-handed top squark. The pair production of top squarks in this model leads to a signature akin to that of $t\bar{t}$ production, but with additional missing transverse momentum in the final state, due to the weakly interacting neutralinos. The signals are parametrised by the masses of the top squark and the neutralino. In this dissertation, only the case $m_{\tilde{t}_1} > m_t + m_{\tilde{\chi}_1^0}$ is considered.

Previous searches targeting this model have been carried out by the ATLAS and CMS collaborations at centre-of-mass energies of $\sqrt{s} = 8$ TeV and 13 TeV. Figure 3.6 shows a summary of the $\sqrt{s} = 8$ TeV results by ATLAS [61]. The search excludes stop masses below 700 GeV at 95% CL, for neutralino masses below 100 GeV. At $\sqrt{s} = 13$ TeV, additionally, the top squark mass region of 745 GeV to 780 GeV is excluded for neutralino masses below 100 GeV to 150 GeV [2]. Similar searches by CMS exclude top squark masses below 800 GeV for neutralino masses below 150 GeV [62, 63].

An alternative model with a bino LSP additionally contains a wino as the next-lightest supersymmetric particle (NLSP). The mass of the wino NLSP is twice that of the bino LSP, following from the relation $M_2 = 2 \times M_1$ which is common in models with a unification of the gauge couplings. When assuming a mostly left-handed top squark, the decay mode $\tilde{t}_1 \rightarrow b + \tilde{\chi}_1^\pm$ is favoured. This model is not targeted by the analysis discussed in this dissertation, but is considered in the publication this analysis is part of [4].
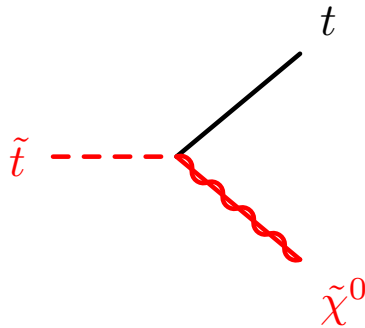
Figure 3.5: Decay of a top squark into a top quark and a neutralino.
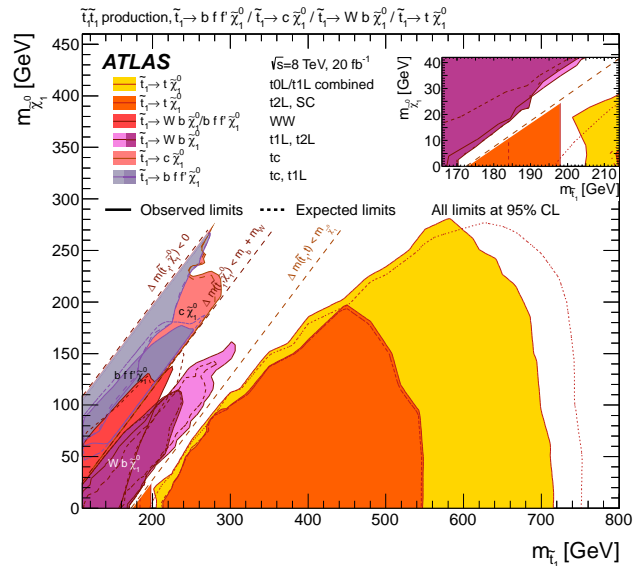
Figure 3.6: 95% CL excluded regions in the plane of $m_{\tilde{t}_1}$ versus $m_{\tilde{\chi}_1^0}$ [61].

3.3.2 Higgsino LSP model

Naturalness arguments support models with light higgsinos [64]. Thus, in addition to the bino LSP model, a model with a higgsino LSP and a light top squark is targeted in the analysis, corresponding to $M_2, M_1 \gg |\mu| \gg m_Z$. As this implies that all higgsino states are light, the model includes the $\tilde{\chi}_1^\pm$ and $\tilde{\chi}_2^0$ particles in addition to the top squark and the lightest neutralino. The mass spectrum is

$$\Delta m(\tilde{\chi}_1^\pm, \tilde{\chi}_1^0) = 0.5 \times \Delta m(\tilde{\chi}_2^0, \tilde{\chi}_1^0) < 30 \, \text{GeV} . \tag{3.11}$$

In addition to the $\tilde{t}_1 \to t + \tilde{\chi}_1^0$ decay mode, this model includes the decays $\tilde{t}_1 \to t + \tilde{\chi}_2^0$ and $\tilde{t}_1 \to b + \tilde{\chi}_1^\pm$. The $\tilde{\chi}_1^\pm$ and $\tilde{\chi}_2^0$ then subsequently decay through the emission of an off-shell W, Z or h boson, as depicted in Figure 3.7. The branching ratios of the decay modes depend on the stop mixing. Due to the structure of the stop-higgsino coupling, the $\tilde{t}_\text{L}$ decays dominantly into a neutralino, while the $\tilde{t}_\text{R}$ decays with a high branching ratio into $b + \tilde{\chi}_1^\pm$. Three different stop mixing assumptions are tested, covering the different topologies, as listed in Table 3.3.
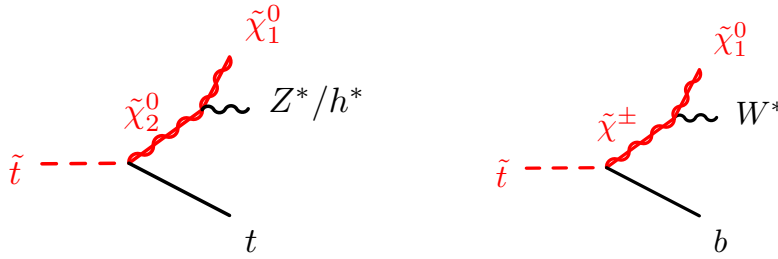
Figure 3.7: Decay of a top squark into a $\tilde{\chi}_2^0$ or a $\tilde{\chi}_1^\pm$, with the subsequent decays into the LSP.

Table 3.3: Decay branching ratios of the three different higgsino LSP models.

Model	$\mathcal{B}(\tilde{t}_1 \to t + \tilde{\chi}_2^0)$	$\mathcal{B}(\tilde{t}_1 \to b + \tilde{\chi}_1^\pm)$	$\mathcal{B}(\tilde{t}_1 \to t + \tilde{\chi}_1^0)$
$\tilde{t}_1 \sim \tilde{t}_\text{R}$	25%	50%	25%
$\tilde{t}_1 \sim \tilde{t}_\text{L}$	45%	10%	45%
$\tilde{t}_1 \sim \tilde{t}_\text{L}$, large $\tan\beta$	33%	33%	33%

3.3.3 Well-tempered neutralino model

The so-called well-tempered neutralino model aims to provide a dark matter candidate which is compatible with cosmological observations [65]. It assumes that $M_1 \simeq |\mu|$, resulting in a bino LSP and light higgsino states close in mass. For a light top squark, the possible decays are then $\tilde{t}_1 \to t + \tilde{\chi}_i^0$ for $i = 1, 2, 3$ and $\tilde{t}_1 \to b + \tilde{\chi}_1^\pm$. The heavier neutralino states, as well as the chargino then decay through the emission of an off-shell W, Z or h boson.

Two signal models are assumed, based on calculations in the pMSSM. Apart from the two scanned masses of the top squark and the bino, the model parameters are here set to fixed values allowing for low fine-tuning and a LSP annihilation rate consistent with the observed dark matter relic density. The two models differ in the stop mixing, with either $\tilde{t}_1 \sim \tilde{t}_\text{R}$ or $\tilde{t}_1 \sim \tilde{t}_\text{L}$. In the latter case, the lighter sbottom mass eigenstate, $\tilde{b}_1$, has a mass similar to the $\tilde{t}_1$ and can contribute to the observed final states. The relevant decays are $\tilde{b}_1 \to b + \tilde{\chi}_i^0$ for $i = 1, 2, 3$ and $\tilde{b}_1 \to t + \tilde{\chi}_1^\pm$.

Chapter 4 Event simulation

Predictions from the Standard Model as well as from Beyond the Standard Model theories rely on the simulation of scattering events, based on Monte Carlo event generators. These programs build on statistical integration methods, so-called "Monte Carlo integration", in order to numerically solve the incurring integrals.

For reliable predictions, complex processes need to be simulated: Starting with the interaction of two partons from the colliding protons, followed by subsequent radiation, the hadronisation of coloured particles, the underlying event, as well as the interaction of the final state particles with the detector material. This is possible due to factorisation, i.e. processes at different energy or length scales factorise and can be treated independently. In a coarse overview, the event simulation comprises the following steps:

- the modelling of the partons inside the proton,

- the actual parton–parton interaction in the so-called hard scattering event,

- the emission of radiation in the parton shower,

- low energy QCD effects like the hadronisation of coloured particles, followed by

- the simulation of the ATLAS detector.

The individual steps are discussed in this chapter, and can be found in more detail in Ref. [66]. Figure 4.1 illustrates the different steps outlined above.
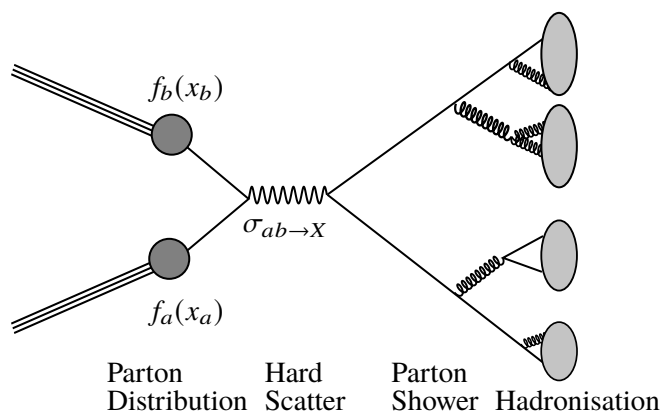
Figure 4.1: Sketch of a proton–proton collision with the different steps of the event simulation.

4.1 Factorisation and parton density functions

Due to the effect of asymptotic freedom, the partons inside the colliding protons behave nearly as free particles in the hard scattering event. This allows to formulate a proton–proton collision as the collision of two partons. With the factorisation theorem [67], the cross-section for the production of a final state X is given by

$$\sigma_{pp \to X} = \sum_{a,b} \int_0^1 dx_a dx_b f_a\left(x_a, \mu_F^2\right) f_b\left(x_b, \mu_F^2\right) \sigma_{ab \to X}\left(x_a p, x_b p, \mu_F^2\right) . \tag{4.1}$$

Here, a and b are all parton types which can lead to a final state X, and $\sigma_{ab \to X}$ is the cross-section for the process $ab \to X$. The parton density functions (PDFs) $f_i(x, \mu_F^2)$ give the probability of a parton of type i carrying a momentum fraction x of the proton. The factorisation scale μ_F separates the hard process from the parton density inside the proton. The effective centre-of-mass energy of the process is then $\hat{s} = x_a x_b s$.

Parton density functions are universal and do not depend on the particular process. As the parton density is a non-perturbative QCD effect, no analytical solutions exist for the PDFs. Instead, parametrised functions are fitted to measurements of deep inelastic scattering processes and from hadron colliders. The dependence of the PDFs on the energy scale Q is expressed by the QCD evolution equations [68–70]. Figure 4.2 shows as an example the PDFs for u, d and s quarks and the gluon at $Q^2 = (100\,\text{GeV})^2$, from the CT14 PDF set [71].
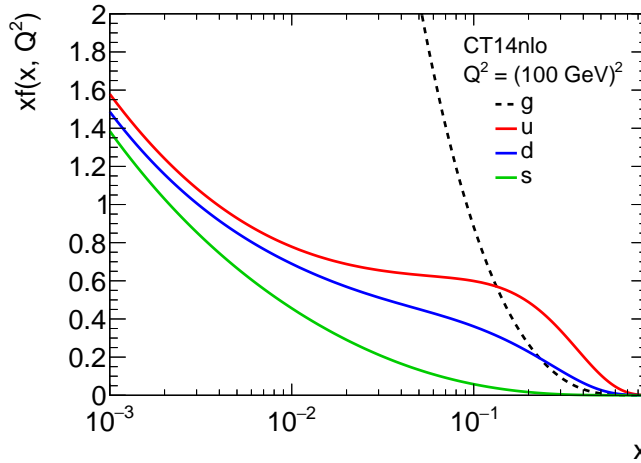
Figure 4.2: The CT14 parton density functions [71, 72] for gluons, u, d and s quarks at $Q^2 = (100\,\text{GeV})^2$.

4.2 Calculation of the hard scattering cross-section

The partonic cross-section $\sigma_{ab \to X}$ involves only high energy transfers and can be calculated in perturbative QCD. The calculation of the hard scattering cross-section involves the final state phase-space, as well as the matrix element $\mathcal{M}$ of the process. The matrix element is determined from the relevant Feynman diagrams, which represent the possible transitions of the initial to the

final state. Schematically, the cross-section can be written as

$$\sigma_{ab \to X} = \int d\Phi \, |\mathcal{M}_{ab \to X}(\Phi; \mu_R, \mu_F)|^2 \,, \tag{4.2}$$

where $d\Phi$ is the phase-space factor. The matrix element $\mathcal{M}$ additionally depends on the renormalisation scale μ_R and the factorisation scale μ_F.

The calculation of the cross-section is usually done at a fixed order in the strong coupling constant α_S, including effects of virtual corrections ("loops") and real emission ("legs"). Divergences from both kind of corrections cancel at any fixed order, following the KLN theorem [73, 74].

4.3 Parton shower

The matrix element calculation gives the cross-section for the exclusive final state X. Using a parton shower algorithm, the effects of higher orders, e.g. the radiation of additional jets, can be simulated [66]. Parton showers are typically formulated as the evolution of the momentum transfer from the hard process down to a low scale Q_0 in the order of $\mathcal{O}(1 \text{ GeV})$.

Parton shower algorithms simulate the emission of quarks and gluons from coloured particles. They can also include electromagnetic radiation, which is suppressed by a factor of α_{em}/α_S.

The cross-section for a final state with $n + 1$ partons can be approximated to

$$d\sigma_{n+1} \simeq d\sigma_n \frac{\alpha_S}{2\pi} \frac{dq^2}{q^2} dz \, P_{ji}(z) \,, \tag{4.3}$$

assuming almost collinear splitting. Here, $P_{ji}(z)$ are the Altarelli-Parisi splitting functions [70], which give the probability distribution of splitting an initial particle i into a particle j with the momentum fraction z. The process also depends on the phase-space of the splitting, parametrised by the virtuality q^2. The three possible emissions in QCD are the radiation of a gluon from either a quark or a gluon, $q \to qg$ and $g \to gg$, or the splitting of a gluon into a quark–anti-quark pair, $g \to q\bar{q}$.

The splitting functions P_{ji} diverge for soft or collinear emissions. In order to remove these divergences, a cutoff Q_0 is introduced on the transverse momentum of the daughter particle j relative to the parent particle i. Any emission below the cutoff is not resolvable and can be interpreted as no emission. In order to compute the probability of no resolvable emission, a unitarity argument is used: the sum of the probability of no resolvable emission and that of any resolvable emission has to be unity, giving a way to formulate the former in terms of the latter.

Given an initial scale Q^2 and a lower, final scale q^2, the Sudakov form factor $\Delta_i(Q^2, q^2)$ then gives the probability of no resolvable emission from a parton i during the evolution from Q^2 to q^2. The form factor is given by

$$\Delta_i(Q^2, q^2) = \exp \left(- \sum_j \int_{q^2}^{Q^2} \frac{dk^2}{k^2} \frac{\alpha_S}{2\pi} \int_{z_{min}(k^2)}^{z_{max}(k^2)} dz \, P_{ji}(z) \right) \,, \tag{4.4}$$

where the sum goes over all possible emissions, and the integration limits z_{min} and z_{max} take the cutoff into account.

The parton shower algorithm then applies the following steps to simulate final state radiation: Starting with the scale Q^2, splittings are generated for each outgoing parton with a probability of $d\Delta_i(Q^2, q^2)/dq^2$. This is repeated for all partons, now starting from the lower scale q^2, until q^2 is below the cutoff value.

Initial state radiation is simulated in a similar fashion by evolving the energy scale backwards from the hard scattering, while taking into account the PDF effects.

When adding the emission simulated by a parton shower algorithm to a higher order matrix element calculation, double counting of certain phase-space regions can happen. In order to prevent this, emissions generated by the parton shower are merged with the matrix element calculation. Techniques for this merging are implemented in the CKKW [75] and MLM [76] algorithms.

4.4   Hadronisation and low energy QCD effects

The parton shower stops at the hadronisation scale of $Q_0 \simeq 1$ GeV, at which the effect of confinement leads to the formation of hadrons. At this scale, the strong coupling constant α_S is large, and non-perturbative QCD effects dominate the processes. Event generators rely on phenomenological models to describe the formation of colour-singlet states. The two common models used are the string model [77] and the cluster model [78].
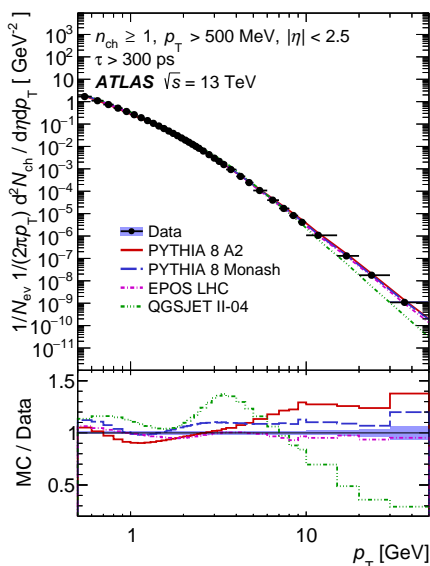
Figure 4.3: Charged-particle multiplicity as a function of the p_T in minimum bias events [1].

In the string model, the effects of confinement are modelled as colour strings with a linearly rising potential depending on the distance between two partons. When the partons move apart, the potential rises and breaks the string via the formation of new quark–anti-quark pairs. This process is repeated until all energy is converted into quark–anti-quark pairs, which then form the hadrons.

In the cluster model, partons are grouped to form colour-singlet clusters, after splitting each final state gluon into a quark–anti-quark pair. Clusters with a large mass are split. The clusters are then treated as excited states of hadrons, which then decay further.

Further low energy QCD effects have to be considered in the generation of proton–proton events. Additional activity is expected from the influence of the beam remnants and from multiple soft interactions between partons of the colliding protons. This activity is called the underlying event. Additional proton–proton collisions in the same bunch crossing, called pile-up, are modelled as so-called minimum bias interactions. These are soft QCD interactions, for which phenomenologically inspired models have to be used. These models are tuned to inclusive measurements, such as the charged-particle multiplicity in dependence of various observables, as shown in Figure 4.3.

4.5   Detector simulation

The simulation of the interactions of the final state particles from the generated events with the detector are performed using the GEANT 4 [79] particle-simulation toolkit. A detailed model of the ATLAS detector [80] is used to simulate the electromagnetic and hadronic interactions of the long-lived particles with the detector material. The detector response is digitised into the same format as measured, real events.

The ATLAS experiment at the Large Hadron Collider

Chapter 5 The Large Hadron Collider

The Large Hadron Collider (LHC) [81] is a particle accelerator at CERN, near Geneva. It is a two-ring superconducting synchrotron, with a circumference of nearly 27 km and a design centre-of-mass energy of 14 TeV for proton–proton collisions. At the four collision points of the accelerator ring, the major experiments are located: ALICE [82], ATLAS [83], CMS [84] and LHCb [85]. The ATLAS and CMS experiments are multi-purpose detectors with a nearly 4π solid angle coverage. The LHCb detector is designed for the study of b-hadron properties, and the ALICE experiment focuses on heavy-ion collisions.

Initially, the LHC was operated at about half its design energy and delivered proton–proton collisions at $\sqrt{s} = 7$ TeV in 2010 and 2011, as well as at $\sqrt{s} = 8$ TeV in 2012. In the run following the first long shutdown (LS1, 2013-14) the centre-of-mass energy was increased to $\sqrt{s} = 13$ TeV for 2015 and 2016. In addition to proton–proton collisions, the LHC can accelerate and collide heavy ions, producing lead–lead (Pb-Pb) collisions as well as proton–lead (p-Pb) collisions.
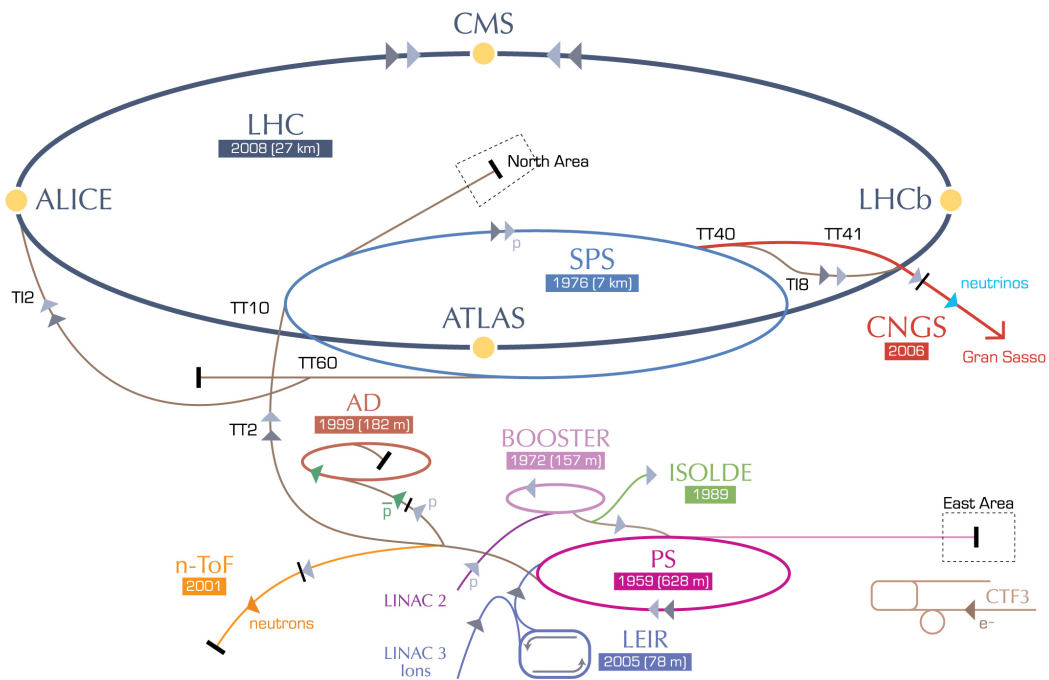
Figure 5.1: Schematic view of the CERN accelerator complex [86].

An overview of the CERN accelerator complex is shown in Figure 5.1. The protons for the LHC are accelerated in several steps. At first, protons are extracted from hydrogen gas using an electric field. The first acceleration step is carried out by the linear accelerator LINAC2, where the proton beam is accelerated to an energy of 50 MeV. The beam is then transferred into the Proton Synchrotron Booster (PSB), where it is accelerated to 1.4 GeV. The next accelerator in the sequence is the Proton Synchrotron (PS), in which the beam is accelerated to an energy of 25 GeV before being transferred into the Super Proton Synchrotron (SPS). This is the final pre-accelerator and increases the proton energy to 450 GeV, before the beams are injected into the LHC.

In the LHC, the proton beams are accelerated to an energy of 6.5 TeV per beam for the runs in 2015 and 2016, with the design value of 7 TeV per beam. The magnetic field needed in the dipole magnets, which are responsible for keeping the beam on a circular path, is 8.3 T. To realise this field strength, superconducting Niobium-Titan coils are used, which are cooled to a temperature of 1.9 K using superfluid Helium.

The event rate of a specific process in the proton–proton collisions depends on its cross-section, σ, as well as the instantaneous luminosity, $\mathcal{L}$, of the collider:

$$\frac{\mathrm{d}N}{\mathrm{d}t} = \mathcal{L} \cdot \sigma \ . \tag{5.1}$$

The instantaneous luminosity is defined in terms of machine parameters,

$$\mathcal{L} = \frac{n_b f_r n_1 n_2}{2\pi \Sigma_x \Sigma_y} \ , \tag{5.2}$$

where n_b is the number of proton bunches colliding each revolution, with the revolution frequency f_r and the numbers n_1 and n_2 of protons in the respective bunches. Σ_x and Σ_y specify the horizontal and vertical width of the beam, respectively. The beam dimensions can alternatively be described by the emittance and the β^* parameter, which is the envelope of the beam at the focus points. Table 5.1 gives an overview of the LHC machine parameters during 2015 and 2016, compared to the design values. The peak instantaneous luminosity in 2016 exceeded the design value by more than 40% with a value of $1.4 \times 10^{34} \, \mathrm{cm}^{-2}\mathrm{s}^{-1}$.

Integrating the instantaneous luminosity over the time with active collisions gives the total integrated luminosity. It is related via the cross-section to the number of events expected for a process,

$$N = \sigma \cdot \int \mathcal{L} \, \mathrm{d}t \ . \tag{5.3}$$

Table 5.1: Machine parameters of the LHC for 2015 and 2016 [87], compared to the design parameters [81].

Parameter	Design	2015	2016
Beam energy [TeV]	7	6.5	6.5
Bunch spacing [ns]	25	25	25
Beam focus β^* [cm]	55	80	40
Number of protons per bunch	1.15×10^{11}	1.15×10^{11}	1.15×10^{11}
Number of bunches per beam	2808	2244	2220
Peak luminosity [cm^{-2}s^{-1}]	1×10^{34}	0.5×10^{34}	1.4×10^{34}

The integrated luminosity delivered to the ATLAS experiment is shown in Figure 5.2, as a function of the time.
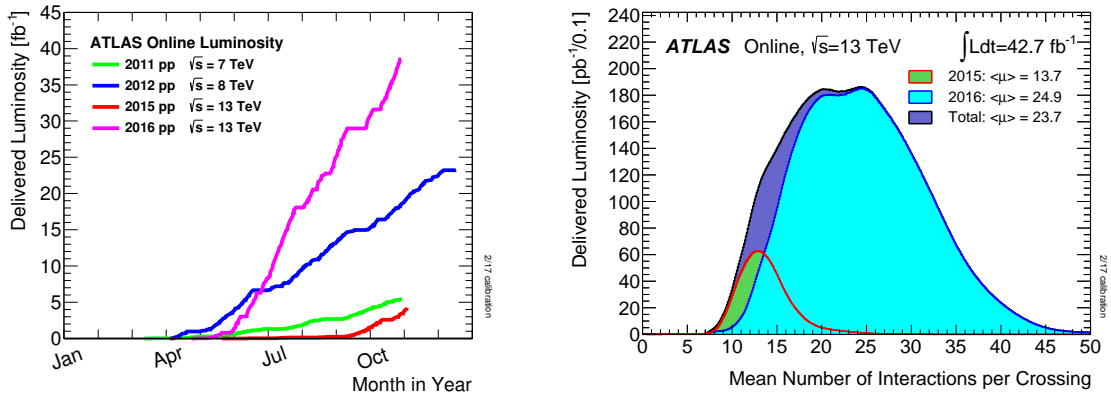
Figure 5.2: Integrated luminosity delivered to ATLAS versus the day (left) and the luminosity weighted distribution of the mean number of interactions per bunch crossing for 2015 and 2016 (right) [88, 89].

Due to the high instantaneous luminosity, typically more than one inelastic proton–proton collision occurs simultaneously in one bunch crossing, called pile-up. In addition to the in-time pile-up of events in the same bunch crossing, traces from events before the bunch crossing can be recorded and are referred to as out-of-time pile-up. The mean number of interactions per bunch crossing, $\langle \mu \rangle$, is shown in Figure 5.2 and gives a measure of the pile-up activity.

In total, the ATLAS experiment recorded an integrated luminosity of $39.5\,\mathrm{fb^{-1}}$ during stable-beam data taking with an overall efficiency of more than 92%, compared to the delivered luminosity of $42.7\,\mathrm{fb^{-1}}$. Of the recorded dataset, more than 90%, corresponding to $36.1\,\mathrm{fb^{-1}}$, fulfil all data quality requirements and are used for physics analyses. The mean number of interactions per bunch crossing in this period is $\langle \mu \rangle = 23.7$.

Chapter 6 The ATLAS experiment

The ATLAS experiment is one of the two general-purpose detectors at the LHC. Figure 6.1 shows a sketch of the 44 m long detector, with a radius of 25 m. The diverse physics goals of ATLAS, including the measurements of the Higgs boson properties in the various decay channels, as well as searches for physics beyond the Standard Model, demand a nearly full coverage around the collision point. This is realised by a cylindrical system, in which the sub-detectors are arranged in layers around the interaction point (IP). To extend the coverage in the forward regions, disks or end-caps are placed perpendicular to the beam direction at the end of the barrel parts.

The central part of the detector, the Inner Detector (ID), is a tracking system. It is surrounded by a superconducting Solenoid, providing a magnetic field of 2 T in order to bend the trajectories of charged particles and provide a measure of their momenta. The calorimeter is located outside the tracking system. It consists of two parts, the electromagnetic and the hadronic calorimeter, which stop most of the particles produced in the event and measure their energy. The outermost sub-detector is the Muon Spectrometer (MS) with superconducting toroid magnets. Table 6.1 gives the performance goals of the sub-systems.
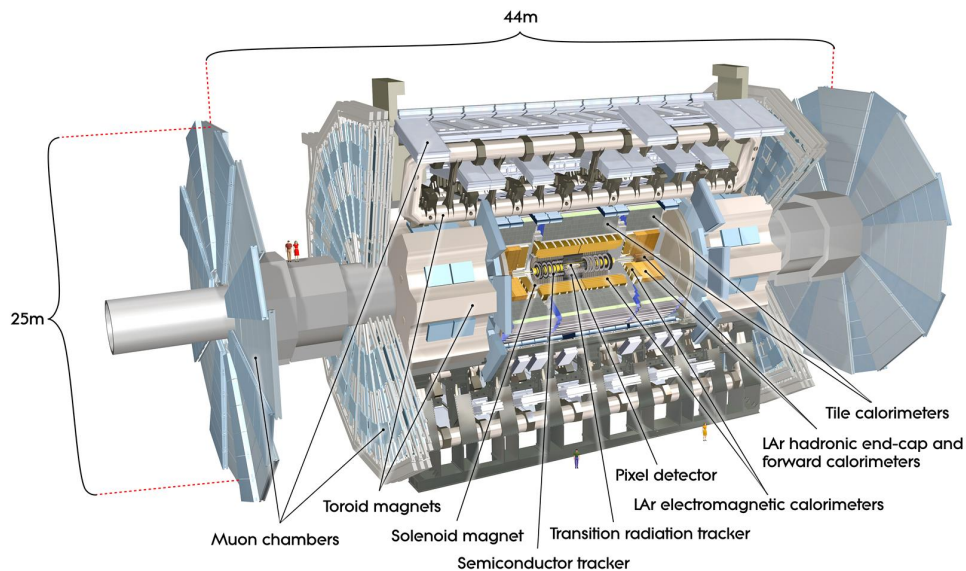
Figure 6.1: Overview of the ATLAS detector, with the different sub-detectors and the magnet systems [90].

39

Table 6.1: Performance goals of the ATLAS detector [83]. The units for E and p_{T} are in GeV.

Sub-detector	Resolution	Coverage
Inner Detector	$\sigma_{p_{\mathrm{T}}}/p_{\mathrm{T}} = 0.05\% \cdot p_{\mathrm{T}} \oplus 1\%$	$|\eta| < 2.5$
EM Calorimeter	$\sigma_E/E = 10\%/\sqrt{E} \oplus 0.7\%$	$|\eta| < 3.2$
Hadronic Calorimeter	$\sigma_E/E = 50\%/\sqrt{E} \oplus 3\%$	$|\eta| < 3.2$
Forward Had. Calorimeter	$\sigma_E/E = 100\%/\sqrt{E} \oplus 10\%$	$3.1 < |\eta| < 4.9$
Muon Spectrometer	$\sigma_{p_{\mathrm{T}}}/p_{\mathrm{T}} = 10\%$ at $p_{\mathrm{T}} = 1\,\text{TeV}$	$|\eta| < 2.7$

6.1 Coordinate system

ATLAS uses a right-handed, Cartesian coordinate system, with the origin at the place of the nominal interaction point. The z-axis points along the beam in anti-clockwise direction, the x-axis from the IP towards the centre of the LHC ring and the y-axis upwards. The azimuthal angle ϕ is measured perpendicular to the beam and the polar angle θ is defined with respect to the z-axis.

Since the initial momentum of the partons in the collision along the z-axis is not known, often the transverse momenta and energies of particles are used,

$$p_{\mathrm{T}} = p \cdot \sin\theta = \sqrt{p_x^2 + p_y^2} \;, \tag{6.1}$$

$$E_{\mathrm{T}} = E \cdot \sin\theta \;. \tag{6.2}$$

The initial state has zero transverse momentum. Instead of the angle θ, often the rapidity y of a particle is used:

$$y = \frac{1}{2} \ln\left(\frac{E + p_z}{E - p_z}\right) \;. \tag{6.3}$$

For particles that are massless or have high momentum compared to their rest mass the rapidity equals the pseudo-rapidity η, which can directly be related to the angle θ,

$$\eta = \frac{1}{2} \ln\left(\frac{|p| + p_z}{|p| - p_z}\right) = -\ln\left(\tan\frac{\theta}{2}\right) \;. \tag{6.4}$$

Differences in rapidity, Δy, are boost-invariant along the z-axis. The geometrical distance between particles is usually given in terms of ΔR,

$$\Delta R = \sqrt{(\Delta\phi)^2 + (\Delta\eta)^2} \;. \tag{6.5}$$

6.2 Inner Detector

The Inner Detector is the innermost sub-detector of the ATLAS experiment [91, 92]. Its task is to measure the trajectories of charged particles, allowing for the reconstruction of interaction and secondary decay vertices, as well as the measurement of charged-particle momenta. It covers the region $|\eta| < 2.5$. To enable the momentum measurement, the ID is embedded in a superconducting solenoid magnet, which provides a 2 T magnetic field parallel to the beam direction. Charged particles traversing the field are bent in the ϕ direction, with a radius proportional to their momenta.
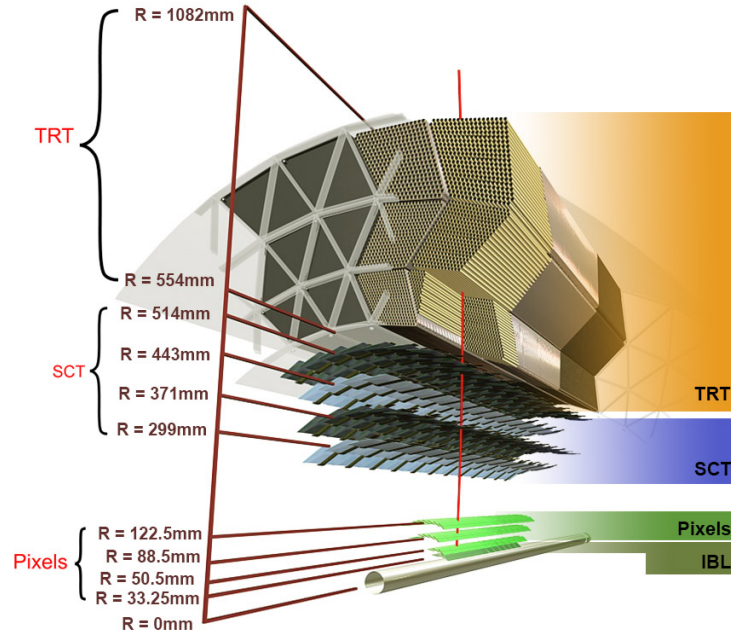
Figure 6.2: Schematic view of the barrel part of the inner detector [93].

The ID has a length of 6.2 m with a 2.1 m diameter, and consists of multiple layers of sensors in the barrel part, as well as discs placed perpendicular to the beam covering the forward region. Figure 6.2 shows a schematic view of the ID layers in the barrel region. The ID is divided into three sub-detectors, named Pixel detector, Semi-Conductor Tracker (SCT) and Transition Radiation Tracker (TRT).

Pixel detector

The Pixel detector is the innermost sub-detector of the ATLAS experiment and consists of four layers of silicon semi-conductor sensors (pixels), as well as three disks at each end of the sub-detector, covering the region $|\eta| < 2.5$. The innermost layer, called insertable b-layer (IBL), was added during the long shutdown of the LHC in 2013 and 2014 in order to improve the resolution of the tracking system [94]. It is located at a radius of 33 mm and consists of pixels with a size of 50 μm×250 μm. The outer three layers, as well as the disks, consist of pixels with a size of 50 μm×400 μm. The last layer is located at a radius of 12.25 cm. In total, the pixel detector has 86.6 million readout channels. The precision of the location measurement of particles traversing the detector is 10 μm in the $R - \phi$ plane and 115 μm in the z-coordinate (R-coordinate for the disks). The smaller pixel size of the IBL provides an improved resolution of 70 μm in the z-coordinate. Together with the smaller distance to the IP this leads to improvements in the impact parameter resolution, the vertexing, as well as the tagging of jets originating from b quarks (b-jets).

Semi-conductor tracker

The Semi-conductor tracker is a silicon microstrip detector and is located outside the pixel detector, covering the region $|\eta| < 2.5$. It consists of four layers in the barrel region, within radii of 30 cm to 52 cm, as well as nine disks at each end of the detector. Each layer of the sub-detector contains two layers of strips, arranged with a 40 mrad tilt in order to provide a measure of the hit location along

the strip direction. The strips have a size of $80\,\mu m \times 6.4\,cm$, providing in total 6.3 million readout channels. The resulting resolution is $17\,\mu m$ in the $R - \phi$ direction and $580\,\mu m$ in the z-coordinate, along the strips.

Transition radiation tracker

The transition radiation tracker covers the region $|\eta| < 2.0$ at radii between $55\,cm$ and $108\,cm$. It consists of $4\,mm$ diameter straw tubes interleaved with a polyethylene foil. Charged particles traversing this material generate transition radiation depending on their mass. This information is used for the identification of electrons. The straw tubes are segmented in $R - \phi$ and provide a location resolution of $130\,\mu m$.

6.3 Calorimeters

The ATLAS calorimeters are located outside the ID, covering the region $|\eta| < 4.9$. They are used to identify and measure the energy of most particles from the interaction. All calorimeters are sampling calorimeters, with separate layers for the absorption of particles and for the active readout of the signals. Figure 6.3 shows a sketch of the calorimeter layout. In the material, electromagnetically interacting particles lose energy mostly by bremsstrahlung and pair production processes, while particles which primarily interact hadronically are stopped by hadronic interactions. Both types of processes result in particle showers in the absorbers, which lead to a measurable signal in the active layers. The electromagnetic calorimeter is optimised for the first kind of processes, while the outer, hadronic calorimeter targets the second kind.
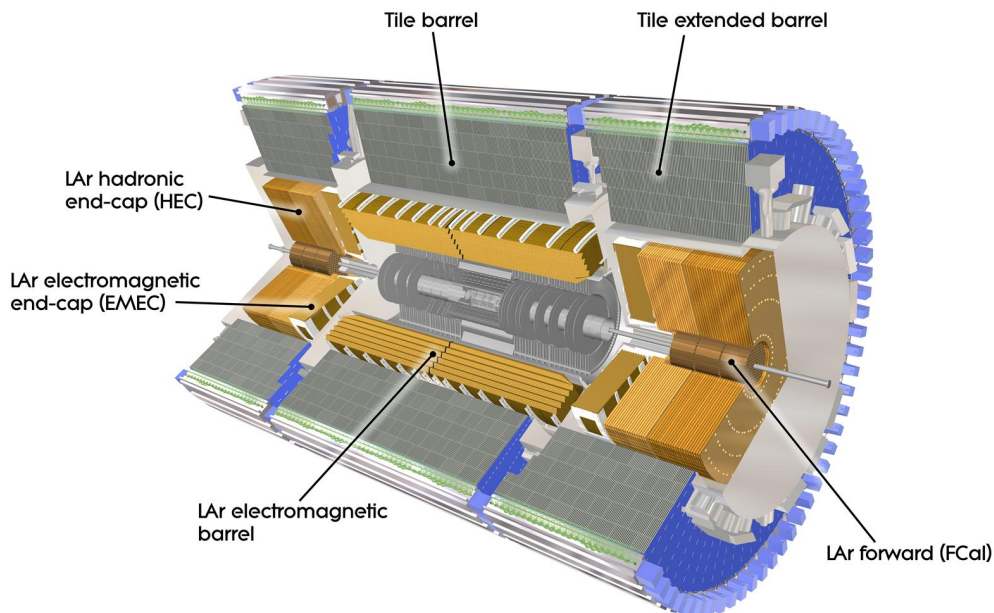
Figure 6.3: Schematic view of the ATLAS calorimeters [95].

Electromagnetic calorimeter

The electromagnetic calorimeter (ECAL) [96] uses liquid argon (LAr) as the active material and lead in the absorber layers. The barrel part covers the region $|\eta| < 1.475$, and is followed by the end-caps which cover the region $1.375 < |\eta| < 3.2$. The total thickness of the ECAL is more than 22 radiation lengths[1] (X_0) in the barrel part, and more than 24 X_0 in the end-caps.

The ECAL consists of three layers with different cell-structures in the $\eta - \phi$ plane. The first layer is finely segmented with a cell size of 0.003×0.1 in $\eta \times \phi$, allowing for a precise measurement of the position of incoming particles. The second layer amounts to 70% of the ECAL depth and has a granularity of 0.025×0.025 in $\eta \times \phi$. It is used to precisely measure the energy of the showers. The third layer has the same granularity and is used to contain the tails of the electromagnetic showers, as well as for triggering purposes.

Hadronic calorimeter

The hadronic calorimeter (HCAL) consists of several parts covering different regions in $|\eta|$: A barrel within $|\eta| < 1.0$, two extended barrels in $0.8 < |\eta| < 1.7$, two end-caps in $1.5 < |\eta| < 3.2$ and two forward calorimeters within $3.1 < |\eta| < 4.9$. In total, the calorimeter has a thickness of more than 9.7 hadronic interaction lengths[2] (λ).

The barrel and extended barrel parts use steel as the absorber material and scintillating tiles as the active material [97]. They are segmented into three layers with a granularity of 0.1×0.1 in $\eta \times \phi$. Both the end-caps, as well as the forward calorimeters use LAr as the active material in order to withstand the higher radiation. The end-caps use copper as absorbers, while the forward calorimeters use tungsten.

6.4 Muon spectrometer

The muon spectrometer is the outermost sub-detector of the ATLAS experiment [98]. It consists of three barrel layers, as well as three wheels placed perpendicular to the beam at each side of the detector. The sub-detector is placed around and within the superconducting toroid magnets. The toroid magnet system consists of a large barrel toroid, with a field of up to 3.9 T, and two end-cap toroids with fields up to 4.1 T. Each toroid consists of eight independent, superconducting coils which are equally distributed around the beam. The open structure of the magnets reduces multiple scattering effects and therefore leads to a better momentum resolution, due to the small amount of material needed. The trajectories of muons are bent in the magnetic field in η direction, towards the end-caps. Figure 6.4 gives a schematic overview of the muon spectrometer.

The muon spectrometer covers the range $|\eta| < 2.7$, and employs four different kinds of sub-detectors: Monitored Drift Tubes (MDT), Cathode Strip Chambers (CSC), Resistive Plate Chambers (RPC) and Thin Gap Chambers (TGC). The various detector components have different position and time resolution, as well as radiation hardness.

Due to their good position resolution, the MDT and CSC detectors are used for the precise measurements of the muon tracks. The MDT detectors are proportional chambers with a 40 μm position resolution and are arranged in three layers with a range of $|\eta| < 2.7$ for the two outer layers. The innermost layer covers the region $|\eta| < 2.0$. At $2.0 < |\eta| < 2.7$ the CSC detectors are used, as

---

[1]The radiation length is defined as the mean distance over which the energy of an electron is reduced to $1/e$ of its initial energy. For a photon, the same reduction occurs over a distance of $9/7X_0$.

[2]The hadronic interaction length is the mean distance over which the energy of a hadron is reduced to $1/e$ of the initial energy.

they withstand the higher rates of particles traversing the detectors. These multi-wire proportional chambers have a comparable resolution to the MDTs.

As the high drift times in the MDTs of up to 700 ns exceed the readout-speed needed for the trigger, additionally RPC and TGC detectors are used for triggering with a time resolution of 1 ns. In the barrel region, the RPC detectors are installed, which are chambers with an active gas between two resistive plates. Signals are read out at two orthogonal pickup strips. In the end-cap wheels, the TGC detectors are used. These are multi-wire proportional chambers, with a small distance between the wire and the cathode to enable a small readout time.
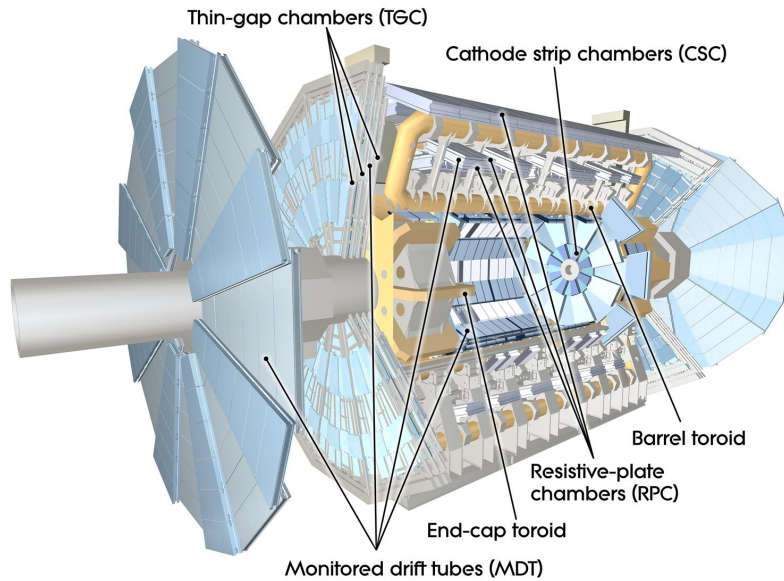
Figure 6.4: Schematic view of the ATLAS muon spectrometer [99].

6.5 Trigger

Due to the high collision rate and technical limitations, the ATLAS detector cannot record every event. In order to select and record events with interesting physics characteristics, a two stage trigger system is employed [100].

At the first stage, the Level 1 (L1) trigger reduces the event rate from up to 40 MHz to 100 kHz. The L1 trigger is a hardware-based system which uses information mainly from the calorimeters and the muon spectrometer. Possible signatures are high-p_T muons, highly energetic electrons, photons jets and τ leptons, as well as a high amount of E_T^{miss} (as defined in Section 7.7). The L1 decision is made in less than 2.5 μs.

In case that a signal passes the L1 trigger selection, a so-called region-of-interest (RoI) in η and ϕ is defined and the accepted event is further processed. The second stage is the High-Level Trigger (HLT), which is a software-based system. Here, the event rate is reduced from 100 kHz to 1 kHz, and the accepted events are stored to disk. In the HLT, first the RoIs of the L1 trigger are used and the specific objects are reconstructed. For events that do not fail the trigger selection at that stage, the complete event can be reconstructed similarly to the offline analysis procedures and a more detailed selection is possible. The mean processing time for the HLT is in the order of 300 ms, and strongly depends on the amount of pile-up.

The ATLAS trigger menu is configured on a LHC run basis and is adapted to the instantaneous luminosity in order to achieve the required rate reduction. Runs with the same conditions are then grouped into periods, in which the trigger thresholds are constant.

6.6 Luminosity measurement

The delivered luminosity is measured in ATLAS by measuring the visible interaction rate per bunch crossing. This is done using several independent detectors [101] in order to control for systematic effects and reliability.

The luminosity can be expressed as

$$\mathcal{L} = \frac{\mu_{\text{vis}} f_r n_B}{\sigma_{\text{vis}}} \ . \tag{6.6}$$

Here, μ_{vis} is the visible interaction rate, f_r is the revolution frequency of the LHC, n_B is the number of colliding bunches and σ_{vis} is the visible cross-section, i.e. the cross-section multiplied with the efficiency and acceptance of the sub-detector. By measuring μ_{vis}, the relative luminosity per bunch crossing can be measured.

The absolute calibration of the measurement is done in so-called van der Meer scans [102]. These are special, low intensity LHC runs, in which the beam separation is scanned in order to determine the beam-beam overlap. The absolute luminosity can then be determined from machine parameters, using Equation (5.2). The total uncertainty in the integrated luminosity of the LHC runs in 2015 and 2016 is determined to be 3.2%, derived following a methodology similar to that in Ref. [101].

The two primary sub-detectors used for the luminosity measurements are called LUCID and BCM. The LUCID detector is a Cherenkov detector located at $z = \pm 17$ m, covering the region $5.6 < |\eta| < 6.0$. The BCM detectors are diamond sensors at the end of the inner detector, ± 1.84 m from the interaction point in z-direction. They are also used to control the beam quality and trigger a beam dump in case of losses, in order to protect the silicon detectors.

Several alternative algorithms, such as track-counting or $Z \rightarrow \mu\mu$ measurements, are used in order to have alternative measurements as a cross check to the primary luminosity detectors.

Chapter 7 Event reconstruction

$\mathbf{S}$ table particles created in the collision are measured by the various sub-detectors and reconstructed by specialised algorithms. First, charged particle tracks are identified by the hits in the Inner Detector and the Muon System. From these tracks, the primary interaction vertex is determined. Then the individual physics objects, electrons, muons, τ leptons, jets, and the missing transverse momentum, are reconstructed. This chapter briefly explains the individual reconstruction and identification algorithms, and gives the selections used in the analyses described in this dissertation. In general, two sets of quality requirements are used to select electrons, muons and jets in the analyses. These are called *baseline* and *signal* requirements, with the former requirements being a subset of the latter. Baseline objects are used to remove the overlap between physics objects and to compute the missing transverse momentum, while signal objects are used to derive kinematic variables and for selection requirements in the analyses.

7.1   Tracks and primary vertex

The reconstruction of charged particle tracks is based on fitting trajectory models to the measurements in the Inner Detector [93, 103]. The trajectories of charged particles are bent by the solenoidal magnetic field in the Inner Detector, with a curvature that is inversely proportional to the momentum of the particle.

Tracks are reconstructed using an *inside-out* algorithm. For this, three measurements in the silicon detectors are combined to form track "seeds", and then the tracks are propagated outwards using a combinatorial Kalman filter [104]. After a hit is added to a track candidate, the reconstructed segment is fitted in a χ^2 minimisation. Good quality tracks in the pixel and SCT detectors are extrapolated into the TRT detector and combined with the measurements there. Hits shared by several tracks are resolved by an ambiguity solving algorithm, in which tracks are sorted according to their quality and shared hits are removed before refitting the track.

Reconstructed tracks are specified by their azimuthal and polar angles, ϕ and θ, the charge over momentum ratio, q/p, and the impact parameters d_0 and z_0, the minimal transverse and longitudinal distance with respect to the centre of the detector. The tracking efficiency is more than 90% in the central part of the detector for $p_\mathrm{T} > 4\,\mathrm{GeV}$, and the resolution of the impact parameters for tracks with $p_\mathrm{T} > 30\,\mathrm{GeV}$ is better than $10\,\mu\mathrm{m}$ in the transverse direction and $50\,\mu\mathrm{m}$ in the longitudinal direction, respectively [5, 105].

The proton–proton interaction vertices in an event are found by an iterative vertex finding algorithm [106]. Vertex candidates are fitted with a χ^2 fit, taking into account the compatibility of tracks with the vertex candidate. The initial vertex position is taken from the transverse beam position and the global maximum of the z-coordinates of all reconstructed tracks. Tracks not

compatible with a vertex are removed and the fit is iterated. All rejected tracks are then used as an input to find further vertex candidates. The vertex with the highest sum of squared transverse momenta of all associated tracks is taken to be the primary interaction vertex. It is required to have at least two associated tracks with $p_T > 400$ MeV. The impact parameters of tracks used in the analyses are taken with respect to the primary vertex and can be used to reject tracks which do not come from the primary event.

7.2 Electrons

Electrons are reconstructed from clusters of energy in the EM calorimeter and an associated track. A sliding-window clustering algorithm [107] with a window size of 3×5 units of the granularity of the central calorimeter layer in $\eta \times \phi$, finds localised, narrow clusters of energy deposits in the calorimeter. In the next step, tracks are associated to all clusters with a minimal energy of 2.5 GeV. For all cluster–track pairs the clusters are re-formed to a 3×7 units size in the barrel, or a 5×5 units size in the end-cap, and the tracks are re-fitted, to account for a possible energy loss due to bremsstrahlung. If no track can be associated to a cluster, it is interpreted as a photon candidate and not further considered in this analysis.

The four-momentum of the electron candidate is built from the calorimeter and track information. While the η and ϕ directions are taken from the track, the energy is determined from the calorimeter measurement, calibrated to the electron's energy based on simulation [108].

The identification of good electron candidates is based on a multivariate, likelihood-based method. It combines information about the shape of the electromagnetic shower in the calorimeter with track-based information from the TRT, the goodness of the track-to-cluster matching and the track quality, including bremsstrahlung effects, into a combined likelihood value. The selection of electron candidates then depends on the likelihood ratio of the signal to the background. Three reference working points are discussed in Ref. [107], *Loose*, *Medium* and *Tight*, and an additional working point called *VeryLoose* is used here, to include a highly efficient selection.

In order to exclude electrons from semi-leptonic decays of heavy hadrons, isolation requirements can be used. Here, the scalar sum of the transverse momentum of tracks with a distance of $\Delta R < \min(0.2, 10 \text{ GeV}/E_T)$ to the electron is used to calculate a measure of the activity close-by the electron. The tracks associated to the electron are excluded from the sum.

The efficiency of the electron reconstruction, identification and isolation is measured in $Z \rightarrow ee$ and $J/\psi \rightarrow ee$ events. Using the *tag and probe* method, one electron is required to fulfil strong requirements in order to *tag* the event, and the second electron is only selected by the mass requirement of the Z or J/ψ resonance, so that no bias is introduced on the measured quantities. The efficiency of this *probe* electron passing the requirements is then measured. From the measurements, E_T and η dependent scale factors are derived in order to correct the simulation where necessary. The electron energy scale and resolution are also calibrated based on this tag and probe method.

The baseline requirements for electrons in the analyses are an $E_T > 7$ GeV, $|\eta| < 2.47$ and the VeryLoose identification selection. Signal electrons are additionally required to pass the Tight identification selection and have $E_T > 28$ GeV. The impact parameters of the tracks associated to signal electrons have to fulfil $|d_0/\sigma_{d_0}| < 5$ and $|z_0 \sin\theta| < 0.5$ mm, with respect to the primary vertex. Additionally, signal electrons are required to be isolated with a surrounding activity of less than 6% of the electron E_T as calculated above. In the search for top squarks, the requirements have been loosened in order to increase the efficiency. For baseline electrons the minimal E_T is lowered to 5 GeV, and for signal electrons to 25 GeV. Additionally, signal electrons only have to fulfil the Loose identification selection.

7.3 Muons

Muons are reconstructed from hits in the Inner Detector and in the Muon Spectrometer. Tracks in the MS are found by combining hit patterns in the individual layers to segments, which are then fitted together to tracks spanning several layers. The combined reconstruction of muons is performed using four algorithms [109]:

- Combined muons (CB) are reconstructed from tracks in the ID and the MS. First, an outside-in algorithm extrapolates MS tracks into the ID. A combined track is fitted using hits from both the ID and the MS, optionally adding or removing MS hits to improve the fit quality. In a second step, an inside-out algorithm fits tracks extrapolated from the ID to the MS.

- Segment-tagged muons (ST) are a combination of an ID track and a track segment in the MS. This reconstruction is useful for low p_T muons that only cross one layer of the MS, or to recover efficiency in regions with a low coverage in the MS.

- Extrapolated muons (ME) are reconstructed in the forward region of the detector, within $2.5 < |\eta| < 2.7$, where the ID has no coverage. Muons are reconstructed from a MS track compatible with the interaction point.

- In the very central part of the detector, $|\eta| < 0.1$, where the MS has a low sensitivity due to the layout of the detector, calorimeter-tagged muons (CT) are reconstructed from a track in the ID and calorimeter measurements compatible with a minimally ionising particle.

Muon candidates reconstructed by several algorithms are identified according to the ID track. Preference is given to the algorithm with the highest purity, prioritising CB muons over ST muons and CT muons.

The identification of good muon candidates is based on the quality of the track fit, taking into account the global χ^2 and hit information, and the compatibility of the ID and the MS measurements. *Medium* muons are required to be reconstructed as CB or ME muons. The *Loose* quality requirements also allow ST and CT muons in order to increase the efficiency in the $|\eta| < 0.1$ region.

Similarly to electrons, the efficiency of the muon reconstruction, identification and isolation requirements are measured using the tag and probe method in $Z \rightarrow \mu\mu$ and $J/\psi \rightarrow \mu\mu$ events. Based on the same technique, the muon momentum scale and resolution are measured. Corrections for the simulation are derived from the measurements in the form of p_T and η dependent scale factors.

In the analyses, the requirements for baseline muons are the Loose identification selection, a $p_T > 6\,\text{GeV}$ and $|\eta| < 2.7$. Signal muons additionally have to fulfil the Medium identification requirements and have $p_T > 28\,\text{GeV}$. Furthermore they have to be compatible with the primary vertex, requiring that $|d_0/\sigma_{d_0}| < 3$ and $|z_0 \sin\theta| < 0.5\,\text{mm}$. The isolation of signal muons is ensured by requiring that the scalar sum of track p_T in a cone of $\Delta R < \min(0.3, 10\,\text{GeV}/p_T)$ to the muon is less than 6% of the muon p_T. In the search for top squarks, the p_T requirement for baseline muons is loosened to $4\,\text{GeV}$ and for signal muons to $25\,\text{GeV}$.

7.4 Jets

Partons generated in the hard scattering hadronise to sprays of collimated hadrons. These jets are reconstructed from energy deposits in the calorimeter based on a jet-finding algorithm. In a first step, the energy measurements in the calorimeter are grouped to clusters. These clusters are input

to an algorithm which combines close-by clusters into jets. In the last step, these jets are calibrated to reflect the four-momentum of the initial parton.

7.4.1   Formation of topo-clusters in the calorimeter

Energy deposits in the calorimeter are combined into topologically connected clusters [110] (short topo-clusters) according to their signal-to-noise ratio. The clusters are used to reconstruct the hadronic shower of a particle in the calorimeter.

Cells with a signal-to-noise ratio of $|S/N| = |E_{\text{cell}}/\sigma_{\text{cell}}| > 4$ seed the formation of topo-clusters. E_{cell} is the energy measured in the cell, and the noise of a calorimeter cell, σ_{cell}, is estimated based on its intrinsic electronic noise and the contributions from pile-up activity.

For each cluster seed, neighbouring cells with $|S/N| > 2$ are added to the cluster, optionally merging connected clusters in this step. A neighbouring cell is a cell that is either in the same calorimeter layer and adjacent to the initial cell, or in an adjacent layer and overlapping in the $\eta \times \phi$ region. Then, neighbouring cells with $|S/N| > 0$ are added to the cluster, capturing the softer tails of the hadronic shower. In a last step, clusters with two or more local maxima are split.

The cell energies are measured at the so-called electromagnetic scale. This means that they correctly reconstruct the activity of an electromagnetic shower, without any correction for the loss in hadronic showers. This effect is later corrected for in the calibration of the reconstructed jets. Topo-clusters are interpreted as mass-less pseudo-particles. The topo-cluster energy and direction are taken from the weighted mean of all cells contributing to the measurement.

7.4.2   The anti-k_t algorithm

Topo-clusters are combined into jets according to the anti-k_t algorithm [111] with a distance parameter of $R = 0.4$. The anti-k_t algorithm is a sequential recombination algorithm. It is infra-red and collinear safe, meaning that neither hard, collinear emissions nor soft emissions at high angles alter the jets in an event. In the algorithm, all inputs i are assigned the distances

$$d_{ij} \quad = \quad \min(k_{t,i}^{-2}, k_{t,j}^{-2}) \frac{\Delta R_{ij}^2}{R^2} \,, \text{ to another input } j, \text{and} \tag{7.1}$$

$$d_{iB} \quad = \quad k_{t,i}^{-2} \,, \text{ to the LHC beam } B, \tag{7.2}$$

where the k_t is the transverse momentum of a pseudo-particle (meaning either a cluster or the combination of multiple clusters), $\Delta R_{ij} = \sqrt{\Delta \eta_{ij}^2 + \Delta \phi_{ij}^2}$ is the distance between pseudo-particles i and j in the $\eta \times \phi$ plane, and the parameter R regulates the size of the final jets. Then, the smallest distance in all d_{ij} and d_{iB} is found. If it is a distance to another input j, the two pseudo-particles i and j are removed from the list and combined into a pseudo-jet, which in turn is added to the list of inputs. If the smallest distance instead is d_{iB}, the input i is declared a final jet and removed from the list. This sequence of computing all distances, combining inputs and finding the final jets is iterated until the list of inputs is empty.

The anti-k_t algorithm assigns small distances to high-momentum particles that are close-by, meaning that hard particles are clustered at the beginning of the sequence. The jets then grow around these seeds while adding the softer constituents, leading to approximately circular jet shapes in the $\eta \times \phi$ plane. The momentum of the jet is determined from the vectorial sum of the topo-cluster momenta, which also determines the mass of the jet. Jets in ATLAS are reconstructed with a radius parameter of $R = 0.4$.

7.4.3 Jet calibration

The resulting jets are calibrated to reflect the four-momentum of the initiating partons [112]. The calibration is mainly based on simulation, and the jet four-momenta are corrected to that of truth jets, built from the stable truth particles in a simulated event. Jets are calibrated in several, consecutive steps, as shown in Figure 7.1 and explained below.

In the origin correction, the four-momentum of the jet is recalculated to point to the primary vertex instead of the centre of the detector. The jet energy is kept constant in this correction, only the direction is changed in order to improve the angular resolution of the jets.

The contributions from pile-up to the energy of a jet are removed in two steps. First, the per-event pile-up contribution is subtracted based on the area of the jet. The energy density, ρ, is determined from the median of the energy density distribution in the event, and the jet area, A, is calculated using ghost association. In this method, so-called ghost particles, pseudo inputs with an infinitesimal momentum, are added uniformly to the jet reconstruction. The jet area is then determined from the fraction of ghost particles clustered into a jet. This method accurately determines the area of a jet even in cases where two jets close to each other are found, resulting in non-circular shapes. The residual dependence of the jet p_T on the number of interaction vertices in the event, N_{PV}, and the mean number of interactions, $\langle \mu \rangle$, are approximated to be linear and uncorrelated to each other. Two $|\eta|$ dependent coefficients, α and β, are determined and used to subtract the residual pile-up contributions. The final, pile-up corrected transverse momentum of the jet is thus

$$p_T^{\text{corr}} = p_T - \rho \cdot A - \alpha \cdot (N_{PV} - 1) - \beta \cdot \langle \mu \rangle \,. \tag{7.3}$$

In the following step, an absolute, MC-based calibration is applied to the jets. Based on simulation, the jet response is derived as the ratio of the reconstructed energy to the true energy of a jet, $\mathcal{R} = E_{\text{jet}}/E_{\text{truth}}$. The jet response $\mathcal{R}$ is determined using isolated jets matched to truth jets within $\Delta R < 0.3$. As the jet response is strongly dependent on the detector geometry, it is parametrised in $|\eta_{\text{det}}|$, the jet η direction pointing from the centre of the detector, which is an unambiguous measure of the location in the detector. The response $\mathcal{R}$ is then inverted numerically to derive a correction based on E_{jet}. A further correction is applied in order to remove a bias for jets which span two calorimeter regions with different energy response characteristics. It is parametrised in $|\eta_{\text{jet}}|$ and $|\eta_{\text{det}}|$, and inverted and applied in a similar fashion.

After the MC-based calibration, the mean jet energy corresponds to the energy of the initial parton. Residual dependencies of the jet energy on the jet shape prevail, and are corrected for in the global sequential calibration (GSC). The GSC comprises several independent correction steps, each correcting for a bias in one observable. The order of these steps, and potential correlations between
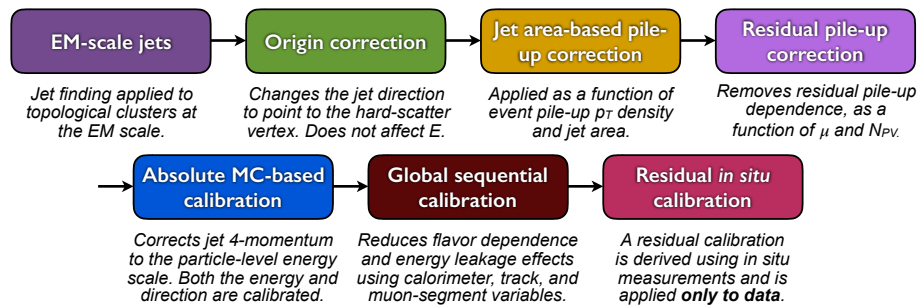
Figure 7.1: Overview of the ATLAS jet calibration scheme [112].

the observables are found to have a negligible impact on the final calibration. Five dependencies are corrected for, with the variables being the fraction of energy in the first layer of the hadronic Tile calorimeter, the fraction of energy in the last layer of the electromagnetic LAr calorimeter, the number of tracks associated to the jet, the p_{T} weighted distance of these tracks to the jet axis, and the number of track segments in the MS associated to the jet. For each of these observables, a p_{T} and $|\eta_{\mathrm{det}}|$ dependent correction is derived, akin to the absolute correction explained before. The correction factors are scaled in such a way that the average energy of the jets is not changed, in order to conserve the overall jet energy scale. The GSC reduces the dependency on the jet calibration on the detector layout, on fluctuations in the particle content of the jet, the shower shapes and on the so-called "punch-through" effect, which describes jets not fully contained in the calorimeters, but leaking into the MS.

In the final step of the calibration procedure, an in-situ calibration is applied to jets in data, in order to correct for detector effects which are not well modelled in the simulation. The in-situ calibration is based on the measurements of jets recoiling against well measured reference objects. With the $Z \rightarrow \ell\ell + \mathrm{jet}$ and $\gamma + \mathrm{jet}$ balance methods, jets recoiling against well measured leptonic or purely electromagnetic detector signatures are calibrated. These methods are sensitive up to a jet p_{T} of 950 GeV, after which the statistical precision deteriorates the measurement. High p_{T} jets are calibrated based on the multi-jet balance method, measuring the recoil of a hard jet against multiple, softer jets, which are calibrated with the aforementioned methods. Iterating this procedure, allows to include even higher p_{T} jets in the multi-jet balance method and makes the calibration available for jets up to 2 TeV. The calibration of jets with $p_{\mathrm{T}} > 2$ TeV is based on single-particle response studies. Forward jets are calibrated using the η-intercalibration method, measuring the energy with respect to well calibrated, central jets.

7.4.4   Jet vertex tagging

Jet vertex tagging [113] is a technique which allows to quantify the compatibility of a jet with the primary interaction vertex. It is used in order to identify and remove jets originating from pile-up events. The JVT measure is based on the tracks associated to the jet. The sensitive observables are the fraction of tracks that come from the primary vertex, as well as the ratio of the track p_{T} sum to the jet p_{T}. These two quantities are combined in a likelihood, which is used in the jet selection to remove soft jets from pile-up interactions.

7.4.5   Jet requirements in the analyses

Baseline jets in the analysis are required to have $p_{\mathrm{T}} > 20$ GeV and $|\eta| < 4.7$, reflecting the kinematic acceptance of the detector. The requirements for signal jets are $p_{\mathrm{T}} > 25$ GeV and $|\eta| < 2.5$. Furthermore, JVT < 0.59 is required for jets within $|\eta| < 2.4$ and $p_{\mathrm{T}} < 60$ GeV.

In the analyses, a technique called jet reclustering is used, where several jets are combined using the anti-k_t algorithm with a large radius parameter, in order to reconstruct particles decaying into several collimated jets, with a distance smaller than $\Delta R \leq 0.4$. It is found to show a good performance in comparison with jets with a large radius built from topo-clusters [114].

7.5   Flavour-tagging

Weakly decaying hadrons containing b quarks are relatively long-lived, with a mean life time of $\tau \sim 1.5$ ps. Their decays therefore can have a measurable distance from the primary interaction
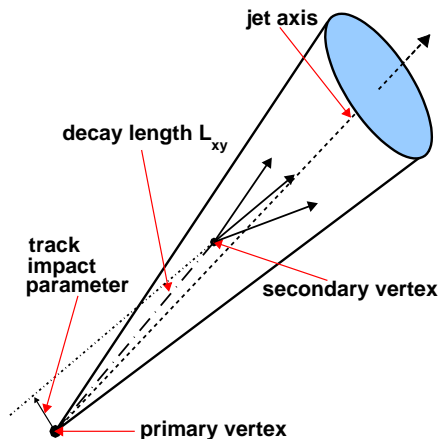
Figure 7.2: Sketch of the *b*-hadron decay in a jet, with the most important variables indicated [117].

vertex (PV), resulting in a secondary vertex (SV). This makes *b*-jets, i.e. jets originating from *b* quarks, identifiable through the use of *b*-tagging algorithms [115, 116]. Several algorithms are used in ATLAS, which rely on the impact parameters (IP) or reconstruct secondary vertices based on the tracks from charged particles matched to the jets. The information of these algorithms are then combined in a multivariate approach to form a final discriminant. Figure 7.2 shows a sketch of a *b*-hadron decay in a jet, with the most important *b*-tagging variables outlined.

The IP2D and IP3D algorithms are based on the signed impact parameter significances of tracks matched to jets. The sign of the IP indicates the track position relative to that of the PV and the jet, with a positive sign meaning that the track lies in front of the PV, relative to the jet. The IP algorithms categorise the tracks according to their quality, and combine the transverse IP, and also the longitudinal IP in the case of IP3D, into a likelihood-ratio based discriminant.

The SV algorithm finds secondary vertices by first reconstructing all two-track vertices of tracks in a jet. Vertices compatible with a K_S or Λ decay as well as from photon conversion or hadronic interactions with the detector material are removed. The secondary vertex is then iteratively refitted and outlier tracks are removed in the process. Discriminant information, in addition to the existence of a secondary vertex in the jet, are the invariant mass of all tracks associated to the vertex, as well as the decay length, i.e. the distance to the PV, and the fraction of energy from the tracks in the vertex to all tracks in the jet.

Secondary vertices are also utilised in the JetFitter algorithm, which reconstructs the full *b*-hadron and subsequently the *c*-hadron decay chain. By assuming that the decay vertices lie on a common line from the PV, the algorithm is able to reconstruct decays with only a single, charged particle in the vertex.

The information obtained by these basic algorithms are used in a multivariate combination, called MV2. This algorithm is based on a boosted decision tree (BDT), trained to discriminate *b*-jets from *c*-jets and light-flavour jets. The training includes information from the IP2D, IP3D, SV and JetFitter algorithms, as well as the p_T and $|\eta|$ of the jet. In order to be independent of the kinematic distributions in the training data set, *b*- and *c*-jets in the training are reweighted to match the two dimensional $p_T \times \eta$ distribution of the light jets. Several variants of the classifier are available, with a different fraction of *c*-jets in the training algorithm and accordingly a different rejection of *c*-jets in the final discriminant. In the analyses presented here, *b*-jets are identified using

a working point of the MV2 algorithm that offers a mean b-jet identification efficiency of 77% in $t\bar{t}$ events, and a rejection factor of 134 for light-flavour jets and 6 for c-jets. An adaptation of the multivariate approach for dense environments is described in Appendix A.

The calibration of the b-tagging algorithms relies on efficiency measurements in samples enriched in either b-jets, c-jets or light-flavour jets. The measurements are reported in the form of scale factors, the relative efficiency measured in data to that in simulation, which are then used to correct the efficiency for the mismodelling effects in the simulation. The b-jet calibration is based on dileptonic $t\bar{t}$ events [118]. The b-jets are selected based on a likelihood method, and a good agreement of data and simulation is found, with a percent-level uncertainty. The calibration of the mis-tagging efficiency for c-jets is based on the reconstruction of $D^{*+} \rightarrow D^0 \pi^+ \rightarrow K^- \pi^+ \pi^+$ decays [119], which is used to select c-jets. Light-flavour jets are selected and calibrated in the *negative tag* method [120]. This method relies on the assumption that the distribution of the signed impact parameters and vertex decay lengths is symmetric for light jets, while b- and c-jets predominantly show positive values. Light jets are selected by requiring negative impact parameters, and then the sign is artificially inverted in order to evaluate the b-tagging algorithms and measure their efficiency on light-jets.

7.6 Hadronically decaying τ leptons

The τ lepton decays with a branching ratio of about 65% into a τ neutrino and one or more charged hadrons (hadronic τs). The most common decay mode includes one charged hadron (one prong), followed by decays with three charged hadrons (three prong). The reconstruction of hadronic τ decays is seeded by jets [121, 122], which are required to have $p_\mathrm{T} > 10$ GeV and lie in the acceptance of the Inner Detector, $|\eta| < 2.5$. The τ candidate energy is calculated from all jet constituents, i.e. topo-clusters, within $\Delta R < 0.2$ to the jet axis. Within the same radius, tracks fulfilling quality requirements and have $p_\mathrm{T} > 1$ GeV are associated to the τ candidate. The constituents in the region $0.2 < \Delta R < 0.4$, as well as the tracks within that radius, are used to calculate isolation variables.

The identification of τ candidates, and the rejection of the QCD jet background, is based on a BDT. The classification relies on variables characterising the decay topology, including a special reconstruction of $\pi^0 \rightarrow \gamma\gamma$ decays, the isolation of the candidate, as well as features of the associated tracks.

In the analyses, hadronic τ candidates are used in order to reject background events based on kinematic features, as described in Chapter 8. Only τ candidates with exactly one or three associated tracks are used, in order to require a reconstruction of either the one or the three prong decay mode. Candidates overlapping within $\Delta R < 0.1$ with an electron candidate are removed, to reject hadronic τ candidates reconstructed from an electrons. Additionally, a p_T threshold of 20 GeV is set.

7.7 Missing transverse momentum

Neutral, weakly-interacting particles, like the neutrino or the neutralino in certain SUSY scenarios, cannot be detected with the ATLAS detector. This creates an apparent imbalance in the total transverse momentum in the event. This missing transverse momentum, $\vec{E}_\mathrm{T}^\mathrm{miss}$, is calculated from the negative vectorial sum of the transverse momenta of all detected particles in an event and its magnitude is referred to as $E_\mathrm{T}^\mathrm{miss}$. The reconstruction of the $\vec{E}_\mathrm{T}^\mathrm{miss}$ includes all calibrated objects in an event, and adds a soft-term that includes any activity which is not associated to calibrated

objects [123, 124]. The missing transverse momentum in the x (y) direction is then

$$E_{\mathrm{T},x(y)}^{\mathrm{miss}} = E_{\mathrm{T},x(y)}^{\mathrm{miss},e} + E_{\mathrm{T},x(y)}^{\mathrm{miss,jets}} + E_{\mathrm{T},x(y)}^{\mathrm{miss},\mu} + E_{\mathrm{T},x(y)}^{\mathrm{miss,soft}} \ . \tag{7.4}$$

In the analyses, the baseline selection is used for objects entering the $E_{\mathrm{T}}^{\mathrm{miss}}$ calculation. The soft-term, $E_{\mathrm{T}}^{\mathrm{miss,soft}}$, is built from the negative vectorial sum of all tracks in the event which are not associated to calibrated objects. This track-based soft-term (TST) ignores contributions from neutral particles. An alternative , calorimeter-based soft-term (CST), includes all topo-clusters not associated with jets in the $E_{\mathrm{T}}^{\mathrm{miss}}$ calculation. While the CST includes neutral activity, it is less resilient against pile-up effects and was found to lead to a worse resolution of the $E_{\mathrm{T}}^{\mathrm{miss}}$ for the analyses presented here. The absolute scale and resolution of the $E_{\mathrm{T}}^{\mathrm{miss}}$ is measured in $Z \to \mu\mu$ events.

7.8 Overlap removal

Detector signatures can be reconstructed as more than one object type, e.g., energy deposits in the calorimeter will likely be reconstructed as electrons and jets. In order to resolve these ambiguities, and not to double count detector measurements, an overlap removal algorithm is used. All objects satisfying baseline quality requirements are input to the algorithm, and only objects passing the overlap removal are used further in the analyses. The two analyses use different overlap removal algorithms.

7.8.1 Overlap removal in the search for vector-like quarks

The overlap removal for the vector-like quark search is harmonised with other VLQ searches in different final states, in order to facilitate a later combination of the results. The procedure is as follows:

1. Electron/jet overlap: if a baseline jet is found within $\Delta R < 0.2$ to a baseline electron, the object is interpreted as an electron and the jet candidate is removed.

2. Muon/jet: if a baseline muon overlaps with a baseline jet within $\Delta R < 0.4$, the overlapping jet is removed, if it has less than three tracks with $p_{\mathrm{T}} > 500\,\mathrm{MeV}$ associated to it. Otherwise, both candidates are retained, and subject to the further steps.

3. Jet/lepton:

   - If a jet overlaps with a muon in a cone of size $\Delta R = \min(0.4, 0.04 + 10\,\mathrm{GeV}/p_{\mathrm{T}}^{\mu})$, the muon candidate is removed, as it either originates from a heavy flavour decay in the jet, or from a jet that is not fully contained in the calorimeter and creates hits in the MS.

   - If a jet overlaps with an electron in a cone of size $\Delta R = 0.4$, the electron candidate is removed.

4. Electron/τ: if an electron overlaps with a hadronic τ candidate within $\Delta R < 0.1$, the τ candidate is removed.

7.8.2 Overlap removal in the search for top squarks

The overlap removal for the top squark search is optimised with respect to the acceptance of prompt leptons, in order to achieve a better signal acceptance. The algorithm is:

1. Electron/muon: if a baseline electron and a baseline muon overlap within $\Delta R < 0.01$, the muon candidate is removed, if it is a CT muon, otherwise the electron is removed.

2. Electron/jet overlap: if a baseline jet is found within $\Delta R < 0.2$ to a baseline electron and the jet is not b-tagged, the object is interpreted as an electron and the jet candidate is removed.

3. Muon/jet: if a baseline muon overlaps with a baseline jet within $\Delta R < 0.4$ and the jet is not b-tagged, the overlapping jet is removed, if it has less than three tracks with $p_T > 500\,\mathrm{MeV}$ associated to it or if $p_T^\mu/p_T^\mathrm{jet} > 0.7$. Otherwise, both candidates are retained, and subject to the further steps.

4. Jet/lepton: if a jet overlaps with a lepton in a cone of size $\Delta R = \min(0.4, 0.04 + 10\,\mathrm{GeV}/p_T^\ell)$, the lepton candidate is removed.

5. Electron/τ: if an electron overlaps with a hadronic τ candidate within $\Delta R < 0.1$, the τ candidate is removed.

The algorithm differs with respect to the one used in the VLQ search in the requirement that electron candidates can only remove non-b-tagged jet candidates, the additional p_T ratio requirement in the muon/jet overlap removal, and the p_T-dependent cone size for electrons in the jet/lepton overlap removal step.

Searches for top quark partners
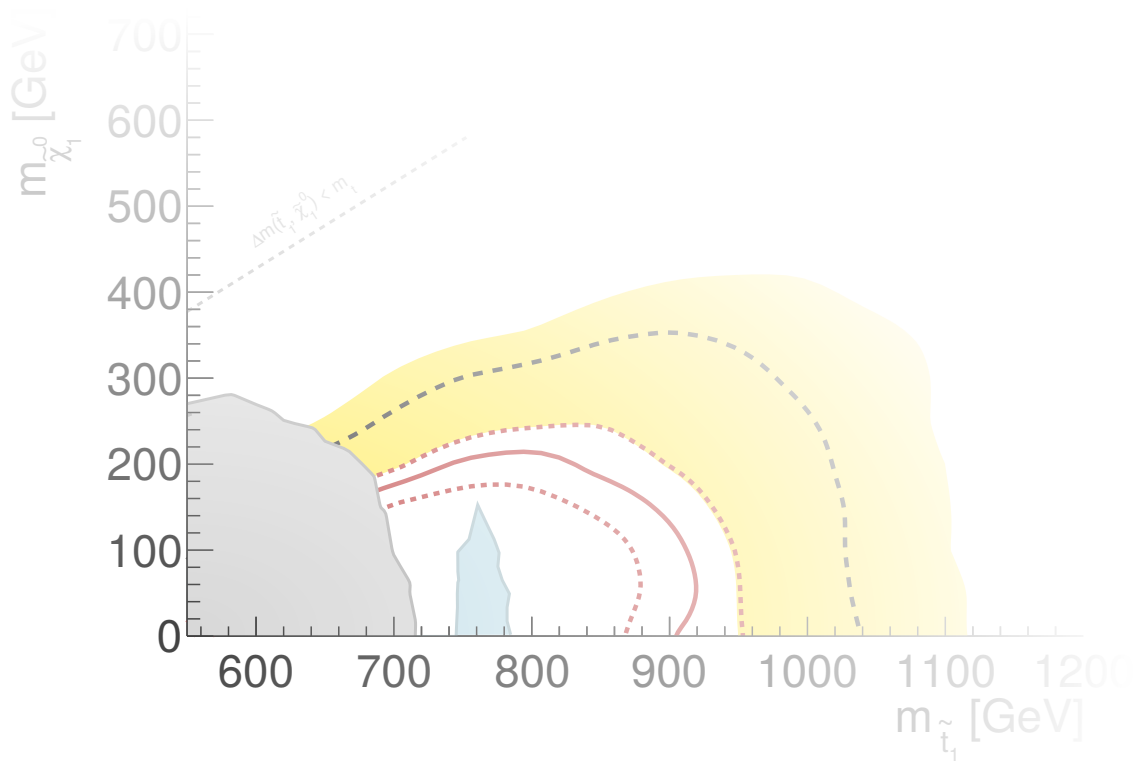
Chapter 8 Common aspects of the searches for top quark partners

In this chapter, the common aspects of the searches for partners of the top quark presented in this dissertation are described. In both extensions to the SM discussed, the pair production of heavy top quark partners can result in final states akin to SM $t\bar{t}$ production, but with additional sources of E_T^{miss}.

The pair production of vector-like top quarks gives rise to many different final states, depending on the decay branching ratio of the VLT. For a $T \rightarrow Zt$ decay, the subsequent decay of $Z \rightarrow \nu\bar{\nu}$ can give rise to large E_T^{miss}. Models with a sizeable fraction of $T \rightarrow Zt$ decays, can therefore result in $t\bar{t} + E_T^{\text{miss}}$ final states with potentially additional activity due to the decay of the second Z boson, or alternatively from the decay of the Higgs boson in the $T \rightarrow Ht$ decay. This is for example realised in the doublet model, in which the $\mathcal{B}(T \rightarrow Zt) \simeq 50\%$ for high T quark masses. The higher branching fraction of the invisible decay of the Z boson, compared to the decay into charged leptons, together with the possibility to distinguish it from pure QCD multijet events, makes this an interesting channel for the search for vector-like top quarks.

In case of supersymmetric light top squarks decaying via $\tilde{t}_1 \rightarrow t + \tilde{\chi}_1^0$, the neutralinos are a source of significant E_T^{miss}, if the mass difference between the $\tilde{t}_1$ and the $\tilde{\chi}_1^0$ is large. Alternative decay modes of the top squark, like $\tilde{t}_1 \rightarrow b + \tilde{\chi}_1^\pm(\rightarrow W^\pm + \tilde{\chi}_1^0)$ or $\tilde{t}_1 \rightarrow t + \tilde{\chi}_2^0(\rightarrow h/Z + \tilde{\chi}_1^0)$, also result in similar topologies, with potential additional activity.

The analysis focuses on events with exactly one charged lepton, either an electron or a muon[1], in the final state. In $t\bar{t}$ and top squark pair production, these events result from the semi-leptonic decay channel of the top quark pair, i.e. with one of the W bosons decaying leptonically, and the other one hadronically. Based on the branching ratio $\mathcal{B}(W \rightarrow \ell\nu) \simeq 11\%$ with $\ell = e, \mu, \tau$ and $\mathcal{B}(\tau \rightarrow \nu_\tau \bar{\nu}_{e/\mu} e/\mu) \simeq 35\%$, the total branching fraction of selectable semi-leptonic $t\bar{t}$ events is about 38%, compared to about 55% for the hadronic and 7% for the dileptonic decay modes. Even though the branching ratio is smaller than for the hadronic decay modes, the requirement of a charged lepton in the final state strongly reduces the QCD multijet background. The semi-leptonic final state thus provides a good balance of background suppression and signal selection efficiency.

---

[1]As hadronically decaying τ leptons have a low identification efficiency and a large QCD jet background, only the leptonic decay modes are considered and the electron or muon from the decay are included in the charged lepton definition. Hadronically decaying τ leptons candidates are used to suppress certain backgrounds.

8.1   Analysis strategy

The analyses discussed in this dissertation follow the same common strategy. A region of phase-space, called the signal region (SR), is defined by requirements which maximise the discovery sensitivity and minimise the SM backgrounds. The signal and background hypotheses are then tested against the number of observed and expected events in the signal region.

The main background processes after the signal selection include $t\bar{t}$ and single top production, W+jets events as well as $t\bar{t}$ production in association with a vector boson ($t\bar{t}+V$). The normalisation of the dominant backgrounds is estimated by building dedicated control regions (CRs), in which one particular background process is enhanced. All control regions and the signal region are disjunct and therefore statistically independent. The statistical interpretation is based on a simultaneous fit to the CRs and the SR, in which the background normalisations and a possible signal contribution are determined, while taking into account the experimental and theoretical systematic uncertainties. The background modelling and normalisation, as predicted by the fit, is tested in dedicated validation regions (VRs) for the dominant backgrounds.

8.2   Data sample

The analyses presented here are based on a dataset collected with the ATLAS detector in pp collisions in 2015 and 2016. The centre-of-mass energy was $\sqrt{s} = 13$ TeV and the collected events correspond to an integrated luminosity of 36.1 fb^{-1} with an uncertainty of 3.2%, after requiring that all sub-detectors were fully operational during data taking.

The events are collected using the lowest missing transverse momentum trigger in each period of data taking. For the data collected in 2015 a trigger with a threshold of $E_T^{\text{miss}} > 70$ GeV is used. During 2016 the online threshold of the trigger was successively increased in order to keep an overall stable trigger rate with increasing instantaneous luminosity. The trigger thresholds used are

- $E_T^{\text{miss}} > 90$ GeV for runs 296939 to 302872, (Periods A–D3)

- $E_T^{\text{miss}} > 100$ GeV for runs 302919 to 303892, (Periods D4–F1)

- $E_T^{\text{miss}} > 110$ GeV for runs from 303943 (Periods F2–end)

The online E_T^{miss} in the trigger is calculated from the negative vectorial sum of all jet transverse momenta in the event. The trigger efficiency surpasses 95% starting from an offline E_T^{miss} of about 200 GeV, due to resolution effects.

8.3   Signal and background modelling

Samples of MC simulated events are used for the description of the background and to model the signal processes. As summarised in Table 8.1, Powheg-Box v2 [125–128] interfaced to Pythia v6.428 [129] is used to simulate $t\bar{t}$ production as well as single top production in association with a W boson, while electroweak t-channel single top quark events are generated using the Powheg-Box v1 generator. W+jets events are simulated using the Sherpa v2.2.0 event generator [130–132], while for diboson events, Sherpa v2.1.1–2.2.1 is used. For the simulation of $t\bar{t}+V$ events, the MadGraph5_aMC@NLO v2.3.3 [133] event generator interfaced with Pythia v8.186 is used.

VLT pair production signal events are generated with Protos v2.2 [38, 39], interfaced to Pythia v8 for the parton shower and hadronisation. Signal events for the top squark pair production

Table 8.1: Overview of the nominal simulated samples.

Process	ME Generator	ME PDF	Fragmentation
$t\bar{t}$	Powheg-Box v2	CT10	Pythia v6.428
Single top	Powheg-Box v1/v2	CT10	Pythia v6.428
W+jets	Sherpa v2.2.0	NNPDF3.0	Sherpa
Diboson	Sherpa v2.1.1–2.2.1	CT10	Sherpa
$t\bar{t} + V$	MadGraph5_aMC@NLO v2.3.3	NNPDF2.3	Pythia v8.186
VLT signal	Protos v2.2	CT10	Pythia v8.186
SUSY signal	MadGraph5_aMC@NLO v2.2.3	NNPDF3.0	Pythia v8.186

are generated with MadGraph5_aMC@NLO v.2.2.3, including up to two additional partons, interfaced to Pythia v8.

All MC samples are normalised using the highest-order inclusive cross-sections available at $\sqrt{s} = 13$ TeV. The parton distribution function (PDF) sets used are CT10 [134] for the Powheg-Box and Sherpa v2.1.1 generators, NNPDF 3.0 NNLO [135] for Sherpa v2.2.0, and NNPDF 2.3 LO [136] for MadGraph5_aMC@NLO. The top quark mass is set to 172.5 GeV in all simulated samples. The samples produced with Protos, MadGraph5_aMC@NLO and Powheg-Box use EvtGen v1.2.0 [137] for the modelling of b-hadron decays. All simulated samples, except for the SUSY signals, are processed with the full simulation of the ATLAS detector [80] using Geant 4 [79]. The SUSY signal samples are processed with a fast simulation of the detector [80].

The simulated events are then reconstructed using the same software as for data and corrected so that the particle identification efficiencies, as well as the energy scales and resolutions, match the values measured in data control samples. Varying numbers of simulated minimum-bias interactions generated with Pythia 8 are overlaid on the hard-scattering event to account for pile-up interactions.

8.4 Basic event selection

A common event preselection is defined, guided by the general properties of the chosen final state. After fulfilling the trigger requirements as stated above, events have to pass basic quality requirements, referred to as *event cleaning*. Only events in which all sub-detectors are fully functional are used, based on the *Good Runs List*, a list of time spans for which the full detector is operational. Additionally, individual events with noise bursts in the calorimeters or data integrity problems are removed. In order to reject events with badly measured jets, any event is vetoed which contains a jet, after overlap removal, which fails the loose jet-cleaning recommendations.

Events are required to have exactly one reconstructed signal electron or muon, satisfying the quality requirements detailed in Chapter 7. A veto on events with a second baseline lepton reduces the contributions from dileptonic $t\bar{t}$ production. In addition, at least four jets and at least one b-jet are required. To remove possible contributions of events with badly measured jets and QCD multijet event contributions, a minimal azimuthal separation between the leading two jets and the E_T^{miss} is required, $|\Delta\phi(j_i, \vec{E}_T^{miss})| > 0.4$ for $i = 1, 2$. The choice of E_T^{miss} triggers, motivated by the additional E_T^{miss} in the signals, leads to a minimal E_T^{miss} requirement of 200 GeV, for which the trigger selection is fully efficient. Due to the large E_T^{miss} in the signal processes, this threshold is raised to 300 GeV in

Table 8.2: Common preselection requirements.

Preselection
E_T^{miss} trigger
Event cleaning
Exactly one lepton
≥ 4 jets
≥ 1 b-jet
$|\Delta\phi(j_i, \vec{E}_T^{miss})| > 0.4$ for $i = 1, 2$
$E_T^{miss} > 300\,\text{GeV}$
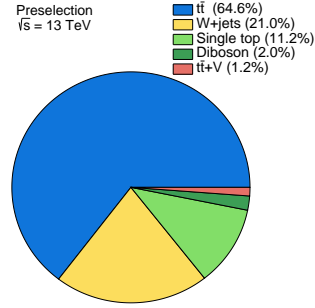
Figure 8.1: Relative contribution of the SM processes after the preselection.

order to achieve further background suppression. The full preselection is summarised in Table 8.2 and the relative contributions of the SM processes after this selection is shown in Figure 8.1. The dominant processes are $t\bar{t}$ and W+jets production, which together account for more than 85% of the events. Subdominant contributions come from single top production, followed by a smaller fraction of diboson and $t\bar{t} + V$ events. Z+jets events are strongly suppressed by the high E_T^{miss} requirement and the veto on a second lepton in the event. Due to the lepton requirements and the high E_T^{miss} threshold the contribution of QCD multijet events is negligible.

Considering two benchmark signal models, direct top squark production with $m_{\tilde{t}_1} = 1\,\text{TeV}$ and a nearly massless neutralino, and VLT production for $m_T = 1\,\text{TeV}$ in the $T \to Zt$ decay channel, the efficiency of the preselection is about 20% for the SUSY signal and about 6% for the VLQ signal. Relative to the branching ratio of 35% for the semi-leptonic $t\bar{t}$ decay mode and additionally 20% for $Z \to \nu\bar{\nu}$ and the requirement of no $Z \to \ell\ell$ decay in the case of the VLQ signal, the selection efficiencies are 60% and 55%, respectively. The efficiency for $t\bar{t}$ and W+jets events is below 1% each.

8.5 Properties of signal and background

Common properties of the signals resulting in $t\bar{t} + E_T^{miss}$ final states can be used to suppress major contributions of SM backgrounds. The dominant backgrounds after the preselection are semi-leptonic $t\bar{t}$ and W+jets production. Both processes contain a leptonically decaying W boson in the final state, of which the transverse mass can be calculated to

$$m_T = \sqrt{2p_T^\ell E_T^{miss}(1 - \cos\Delta\phi)}, \tag{8.1}$$

where p_T^ℓ is the transverse momentum of the lepton, $\Delta\phi$ is the azimuthal angle between the lepton and the direction of the E_T^{miss}, and the masses of the lepton and the invisible particle are neglected. Apart from resolution effects, this variable is bound from above by the mass of the W boson, in events where the lepton and the E_T^{miss} only come from a leptonic W boson decay. For signal processes with additional sources of E_T^{miss}, this bound can be evaded. Figure 8.2 compares the distributions of E_T^{miss} and m_T for the dominant backgrounds and the two benchmark signal models. Even after the high threshold in the preselection, the E_T^{miss} still offers a good separation between the backgrounds and both signal models. The m_T distribution shows the kinematic endpoint for the background processes, which is evaded by the signal models. The VLT signal has a small
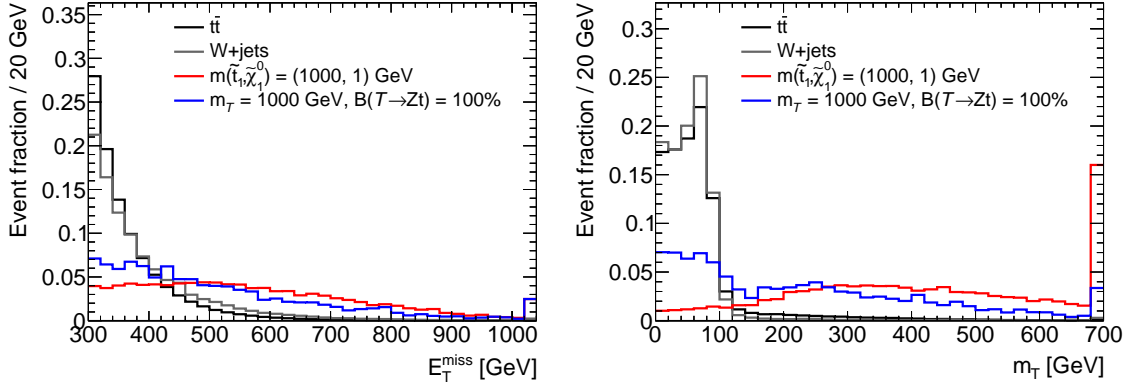
Figure 8.2: Comparison of the distributions of E_T^{miss} (left) and m_T (right) for the dominant background processes $t\bar{t}$ and W+jets, and for two signal models after the preselection. The individual distributions are normalised to a unit area.
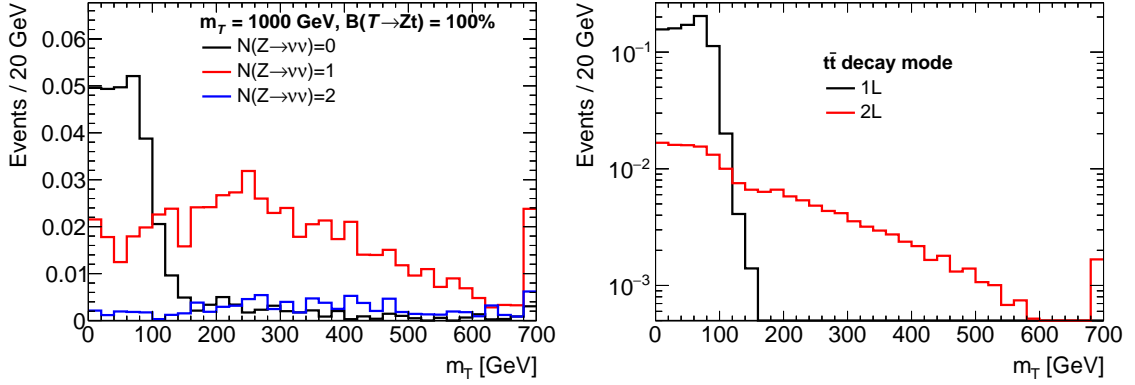
Figure 8.3: Comparison of the distributions of m_T for VLT signal events with different numbers of $Z \to \nu\bar{\nu}$ decays (left) and for different $t\bar{t}$ decay modes (right) after the preselection. In both plots the sum of the distributions is normalised to unity, preserving the relative fraction of events of the categories.

contribution from events in which none of the Z bosons decay invisibly, for which the kinematic end point holds. This can be seen in Figure 8.3.

In the construction of the m_T variable, the E_T^{miss} is assumed to come essentially from the neutrino from the leptonically decaying W boson. There can be additional contributions in dileptonic $t\bar{t}$ events ($t\bar{t}$ 2L), in which one of the leptons fails detection or identification. In contrast to the semi-leptonic $t\bar{t}$ process ($t\bar{t}$ 1L), additional jets from QCD radiation are required to pass the preselection requirements. As hadronically decaying τ leptons are generally reconstructed as a jet in the detector, dileptonic $t\bar{t}$ decay modes with a hadronic τ decay only need one additional jet, while for other dileptonic $t\bar{t}$ events at least two additional jets are required. The m_T distribution of semi-leptonic and dileptonic $t\bar{t}$ events is compared in Figure 8.3, showing also the relative fraction of these categories after the preselection. Requirements on m_T above the W boson mass are effective in reducing the semi-leptonic $t\bar{t}$ background, while dileptonic $t\bar{t}$ events are less affected.

In order to suppress the dileptonic $t\bar{t}$ background, the am_{T2} variable [138] is used, which is a variant of the general m_{T2} variable [139–141]. This is a variable that targets decay topologies in

which pair produced particles decay into two branches, both with particles measured in the detector and invisible particles, like neutrinos. m_{T2} is the minimum mass of a parent particle, assuming pair production and the subsequent decay into the visible and invisible particles in the two branches. The transverse mass of the particles in branch i is given by

$$m_{T,i}^2 = \left(\sqrt{p_{T,i}^2 + m_{p_i}^2} + \sqrt{q_{T,i}^2 + m_{q_i}^2} \right)^2 - \left(\vec{p}_{T,i} + \vec{q}_{T,i} \right)^2 , \qquad (8.2)$$

where p denotes the sum of the visible particles momenta and q the sum of the invisible momenta in the branch. Assuming that the missing transverse momentum in the event entirely consists of the invisible particles in the two branches a and b, m_{T2} is defined as the minimisation over any possible splitting of $\vec{E}_T^{miss}$ into two parts, $\vec{q}_{T,a} + \vec{q}_{T,b} = \vec{E}_T^{miss}$, of the maximum of the corresponding transverse masses $m_{T,a}$ and $m_{T,b}$,

$$m_{T2} = \min_{\vec{q}_{T,a} + \vec{q}_{T,b} = \vec{E}_T^{miss}} \left[\max \left(m_{T,a}, m_{T,b} \right) \right] . \qquad (8.3)$$

In general, the choice of visible particles and the assumed masses m_{q_a} and m_{q_b} of the invisible particles define the specific variant of the m_{T2} variable.

The am_{T2} variable targets dileptonic $t\bar{t}$ decays with one undetected charged lepton, rendering the W boson decay effectively invisible. The two decay branches are therefore the charged lepton, the neutrino and the b-jet on the one side, and the b-jet and undetected W boson decay on the other side. Accordingly, the measured particles for branch a are the charged lepton and the b-jet, with the invisible particle assumed to be massless. Branch b consists of the second b-jet as the measured particle and the undetected W boson as the invisible particle, leading to an assumed mass of $m_{q_b} = m_W = 80\,\text{GeV}$. The b-jets are identified based on the highest b-tagging weights, as only one b-jet is required in the preselection. As the choice of which b-jet is combined with the lepton is ambiguous, both am_{T2} variants are calculated and the minimum is kept as the final discriminant.

For dileptonic $t\bar{t}$ events the am_{T2} distribution is expected to show a kinematic endpoint at the mass of the top quark. As the underlying assumptions do not hold in the case of signal events with additional sources of E_T^{miss}, for these processes the am_{T2} can exceed the bound and generally tends to higher values due to the higher E_T^{miss}. Figure 8.4 shows the distribution of am_{T2} for the dominant backgrounds and two benchmark signals, requiring the preselection and additionally $m_T > 120\,\text{GeV}$ in order to suppress the semi-leptonic $t\bar{t}$ process and therefore increase the fraction of dileptonic $t\bar{t}$ events. The expected kinematic bound is well represented in the distribution for the $t\bar{t}$ background, with only a small fraction of events having $am_{T2} > m_t$. This can happen in case that the b-jets from the $t\bar{t}$ decay are not correctly identified or when the track of the lost lepton is reconstructed and enters the soft-term of the E_T^{miss}, as in that case not the full transverse momentum of the W boson is undetected. Another decay mode which allows $t\bar{t}$ events to have $am_{T2} > m_t$ are dileptonic $t\bar{t}$ decays with a hadronically decaying τ lepton, which can be reconstructed as a jet.

A second m_{T2} variant, called m_{T2}^τ, is used to suppress dileptonic $t\bar{t}$ events with a hadronically decaying τ lepton. The m_{T2}^τ is computed in events with a hadronic τ candidate, with the τ as the visible particle for the one branch, and the observed lepton for the other branch. Hadronic τ candidates are required to have the opposite charge of the selected signal lepton. The invisible particles are the neutrinos from the W boson decays as well as from the τ decay, leading to $m_{q_a} = m_{q_b} = 0\,\text{GeV}$. The m_{T2}^τ variable therefore has a kinematic endpoint at the W boson mass for dileptonic $t\bar{t}$ events with a hadronic τ. As for the am_{T2} variable, for signal events the underlying assumptions do not hold and larger values of m_{T2}^τ are reached. Figure 8.4 shows the distribution of m_{T2}^τ, as well as the fraction of events without a hadronic τ candidate. For the $t\bar{t}$ background about
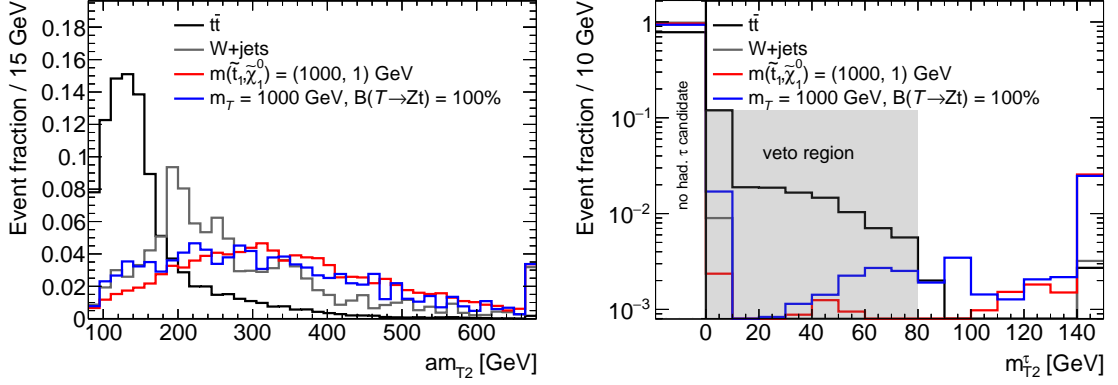
Figure 8.4: Comparison of the distributions of am_{T2} (left) and m_{T2}^{τ} (right) for the dominant background processes $t\bar{t}$ and W+jets, and for two signal models, after the preselection and $m_T > 120\,\text{GeV}$. Due to the m_T requirement, the $t\bar{t}$ process is dominated by dileptonic decay modes. The left-most column of the right plot shows the fraction of events without a hadronic τ candidate.

20% of the events feature a hadronic τ candidate after the preselection and $m_T > 120\,\text{GeV}$, with only a small fraction of those exceeding the $m_{T2}^{\tau} < m_W$ bound. In order to reject $t\bar{t}$ events with a hadronic τ lepton, events with a hadronic τ candidate and $m_{T2}^{\tau} < 80\,\text{GeV}$ are removed.

A different type of variable used to suppress the backgrounds is the $H_{T,\text{sig}}^{\text{miss}}$, which estimates the significance of the missing transverse momentum, here calculated using only the calibrated objects in the analysis [142]. It can be used to ensure a good measurement quality and reject events with E_T^{miss} due to mismeasured objects. It is defined by

$$H_{T,\text{sig}}^{\text{miss}} = \frac{\left|\vec{H}_T^{\text{miss}}\right| - 100\,\text{GeV}}{\sigma_{\vec{H}_T^{\text{miss}}}}\,, \tag{8.4}$$

where $\vec{H}_T^{\text{miss}}$ is the negative vectorial sum of the jet and lepton momenta and $\sigma_{\vec{H}_T^{\text{miss}}}$ its resolution. For each event, the jet momenta are smeared 1000 times according to the per-jet energy resolution and the $\vec{H}_T^{\text{miss}}$ is recalculated. The $\sigma_{\vec{H}_T^{\text{miss}}}$ is taken as the RMS of the $\vec{H}_T^{\text{miss}}$ distribution obtained from the smeared jets. The lepton energy resolution is assumed to be negligible in this calculation. The expected mean $\vec{H}_T^{\text{miss}}$ for the background processes, taken to be $100\,\text{GeV}$, is subtracted. This value was optimised in a previous analysis [143]. Figure 8.5 shows the $H_{T,\text{sig}}^{\text{miss}}$ distribution for the dominant backgrounds and two benchmark signals. In general, the signal models tend to higher $H_{T,\text{sig}}^{\text{miss}}$ values than the background processes. Even though the E_T^{miss} distribution is similar for the stop signal and the VLT signal, the stop signal extends to higher $H_{T,\text{sig}}^{\text{miss}}$ values. This is due to the higher number of jets in the VLT signal model, which affect the resolution of the $\vec{H}_T^{\text{miss}}$ distribution, as shown in Figure 8.5.

In general, the separation of signals with a $t\bar{t} + E_T^{\text{miss}}$ final state from the dominant SM backgrounds relies on the additional E_T^{miss}. While the invisible particles in the final state make it difficult to directly reconstruct the signal particle masses, the absolute value of the E_T^{miss} and also supplementary information like its significance and kinematic constraints offer methods to suppress the dominant $t\bar{t}$ and W+jets backgrounds.
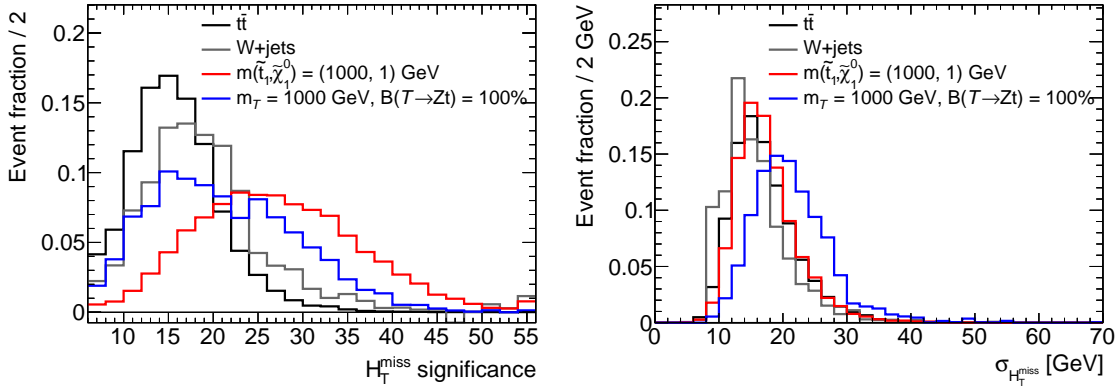
Figure 8.5: Comparison of the distribution of $H_{\mathrm{T,sig}}^{\mathrm{miss}}$ (left) and the $\vec{H}_{\mathrm{T}}^{\mathrm{miss}}$ resolution (right) for the dominant background processes $t\bar{t}$ and W+jets, and for two signal models, after the preselection and $m_{\mathrm{T}} > 120\,\mathrm{GeV}$.

8.6 Systematic uncertainties

In addition to the statistical uncertainties, due to the finite number of events, systematic uncertainties affect the background estimates and also the signal modelling. These come from uncertainties in the theoretical predictions on the one side, and the imperfect knowledge of the experimental conditions and the finite precision of the object calibration on the other side. In general, these uncertainties affect the overall normalisation of the estimates, as well as the relative fraction of events in the control and signal regions. For backgrounds which are normalised in the simultaneous fit, systematic effects on the normalisation alone are absorbed by the normalisation parameters in the fit. The uncertainties on such backgrounds thus affect the transfer factor, i.e. the ratio of expected events in the signal to the control regions.

In this section the sources of systematic uncertainties are discussed, while the details of the estimation and the size of the effects are given in the chapters of the respective analyses.

8.6.1 Theory uncertainties

In general, the uncertainties in the modelling of a process come from the choice of MC event generator, the hadronisation and fragmentation modelling, as well as the choice of factorisation and renormalisation scales. In addition, the uncertainty in the total cross-section of the process affects the overall normalisation of the estimated events.

8.6.1.1 $t\bar{t}$ modelling uncertainty

The uncertainty in the $t\bar{t}$ MC generator is estimated by comparing events produced with Powheg-Box and with MadGraph5_aMC@NLO, both interfaced to Herwig++ for the showering. The hadronisation and fragmentation uncertainties are assessed by comparing events generated with Powheg-Box and showered with either Pythia or Herwig++. The uncertainty in the amount of initial- and final-state radiation is estimated by comparing Powheg-Box–Pythia samples with different parton-shower radiation settings and different settings for the QCD radiation at NLO accuracy. Additionally, the factorisation and renormalisation scales are varied by factors of 0.5 and 2.

As the $t\bar{t}$ background is normalised in a dedicated control region in the analyses, the uncertainty in the total cross-section does not affect the background estimate.

8.6.1.2 *W*+jets modelling uncertainty

The *W*+jets modelling uncertainty is estimated by comparing the nominal sample generated with SHERPA to a sample generated with MADGRAPH5_aMC@NLO and showered with PYTHIA v8, covering both differences in the event generation as well as the hadronisation and fragmentation modelling. Additionally, the effects of independently varying the scales for the factorisation, renormalisation and resummation by factors of 0.5 and 2, as well as varying the scale of the matching scheme related to the merging of matrix elements and parton showers between 15 GeV and 30 GeV, are taken into account.

As the *W*+jets background is normalised in a dedicated control region in the analyses, the uncertainty in the total cross-section does not affect the background estimate.

8.6.1.3 Single top modelling uncertainty

The uncertainties in the choice of MC event generator, the hadronisation and fragmentation modelling, and the initial- and final-state radiation for the single top process are estimated in the same way as for the $t\bar{t}$ process. The total cross-section uncertainty is 5.3% [144], derived from the uncertainty in PDF effects and the scales.

Additionally, the single top background estimate is affected by the modelling of the interference between the $t\bar{t}$ and the Wt processes at NLO. As the final states for the processes $pp \rightarrow t\bar{t} \rightarrow W^+bW^-\bar{b}$ and $pp \rightarrow W^-\bar{b}t\,(\rightarrow W^+b)$ are identical, interference effects have to be taken into account. Following the "Diagram Removal" scheme [145], the diagrams containing two top quark resonances are removed in the generation of the single top Wt events at NLO. In order to estimate an uncertainty in this procedure, the sum of the $t\bar{t}$ and Wt events are compared to an sample of inclusive $WWbb$ events generated using MADGRAPH.

8.6.1.4 $t\bar{t} + V$ modelling uncertainty

The uncertainties in the $t\bar{t} + V$ modelling are assessed by comparing samples generated with renormalisation and factorisation scales modified by factors of 0.5 and 2. Additionally, the nominal prediction generated with MADGRAPH5_aMC@NLO is compared to a sample generated with SHERPA. The uncertainty in the total cross-section is 13% [133].

8.6.1.5 Diboson modelling uncertainty

The uncertainties in the modelling of diboson processes are assessed by comparing samples generated with renormalisation, factorisation and resummation scales modified by factors of 0.5 and 2. The uncertainty in the total cross-section for the diboson process is 6% [146].

8.6.2 Experimental uncertainties

The experimental sources of systematic uncertainties are the finite precision of the calibration of physics objects, as well as the imperfect knowledge of the exact experimental conditions, like the total integrated luminosity. Some of these experimental uncertainties, namely the lepton-calibration related effects, are found to be negligible and are not included in the final statistical evaluation.

Jet calibration   The uncertainties in the jet energy scale calibration are evaluated in form of a strongly reduced parametrisation [147]. For this, the different uncertainties which affect the jet energy scale are combined to three parameters, with one additional parameter describing the non-closure in the η-intercalibration. Additionally, the uncertainty in the jet energy resolution is considered.

Flavour tagging uncertainties   The flavour tagging uncertainties comprise the errors in the b-tagging efficiency calibration, as well as the uncertainty in the c-jet and light-flavour jet mis-tag rates. As the latter two calibrations are based on measurements at 8 TeV, additional uncertainties in the simulation based extrapolation are considered as well. The efficiency calibration is extrapolated for jets with $p_T > 500$ GeV, and an additional uncertainty based on simulation is included.

Lepton calibration   The effects of the uncertainties in the measurement of the reconstruction, identification and isolation efficiencies for electrons and muons are evaluated and found to be negligible. The resulting uncertainty in the total background prediction is well below 1% in all cases.

Missing transverse momentum   The missing transverse momentum is mainly affected by the calibrated objects in the event and the uncertainties in the calibration of the high momentum objects are propagated through the calculation of the E_T^{miss}. Additionally, the uncertainties in the scale and the resolution of the soft-term are considered, which includes all tracks that are not associated to hard, calibrated objects in the event. These affect both the magnitude as well as the direction of the E_T^{miss}.

Other experimental uncertainties   The analyses are subject to the uncertainties in the integrated luminosity and the pile-up profile. The former amounts to an overall normalisation effect of 3.2%.

8.7   Comparison of data and simulation

The general modelling of the SM prediction is validated after the preselection by comparing the distributions of data and simulation of the sensitive variables.

First, the efficiency of the trigger selection is compared in data and simulation. The events are collected using single-lepton triggers as control triggers, which are uncorrelated in the trigger logic and have a high efficiency. The trigger efficiency is then the ratio of the number of events passing both the E_T^{miss} and the control triggers, to the number of all events passing the control triggers. For the comparison, events are required to have exactly one lepton, at least four jets, at least one b-jet and $m_T > 30$ GeV. Figure 8.6 shows the efficiency as a function of the offline E_T^{miss} for data and $t\bar{t}$ simulation. The trigger is fully efficient, $\varepsilon > 99\%$, at the preselection requirement of $E_T^{miss} > 300$ GeV and the efficiency is well modelled in the simulation.

Figures 8.7 to 8.8 show the distributions of the introduced variables. In general, no significant deviation between data and the prediction is seen. In the intermediate m_T and am_{T2} regions the simulation predicts slightly less events than observed in data, but the difference is insignificant compared to the systematic uncertainties. The E_T^{miss} and $H_{T,sig}^{miss}$ distributions show very good agreement, as does the m_{T2}^τ variable for events with a hadronic τ candidate.
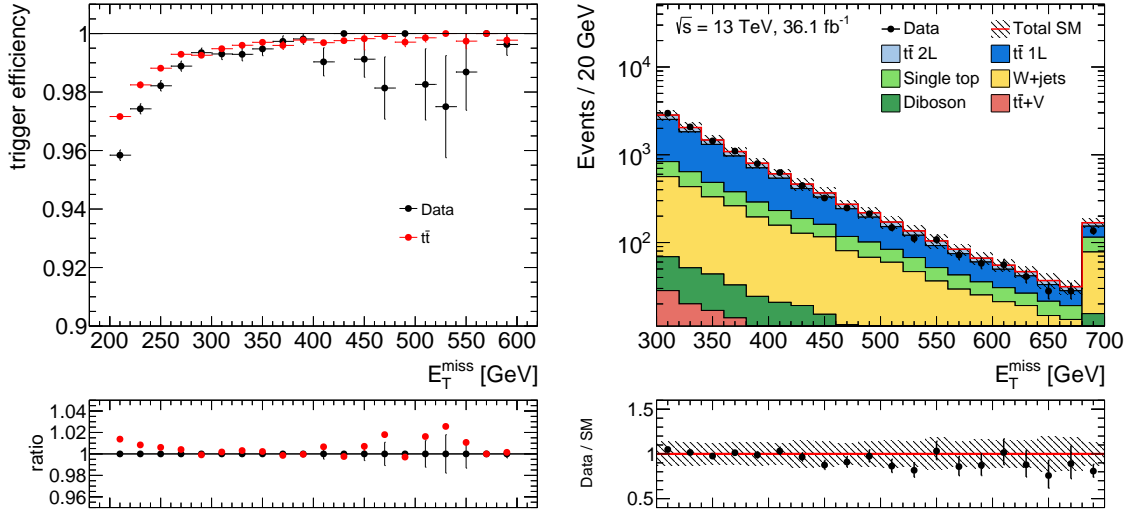
Figure 8.6: Comparison of the trigger efficiency for data and $t\bar{t}$ simulation (left), and comparison of data and simulation in the E_T^{miss} distribution after preselection (right). The lower panels show the ratio of the data to the prediction. The error bands include statistical and systematic uncertainties.
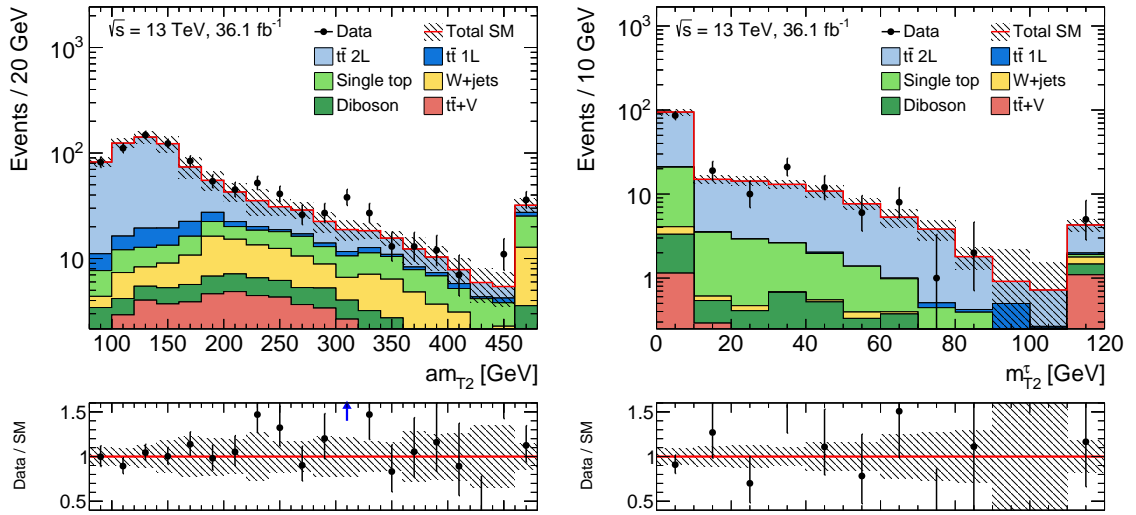
Figure 8.7: Comparison of data and simulation in the am_{T2} and m_{T2}^{τ} distributions after the preselection and $m_T > 120\,\text{GeV}$. The lower panels show the ratio of the data to the prediction. The error bands include statistical and systematic uncertainties. The m_{T2}^{τ} distribution is shown only for events with a hadronic tau candidate.
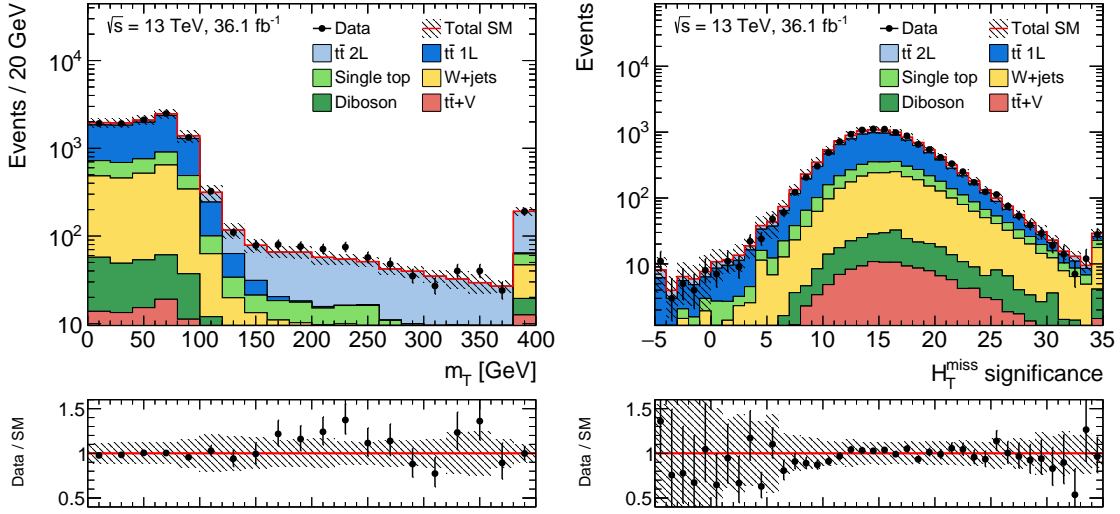
Figure 8.8: Comparison of data and simulation in the m_T and $H_{T,sig}^{miss}$ distributions after the preselection. The lower panels show the ratio of the data to the prediction. The error bands include statistical and systematic uncertainties.

8.8 Statistical evaluation

The statistical evaluation of the analyses is based on maximum likelihood fits involving the expected and observed number of events in the signal and control regions [148]. The expected number of events in a region is given by the sum over all background processes and optionally a signal contribution. Backgrounds that are normalised in the fit, in contrast to those taken purely from simulation, carry a normalisation factor μ_i, where i is a symbolic label for the background. If a signal model is included in the fit, its normalisation is given by an additional, free parameter μ.

Systematic uncertainties are included as nuisance parameters in the fit. They are implemented as smearing factors for the expected events with a Gaussian constraint in the likelihood. The mean of the constraint is given by the nominal prediction and the standard deviation is given by the size of the systematic uncertainty. Additionally, nuisance parameters with a Gamma constraint are included to account for the statistical uncertainties due to the finite number of simulated events, when the relative statistical uncertainty of the events in a bin is larger than 5%.

The likelihood takes the form

$$L(\mu, \theta) = \prod_{r \in \text{Regions}} \frac{(\mu \cdot s_r + b_r)^{n_r}}{n_r!} e^{-(\mu \cdot s_r + b_r)} \cdot \prod_{k=1}^{m} \rho(\theta_k), \tag{8.5}$$

where n_r is the observed number of events in region r, s_r and b_r are the signal and background expectations in that region, implicitly depending on the nuisance parameters and the background normalisation factors, and θ stands for the nuisance parameters, with their constraint terms $\rho(\theta_k)$. Depending on the nuisance parameter, the constraint can take different functional forms. As detailed above, systematic uncertainties are included with a Gaussian constraint, with the probability density function (pdf)

$$\rho(\theta) = \frac{1}{\sqrt{2\pi}\sigma} \exp\left(-\frac{(\theta - \theta_0)^2}{2\sigma^2}\right), \tag{8.6}$$
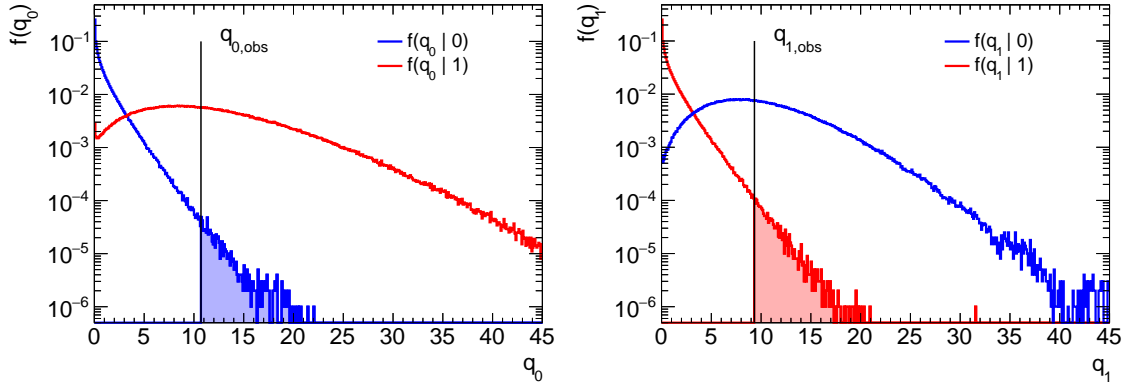
Figure 8.9: Distributions of the q_0 (left) and q_1 (right) test statistics under the background-only hypothesis (blue) and the signal-and-background hypothesis (red). The observed values of the test statistics are taken from the median of $f(q_0|1)$ (left) and $f(q_1|0)$ (right) and the filled areas give the p_0 and p_1, respectively.

with the nominal value θ_0 and the standard deviation σ. Typically, the nuisance parameters are substituted by $\alpha = (\theta - \theta_0)/\sigma$, so that the nominal value of the parameter is 0 and the standard deviation is 1.

In the so-called *background only fit* the likelihood is maximised with μ fixed to 0, i.e. without any signal contribution, and without the signal region. This gives the nominal background normalisation factors.

In order to conclude on the existence of a signal, hypothesis tests are performed. The null-hypothesis corresponds to the SM prediction, i.e. the estimate for $\mu = 0$. The alternative hypothesis is that of the SM prediction with the addition of the signal. The so-called profile-likelihood ratio [148] is used as the test-statistic, defined as

$$\lambda(\mu) = \frac{L(\mu, \hat{\hat{\theta}})}{L(\hat{\mu}, \hat{\theta})} \, . \tag{8.7}$$

Here $L(\hat{\mu}, \hat{\theta})$ refers to the likelihood maximised with respect to both μ and θ, and $L(\mu, \hat{\hat{\theta}})$ to the likelihood maximised with respect to θ for a fixed signal normalisation μ. The profile likelihood ratio takes values in the range $0 < \lambda < 1$, where larger values indicate better agreement between the data and the estimate with the signal strength μ. Commonly the form $q_\mu = -2 \ln \lambda(\mu)$ is used.

Using the test statistics, a p-value can be computed, which gives the compatibility between the observed data and the hypothesised value of μ. It is defined as

$$p_\mu = \int_{q_{\mu,\text{obs}}}^{\infty} f(q_\mu|\mu) \, dq_\mu \, , \tag{8.8}$$

where $f(q_\mu|\mu)$ is the pdf of q_μ under the hypothesis of μ, and $q_{\mu,\text{obs}}$ is the observed value of the test statistics in data. The compatibility of the background-only hypothesis with the observed data is therefore p_0, while p_1 gives the compatibility of the observation with the nominal signal prediction.

Figure 8.9 gives examples for the pdf of the test statistics q_0 and q_1 and the expected p_0 in a signal case, and the p_1 in the background-only case. The q_0 distributions are shown for the background only hypothesis in blue and for the nominal signal-plus-background hypothesis, with $\mu = 1$, in red. The median of the distribution $f(q_0|1)$, i.e. of the distribution of the q_0 value assuming a typical

signal, gives the median significance for a discovery. Accordingly, the blue, filled area corresponds to the area under the background only distribution for which $q_0 > q_{0,\mathrm{obs}}$, i.e. it corresponds to the expected p_0 value in the case of a signal. For the distribution of q_1, the median of the background only distribution $f(q_1|0)$ is shown. The red, filled area corresponds to the expected p_1 value.

Conventionally, a signal is said to be excluded at 95% confidence level (CL) if $p_1 < 0.05$, corresponding to a Gaussian significance of $Z = 1.64$. Much stronger requirements are placed on the claim of rejecting the background-only hypothesis, corresponding to the SM. Evidence of new physics is achieved for $p_0 < 1.3 \times 10^{-3}$, equivalent to $Z = 3$, and a discovery is claimed for $p_0 < 2.9 \times 10^{-7}$ ($Z = 5$).

In order to derive limits on the cross-section of a signal process, the signal strength μ is scanned and p_μ is calculated repeatedly. The value of μ for which $p_\mu = 0.05$ is the 95% CL upper limit on the signal strength, and can be translated to an upper limit on the signal cross-section by scaling the nominal cross-section with the signal strength limit. Additionally, an upper limit on any non-background contribution to the signal region can be obtained by assuming a signal model which only contributes to the signal region and deriving a limit on its strength.

The distribution of the test statistics can be obtained from MC simulation, by repeatedly generating "toy" observations following the assumed hypothesis and calculating the test statistics. For large number of observed events, an approximation can be used to describe the profile likelihood ratio [149],

$$q_\mu = \frac{(\mu - \hat{\mu})^2}{\sigma^2} + O(1/\sqrt{N}) . \tag{8.9}$$

The best-fit signal strength $\hat{\mu}$ follows a Gaussian distribution with mean μ' and standard deviation σ. Neglecting the $O(1/\sqrt{N})$ term, the approximate q_μ then follows a non-central χ^2-distribution with one degree of freedom.

The CL_s method [150] is introduced in order to avoid unreasonably strong limits on μ in the case of a downwards fluctuation of the observed data. The CL_s value is defined as

$$CL_s = \frac{p_\mu}{1 - p_0} . \tag{8.10}$$

For searches at the LHC, the CL_s value is used in order to derive limits on the signal strength, and a signal is excluded at 95% CL if $CL_s < 0.05$ for $\mu = 1$. In the statistical evaluation of the analyses, the `HistFitter` [151] program is used.

Chapter 9 Search for vector-like top quarks in the $T \rightarrow Zt$ channel

$\mathbf{I}$n this chapter, the search for vector-like top quarks in the $T \rightarrow Zt$ channel is described. The analysis is based on the common analysis strategy described in the previous chapter. The discrimination relies on the general properties of signals in final states similar to $t\bar{t} + E_{\mathrm{T}}^{\mathrm{miss}}$ in addition to the special features of the vector-like top quark decay. The results of this analysis have been published in Ref. [3].

Due to the distinct features of the different vector-like top quark decay modes, this search has been optimised for the $T \rightarrow Zt$ decay mode. Other searches with the ATLAS experiment focus on other decay modes, like $T \rightarrow Ht$ [152] or $T \rightarrow Wb$ [153], using Run 2 data from 2015 and 2016. These searches set lower limits on the mass of the vector-like top quark in the range of 1.1–1.2 TeV, depending on the branching ratios. The ATLAS analyses have been designed with common physics object definitions in order to ease a future combination of the results.

9.1   Signal modelling and properties

In addition to the common properties of signals in $t\bar{t} + E_{\mathrm{T}}^{\mathrm{miss}}$ final states, the vector-like top quark pair production leads to distinct features that differentiate it from the SM background. As the top quark partners have a large mass, $m_T \approx O(1\,\mathrm{TeV})$, the decay products receive a large transverse momentum. Due to this boost, the jets from subsequent hadronic decays of the decay products of the vector-like top quarks can be nearby or even overlapping in the detector. In order to capture these boosted hadronic decays, jets with a large radius parameter, called large-R jets, are used. These are clustered with the anti-k_t algorithm with $R = 1.0$, using as input constituents the calibrated $R = 0.4$ ("small-radius") jets in the event. This so-called jet re-clustering [154] has the advantage that no dedicated calibration is required and the kinematic properties, such as the transverse momentum and the mass, can directly be derived from the inputs. In order to improve the mass resolution a technique akin the trimming of large-radius jets build from topo-clusters [155] is applied. Small-radius jets are removed from a large-R jet if their p_{T} is less than 5% of the large-R jet p_{T}. The minimal kinematic requirements for large-R jets in the analysis are $p_{\mathrm{T,jet}} > 150\,\mathrm{GeV}$ and $m_{\mathrm{jet}} > 50\,\mathrm{GeV}$, to ensure that the objects fall loosely in the category of massive, boosted resonances. The exact requirements are later refined in the optimisation of the signal region selection.

No explicit requirement on the number of constituents is made, therefore large-R jets containing exactly one small-radius jet are possible. The transverse momentum of the Z bosons in signal events is often large enough that the resulting two jets from the decay products overlap in the detector. The resulting two jets from the decay products then often overlap in the detector. These jets cannot be
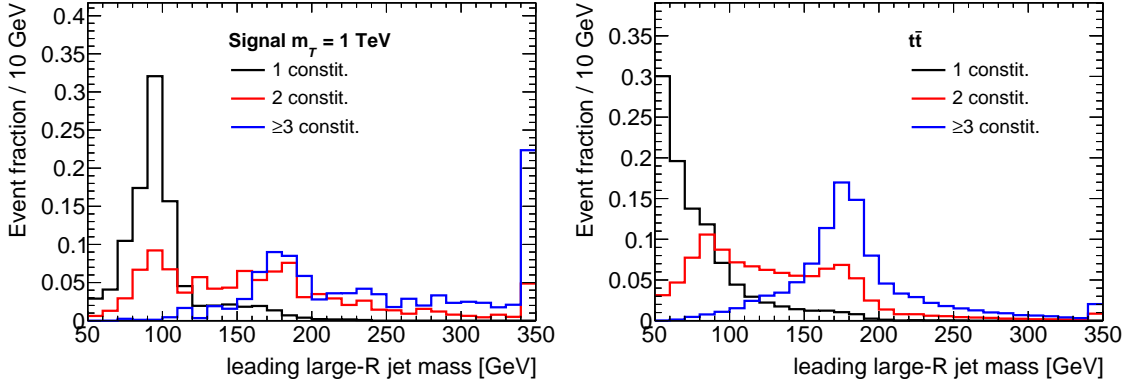
Figure 9.1: Mass of the leading large-R jet for different number of constituent jets for a benchmark signal (left) and for $t\bar{t}$ events (right).

resolved when their distance is less than $\Delta R = 0.4$ and are then reconstructed as a single, massive, small-radius jet. This behaviour can be seen in Figure 9.1, where the large-R jet mass is shown in dependence on the number of constituents. For the signal events, a clear peak can be seen at the Z boson mass for large-R jets containing exactly one constituent jet. For higher constituent multiplicities, peaks are located in the mass range of W and Z bosons and at the mass of the top quark. For the $t\bar{t}$ background, large-R jets with only one constituent peak at the minimal mass requirement of 50 GeV, while for larger number of constituent jets, the W boson or the top quark mass can be reconstructed.

A comparison of the p_T-leading and sub-leading large-R jet masses for the dominant backgrounds and a signal process is shown in Figure 9.2. For the W+jets background, no distinct peak can be seen, as no hadronically decaying resonances are produced in this process. For $t\bar{t}$ events, the leading large-R jet often contains the hadronic top quark decay, resulting in a peak at the top quark mass. For less boosted events, the large-R jet captures the subsequent hadronic W boson decay. In the signal, the mass peaks of hadronically decaying Z bosons and top quarks can be seen. The mass distribution of the sub-leading large-R jet shows that for the signal processes generally a second, hadronic resonance can be reconstructed, while for the backgrounds no distinct mass peaks are found.
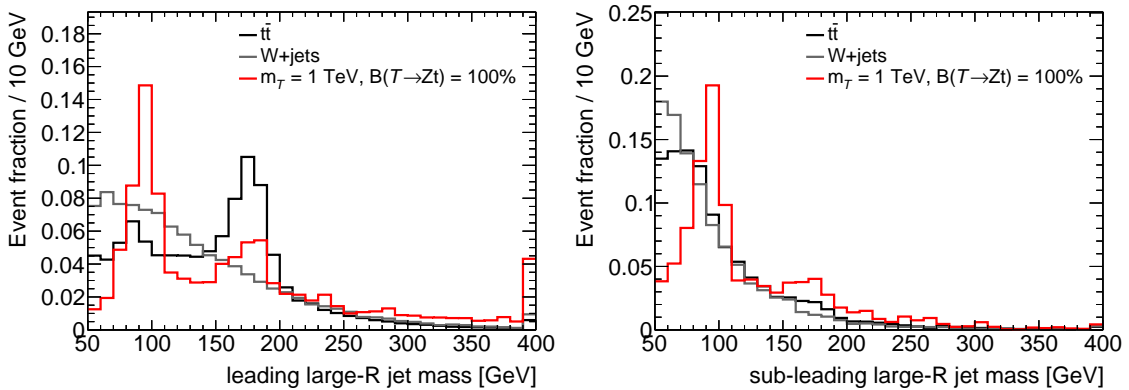
Figure 9.2: Comparison of the mass of the leading (left) and the sub-leading large-R jet (right) for the dominant background processes $t\bar{t}$ and W+jets, and for a signal process after the preselection.
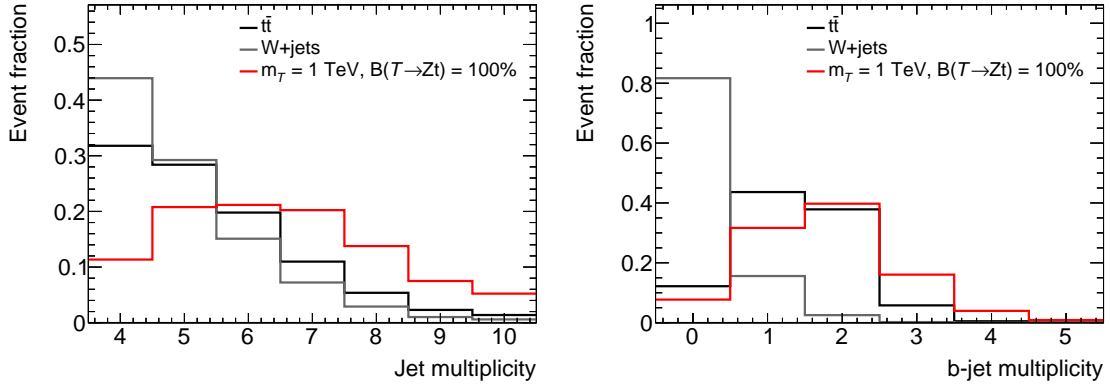
Figure 9.3: Comparison of the jet multiplicity (left) and *b*-jet multiplicity (right) for the dominant background processes $t\bar{t}$ and *W*+jets, and for a signal process after the preselection. No requirement on the *b*-jet multiplicity is set for the right plot.

Figure 9.3 shows the jet and *b*-jet multiplicities for the dominant backgrounds and a signal. Generally, the signal events tend to contain more jets and more *b*-jets than the background, due to the additional particles produced in the decay of the vector-like top quarks. The *b*-jet multiplicity is increased by the subsequent $Z \rightarrow b\bar{b}$ decays, for which the branching fraction is about 15%. In view of a possible combination with other searches for vector-like top quarks, especially those focusing on the $T\bar{T} \rightarrow HtH\bar{t}$ decay mode which features a large *b*-jet multiplicity, no stronger requirements are set on the jet and *b*-jet multiplicities than the preselection of ≥ 4 jets and ≥ 1 *b*-jet.

Figures 9.4 and 9.5 show comparisons of the properties of signals with different masses and decay branching ratios. Additional comparisons for other variables are shown in Appendix B.1.1. As can be seen, higher vector-like top quark masses lead to stronger kinematic features. The E_T^{miss} distribution for $m_T = 1.2\,\mathrm{TeV}$ tends towards higher values, while for $m_T = 800\,\mathrm{GeV}$ a surplus of events at lower values can be seen. As the final state does not differ, properties like the jet multiplicity are less affected by the mass of the vector like top quark.

Differences in the signal model, or more general in the decay branching ratios, have a visible impact on the signal properties. Models with a high $\mathcal{B}(T \rightarrow Wb)$, like the singlet model, have a lower E_T^{miss}. Additionally, the basic assumption that the E_T^{miss} is not only due to a leptonic *W* boson decay does not always hold for such models, leading to differences in variables like the m_T. The $T \rightarrow Ht$ decay, which has a branching ratio of 50% in the doublet model, leads to a higher jet and also *b*-jet multiplicity in the final state, due to the Higgs boson decay. This model can also feature a peak at 125 GeV in the distribution of the large-*R* jet masses.

In general, the decay branching modes have a larger impact on the final state and signal properties than the VLT masses. As discussed in the introduction, this analysis therefore focuses on the $T \rightarrow Zt$ decay, while other analyses are optimised for different scenarios. While the analyses are optimised and designed individually, basic parameters like the physics objects definitions are harmonised in view of a possible combination of the results.
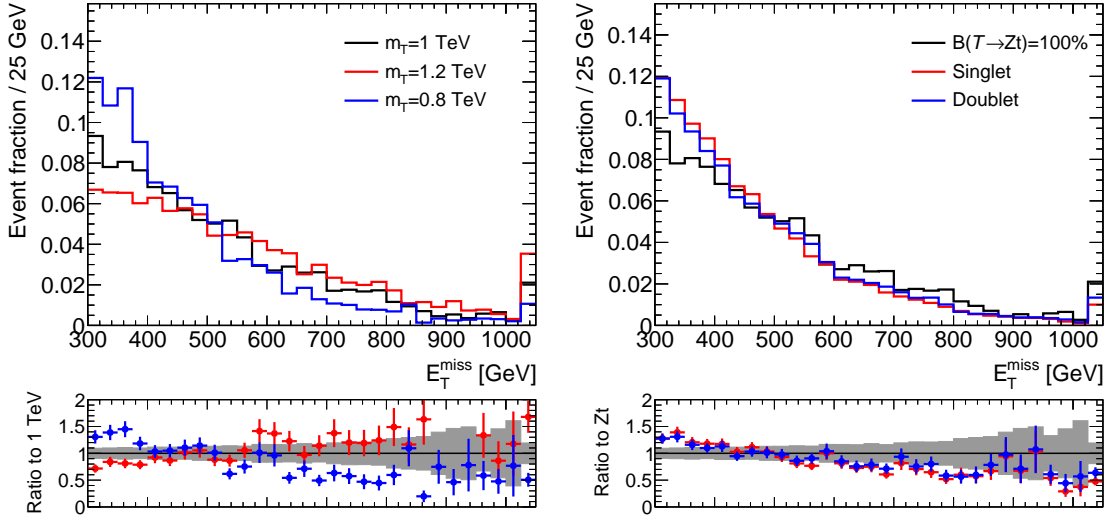
Figure 9.4: Comparison of the E_T^miss distribution for different signal masses for $\mathcal{B}(T \to Zt) = 100\%$ (left) and for different decay modes for $m_T = 1$ TeV (right) after the preselection.
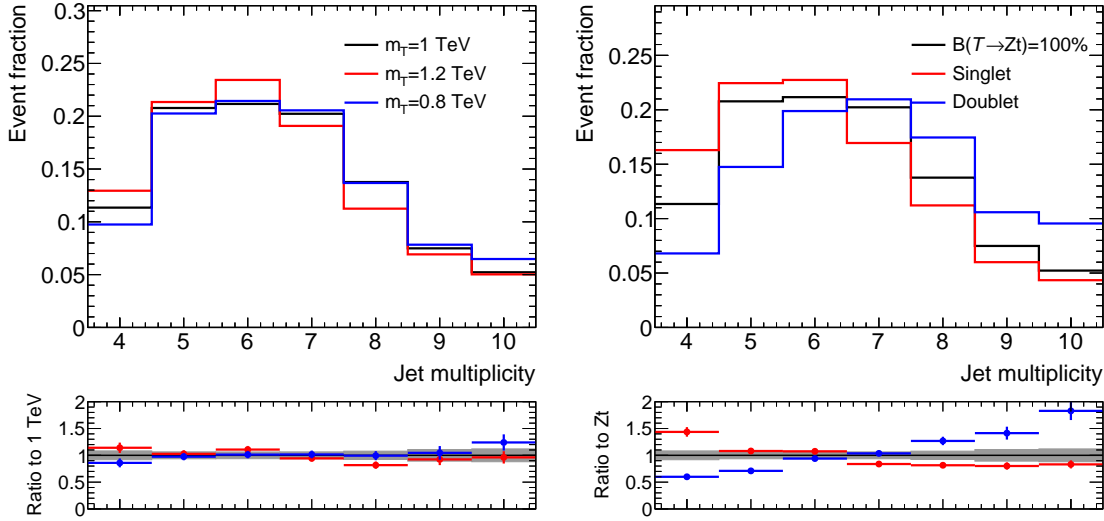
Figure 9.5: Comparison of the jet multiplicity distribution for different signal masses for $\mathcal{B}(T \to Zt) = 100\%$ (left) and for different decay modes for $m_T = 1$ TeV (right) after the preselection.

9.1.1 Signal modelling

As discussed in Section 8.3, the VLQ signal samples are generated with the PROTOS MC generator for 15 different masses of the vector-like top quark between 500 GeV and 1.4 TeV. The samples are produced with equal branching ratios into each of the three decay modes. Desired decay branching ratios are then obtained by reweighting the samples based on generator information. The weight

applied to the cross-section for each event is

$$w(a, b) = \frac{\mathcal{B}_{\text{new}}(T \to a)}{\mathcal{B}_{\text{orig}}(T \to a)} \cdot \frac{\mathcal{B}_{\text{new}}(\bar{T} \to b)}{\mathcal{B}_{\text{orig}}(\bar{T} \to b)}, \tag{9.1}$$

for an event in which the vector-like top quarks decay via $T \to a$ and $\bar{T} \to b$, as determined from the MC truth information. The originally simulated branching ratios, $\mathcal{B}_{\text{orig}}(T \to a)$ and $\mathcal{B}_{\text{orig}}(\bar{T} \to b)$ are $1/3$, as all decay modes have equal probability in the simulation. The weight then applies the desired branching ratios $\mathcal{B}_{\text{new}}(T \to a)$ and $\mathcal{B}_{\text{new}}(\bar{T} \to b)$ for the event, normalised to the original ones. For example, when reweighting to $\mathcal{B}(T \to Zt) = 100\%$, the weight for an event with both vector like top quarks decaying to Zt would be $w(Zt, Z\bar{t}) = 100\% \cdot 100\%/(1/3 \cdot 1/3) = 9$ and for an event with one of the VLQs not decaying into Zt, the weight would be zero, e.g. $w(Ht, Z\bar{t}) = 0$ as $\mathcal{B}_{\text{new}}(T \to Ht) = 0\%$.

The vector-like top quark events are generated assuming couplings according to the singlet model. In order to test the effects on the signal kinematics, a comparison is made with a sample generated according to the doublet couplings. Figure 9.6 shows illustrative distributions for the comparison of the coupling effects. The couplings affect the helicity of the top quark in the $T \to Zt$ decay, with the doublet couplings leading to a higher momentum of the charged lepton. Accordingly, the m_T distribution is harder for the doublet couplings. Due to the polarised W boson decay, the neutrino receives less momentum, but as the E_T^{miss} is dominated by the $Z \to \nu\bar{\nu}$ decay, the E_T^{miss} distribution is not affected by the differences. In general, the doublet couplings lead to a slightly higher acceptance for the signal, making the results obtained with the singlet model couplings conservative.
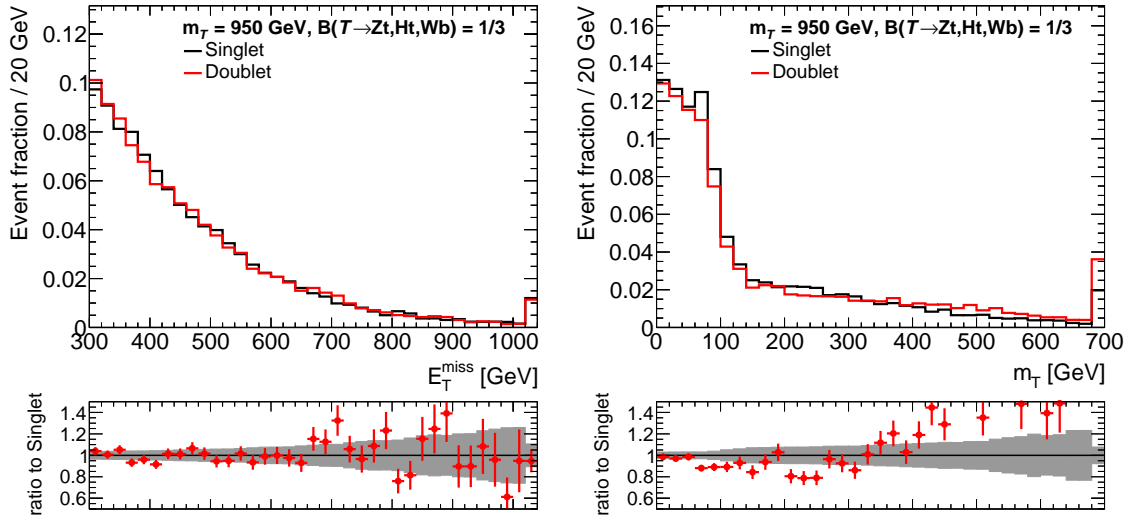
Figure 9.6: Comparison of the E_T^{miss} and the m_T distribution for a vector-like top quark signal with a mass of $m_T = 950\,\text{GeV}$ and equal branching ratios into all three decay modes for couplings according to the singlet and the doublet models after the preselection.

9.2 Signal region

The signal region selection is defined targeting a benchmark signal with a VLQ mass of 1 TeV and a branching ratio of $\mathcal{B}(T \rightarrow Zt, Ht, Wb) = (80, 10, 10)\%$ for each VLQ T decay. In order to keep some sensitivity to decays besides the $T \rightarrow Zt$ decay, the branching ratio of the benchmark signal is not fixed to the extreme value of 100% for the Zt decay.

9.2.1 Selection optimisation

The selection for the signal region is optimised starting with the common preselection (see Table 8.2). Additionally, $m_T > 120$ GeV is required to further reduce the dominant backgrounds, and $am_{T2} > 175$ GeV and $m_{T2}^{\tau} > 80$ GeV in order to reject dileptonic $t\bar{t}$ events. The optimisation follows a two-step approach, maximising the expected significance [156] of the signal process.

At first, all available variables are ranked according to the highest expected significance that can be achieved by cutting on that variable. After this ranking, a cut is applied on the highest ranked variable, maximising the figure of merit. These two steps, i.e. the ranking of variables and the cut application, are iterated until no significant change in the figure of merit can be achieved. A flat systematic uncertainty of 30% is assumed for all backgrounds. In order to account for correlations between the variables, a damping function is applied. It limits the background efficiency of a cut depending on the iteration. In the first step, at least 50% of the background has to survive the cut. This limit is halved in each iteration. Using this procedure, the first cuts are less powerful than the optimal cuts determined in the respective step and therefore less prone to washing out useful correlations to other variables. In case that correlation effects do not have a strong impact, later iterations of the algorithm will restore the optimal cuts, as the damping effect gets smaller.

In the optimisation, the following variables are considered:

- E_T^{miss},

- m_T,

- $H_{T,\text{sig}}^{\text{miss}}$,

- the p_T of the small-radius jets, and

- the number of large-R jets, as well as their p_T and mass requirements.

The highest ranked variables are the large-R jet multiplicity and its p_T, followed by the E_T^{miss} and the m_T requirement and cuts on the $H_{T,\text{sig}}^{\text{miss}}$ and the p_T of the small-radius jets.

9.2.2 Signal region selection

The final selection requirements are listed in Table 9.1. At least two large-R jets are required for the signal region. These are intended to capture the decay products of a hadronically decaying top quark (or the W boson, in case of insufficiently boosted events) and a hadronically decaying boson from one of the VLT decays. The requirement on the $H_{T,\text{sig}}^{\text{miss}}$ favours events with large, real missing momentum, compared to mismeasured jets and similar sources.

Table 9.2 shows the expected number of events for the backgrounds and the benchmark signal, in the signal region. The fraction of the individual contributions is visualised in Figure 9.7. In total 6.5 ± 0.7 background events are expected, compared to 13.4 ± 0.5 events for the benchmark signal. About 95% of the signal events contain an invisibly decaying Z boson, with the remaining events

Table 9.1: Signal region selection for the search for vector-like top quark partners. For jet p_T and large-radius jet masses, multiple numbers refer to the objects ordered in p_T.

Variable	SR
E_T^{miss}	> 350 GeV
m_T	> 170 GeV
am_{T2}	> 175 GeV
m_{T2}^τ	> 80 GeV
$H_{T,sig}^{miss}$	> 12
Jet p_T	> 120, 80, 50, 25 GeV
$|\Delta\phi(j_i, E_T^{miss})|, i = 1, 2$	> 0.4
# b-tagged jets	≥ 1
# large-radius jets	≥ 2
Large-R jet mass	> 80, 60 GeV
Large-R jet p_T	> 290, 290 GeV if $E_T^{miss} < 450$ GeV > 200, 200 GeV if $E_T^{miss} > 450$ GeV

entering the signal region due to the E_T^{miss} from high momentum W boson decays. This number decreases to 75% for the singlet model with a T quark mass of 1 TeV, where $\mathcal{B}(T \to Wb) \simeq 50\%$. The dominant background in the signal region stems from dileptonic $t\bar{t}$ events, followed by W+jets events. The next dominant sources are single top (Wt) and $t\bar{t} + Z$ events, followed by diboson processes.

The optimisation process finds an optimal E_T^{miss} threshold of 450 GeV for the benchmark signal of $m_T = 1$ TeV. As can be seen in Figure 9.4, lower signal masses lead to a softer E_T^{miss} distribution. Therefore an additional optimisation is performed in the region 350 GeV < E_T^{miss} < 450 GeV, in order to recover sensitivity for lower signal masses. This second optimisation for lower E_T^{miss} results in very similar cuts, apart from the tighter large-R jet p_T requirements. At lower E_T^{miss}, stronger

Table 9.2: Events expected from simulation in the signal region with MC statistical uncertainties.

SR	e-channel	μ-channel	Total
$t\bar{t}$ 2L	1.1 ± 0.3	1.2 ± 0.3	2.3 ± 0.4
$t\bar{t}$ 1L	0.0 ± 0.0	0.1 ± 0.1	0.1 ± 0.1
Single top	0.4 ± 0.1	0.7 ± 0.1	1.1 ± 0.2
W+jets	1.0 ± 0.5	0.5 ± 0.1	1.6 ± 0.5
Diboson	0.3 ± 0.1	0.3 ± 0.1	0.6 ± 0.1
$t\bar{t} + V$	0.4 ± 0.1	0.5 ± 0.1	0.9 ± 0.1
Total SM	3.2 ± 0.6	3.4 ± 0.4	6.5 ± 0.7
Benchmark Signal	6.5 ± 0.4	6.8 ± 0.4	13.4 ± 0.5

SR
$\sqrt{s}$ = 13 TeV

- $t\bar{t}$ (36.2%)
- W+jets (23.8%)
- Single top (17.4%)
- $t\bar{t}$+V (14.0%)
- Diboson (8.7%)
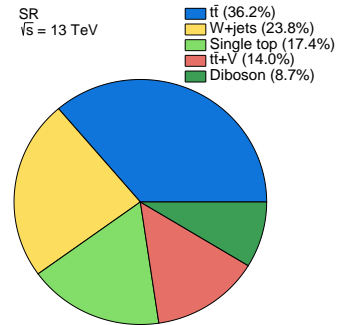
Figure 9.7: Breakdown of the individual SM contributions in the signal region.
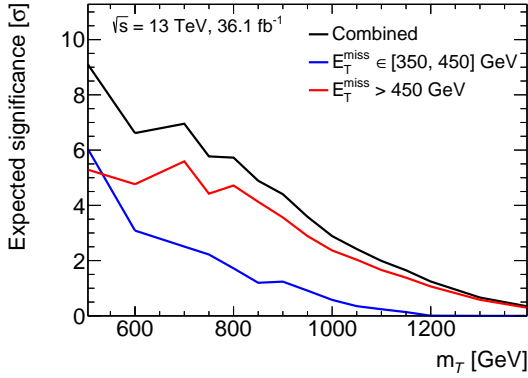
Figure 9.8: Expected significance assuming a 30% total background uncertainty for the SR selection and for the separate selections for low and high E_T^{miss}.
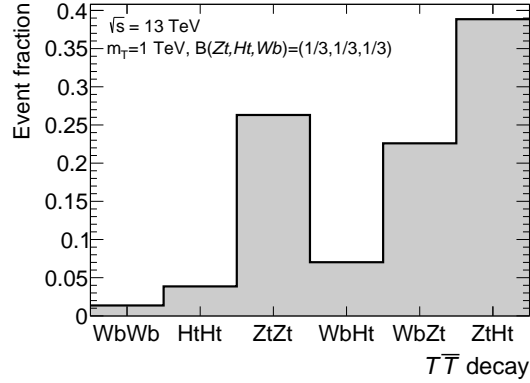
Figure 9.9: Relative fraction of events in the signal region for the different decay modes of a vector-like top pair with $m_T = 1$ TeV and equal branching ratios for all decay modes, $\mathcal{B}(T \to Zt)$ $= \mathcal{B}(T \to Ht) = \mathcal{B}(T \to Wb) = 1/3$.

requirements are set in order to better discriminate between signal and background. In the higher E_T^{miss} region the background is reduced, therefore looser large-R jet p_T requirements are sufficient. Small differences in the selection for the two E_T^{miss} regions are harmonised, favouring the looser selection. Figure 9.8 shows the expected significance of a signal in the signal region as a function of the VLT mass, assuming a 30% total background uncertainty. The significance is compared to the expected significance using only the low or high E_T^{miss} part of the selection, in order to show the impact of the addition of the 350 GeV $< E_T^{miss} < 450$ GeV selection. At high signal masses the inclusion of the low E_T^{miss} region only brings a marginal increase in sensitivity. At lower vector-like top quark masses the events with low E_T^{miss} become more important and the addition of the $E_T^{miss} < 450$ GeV selection results in a significant sensitivity increase.

Figure 9.9 shows the composition of the various VLT decay modes in the signal region, when assuming equal branching ratios. In almost 90% of the selected events at least one VLT decays into Zt. The decay modes of the second T are dominated by decays with hadronically decaying Z or H bosons, as required by the second large-R jet requirement. A small preference for the mixed $ZtHt$ decay can be seen, due to the combinatorial effect that $\mathcal{B}(T \to HtZt/ZtHt) = 2 \times \mathcal{B}(T \to ZtZt)$ before the selection. An additional effect is the higher mass of the H boson, which makes the mass cut on the second large-R jet more efficient. Also, as the Higgs decays predominantly into b quarks, the b-jet requirement is more efficient.

Table 9.3 shows a cutflow for the benchmark signal and the dominant SM backgrounds. Most of the signal region requirements have an individual efficiency of 80% for the signal, with the notable exception of the requirements on the E_T^{miss}, m_T and the 2nd large-R jet. These requirements select the targeted signal decay mode from all possibilities, i.e. they restrict the selection to the semi-leptonic decay mode with a $Z \to \nu\bar{\nu}$ decay and a second hadronic resonance. The efficiency of the full event selection for the benchmark signal is 1%, taking all decay modes into account. For events with $Z \to \nu\bar{\nu}$ and one leptonically decaying W boson from a top quark decay, the selection efficiency is about 10%.

Table 9.3: Cutflow for the $t\bar{t}$ and W+jets backgrounds and the benchmark signal. The $t\bar{t}$ and W+jets processes only contain events with at least one lepton, while for the signal also pure hadronic decays are included. The requirements on the first and second large-R jet implicitly include requirements on the large-R jet multiplicity.

Cut	$t\bar{t}$	W+jets	Signal
Event cleaning	99 %	99 %	99 %
≥ 1 baseline lepton	90 %	98 %	61 %
≥ 1 signal lepton	76 %	78 %	69 %
$= 1$ signal lepton	92 %	100 %	69 %
$= 1$ baseline lepton	81 %	99 %	74 %
$E_{\mathrm{T}}^{\mathrm{miss}} > 200\,\mathrm{GeV}$	1.6 %	0.05 %	57 %
≥ 4 jets	70 %	24 %	95 %
Trigger	100 %	100 %	100 %
$|\Delta\phi(j_i, E_{\mathrm{T}}^{\mathrm{miss}})| > 0.4, i = 1, 2$	87 %	91 %	85 %
$m_{\mathrm{T}} > 120\,\mathrm{GeV}$	9.2 %	3.7 %	49 %
≥ 1 b-jet	89 %	18 %	92 %
$am_{\mathrm{T2}} > 175\,\mathrm{GeV}$	21 %	72 %	82 %
$m_{\mathrm{T2}}^{\tau} > 80\,\mathrm{GeV}$	85 %	99 %	96 %
$E_{\mathrm{T}}^{\mathrm{miss}} > 350\,\mathrm{GeV}$	10 %	17 %	70 %
$m_{\mathrm{T}} > 170\,\mathrm{GeV}$	72 %	73 %	89 %
$H_{\mathrm{T,sig}}^{\mathrm{miss}} > 12$	91 %	94 %	94 %
small-R jet p_{T}	73 %	57 %	96 %
1st large-R jet	45 %	56 %	88 %
2nd large-R jet	15 %	19 %	57 %
Total efficiency	2×10^{-5} %	3×10^{-7} %	0.95 %

9.2.3   Distributions in the signal region
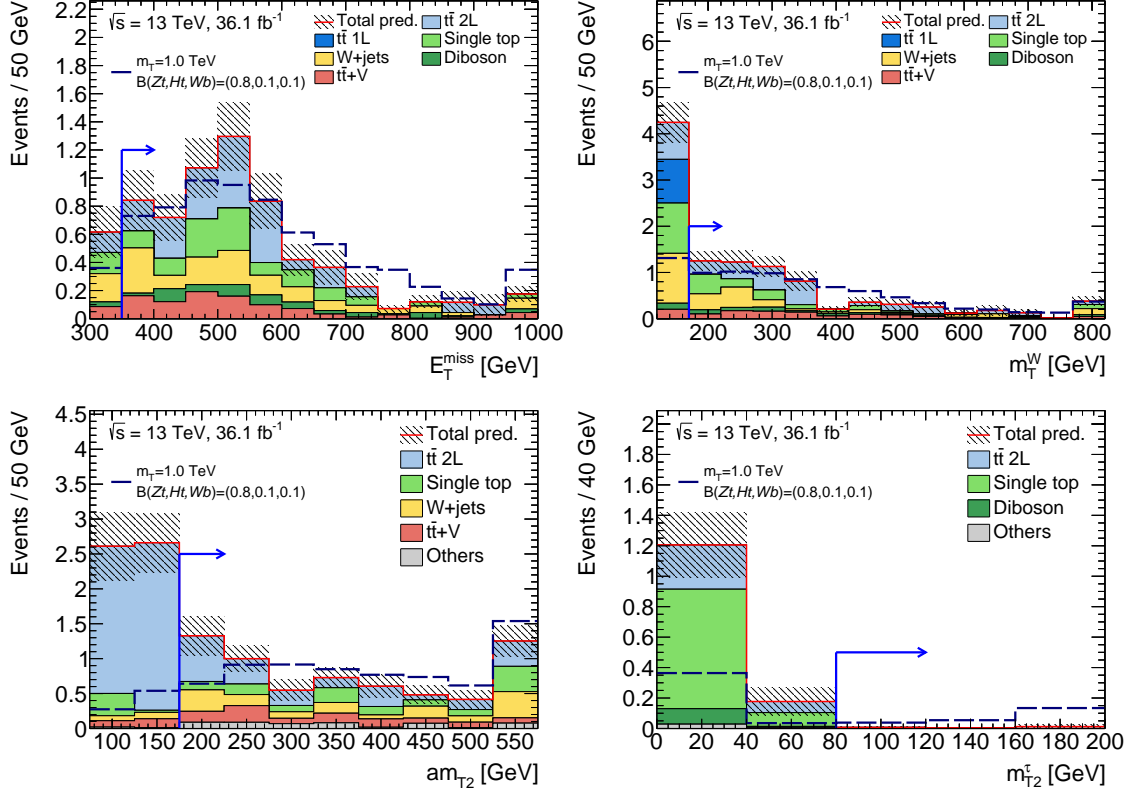
Figure 9.10: Distributions of the E_T^{miss}, the m_T, the am_{T2} and the m_{T2}^τ in the signal region. The requirement on the displayed distribution, as indicated by the vertical line, is not applied. The m_{T2}^τ distribution is shown for events with an hadronic τ candidate.

Figures 9.10 to 9.12 show the distributions of the variables that define the signal region, without the selection requirement on that variable applied. A comparison of the distributions for various signal masses and decay branching ratios is shown in Appendix B.1.2.

The m_T requirement strongly reduces the backgrounds in which the E_T^{miss} only comes from a leptonic W boson decay. It almost completely removes semi-leptonic $t\bar{t}$ events, and strongly reduces the single top and W+jets backgrounds. The am_{T2} variable is strong against the dileptonic $t\bar{t}$ background in the signal region, as it is specifically designed against this final state. In the distributions of the leading large-R jet properties, the requirement on the second large-R jet are not applied, as they would implicate requirements on the leading one as well. Nonetheless it can be seen that the signal region selection has a high signal efficiency, while the backgrounds are reduced. The jet p_T requirements, as shown in Figure 9.12, are implicitly fulfilled due to correlations with the E_T^{miss} and the large-R jets and do not affect the signal and background selection efficiency. They are explicitly included in the SR definition and kept constant in the selection for the control regions, in order to reduce the effect of the jet energy scale uncertainty and make the analysis resilient against potential mismodelling in the jet p_T distributions. As discussed before, the b-jet multiplicity offers a strong separation between the signal and the background, even after the full signal region selection. No stronger requirements are placed in view of a possible combination with the search optimised for $T \rightarrow Ht$, which requires a high number of b-jet.
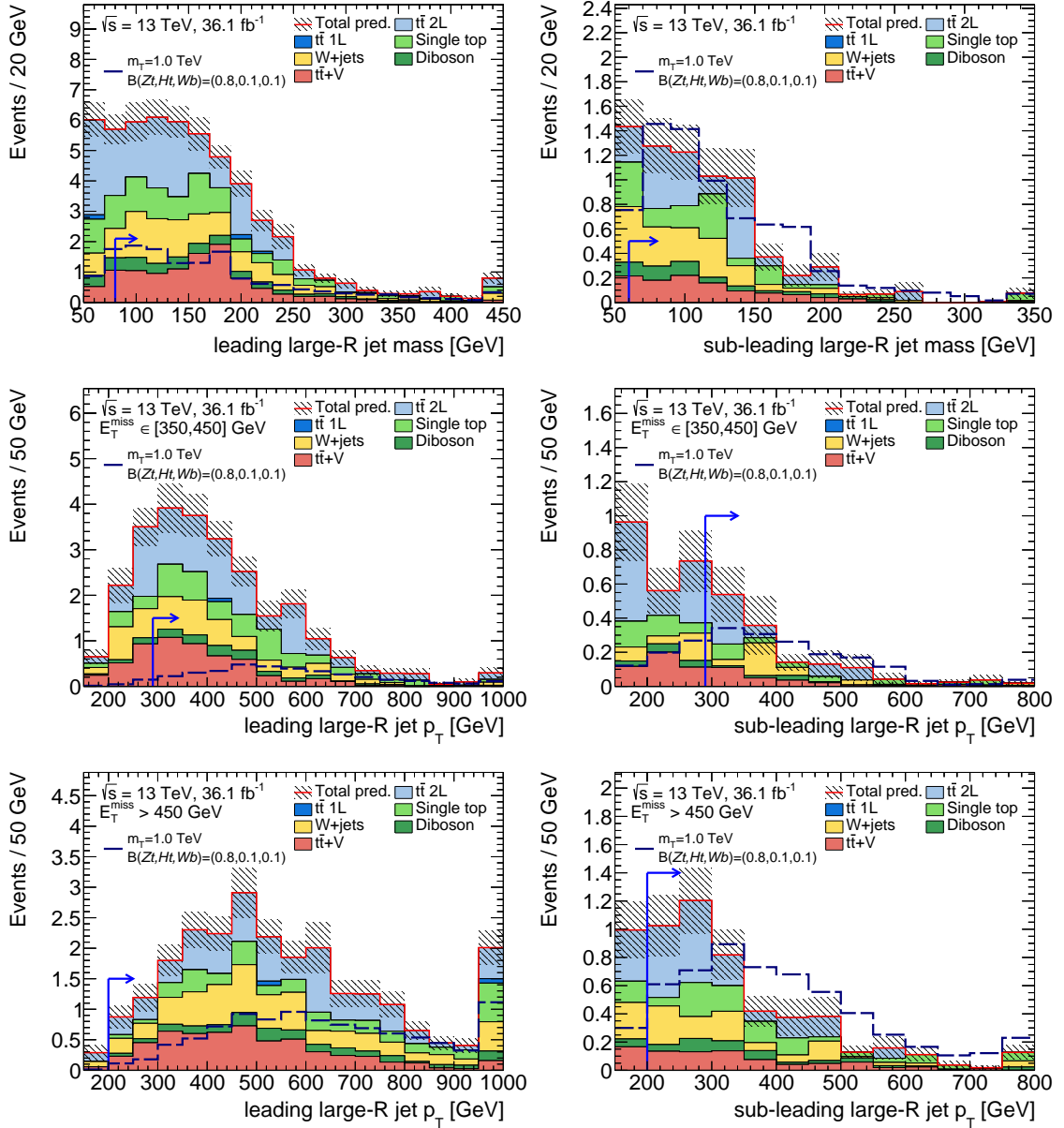
Figure 9.11: The mass of the leading and sub-leading large-R jet in the signal region, and p_T of the leading and sub-leading large-R jet in the signal region, for events with $350\,\text{GeV} < E_T^{\text{miss}} < 450\,\text{GeV}$ (middle) or $E_T^{\text{miss}} > 450\,\text{GeV}$ (bottom). The requirement on the displayed distribution, as indicated by the vertical line, is not applied. Additionally, the second large-R jet requirement is removed, as it would implicitly include requirements on the leading large-R jet.
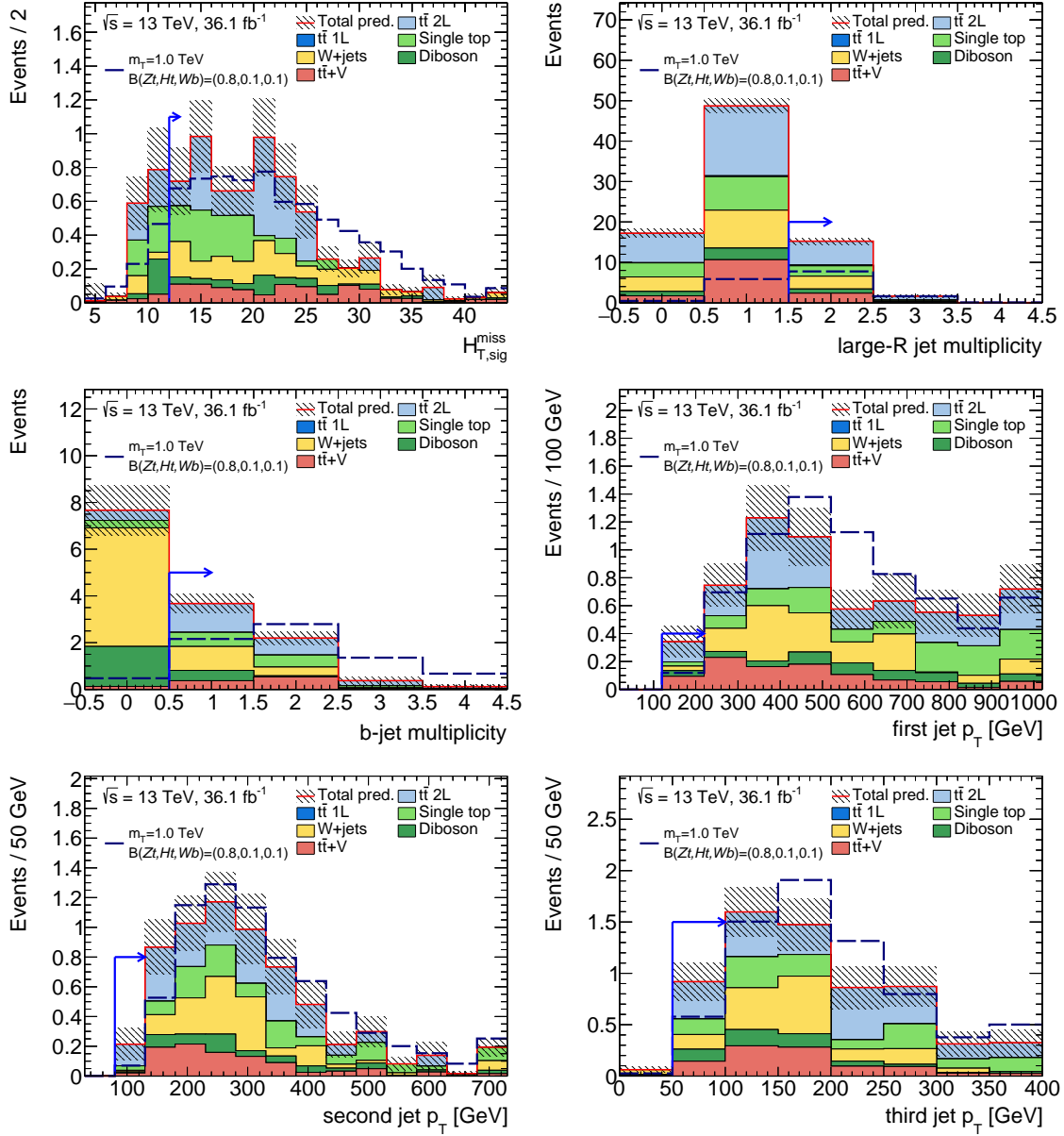
Figure 9.12: The $H_{T,sig}^{miss}$ distribution, the large-R jet and b-jet multiplicities, as well as the p_T of the leading three jets in the signal region. The requirement on the displayed distribution, as indicated by the vertical line, is not applied. All large-R jets fulfilling the reconstruction requirements of $p_{T,jet} > 150\,\text{GeV}$ and $m_{Jet} > 50\,\text{GeV}$ are counted in the large-R jet multiplicity.

9.3 Background estimation

The normalisation of the dominant backgrounds in the signal region is estimated by a data driven method, using control regions enriched in the respective background processes.

The dominant background in the signal region is $t\bar{t}$ production, which contributes more than 35 % of all SM events. The second most dominant contribution comes from W+jets events. The control regions are kinematically close to the signal region, but enriched in either $t\bar{t}$ or W+jets events and with a low signal contribution. One of the most effective variables to suppress $t\bar{t}$ and W+jets production are m_T and the b-jet multiplicity, respectively. Vice versa, inverting the selection yields samples that are enriched with the background processes but are otherwise kinematically similar to the signal region, without having itself a sizeable signal fraction. Both control regions are thus defined by changing the m_T requirement and imposing a window cut on $m_T \in [30, 90]$ GeV. To increase the statistical power, the requirements on the E_T^{miss} and the am_{T2} are relaxed and requirements on the $H_{\text{T,sig}}^{\text{miss}}$ are removed. The W+jets control region is additionally defined by a veto on b-jets, in contrast to the requirement of at least one b-jet in the signal region and the $t\bar{t}$ control region. Table 9.4 lists the selection for the control regions in comparison to the signal region definition. The jet p_T requirements are the same in the signal and the control regions, in order to reduce the impact of jet related systematic uncertainties.

The observed events in the $t\bar{t}$ CR are compatible with the expectation from the simulation, while in the W+jets CR less events are observed than expected. The background normalisation factors obtained from a simultaneous fit to the two control regions are $\mu_{t\bar{t}} = 1.05 \pm 0.17$ and $\mu_{W+\text{jets}} = 0.70 \pm 0.10$, respectively. Further details on the control regions are given in the following subsections.

The subdominant backgrounds considered in the analysis are taken from simulation. Additional rare backgrounds, such as the associated production of $t\bar{t}$ with a Higgs boson are checked in simulation and found to be negligible.

Table 9.4: Selection of the $t\bar{t}$ (TCR) and the W+jets control region (WCR), compared to the signal region (SR). For jet p_T and large-radius jet masses, multiple numbers refer to the objects ordered in p_T.

Variable	SR	TCR	WCR
E_T^{miss}	> 350 GeV	> 300 GeV	
m_T	> 170 GeV	$\in [30, 90]$ GeV	
am_{T2}	> 175 GeV	> 100 GeV	
m_{T2}^{τ}	> 80 GeV	> 80 GeV	
$H_{\text{T,sig}}^{\text{miss}}$	> 12	–	
Jet p_T	> 120, 80, 50, 25 GeV	> 120, 80, 50, 25 GeV	
$\|\Delta\phi(j_i, E_T^{\text{miss}})\|, i = 1, 2$	> 0.4	> 0.4	
# b-tagged jets	≥ 1	≥ 1	$= 0$
# large-radius jets	≥ 2	≥ 2	
Large-radius jet mass	> 80, 60 GeV	> 80, 60 GeV	
Large-radius jet p_T	> 290, 290 GeV if $E_T^{\text{miss}} < 450$ GeV > 200, 200 GeV if $E_T^{\text{miss}} > 450$ GeV	> 200, 200 GeV	

9.3.1 Control region for $t\bar{t}$

Table 9.5 gives the expected events in the TCR, with the relative contributions visualised in Figure 9.13. In the control region, $t\bar{t}$ events make up 55% of the expected events, giving a good power to constrain this process. The expected contribution of the benchmark signal in the TCR amounts to 10 events, which is less than 3% of the total yield. The $t\bar{t}$ CR is dominated by semi-leptonic $t\bar{t}$ events, while in the SR dileptonic $t\bar{t}$ is the dominant background. This extrapolation is validated in the $t\bar{t}$ validation region, as discussed in Section 9.4.1.

Figures 9.14 and 9.15 show illustrative distributions in the TCR after applying the normalisation factors obtained in the background only fit. As the requirements on the E_T^{miss}, am_{T2} and $H_{T,sig}^{miss}$ are relaxed with respect to the signal region selection, significant deviations in these variables would lead to a bias in the background estimate in the signal region. Good agreement between the data and the prediction is observed in the control region distributions. Additional distributions are shown in Appendix B.2.1.

Table 9.5: Observed and expected events in the TCR. The individual uncertainties are correlated, and do not add up quadratically to the total uncertainty.

Region	TCR
Observed events	437
Total background events	437 ± 21
Fitted $t\bar{t}$ events	280 ± 40
Fitted W + jets events	70 ± 28
single top events	63 ± 24
$t\bar{t} + V$ events	9.7 ± 1.6
diboson events	11 ± 5
MC exp. background events	450 ± 50
MC exp. $t\bar{t}$ events	270 ± 7
MC exp. W + jets events	100 ± 35
MC exp. single top events	63 ± 24
MC exp. $t\bar{t} + V$ events	9.7 ± 1.6
MC exp. diboson events	11 ± 5
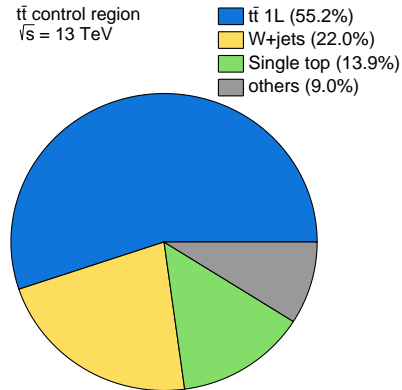
Figure 9.13: Breakdown of the individual SM contributions in the TCR.
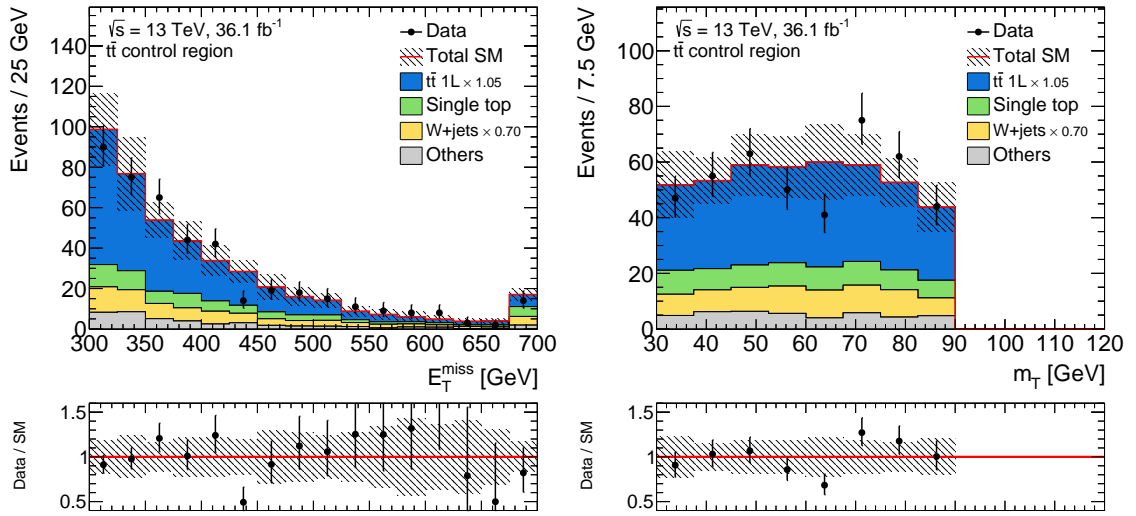
Figure 9.14: Distribution of $E_{\mathrm{T}}^{\mathrm{miss}}$ (left) and m_{T} (right) in the $t\bar{t}$ control region. The $t\bar{t}$ and W+jets normalisation factors are applied as indicated in the legend and the last bin contains overflow events. The lower panels show the ratio of the data to the prediction. The error bands include statistical and systematic uncertainties.
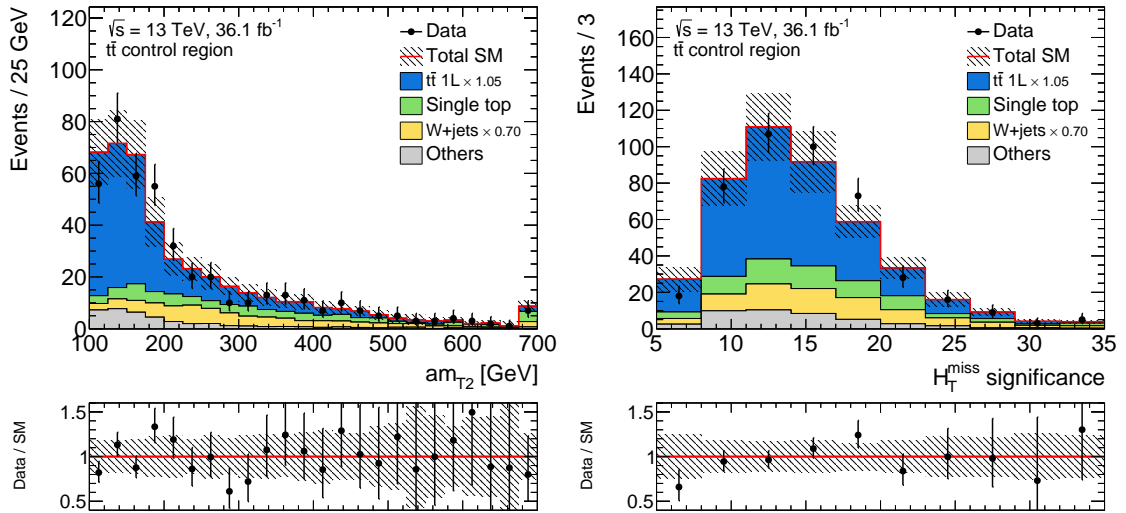
Figure 9.15: Distribution of $am_{\mathrm{T}2}$ (left) and $H_{\mathrm{T,sig}}^{\mathrm{miss}}$ (right) in the $t\bar{t}$ control region. The $t\bar{t}$ and W+jets normalisation factors are applied as indicated in the legend and the last bin contains overflow events. The lower panels show the ratio of the data to the prediction. The error bands include statistical and systematic uncertainties.

9.3.2   Control region for *W*+jets

Table 9.6 gives the expected events in the WCR and the relative contributions are visualised in Figure 9.16. *W*+jets events make up 80% of the SM events in the control region. The contribution of the benchmark signal in the WCR amounts to about 1 event, much less than 1% of the total yield.

Figures 9.17 and 9.18 show illustrative distributions in the WCR after applying the normalisation factors obtained in the background only fit. Even though the normalisation of the *W*+jets process deviates from the prediction and is corrected by the fit, $\mu_{W+\text{jets}} = 0.70 \pm 0.10$, the shape of the distributions agree well within the uncertainties. As for the TCR, no deviation can be seen for variables over which the normalisation is extrapolated to the SR. Additional distributions are shown in Appendix B.2.2.

Figure 9.19 shows the breakdown of the flavour components of the jets in the *W*+jets events. Due to the requirement of at least one *b*-jet in the SR the *W*+heavy flavour components are strongly enhanced there, while in the CR the *W*+light jet process dominates. The extrapolation from the CR to the SR therefore relies on the correct modelling of the flavour composition in the simulation. This was measured in 7 TeV data [157] and the measurement uncertainties are included as a systematic uncertainty in the *W*+jets yields in all regions requiring at least one *b*-jet.

Table 9.6: Observed and expected events in the WCR. The individual uncertainties are correlated, and do not add up quadratically to the total uncertainty.

Region	WCR
Observed events	303
Total background events	303 ± 17
Fitted $t\bar{t}$ events	38 ± 15
Fitted W + jets events	224 ± 27
single top events	10 ± 5
$t\bar{t} + V$ events	1.03 ± 0.30
diboson events	30 ± 12
MC exp. background events	398 ± 25
MC exp. $t\bar{t}$ events	36 ± 12
MC exp. W + jets events	321 ± 13
MC exp. single top events	10 ± 5
MC exp. $t\bar{t} + V$ events	1.03 ± 0.30
MC exp. diboson events	30 ± 12

W+jets control region
√s = 13 TeV

W+jets (80.6%)

others (19.4%)
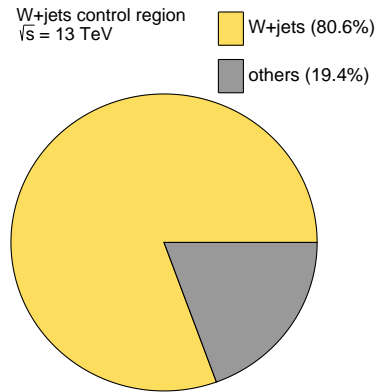
Figure 9.16: Breakdown of the individual SM contributions in the WCR.
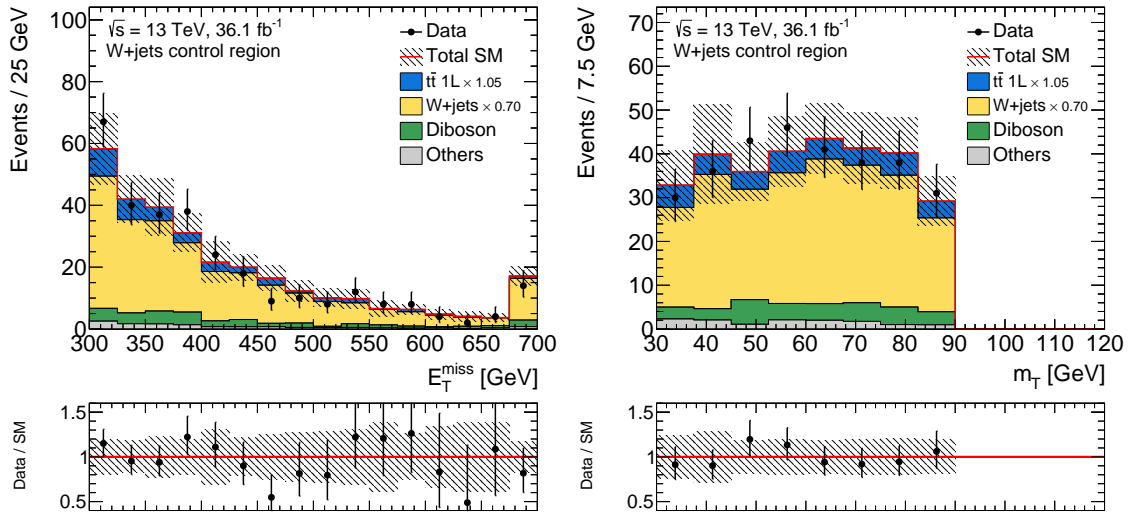
Figure 9.17: Distribution of E_T^{miss} and m_T in the W+jets control region. The $t\bar{t}$ and W+jets normalisation factors are applied as indicated in the legend and the last bin contains overflow events. The lower panels show the ratio of the data to the prediction. The error bands include statistical and systematic uncertainties.
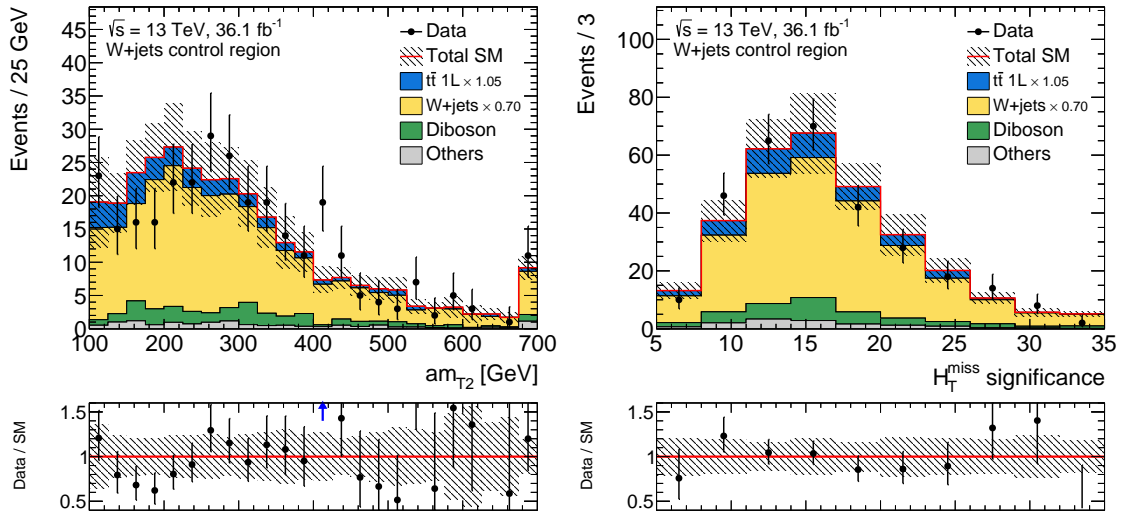
Figure 9.18: Distribution of am_{T2} and $H_{T,sig}^{miss}$ in the W+jets control region. The $t\bar{t}$ and W+jets normalisation factors are applied as indicated in the legend and the last bin contains overflow events. The lower panels show the ratio of the data to the prediction. The error bands include statistical and systematic uncertainties.
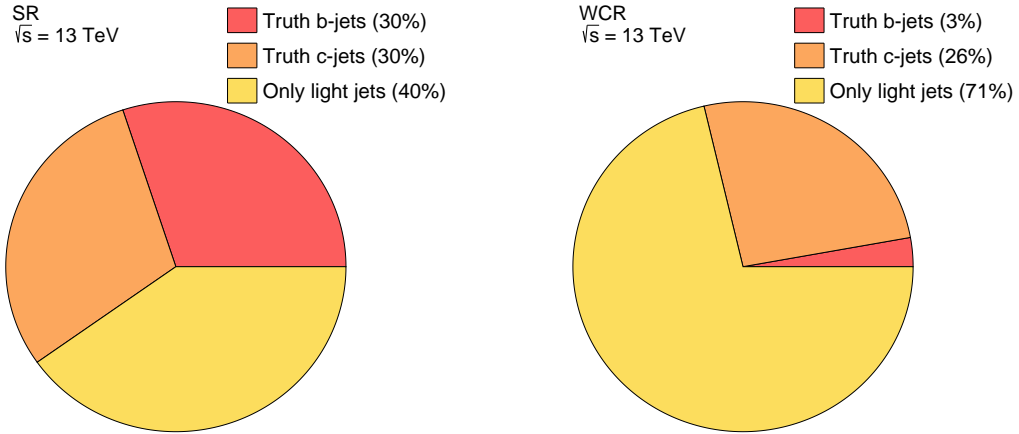
Figure 9.19: Breakdown of the flavour components of the *W*+jets process in the SR (left) and the *W*+jets control region (right). Events are classified as containing truth *b*-jets, when one or more of the reconstructed jets originates from a MC truth *B* hadron. Events with truth *c*-jets are classified accordingly, if they are not already classified as containing a truth *b*-jet. Events not falling in either category are marked as "only light jets".

9.3.3 Other backgrounds

Additional backgrounds considered in the signal region are single top, $t\bar{t} + V$ (both $t\bar{t} + Z$ and $t\bar{t} + W$) and diboson production. As these backgrounds are small compared to the dominant $t\bar{t}$ process, no dedicated control regions are used for them and their yields are estimated from simulation.

In addition to the backgrounds mentioned above, the expected events of additional rare processes have been checked in the signal region: $t\bar{t} + H$, $t\bar{t} + WW$ and tZ in addition to Z+jets production. The expected yields in the signal region are listed in Table 9.7. Each individual process, and the sum of all, is smaller than the statistical uncertainty in the expected yields in the SR (see Table 9.2). These small backgrounds are therefore neglected in the further analysis.

Table 9.7: Expected yields for rare backgrounds in the SR, compared to the expected non-rare SM backgrounds and the benchmark signal yields, as shown in Table 9.2.

SR	exp. events
$t\bar{t} + H$	0.07 ± 0.04
$t\bar{t} + WW$	0.00 ± 0.00
tZ	0.07 ± 0.04
Z + jets	0.15 ± 0.07
Total rare SM	0.33 ± 0.07
Total non-rare SM	6.5 ± 0.7
Benchmark signal	13.4 ± 0.5

9.4 Background validation

The reliability of the background estimates in the signal region is crucial for the analysis. In addition to validating the modelling of the data in the control regions, special selections are defined that are called validation regions. They are disjunct from the signal and control regions and therefore statistically independent. The validation regions are not part of the simultaneous fit. Instead, the background normalisation, as obtained in the background only fit, are applied and both the inclusive number of events and the modelling of the data are checked in the VRs.

Three validation regions are defined, one for each of the two dominant backgrounds and one for the single top background. As single top events amount to more than 15% of the SM expectation in the signal region, the prediction is validated specifically. The control regions are defined by inverting the m_T requirement to a window cut around the W boson mass. The validation regions thus require higher values of m_T, allowing to test the extrapolation over this variable. All validation regions require exactly one large-R jet, in order to make them orthogonal to the SR and CR selections. Other cuts are kept close to the SR, but are slightly loosened in order to increase the statistics. For the single top background, the validation region (STVR) requires at least two b-tagged jets and a high am_{T2}, in order to decrease the $t\bar{t}$ and W+jets contributions. The am_{T2} requirement is especially strong to differentiate between single top in the Wtb channel and $t\bar{t}$ events, as it effectively reconstructs the invariant mass of W boson and b-jet pairs, $m(Wb)$. As single top events contain only one top quark resonance, the second Wb pair can have a higher invariant mass compared to $t\bar{t}$ events, where it is distributed around the top quark mass. The W+jets VR (WVR) is defined with a veto on b-tagged jets, as in the WCR. To make the $t\bar{t}$ VR orthogonal to the single top VR, the former one requires low values of am_{T2}. Table 9.8 gives the definition of the validation regions. Details of the selection and the agreement of the observed events with the estimated yields are discussed in the following. In the distributions comparing data and prediction the benchmark signal is overlaid, to show the low signal contamination in the validation regions.

Table 9.8: Overview of the event selections for the $t\bar{t}$ (TVR), W+jets (WVR) and single top (STVR) validation regions, compared to the signal region. For jet p_T and large-radius jet masses, multiple numbers refer to the objects ordered in p_T.

Variable	Signal Region	TVR	WVR	STVR
E_T^{miss}	> 350 GeV	> 300 GeV		
m_T	> 170 GeV	> 120 GeV		> 60 GeV
am_{T2}	> 175 GeV	$\in [100, 200]$ GeV	> 100 GeV	> 200 GeV
m_{T2}^τ	> 80 GeV	> 80 GeV		
$H_{T,sig}^{miss}$	> 12	−		
Jet p_T	> 120, 80, 50, 25 GeV	> 120, 80, 50, 25 GeV		
$\|\Delta\phi(j_i, E_T^{miss})\|, i = 1, 2$	> 0.4	> 0.4		
# b-tagged jets	≥ 1	≥ 1	= 0	≥ 2
# large-radius jets	≥ 2	= 1		
Large-radius jet mass	> 80, 60 GeV	> 80 GeV		
Large-radius jet p_T	> 290, 290 GeV / > 200, 200 GeV	> 200 GeV		

9.4.1 $t\bar{t}$ validation region

Table 9.9 gives the expected and observed events in the TVR, with the relative contributions visualised in Figure 9.20. More than 80% of the expected events come from $t\bar{t}$ and the observed and expected yields are in good agreement. Figure 9.21 shows example distributions in the TVR after applying the normalisation factors obtained in the background only fit to the control regions. Additional distributions are shown in Appendix B.3.1. A good agreement of data and simulation can be observed.

The $t\bar{t}$ control region is defined with a window cut on m_{T} around the W boson mass. As discussed in Section 8.5, this has a strong influence on the dominant $t\bar{t}$ decay mode. While in the control region semi-leptonic $t\bar{t}$ events dominate, the signal region is populated by dileptonic $t\bar{t}$ events with an unidentified lepton. This can also be seen in Figure 9.22, where the relative contributions of the $t\bar{t}$ decay modes in the different regions are shown. The extrapolation of the $t\bar{t}$ normalisation into the signal region therefore relies on the correct modelling of the relative contributions and the mechanisms which cause a lepton to be not correctly identified by the detector or the reconstruction software. The $t\bar{t}$ VR is defined with a high m_{T} threshold, similarly to the SR, and the relative contributions of the $t\bar{t}$ decay modes in the $t\bar{t}$ VR are matching those in the SR, as shown in Figure 9.22. The VR thus serves as a validation of this extrapolation from semi-leptonic to dileptonic $t\bar{t}$ events in a region with reduced signal contamination.

Table 9.9: Observed and expected events in the TVR. The individual uncertainties are correlated, and do not add up quadratically to the total uncertainty.

Region	TVR
Observed events	112
Total background events	109 ± 35
$t\bar{t}$ events	90 ± 40
W + jets events	3.5 ± 2.0
single top events	4.2 ± 2.6
$t\bar{t} + V$ events	7.0 ± 1.4
diboson events	1.3 ± 1.3
MC exp. background events	106 ± 31
MC exp. $t\bar{t}$ events	89 ± 30
MC exp. W + jets events	4.9 ± 2.7
MC exp. single top events	4.2 ± 2.6
MC exp. $t\bar{t} + V$ events	7.0 ± 1.4
MC exp. diboson events	1.3 ± 1.3
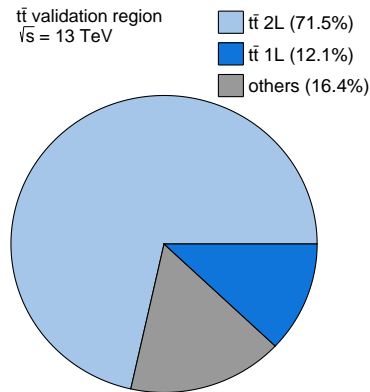
Figure 9.20: Breakdown of the individual SM contributions in the TVR.
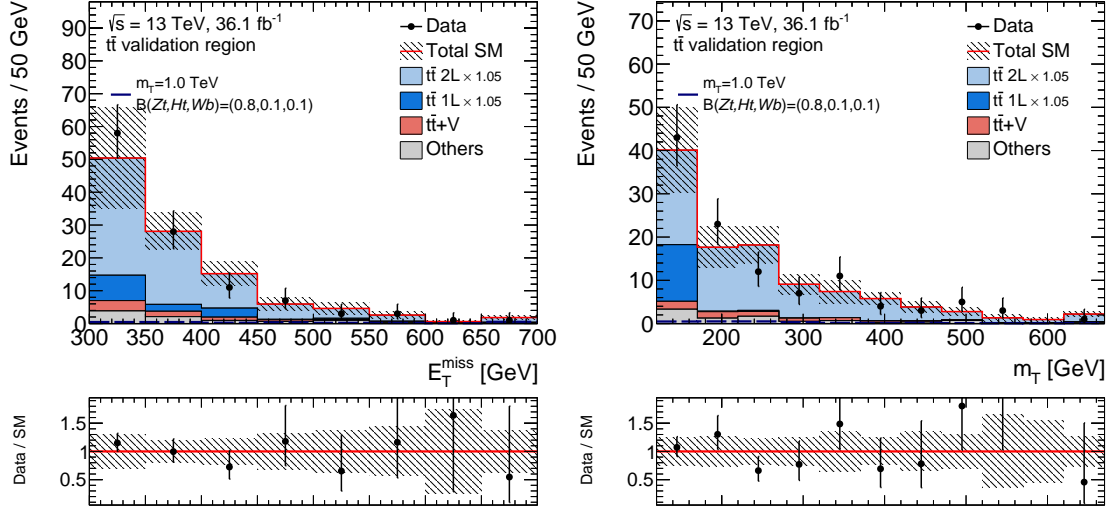
Figure 9.21: Distribution of E_T^{miss} and m_T in the $t\bar{t}$ validation region. The $t\bar{t}$ and W+jets normalisation factors are applied as indicated in the legend and the last bin contains overflow events. The lower panels show the ratio of the data to the prediction. The error bands include statistical and systematic uncertainties.
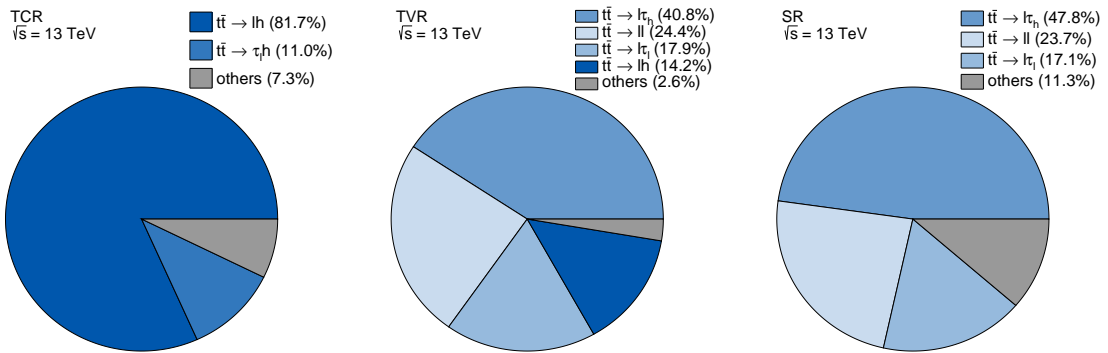
Figure 9.22: Breakdown of the $t\bar{t}$ decay mode into hadrons, h, electrons or muons, l, hadronically decaying τ leptons, τ_h or leptonically decaying τ leptons, τ_l, in the TCR (left), TVR (middle) and SR (right).

9.4.2 *W+jets validation region*

Table 9.10 gives the expected events in the WVR. The relative contributions are visualised in Figure 9.23. Figure 9.24 shows illustrative distributions in the WVR after applying the normalisation factors obtained in the background only fit to the control regions. Additional distributions are shown in Appendix B.3.2. A reasonable agreement of data and simulation can be observed. The low *W*+jets normalisation factor found in the control region conform also to the validation region results. This confirms the proper modelling of the m_T distribution, over which the control region results are extrapolated to the VR, and crucially also to the signal region. The second requirement inverted in the control region definition is on the number of *b*-jets. This is requirement is also inverted in the validation region, and is therefore tested in a dedicated cross check, documented below.

Table 9.10: Observed and expected events in the WVR. The individual uncertainties are correlated, and do not add up quadratically to the total uncertainty.

Region	WVR
Observed events	131
Total background events	127 ± 31
$t\bar{t}$ events	15 ± 8
W + jets events	77 ± 30
single top events	$3.3^{+3.5}_{-3.3}$
$t\bar{t} + V$ events	1.9 ± 0.7
diboson events	31 ± 9
MC exp. background events	160 ± 40
MC exp. $t\bar{t}$ events	14 ± 7
MC exp. W + jets events	110 ± 40
MC exp. single top events	$3.3^{+3.5}_{-3.3}$
MC exp. $t\bar{t} + V$ events	1.9 ± 0.7
MC exp. diboson events	31 ± 9
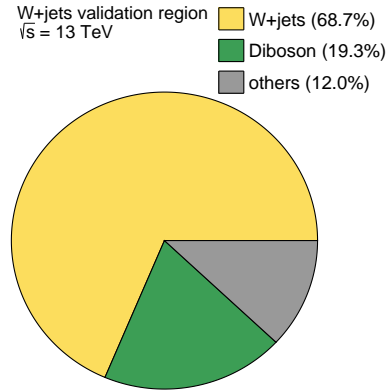
Figure 9.23: Breakdown of the individual SM contributions in the WVR.
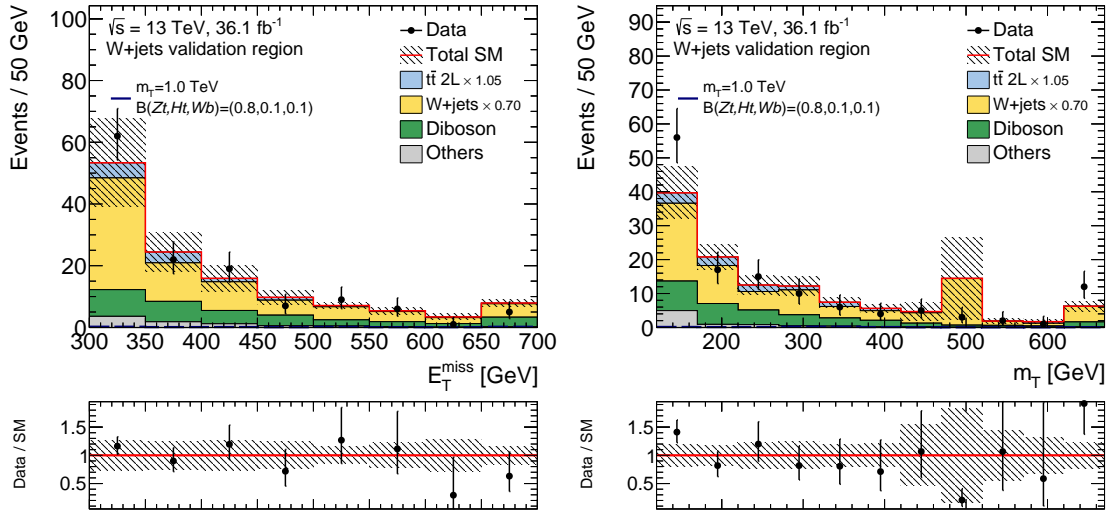
Figure 9.24: Distribution of $E_{\mathrm{T}}^{\mathrm{miss}}$ and m_{T} in the W+jets validation region. The $t\bar{t}$ and W+jets normalisation factors are applied as indicated in the legend and the last bin contains overflow events. The lower panels show the ratio of the data to the prediction. The error bands include statistical and systematic uncertainties.

9.4.2.1 *W + heavy flavour cross-check*

The normalisation of the W+jets process is found to be incompatible with the prediction of the simulation, and a normalisation factor of $\mu_{W+\mathrm{jets}} = 0.70 \pm 0.10$ is found in the background only fit. The W+jets validation region confirms this. As both regions have a veto on b-tagged jets, the heavy flavour fraction differs with respect to the signal region, as discussed in Section 9.3.2. In order to check the normalisation of the W+jets background in a heavy flavour dominated region, a special selection is constructed, which is based on the $t\bar{t}$ control region. Several variables are used to enhance the W+heavy flavour contribution (W+HF) with respect to the other SM backgrounds. The requirement of high am_{T2} values and the veto of events for which the mass of the leading large-R jet falls in the range of $150 - 200\,\mathrm{GeV}$ reduces the $t\bar{t}$ contribution. For events with two or more b-jets a maximal separation of $\Delta R(b_1, b_2) < 1.2$ is required, as the single top background is concentrated at higher separations. Additionally, the charge asymmetry effect for W+jets production
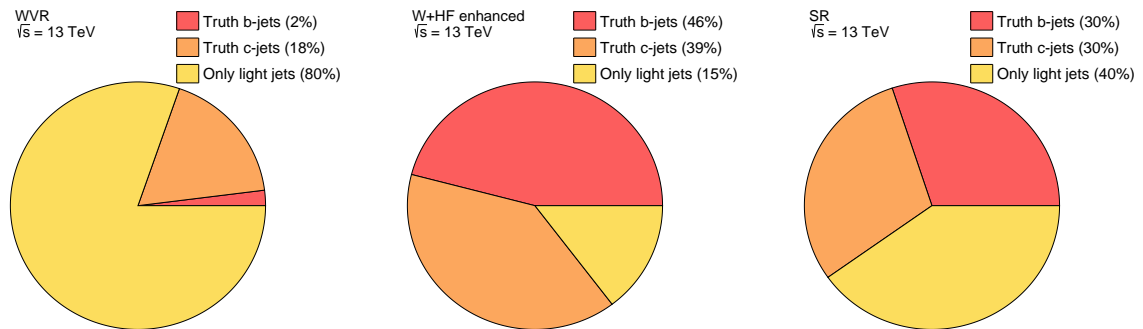
Figure 9.25: Breakdown of the flavour components of the W+jets process in the WVR (left), the cross-check selection (middle) and the SR (right).

Table 9.11: Selection for the cross-check of the *W*+heavy flavour normalisation, compared to the signal region selection requirements.

Variable	Signal Region	*W*+HF
$E_{\mathrm{T}}^{\mathrm{miss}}$	> 350 GeV	> 300 GeV
m_{T}	> 170 GeV	$m_{\mathrm{T}} \in [30, 90]$ GeV
am_{T2}	> 175 GeV	> 250 GeV
$H_{\mathrm{T,sig}}^{\mathrm{miss}}$	> 12	–
Jet p_{T}	> 120, 80, 50, 25 GeV	> 120, 80, 50, 25 GeV
# *b*-tagged jets	≥ 1	≥ 1
$\Delta R(b, b)$	–	< 1.2 (for ≥ 2 *b*-jets)
Lepton charge	–	+1
# large-*R* jets	≥ 2	≥ 2
Large-*R* jet p_{T}	> 290 GeV/> 200 GeV	> 200 GeV
Leading large-*R* jet mass	> 80 GeV	$\in [80, 150]$ GeV or > 200 GeV
Sub-leading large-*R* jet mass	> 60 GeV	> 60 GeV

in *pp* collisions is exploited by requiring a positively charged lepton. Table 9.11 shows the detailed selection requirements for the *W*+HF enhanced region. The *W*+HF selection is not orthogonal to the $t\bar{t}$ control region, as the latter does not apply an upper cut on the am_{T2} variable. As the cross-check selection is not used in the simultaneous fit, this does not introduce a bias. Figure 9.25 shows the flavour breakdown of the *W*+jets validation region, the *W*+HF selection and the signal region. By construction, the heavy flavour enhanced region is dominated by *W*+heavy flavour events.

The expected and observed events for this selection are shown in Table 9.12, with the relative contributions visualised in Figure 9.26. Only statistical uncertainties are evaluated for this cross-check. The *W*+jets events are the leading contribution with 55% of the expected events. The SM expectation, including the normalisation as obtained in the background only fit, agrees well with the observed data. Figures 9.27 shows the distribution of the $E_{\mathrm{T}}^{\mathrm{miss}}$ and the *b*-jet multiplicity in the *W*+HF enhanced region, demonstrating the good agreement of data and prediction. Additional comparisons are shown in Figure 9.28. This cross-check confirms that the deviation of the normalisation factor is not due to the *b*-jet requirement and validates the *W*+jets prediction in the signal region.

Table 9.12: Observed events in the *W*+HF enhanced selection together with the expected background events, scaled to the results of the simultaneous fit to the control regions. Only the statistical uncertainties of the MC and the uncertainties on the background normalisation are included.

Region	*W*+HF enhanced
Observed events	51
Total background events	52 ± 4
$t\bar{t}$ events	15 ± 3
W + jets events	24 ± 3
single top events	9.3 ± 0.7
$t\bar{t}$ + *V* events	0.8 ± 0.1
diboson events	3.1 ± 0.7
MC exp. background events	62 ± 2
MC exp. $t\bar{t}$ events	14 ± 2
MC exp. *W* + jets events	34 ± 1
MC exp. single top events	9.3 ± 0.7
MC exp. $t\bar{t}$ + *V* events	0.8 ± 0.1
MC exp. diboson events	3.1 ± 0.7
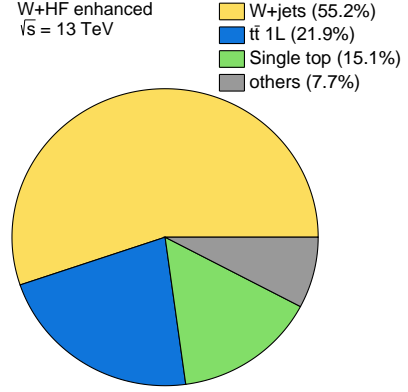
Figure 9.26: Breakdown of the individual SM contributions in the *W*+HF enhanced selection.
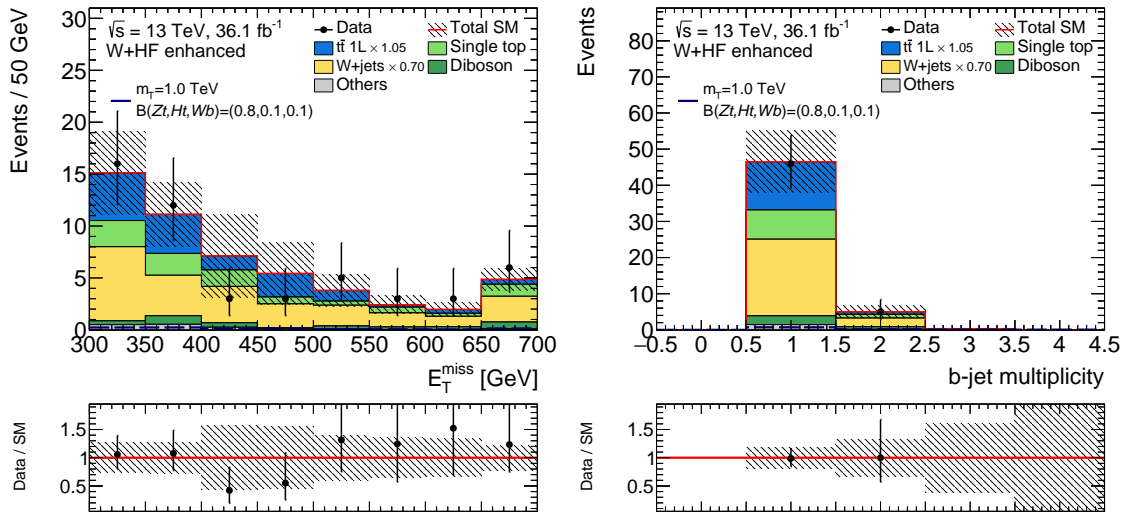
Figure 9.27: Distribution of the E_T^{miss} and the *b*-jet multiplicity in the *W*+HF enhanced region. The $t\bar{t}$ and *W*+jets normalisation factors are applied as indicated in the legend and the last bin contains overflow events. The lower panels show the ratio of the data to the prediction. The error bands include statistical and systematic uncertainties.
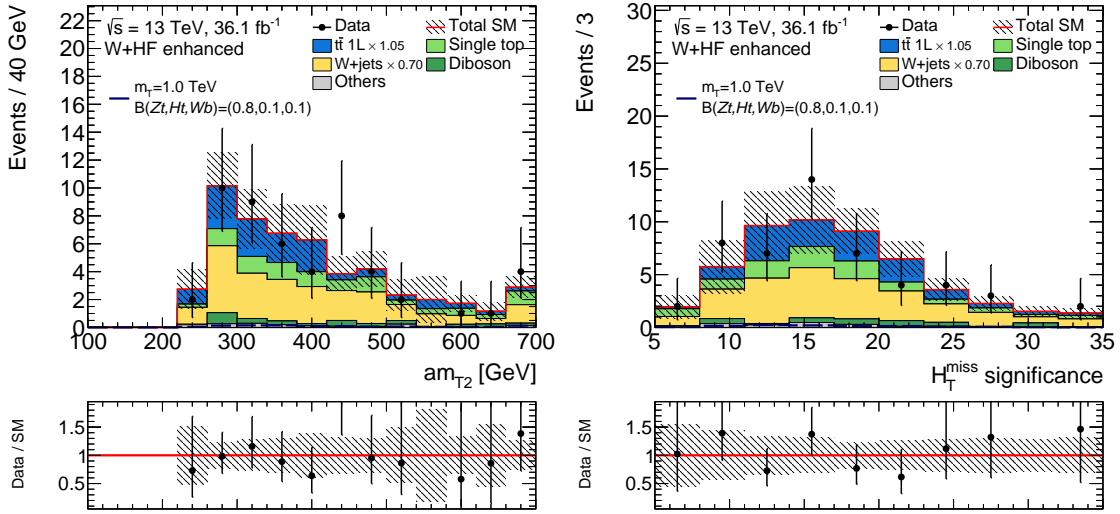
Figure 9.28: Distribution of the am_{T2} and the $H_{T,sig}^{miss}$ in the W+HF enhanced region. The $t\bar{t}$ and W+jets normalisation factors are applied as indicated in the legend and the last bin contains overflow events. The lower panels show the ratio of the data to the prediction. The error bands include statistical and systematic uncertainties.

9.4.3   Single top validation region

Table 9.13 gives the expected events in the STVR. The relative contributions are visualised in Figure 9.29. Figure 9.30 shows the distributions in the STVR after applying the normalisation factors for $t\bar{t}$ and W+jets obtained in the background only fit. Additional distributions are shown in Appendix B.3.3. A reasonable agreement of data and simulation can be observed. This confirms that the single top background is well modelled in the signal region, within the statistical uncertainties and the relatively low purity of the validation region.

Table 9.13: Observed and expected events in the STVR. The individual uncertainties are correlated, and do not add up quadratically to the total uncertainty.

Region	STVR
Observed events	143
Total background events	125 ± 27
$t\bar{t}$ events	53 ± 23
W + jets events	15 ± 7
single top events	46 ± 17
$t\bar{t} + V$ events	8.3 ± 1.4
diboson events	1.7 ± 1.1
MC exp. background events	129 ± 31
MC exp. $t\bar{t}$ events	51 ± 21
MC exp. W + jets events	22 ± 9
MC exp. single top events	47 ± 17
MC exp. $t\bar{t} + V$ events	8.3 ± 1.4
MC exp. diboson events	1.7 ± 1.1
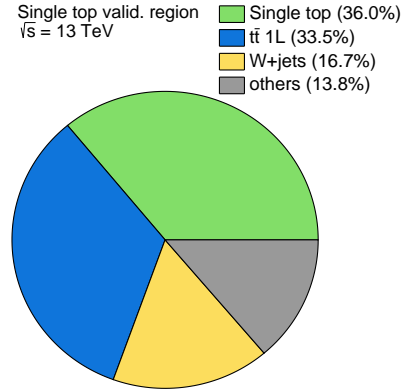
Figure 9.29: Breakdown of the individual SM contributions in the STVR.
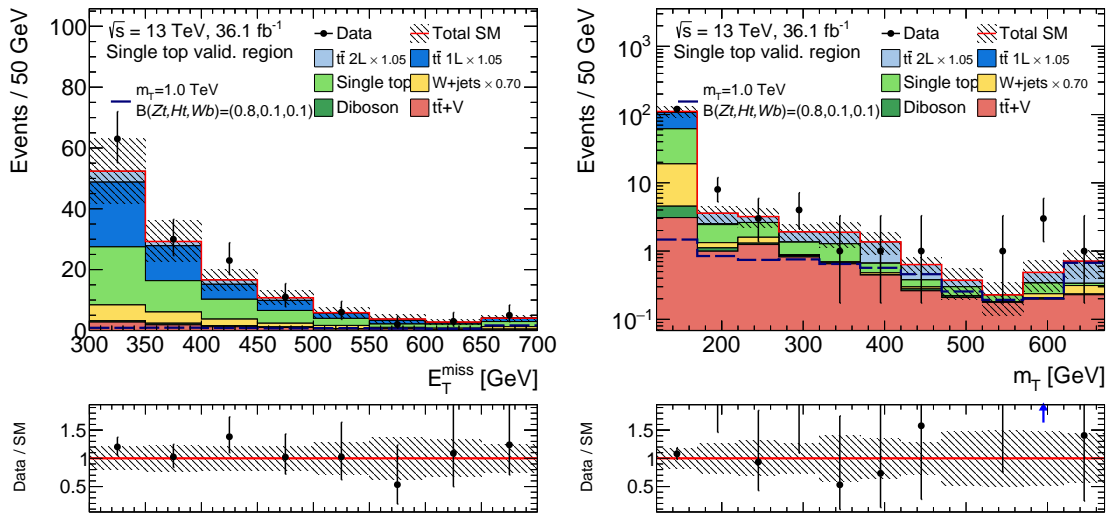
Figure 9.30: Distribution of E_T^{miss} and m_T in the single top validation region. The $t\bar{t}$ and W+jets normalisation factors are applied as indicated in the legend and the last bin contains overflow events. The lower panels show the ratio of the data to the prediction. The error bands include statistical and systematic uncertainties.

9.5 Impact of systematic uncertainties

The sources of systematic uncertainties detailed in Section 8.6 are considered in the analysis. In addition to those, systematic uncertainties in the jet masses and in the heavy flavour fraction in W+jets events are included.

The systematic uncertainties in the background modelling are evaluated by comparing the expected yields in the analysis regions for the nominal prediction and the systematically shifted variations. This approach is affected by the limited number of generated events in the variation samples. To account for this effect, the statistical uncertainty of the estimate is added in quadrature to any of the theory uncertainties. The experimental uncertainties are evaluated on the same sample, but with different experimental conditions, e.g. a different jet energy scale assumption. These uncertainties are therefore not affected by additional statistical fluctuations. As discussed in Section 8.6, the uncertainties in the $t\bar{t}$ and W+jets backgrounds in the SR result from the relative difference of each systematic source in the SR to the respective CR, as the normalisation is determined in the fit.

Additional jet related uncertainties come from the error on the scale and resolution of the small-radius jet masses. As the large-R jets are clustered from small-radius jets, the mass uncertainties affect the mass of the large-R jets, especially in the case of just one small-radius jet constituent. This is relevant for the signal process, as for highly boosted, hadronically decaying Z or H bosons the decay products can overlap in the detector and result in just one, massive $R = 0.4$ jet.

As the W+jets background is normalised in a control region defined with a veto on b-tagged jets and the SR requires at least one b-jet, an additional uncertainty in the heavy flavour fraction of W+jets events is considered. The W+heavy flavour production was measured at $\sqrt{s} = 7$ TeV [157]. The relative uncertainty in this measurement is 24% in events requiring exactly two jets. To account for the extrapolation to the requirement of at least four jets in the analysis, in total a 30% relative uncertainty is assumed on the total W+jets expectation in regions requiring at least one b-jet.

The leading systematic uncertainties in the total background prediction are listed in Table 9.14. The dominant systematic effects are due to the modelling of the $t\bar{t}$ background, amounting to 11%–17% uncertainty in the total background estimate. These uncertainties are strongly affected by the statistical fluctuations because of the small number of generated events in the variation samples. The leading experimental uncertainty is the effect of the jet mass resolution. In general, the systematic uncertainties are smaller than the statistical uncertainties in the data.

Table 9.14: Breakdown of the leading systematic uncertainties in the total background prediction in the signal region. The statistical precision is included in uncertainties derived from the comparison of MC samples. The individual uncertainties are correlated, and do not necessarily add in quadrature to the total background uncertainty. Only uncertainties larger than 1% of the total background prediction are shown.

Uncertainty	**SR**
Total background prediction	6.1
Total statistical ($\sqrt{n_{\exp}}$)	±2.5
Total background uncertainty	±1.9 [31%]
$t\bar{t}$ MC generator	±1.1 [17%]
$t\bar{t}$ fragmentation	±0.8 [14%]
$t\bar{t}$ radiation	±0.7 [11%]
MC stat. (nominal samples)	±0.7 [11%]
$t\bar{t}$ Single-top interference	±0.6 [11%]
Single-top radiation	±0.4 [6.6%]
$\mu_{t\bar{t}}$	±0.4 [6.6%]
Diboson fact. scale	±0.4 [6.5%]
Diboson renorm. scale	±0.4 [6.1%]
W+jets heavy flavour fraction	±0.3 [5.3%]
Jet mass resolution	±0.3 [5.0%]
Diboson resum. scale	±0.3 [4.7%]
Flavour-tagging light-jet mistag rate	±0.3 [4.5%]
Single-top fragmentation	±0.2 [3.5%]
Flavour-tagging c-jet mistag rate	±0.2 [3.4%]
W+jets MC generator	±0.2 [3.1%]
$t\bar{t}$ PDF	±0.2 [2.8%]
$\mu_{W+\text{jets}}$	±0.2 [2.4%]
W+jets merging scale	±0.1 [2.4%]
W+jets renorm. scale	±0.1 [2.3%]
W+jets resum. scale	±0.1 [2.3%]
W+jets fact. scale	±0.1 [2.3%]
Jet energy scale (1st component)	±0.1 [2.0%]
$t\bar{t} + V$ cross-section	±0.1 [1.9%]
$t\bar{t} + V$ scale	±0.1 [1.5%]
Jet energy scale (2nd component)	±0.1 [1.4%]
Jet energy resolution	±0.1 [1.3%]
Trigger efficiency	±0.1 [1.0%]

9.6 Results

The observed and expected number of events are summarised in Table 9.15. No significant excess above the SM expectation is found in the signal region, with 7 observed and 6.1 ± 1.9 expected events. Figure 9.31 also shows the agreement of the observed data and the expected events in the SR, and in the VRs to confirm the proper modelling of the backgrounds. The largest deviation is seen in the STVR and amounts to less than 1σ. The compatibility of the observed data with the background only hypothesis in the SR is calculated to $p_0 = 0.34$, equivalent to a significance of $Z = 0.4\sigma$.

The $E_{\text{T}}^{\text{miss}}$ distribution in the SR is presented in Figure 9.32, where additionally the signal contribution for a mass of $1.1\,\text{TeV}$ is shown. For this signal, nine additional events would be expected in the SR, with the largest contribution at about half the T mass. Additionally, the mass of the leading large-R jet in the SR is shown. With that, the data follows the distribution of the SM prediction and no significant deviation, as expected from a VLT signal, is seen.

As no significant excess above the SM prediction is found, upper limits at 95% CL are derived following the procedure described in Section 8.8. The observed upper limit on any non-SM events in the signal region is $N_{\text{non-SM}} < 8$, with an expected limit of 7.5 events. Additionally, limits on the signal cross-section are derived as a function of the VLT mass. For each signal mass point, the limits are calculated for the weak-isospin singlet and doublet models, as well as for pure $T \rightarrow Zt$ decays. Figure 9.33 shows the resulting limits, interpolated for intermediate masses. The dashed black line shows the expected cross-section limit, with the coloured bands giving the $\pm 1\sigma$ and $\pm 2\sigma$ uncertainty. The solid line shows the observed limit, which is slightly weaker than the expected limit as more events are observed than expected. The upper limits on the signal cross-section lie between $2\,\text{pb}$ and $13\,\text{fb}$.

Table 9.15: Number of events observed in the signal region, together with the estimated SM backgrounds. The uncertainties include all statistical and systematic sources. The individual uncertainties are correlated, and do not necessarily add in quadrature to the total background uncertainty.

Region	SR
Observed events	7
Total background events	6.1 ± 1.9
$t\bar{t}$ events	2.5 ± 1.7
W + jets events	1.1 ± 0.7
single top events	1.1 ± 0.7
$t\bar{t} + V$ events	0.9 ± 0.2
diboson events	0.6 ± 0.6
MC exp. background events	6.5
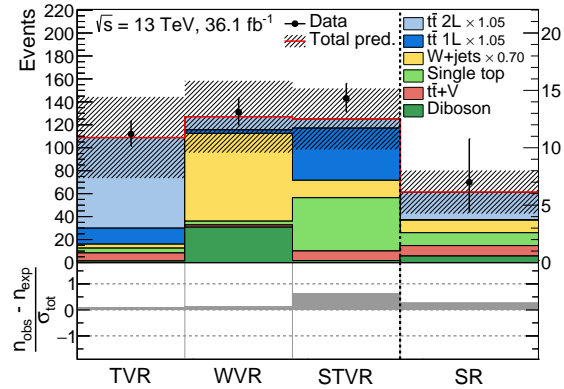
Figure 9.31: Comparison of the observed data (n_{obs}) with the predicted background (n_{exp}) in the VRs and the SR. The bottom panel shows the significance of the difference between data and predicted background, where the significance is based on the total uncertainty (σ_{tot}).
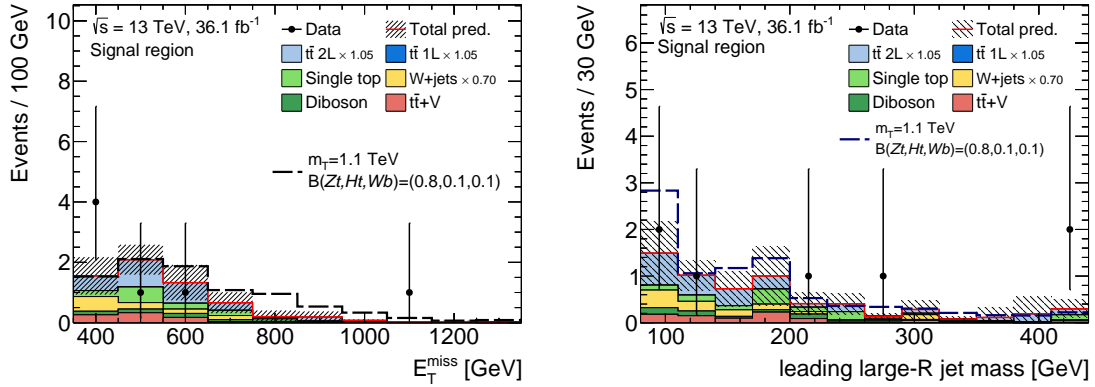
Figure 9.32: Comparison of data and prediction in the E_T^{miss} distribution (left) and the mass of the leading large-R jet (right) in the SR. The error bands include statistical and systematic uncertainties. The expected shape for a signal with $m_T = 1.1$ TeV and $\mathcal{B}(T \to Zt) = 80\%$ is overlaid on the SM prediction.

In the limit setting, no nuisance parameters are constrained or pulled from the pre-fit values, indicating a good fit stability and no discrepancies between data and simulation. The fit setup for the statistical evaluation by construction has no power to further constrain the nuisance parameters beyond the auxiliary measurements. Comparing the cross-section limits to the theoretical expectation for the signal cross-section, lower limits on the T quark mass can be derived. Any vector-like top quark mass for which the limit lies below the expected cross-section is excluded.

The resulting mass limits are summarised in Table 9.16 and range from more than 1.1 TeV for the pure $T \to Zt$ decay to about 900 GeV for the singlet model. The sensitivity to the latter model is lower due to the low $\mathcal{B}(T \to Zt)$, which approaches 25% in the high-mass limit. The contribution from additional vector-like quarks, in particular from the X or B quark in the $(X^{5/3}, T)$ or (T, B) doublets, is neglected, leading to conservative limits on the doublet model.

In order to show the sensitivity in dependence of the decay channels, Figure 9.34 shows the 95% CL observed and expected lower limits on the signal mass as a function of the decay branching ratios. The axes show the branching ratios for the $T \to Wb$ and $T \to Ht$ decays, respectively, and the $\mathcal{B}(T \to Zt)$ completes the branching ratio sum to 100%.[1] Accordingly, the origin of the coordinate system shows the point for which $\mathcal{B}(T \to Zt) = 100\%$. For each branching ratio combination, the cross-section limits are calculated as a function of the mass and the lower mass limits are derived. The mass limits are then grid-wise interpolated. The contour lines show the areas in which the indicated mass is excluded. The highest sensitivity is found in the region of $\mathcal{B}(T \to Zt) \simeq 100\%$, as this is the focus of the analysis. The sensitivity to the mixed $ZtHt$ decay mode is larger than to the $ZtWb$ decay mode. As an example, masses of $m_T < 1$ TeV are excluded for $\mathcal{B}(T \to Ht) < 65\%$ (70% expected) in the former decay mode and for $\mathcal{B}(T \to Wb) < 45\%$ (50% expected) in the latter. This comes from the higher acceptance of the mixed $ZtHt$ signature with respect to the $ZtWb$ final state, as the former events feature a higher b-jet multiplicity and more massive large-R jets (c.f. Figure 9.9).

---

[1] See for example Refs. [158, 159] for a discussion of additional decay modes for the vector-like T quark when $\mathcal{B}(T \to Zt) + \mathcal{B}(T \to Ht) + \mathcal{B}(T \to Wb) < 100\%$, and a recast of the analysis results presented here.
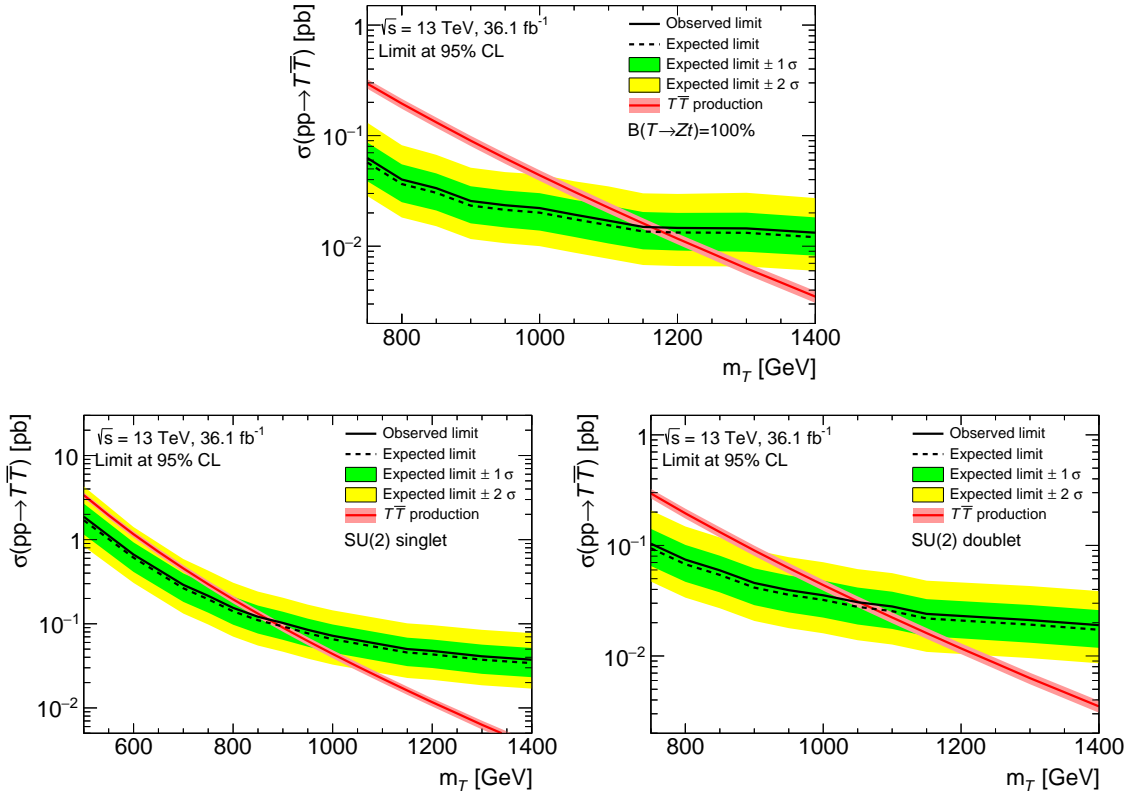
Figure 9.33: Observed and expected 95% CL upper limit on the cross-section times branching ratio for VLT pair production as a function of the T mass for $\mathcal{B}(T \to Zt) = 100\%$ (top) and for branching ratios according to the singlet model (bottom left) and the doublet model (bottom right). Contributions from the X or B quark in the $(X^{5/3}, T)$ or (T, B) doublet models are neglected, leading to conservative limits. The thickness of the theory curve represents the theoretical uncertainty from PDFs, scale and the strong coupling constant α_S.

Table 9.16: Observed and expected 95% CL lower limits on the T quark mass for the pure $T \to Zt$, the singlet model and the doublet model. Contributions from the X or B quark in the $(X^{5/3}, T)$ or (T, B) doublet models are neglected, leading to conservative limits.

Signal	Obs. 95% CL lower mass limit	Exp. 95% CL lower mass limit
$T \to Zt$	1.16 TeV	1.17 TeV
Singlet	0.87 TeV	0.89 TeV
Doublet	1.05 TeV	1.06 TeV
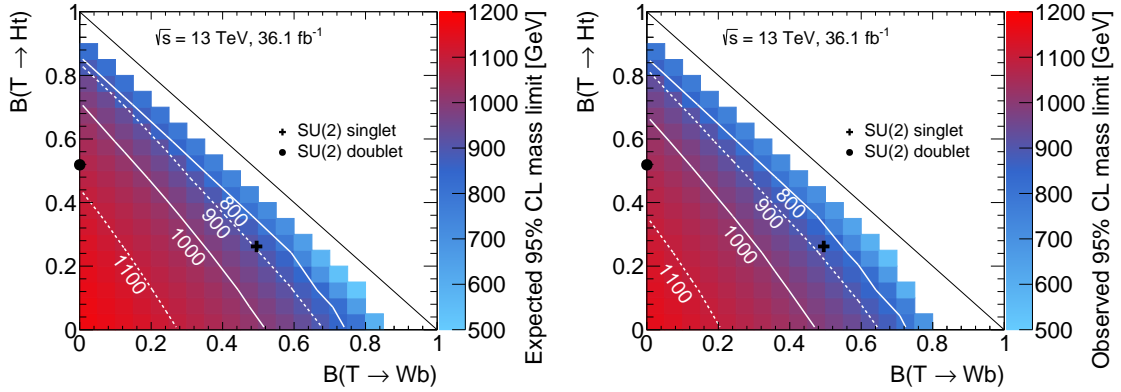
Figure 9.34: Expected (left) and observed (right) 95% CL lower limit on the T quark mass as a function of the decay branching ratios into Wb and Ht. The markers indicate the branching ratios in the singlet and doublet models for masses above about 0.8 TeV, where they are approximately independent of the T quark mass.

9.6.1 Weak-isospin doublet model

In the cross-section limits for the weak-isospin doublet model, either (T, B) or $(X^{5/3}, T)$, any contributions of the second vector-like quark are neglected in the analysis. This results in conservative limits, as events with $B\bar{B}$ (or $X\bar{X}$) production can contribute to the signal region. Additionally, any such events in the control region would lead to an increase in the fitted background normalisation, when they are not included in the signal model.

In order to check the approximate contributions to the CR and the SR, simulated samples of $B\bar{B}$ production are used, generated with the same settings as the $T\bar{T}$ signal samples. The X or B quark are expected to always decay to a Wt final state, and preferred to have a similar mass as the vector-like top quark [38]. As the analysis is not sensitive to the charge of the X or B quark, the $B\bar{B}$ results are valid also for a $(X^{5/3}T)$ doublet. Based on the generated samples, an additional
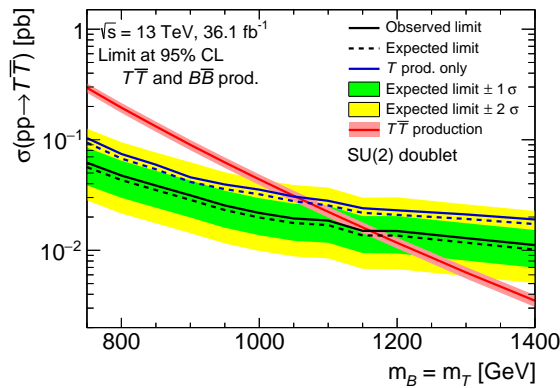
Figure 9.35: Observed and expected 95% CL upper limit on the cross-section times branching ratio for VLT pair production as a function of the T mass for branching ratios according to the doublet model. The contributions of the vector-like bottom quark B pair production, with the same mass as the VLT, are included. They are also valid for a $(X^{5/3}T)$ doublet.

contribution of $B\bar{B}$ with a size of about 50% of the VLT pair production is estimated in the signal region. In the $t\bar{t}$ control region about 80 signal events are expected for $m_B = 800$ GeV, and about 10 events for $m_B = 1.2$ TeV, compared to about 450 expected events from the SM. Due to the veto on b-jets in the W+jets control region, no additional signal contribution is expected there.

Figure 9.35 shows the potential improvement in the cross-section limit as a function of the vector-like top mass for the doublet model, when including the contributions of the second vector-like quark. For this, the $B\bar{B}$ production estimate is included in the analysis. The limits are set on a combined signal strength factor μ for the sum of the $T\bar{T}$ and $B\bar{B}$ production for $m_B = m_T$. For comparison with the previous results, this signal strength limit is then compared to the limit on the $T\bar{T}$ production cross-section alone. The cross-section limit improves by about 40%, constant over the tested mass range. The limit on the vector-like top mass increases by about 100 GeV, accordingly.

As the vector-like top and bottom quark contributions are estimated separately, any mixed production of T and B quarks is neglected in this study. To a larger effect, the signal model also assumes singlet model couplings for both vector-like quarks, and any acceptance increases due to the kinematic differences are not included in the evaluation. In summary, a complete model of vector-like quarks in the doublet model, would potentially lead to a strong increase in the sensitivity. This comes for the drawback of an increased signal model dependence, including the decay mode of the second vector-like quark, the mass difference between the VLQs, as well as the actual couplings.

9.7 Comparison to similar searches

Vector-like top quarks have been searched for in several ATLAS analyses at $\sqrt{s}$ = 13 TeV. Figure 9.36 shows the exclusion limits in the decay branching ratio plane for several VLT masses for the most recent searches overlaid. For large values of $\mathcal{B}(T \to Wb)$, as motivated by the singlet model, the $Wb + X$ analysis [153] is the most sensitive. The analysis reconstructs the mass of the vector-like top from a b-jet, a charged lepton and the $E_\mathrm{T}^\mathrm{miss}$, using the W boson mass constraint in order to reconstruct the third component of the neutrino momentum. The same-sign analysis [161] is based on a selection of two same-sign leptons and is mostly sensitive to the doublet model. The signal is extracted in several regions differing in the b-jet multiplicity, the $E_\mathrm{T}^\mathrm{miss}$ and the H_T. The $Ht + X$ analysis [152] is the most sensitive analysis for large values of $\mathcal{B}(T \to Ht)$ and selects events with zero or one lepton, and a large number of b-jets. A multitude of signal regions is defined based on the large-R jet and b-jet multiplicity and other kinematic features. As can be seen, the analyses have been designed to achieve complementary sensitivity to the different decay branching ratios. In contrast to the search presented here, the other ATLAS analyses are based on multiple bins in order to extract the signal. The excluded masses reach above 1.1 TeV for the pure decay modes, and up to above 1.3 TeV for the $T \to Wb$ decay channel.

Searches with the CMS detector follow a more inclusive strategy, compared to the ATLAS analyses. At $\sqrt{s}$ = 8 TeV, a combination of five analyses was achieved [46]. Of those, two are optimised for the $T \to Wb$ decay, two for the $T \to Ht$ decay and one inclusively for all decay modes. At $\sqrt{s}$ = 13 TeV, a search in single-lepton final states [49] is mostly sensitive to the $T \to Wb$ and $T \to Ht$ decay channels. The most stringent limit on the $T \to Zt$ channel is from the inclusive 8 TeV analysis with a boosted decision tree based search in several regions, categorised by the number of
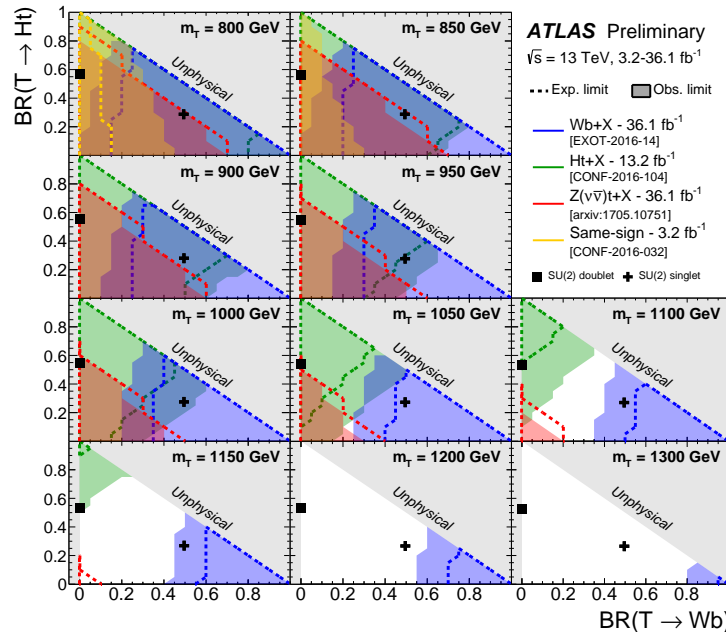
Figure 9.36: Observed and expected 95% CL exclusion as a function of the decay branching ratios into Wb and Ht for different values of the vector-like top quark mass for different analyses [160]. The markers indicate the branching ratios in the singlet and doublet models.

selected leptons, jets and kinematic features. There, vector-like top masses below 780 GeV can be excluded.

Chapter 10 Search for supersymmetric partners of the top quark

The search for supersymmetric partners of the top quark is presented in this chapter. It relies on the common properties of signals in final states similar to $t\bar{t} + E_T^{miss}$ in addition to the special features of the top squark decay. The results of this analysis are part of the searches published in Ref. [4]. In the publication several signal regions are constructed in order to achieve sensitivity to different signal parameter ranges. Here, the focus lies on the selection optimised for high top squark masses in the $\tilde{t}_1 \rightarrow t\tilde{\chi}_1^0$ decay.

10.1 Signal properties
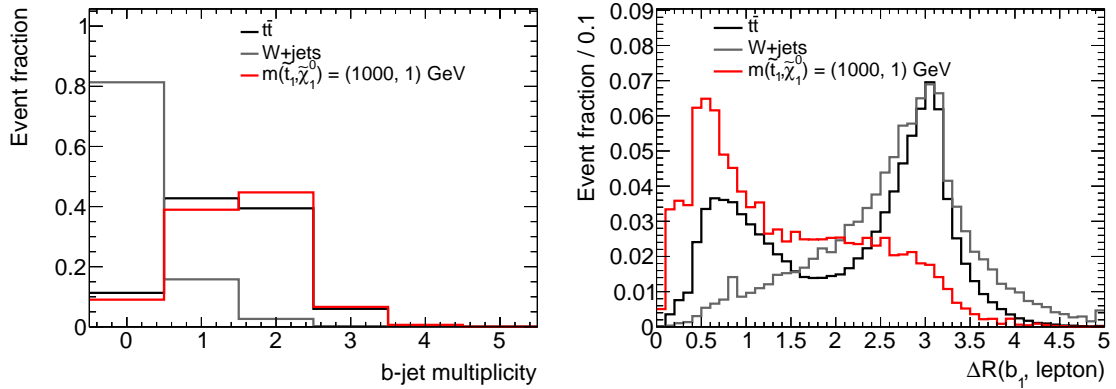
Figure 10.1: Comparison of the b-jet multiplicity (left) and the distance of the lepton and the b-jet (right) for the dominant background processes $t\bar{t}$ and W+jets, and for a signal process after the preselection. No requirement on the b-jet multiplicity is set for the left plot.

The final state of the signal process is very similar to that of $t\bar{t}$ events, with the only difference being the two additional, undetectable neutralinos. In contrast to the vector-like quark signal, the b-jet multiplicity, as shown in Figure 10.1, does not differ strongly between $t\bar{t}$ and the signal process.

Figure 10.1 also shows the distance of the lepton and the b-jet. In case that more than one b-jet is tagged in the event, the one with larger transverse momentum is used for this variable. For the $t\bar{t}$ decay either the b-jet from the leptonic top decay is selected, which tends to be close to the lepton, or the b-jet from the other top quark decay is selected, leading to a larger distance. While the same holds true for the signal, there the top quarks are commonly recoiling against the neutralinos in

the event, leading to smaller separations of the top quark decay products in general. For W+jets, generally larger distances are seen.

10.1.1 Hadronic top decay reconstruction

The reconstruction of the hadronically decaying top quark (hadronic top) can provide a strong tool to suppress backgrounds like dileptonic $t\bar{t}$, which do not contain such a decay. In order to reconstruct the hadronic top decay, an algorithm based on the anti-k_t clustering of small-radius jets is developed. In comparison to the fixed radius large-R jets, as used in the vector-like quark search, the newly developed algorithm is tuned to achieve higher signal efficiencies. As the production cross-section for the SUSY signal is about 7 times lower than for the VLT signal, a higher selection efficiency is needed. Additionally, the highly efficient reconstruction is used to reduce the contribution of semi-leptonic $t\bar{t}$ events to background control regions, by vetoing events with a reconstructed hadronic top quark decay.

Assuming massless decay products, the distance of the child particles in a two body decay of a mother particle with mass m can be approximated to $R(p_T) = 2 \times m/p_T$. While the mass of the W boson in the top quark decay cannot be neglected, this relation nonetheless gives a usable approximation for the spread of the three partons in a fully hadronic top quark decay. The distribution of the maximum separation of the top quark decay products as a function of the p_T is shown in Figure 10.2. As can be seen, especially at large p_T the approximation holds true, while for lower top quark p_T the true separation has a large spread and is often smaller than $R(p_T)$. A reconstruction of the hadronic top decay should thus cluster jets in a distance of approximately $R(p_T)$ to include all decay products of the top quark, but no additional jets. As the transverse momentum of the top quark decay is not known before the decay products are found, an algorithm is designed to iteratively adjust the radius of candidate objects to match the transverse momentum of the candidate.

Initially, all small-radius jets in the event are clustered using the anti-k_t algorithm with a large radius parameter R_0. The resulting very large radius jets are the seeds for the iterative reclustering, in which each candidate is shrunk until their radii match their p_T, according to the above approximation. A candidate in step i is considered too large, if $R(p_T) \leq R_{i-1} - R_{down}$, where R_{i-1} is the radius obtained in the previous step and the R_{down} parameter is adjusted to balance the frequency of further shrinking good candidates, and of retaining spurious constituents. In case that $R(p_T) \geq R_{i-1} + R_{up}$ the candidate is discarded. This requirement mainly removes low momentum seeds from the initial
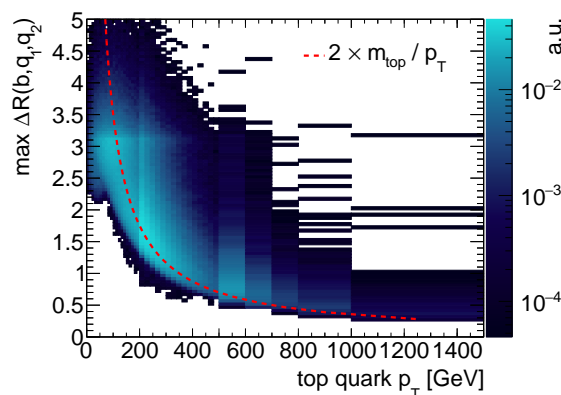
Figure 10.2: Distribution of the maximal separation of the top quark decay products versus the top quark p_T. The red dotted line shows the approximation $R(p_T) = 2 \times m/p_T$.
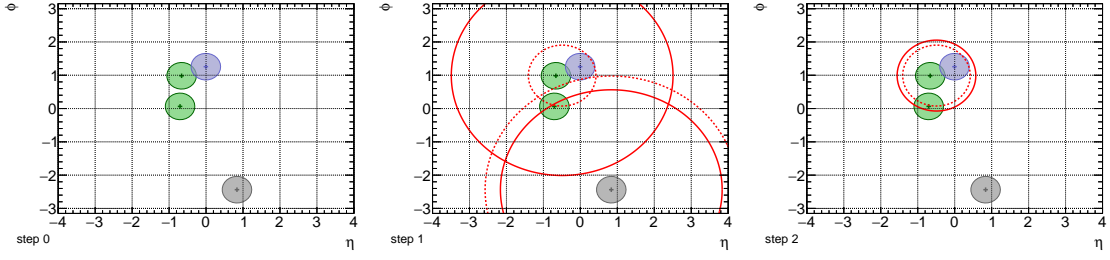
Figure 10.3: Illustrative display of the jets in the $\eta \times \phi$ plane for one event in the different steps of the hadronic top reconstruction algorithm. The *b*-jet of the hadronic top decay is marked in blue, the light jets from the top decay in green and other jets in the event are shown in grey. The actual radius of the candidates is shown with red solid lines, the "optimal" radius according to the p_T with red dashed lines.

clustering. The exact values of the parameters are tuned to achieve a high reconstruction efficiency, as discussed below. In detail, the algorithm follows these steps:

1. All signal small-radius jets in the event are reclustered with the anti-k_t algorithm with an initial radius $R_0 = 3.0$.

   - The initial radius parameter corresponds to a hadronic top quark p_T of 120 GeV. The exact value is checked to have a small impact on the reconstruction efficiency.

2. For each candidate object, the "optimal" radius is computed, using $R(p_T) = 2 \times m/p_T$, with the mass parameter set to the top quark mass, $m_t = 175$ GeV. This optimal radius is then compared with the radius assumed in the previous step, R_{i-1}, and the candidate is either reclustered again, discarded or taken. This procedure is iterated, until all initial candidate objects are taken (2c) or discarded (2b).

   (a) If the optimal radius is much lower than the current radius, i.e. if $R(p_T) \leq R_{i-1} - R_{\text{down}}$, then the constituents of the candidate jet are reclustered with a smaller radius, $R_i = R(p_T) + 1/2 \times R_{\text{down}}$.

      - The new radius R_i is limited to be not less than half the previous radius, $R_i \geq 1/2 R_{i-1}$, in order to prevent splitting good candidates for which the $R(p_T)$ approximation does not hold completely.
      - After this, the new optimal radius is calculated with the updated momentum and the comparison in step 2 is followed again.

   (b) Else, if the optimal radius is much higher than the current radius, i.e. if $R(p_T) \geq R_{i-1} + R_{\text{up}}$, then the candidate is discarded.

      - With this requirement, low momentum contributions from jets not from a hadronic top quark decay are mostly removed.

   (c) Else, if the optimal radius approximately matches the current radius ($R_{i-1} - R_{\text{down}} \leq R(p_T) \leq R_{i-1} + R_{\text{up}}$), then the candidate is taken as a hadronic top candidate.

Figure 10.3 shows an event display for the different steps of the top reconstruction algorithm. Initially, two candidate objects are found, corresponding to the hadronic top decay and an additional jet, respectively. As the transverse momentum of the top quark decay is large, the optimal radius
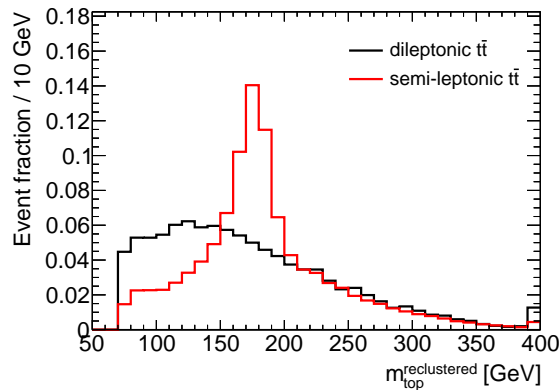
Figure 10.4: Distribution of the mass of the reconstructed hadronic top candidates for dileptonic $t\bar{t}$ events, where the candidate always is a fake, in black and for semi-leptonic $t\bar{t}$ events in red.
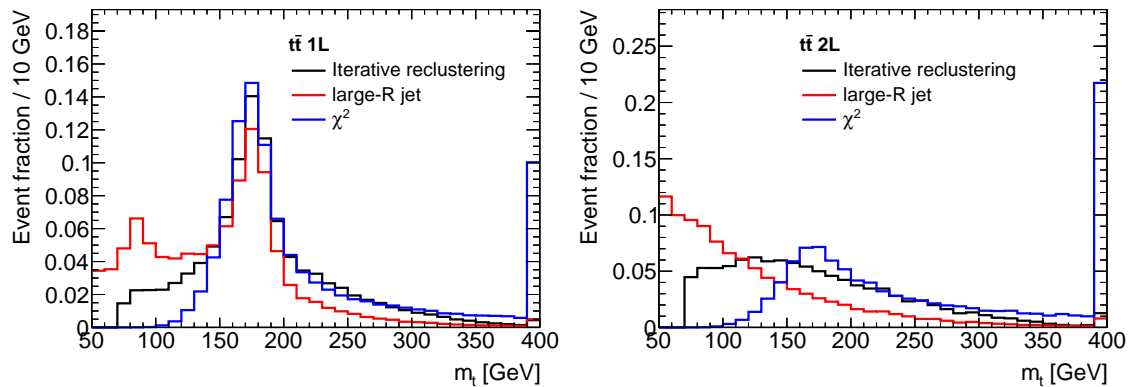
Figure 10.5: Distribution of the mass of reconstructed hadronic top candidates for semi-leptonic $t\bar{t}$ events (left) and dileptonic $t\bar{t}$ events (right), where the candidate always is a fake, in comparison for different reconstruction techniques. Events are required to fulfil the preselection requirements.

is much lower than the initial radius for this case. For the additional jet, i.e. the second candidate, the transverse momentum is small compared to the initially assumed radius. In the second step, the additional jet is therefore discarded (following the 2b branch), and only the first candidate is processed further. Its radius is shrunk and the three constituent jets are reclustered again (following the 2a branch). The three constituents still fall into the jet with a smaller radius, which now matches the p_T. This candidate is then taken.

Figure 10.4 shows the distribution of the mass of the hadronic top candidates for events with and without a true, hadronically decaying top quark. For events with a true hadronic top quark, the expected peak at the top mass can clearly be seen. In a small fraction of events, the top decay is not fully captured, resulting in a shoulder at the W boson mass. In some cases, additional jets enter the top candidate, leading to a tail in the distribution towards larger masses. For the background, i.e. the events without a true hadronic top quark, the distribution is smoothly falling from approximately 120 GeV, without a peak at the top quark mass.

The method is compared to techniques previously used for reconstructing hadronic top quark decays. In the search for vector-like top quarks, reclustered large-radius jets with a radius parameter of $R = 1.0$ are used. An alternative technique aiming at less boosted decays is a χ^2-minimisation
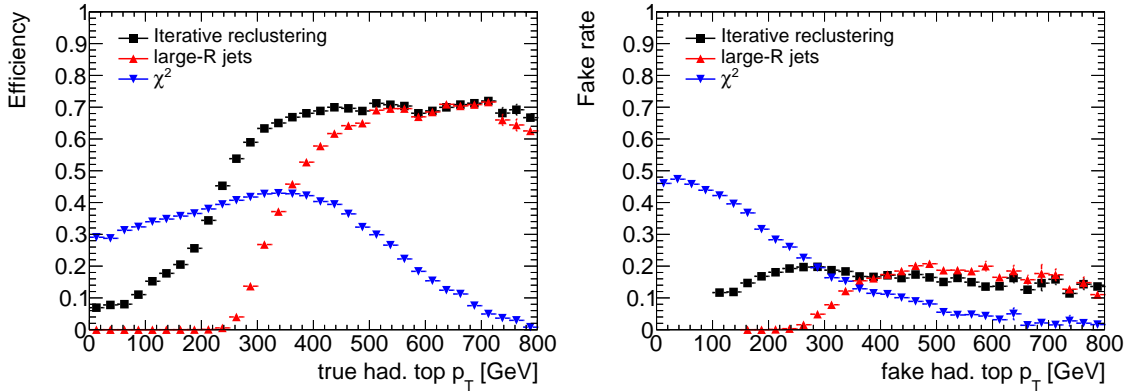
Figure 10.6: Efficiency of reconstructing exactly the hadronic top decay as a function of the hadronic top p_T (left) and the fake rate as a function of the reconstructed top p_T (right) for the recursive reclustering algorithm, for $R = 1.0$ large-R jets and for the χ^2 minimisation.

based algorithm used in previous searches for top squarks [143]. In the χ^2 method, the three jets in the event that are most compatible with the hadronic top decay are found by minimising $\chi^2 = (m_{bj_1j_2} - m_t)^2/\sigma^2_{bj_1j_2} + (m_{j_1j_2} - m_W)^2/\sigma^2_{j_1j_2}$ over all possible jet and b-jet permutations, with the resolutions σ based on the jet energy resolutions. Figure 10.5 compares the resulting mass spectra of the three reconstructing algorithms for events with and without a hadronic top quark, after the preselection. For events with a true hadronically decaying top quark, all three methods produce a clear peak at the top quark mass. The large-radius jet reconstruction also finds a second mass peak at the W boson mass, in events in which the boost of the top quark decay is lower and the large-radius jet only contains the W boson decay products. In contrast, the χ^2 technique shows a large tail towards higher masses, indicating wrong combinations. In the case of background events, both reclustering methods show a smoothly falling spectrum. The χ^2 combination also generates a peak at the top quark mass for events without a hadronic top quark decay, purely due to combinatorial reasons.

Figure 10.6 shows the efficiency and fake rate of the different methods which are tested to reconstruct hadronic tops. The reconstruction efficiency is defined as the fraction of events with a hadronically decaying top quark in which the top quark decay is exactly reconstructed. For the χ^2 method this means, that the three selected jets are matched to the partons from the top decay, and for the two reclustering approaches the partons from the top decay have to be matched to jets that are included in the candidate. Additionally the candidate is required to have a mass $150\,\text{GeV} < m < 200\,\text{GeV}$, in order to exclude candidates which include additional high momentum jets. The fake rate is defined as the number of candidates falling in the mass window in events without a hadronic top decay.

The approach described here shows a better efficiency with respect to the simple reclustering of jets with a fixed radius of $R = 1.0$. At very low top quark momentum, the χ^2 fit reconstruction becomes the algorithm with highest efficiency. The fake rate is comparable for fixed radius large-R jets and the reclustering algorithm, while the χ^2 method has a much higher fake rate, as it is strongly biased to find a candidate with approximately the top quark mass.

Figures 10.7 and 10.8 show the effect of varying the parameters of the algorithm. The distributions are normalised to the expected number of the events, and thus give an estimate of both the reconstruction efficiency and the impact on the shape of the mass distribution. The R_{down} parameter has the largest effect on the mass distribution, as it controls the splitting of "large" candidates. At
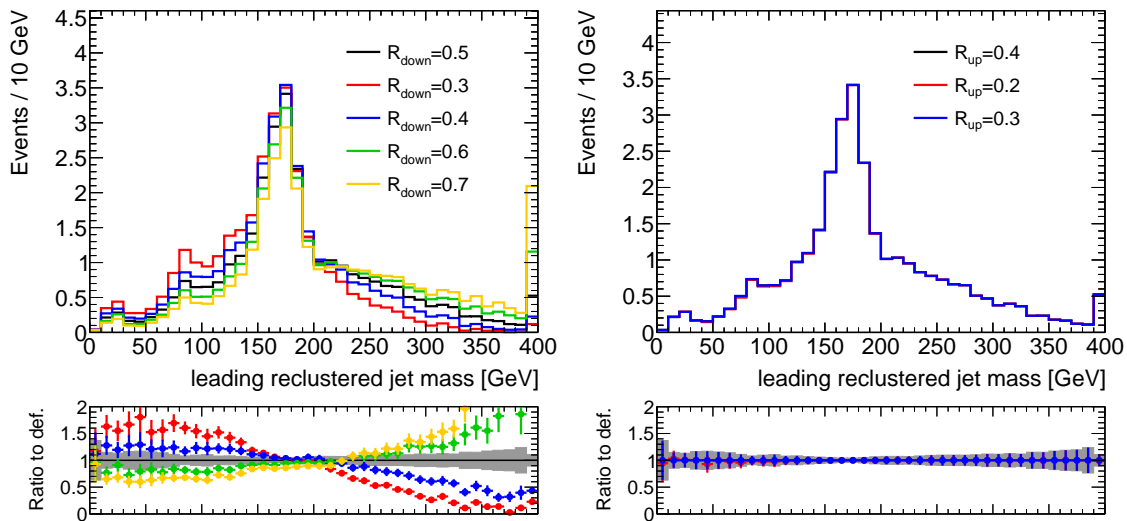
Figure 10.7: Distribution of the mass of the leading top candidate for different parameters in the algorithm, varying R_{down} (left) and R_{up} (right). Only one parameter is varied at a time, with the first setting in the list being the default value.

high values, which make the splitting less likely, a large amount of candidates contain additional jets and are reconstructed at masses much larger than the top quark mass. For low values of R_{down}, the peak at the W boson mass rises, as more good candidates are split. The default value of $R_{down} = 0.5$ was chosen in order to balance the number of candidates falling in either extreme. In events without a hadronic top quark decay, the R_{down} parameter influences the endpoint of the distribution. For higher values of R_{down}, the endpoint increases and more events are expected at high candidate masses. The other parameters, e.g. R_{up}, do not influence the mass distribution strongly. When limiting the initial radius R_0, additional candidates are found at very low masses. They are then not removed in step 2b, as the initial radius is lower and better matches the momentum of the object. The limit in the radius reduction in step 2a insignificantly increases the number of candidates above the W mass. A procedure akin to jet trimming has been tested, but found to have negligible impact. For this, constituent jets with less than 5% of the transverse momentum of the candidate are removed.

In case that multiple candidates are found in an event, the candidate with the mass closest to the top mass is taken. Figure 10.9 shows the top candidate multiplicity and the mass of the selected candidate for the dominant backgrounds and the benchmark signal. In addition to the preselection, $m_T > 120\,\text{GeV}$ is required, making dileptonic events the main contribution for the $t\bar{t}$ process. As can be seen, the efficiency of finding at least one candidate is larger than 90% for the signal, while approximately 20% of the background events are rejected by an requirement of a top candidate. In addition, the reconstructed mass shows a peak at the top quark mass, while for the backgrounds often lower values are found. Due to the long tails towards higher masses, indicating additional jets not from the top decay in the candidate objects, the signal and background distributions are similar for masses above 200 GeV.

Figure 10.10 shows the constituent jet multiplicity and the number of b-tagged constituent jets in the top candidate. For the signal, most of the times the candidate contains two or three constituent jets, with one of them being b-tagged. Although the distribution shows differences to the background, no requirements can be set without strongly reducing the signal efficiency. The fraction of top candidates with only one constituent jet is below 5%.
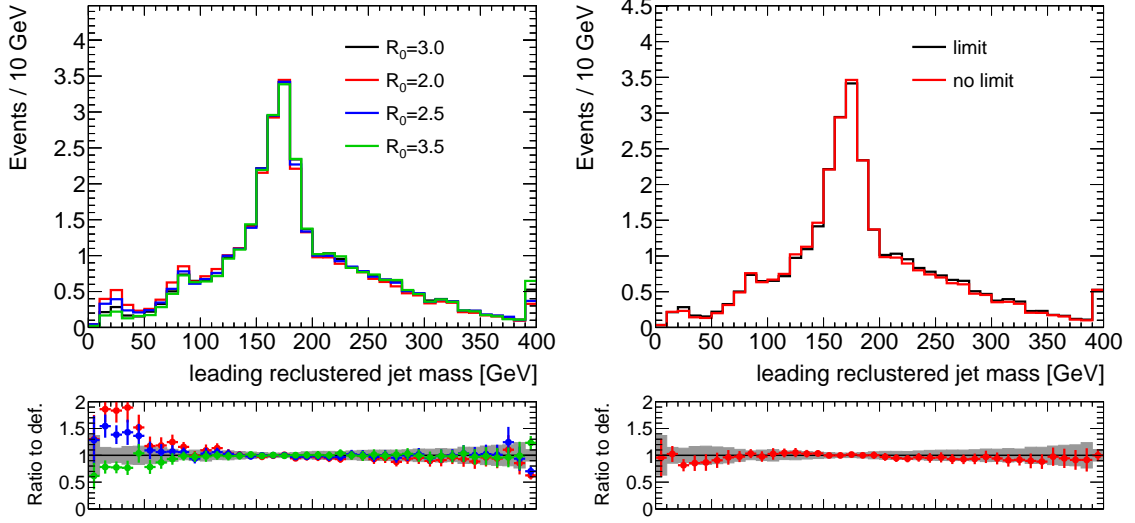
Figure 10.8: Distribution of the mass of the leading top candidate for different parameters in the algorithm, varying R_0 (left) or the limit on the minimal size of the new radius (right). Only one parameter is varied at a time, with the first setting in the list being the default value.
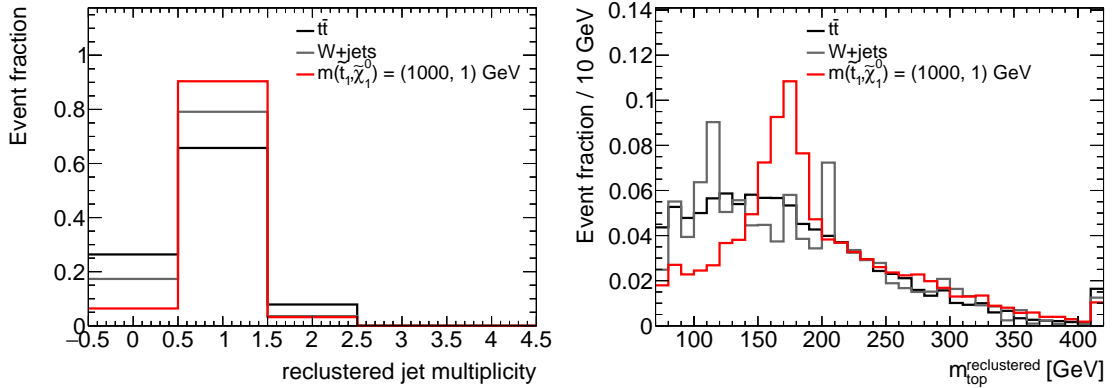
Figure 10.9: Comparison of the hadronic top candidate multiplicity (left) and the mass of the hadronic top candidate (right) for the dominant background processes $t\bar{t}$ and W+jets, and for a signal process after the preselection and $m_T > 120$ GeV. Peaks in the distribution for W+jets come from the low statistics after the m_T requirement.

Although the algorithm presented here is developed primarily to reconstruct hadronic top quark decays, it can easily be adapted to other hadronic resonances. For example, in order to reconstruct W boson decays into jets, the target mass is set to $m = 80$ GeV and only non-b-tagged jets are considered in the clustering. This is used in Ref. [4] to construct signal regions targeting the $\tilde{t}_1 \rightarrow b\tilde{\chi}_1^\pm(\rightarrow W^\pm \tilde{\chi}_1^0)$ decay. For this signal there are no top quark resonances, but one of the W bosons is expected to decay hadronically.

Figure 10.11 shows a comparison of data and simulation in the mass distributions of the hadronic top quark and hadronic W boson candidates after the preselection. The reconstruction is well modelled in the simulation and no significant deviations can be seen.
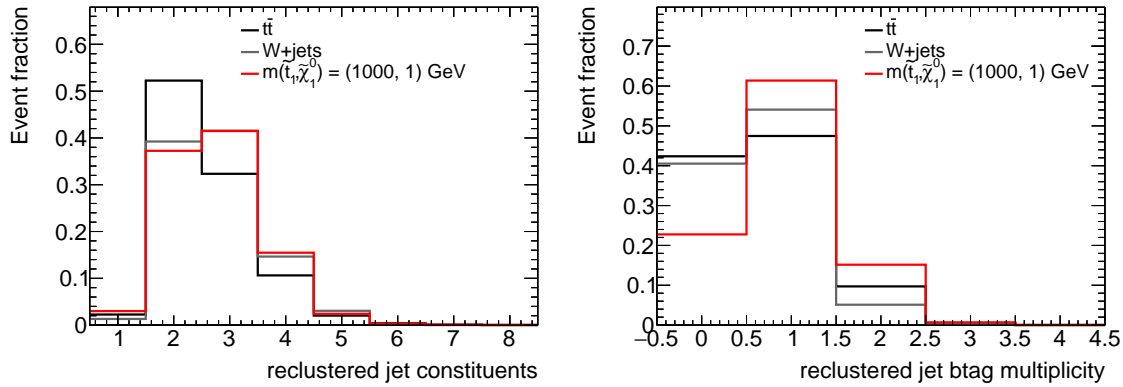
Figure 10.10: Comparison of constituent jet multiplicity (left) and constituent *b*-jet multiplicity (right) in the hadronic top candidate for the dominant background processes $t\bar{t}$ and W+jets, and for a signal process after the preselection and $m_\mathrm{T} > 120\,\mathrm{GeV}$.
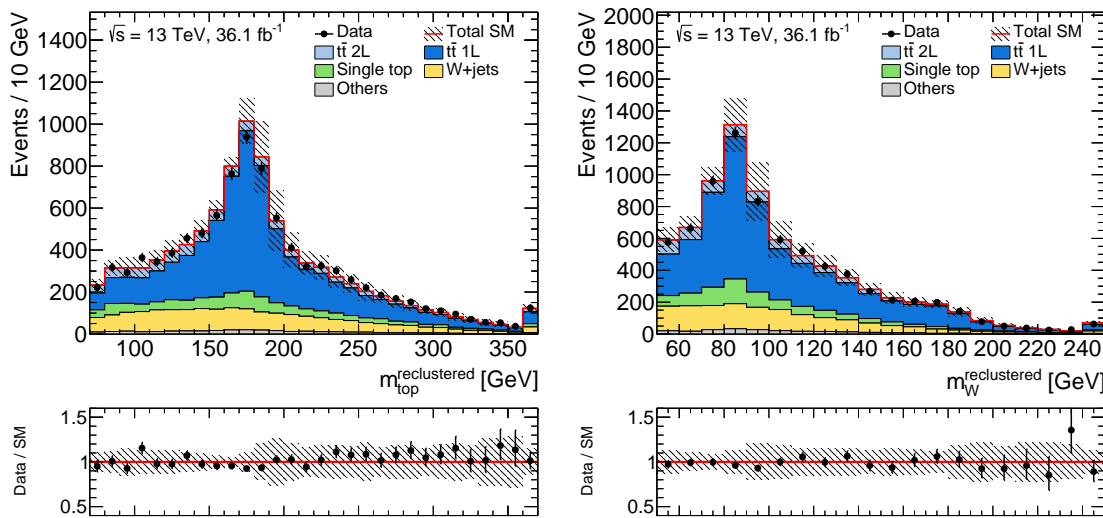
Figure 10.11: Comparison of data and simulation in the distributions of the hadronic top quark and W boson candidates after the preselection. The lower panels show the ratio of the data to the prediction. The error bands include statistical and systematic uncertainties.

10.2 Signal region

The signal region for the top squark search is defined targeting a benchmark signal with $m_{\tilde{t}_1} = 1$ TeV and a nearly massless neutralino. The optimisation of the selection follows the same approach as for the VLQ search, as detailed in Section 9.2.1. Instead of the fixed-radius large-R jets, the properties of the hadronic top candidates are used in the optimisation. In the context of Ref. [4] the signal region is called "tN_high", as it targets the decay of the top squark into a top quark and a neutralino (tN) for a high mass difference $\Delta m(\tilde{t}_1, \tilde{\chi}_1^0)$. The most important variables in the optimisation are the E_T^{miss} and the $H_{T,\text{sig}}^{\text{miss}}$, due to the high mass difference in the signal model.

10.2.1 Signal region selection

The resulting selection for the signal region is shown in Table 10.1. The tN_high signal region is characterised by large E_T^{miss} and $H_{T,\text{sig}}^{\text{miss}}$, as well as the presence of a hadronic top quark candidate with a mass of at least 130 GeV. Further requirements are placed on the m_T, as well as on the distance between the lepton and the b-jet, $\Delta R(b, \ell)$.

The expected SM events in the signal region are shown in Table 10.2, with the fraction of the individual contributions visualised in Figure 10.12. In total, about four SM events are expected, compared to six events from the benchmark signal. The dominant backgrounds are the irreducible $t\bar{t} + Z(\to \nu\bar{\nu})$ process, followed by W+jets and dileptonic $t\bar{t}$ events. The latter two backgrounds are strongly reduced by the high E_T^{miss} requirement, as well as the hadronic top tagging.

A cutflow for the signal, as well as for the dominant backgrounds is shown in Table 10.3. All requirements have close to 90% signal efficiency, with the exception of the choice of the single lepton channel, as well as the E_T^{miss} requirement. The latter requirement reduces the backgrounds by 95%–98%. The total signal efficiency is 4%. For events with one leptonically decaying top quark, the selection efficiency is about 11%.

Table 10.1: Signal region selection for the search for supersymmetric top quark partners. For the jet p_T requirement, the numbers refer to the objects ordered in p_T.

Variable	SR
E_T^{miss}	> 550 GeV
m_T	> 160 GeV
am_{T2}	> 175 GeV
m_{T2}^{τ}	> 80 GeV
$H_{T,\text{sig}}^{\text{miss}}$	> 27
Jet p_T	> 100, 80, 50, 30 GeV
$|\Delta\phi(j_i, E_T^{\text{miss}})|, i = 1, 2$	> 0.4
# b-tagged jets	≥ 1
$\Delta R(b, \ell)$	< 2
Had. top mass	> 130 GeV

Table 10.2: Events expected from simulation in the signal region with MC statistical uncertainties.

tN_high	e-channel	μ-channel	Total
$t\bar{t}$ 2L	0.25 ± 0.04	0.26 ± 0.05	0.51 ± 0.06
$t\bar{t}$ 1L	0.02 ± 0.01	0.0 ± 0.0	0.02 ± 0.01
Single top	0.09 ± 0.05	0.10 ± 0.05	0.20 ± 0.07
W+jets	0.56 ± 0.14	0.51 ± 0.14	1.08 ± 0.20
Diboson	0.23 ± 0.06	0.19 ± 0.05	0.42 ± 0.07
$t\bar{t}$+V	0.87 ± 0.15	0.81 ± 0.13	1.68 ± 0.20
Total SM	2.03 ± 0.22	1.87 ± 0.21	3.90 ± 0.31
Signal	3.04 ± 0.09	3.00 ± 0.09	6.04 ± 0.13

tN_high
$\sqrt{s}$ = 13 TeV

- $t\bar{t}$+V (43.0%)
- W+jets (27.6%)
- $t\bar{t}$ 2L (13.1%)
- Diboson (10.8%)
- others (5.5%)
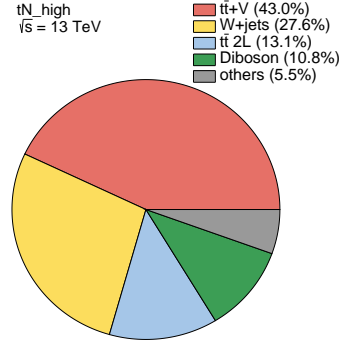
Figure 10.12: Breakdown of the individual SM contributions in the signal region.

Table 10.3: Cutflow for the dominant backgrounds and the benchmark signal. The $t\bar{t}$ and W+jets processes only contain events with at least one lepton, while for the signal and for $t\bar{t} + V$ also pure hadronic decays are included.

Cut	Signal	$t\bar{t}$	$t\bar{t} + V$	W+jets
Event cleaning	99 %	97 %	99 %	100 %
≥ 1 baseline lepton	60 %	91 %	79 %	98 %
≥ 1 signal lepton	70 %	83 %	77 %	91 %
$= 1$ signal lepton	90 %	91 %	87 %	100 %
$= 1$ baseline lepton	80 %	82 %	78 %	96 %
Trigger	100 %	70 %	78 %	73 %
≥ 4 jets	80 %	97 %	97 %	81 %
$E_{\mathrm{T}}^{\mathrm{miss}} > 230\,\mathrm{GeV}$	90 %	9 %	20 %	13 %
$\lvert \Delta\phi(j_i, E_{\mathrm{T}}^{\mathrm{miss}}) \rvert > 0.4, i = 1, 2$	90 %	85 %	87 %	91 %
$m_{\mathrm{T}} > 120\,\mathrm{GeV}$	90 %	9 %	36 %	3 %
≥ 1 b-jet	90 %	90 %	91 %	18 %
$am_{\mathrm{T2}} > 175\,\mathrm{GeV}$	90 %	22 %	61 %	77 %
$m_{\mathrm{T2}}^{\tau} > 80\,\mathrm{GeV}$	99 %	81 %	96 %	99 %
$E_{\mathrm{T}}^{\mathrm{miss}} > 550\,\mathrm{GeV}$	50 %	2 %	5 %	5 %
$m_{\mathrm{T}} > 160\,\mathrm{GeV}$	100 %	75 %	90 %	90 %
$H_{\mathrm{T,sig}}^{\mathrm{miss}} > 27$	80 %	30 %	70 %	70 %
small-R jet p_{T}	90 %	80 %	85 %	60 %
had. top mass	85 %	50 %	90 %	65 %
$\Delta R(b, \ell)$	100 %	80 %	90 %	70 %
Total efficiency	4 %	6×10^{-6} %	0.01 %	2.11×10^{-7} %

10.2.2 Distributions in the signal region
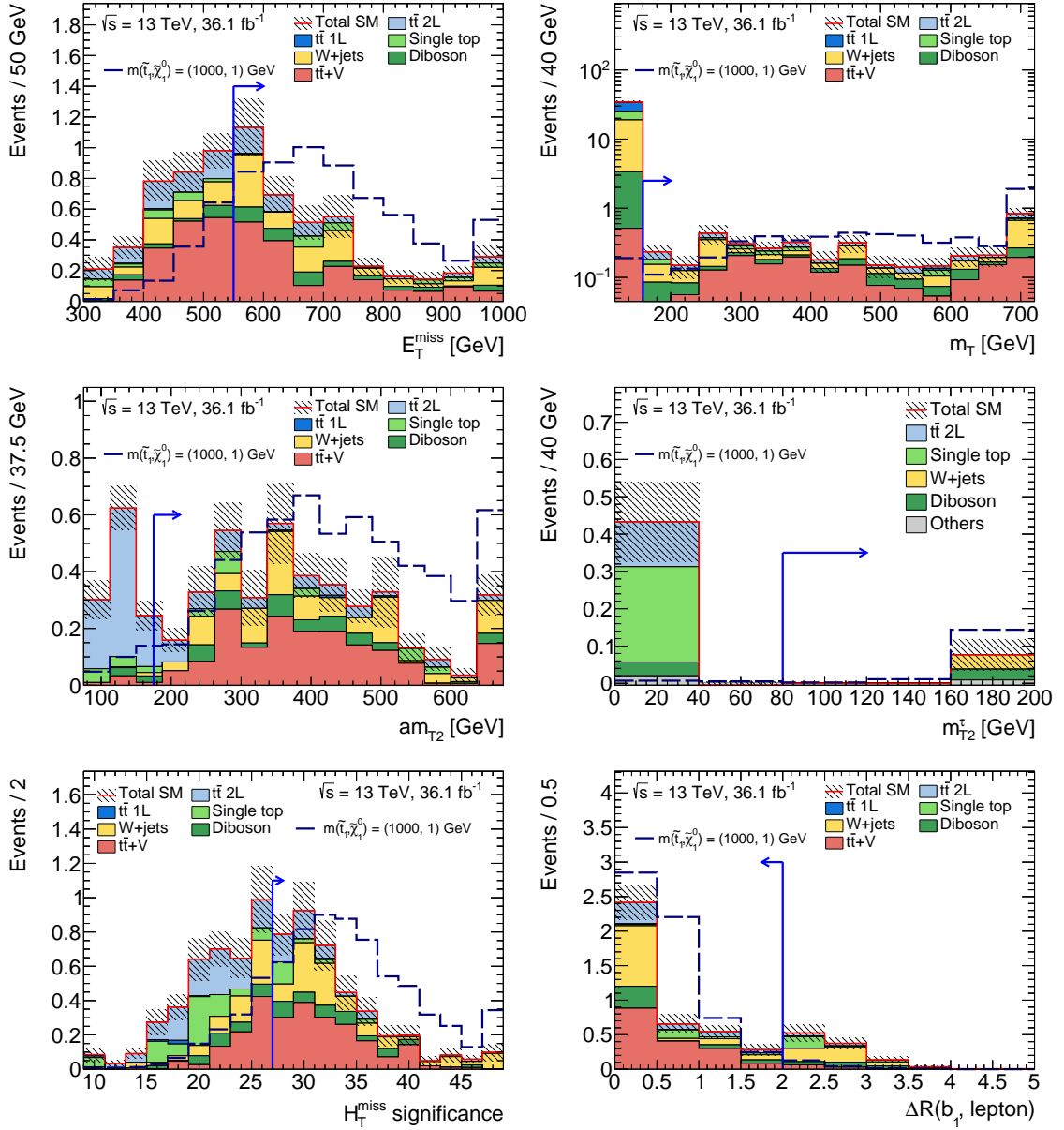
Figure 10.13: Distributions of the E_T^{miss}, the m_T, the am_{T2} and the m_{T2}^τ, the $H_{T,sig}^{miss}$ and the $\Delta R(b_1, \ell)$ in the signal region. The requirement on the displayed distribution, as indicated by the vertical line, is not applied. The m_{T2}^τ distribution is shown for events with a hadronic τ candidate.

Figures 10.13 and 10.14 show the distributions of the variables that define the signal region, without the selection requirement on that variable applied. As can be seen, the high E_T^{miss} requirement strongly reduces the background and is the most efficient cut against the $t\bar{t} + V$ process. Together with the requirements on m_T and am_{T2}, the $t\bar{t}$ background is almost completely reduced.

The hadronic top reconstruction further reduces the single top and W+jets backgrounds, which do not include a hadronic top quark decay. The b-jet related requirements, i.e. the cut on the multiplicity and the distance to the lepton, are effective in reducing the W+jets and diboson

backgrounds. As in the VLQ search the jet p_T requirements are mostly implicitly fulfilled due to the correlations with the E_T^{miss} cut, but are made explicit and kept constant in the control and validation regions.
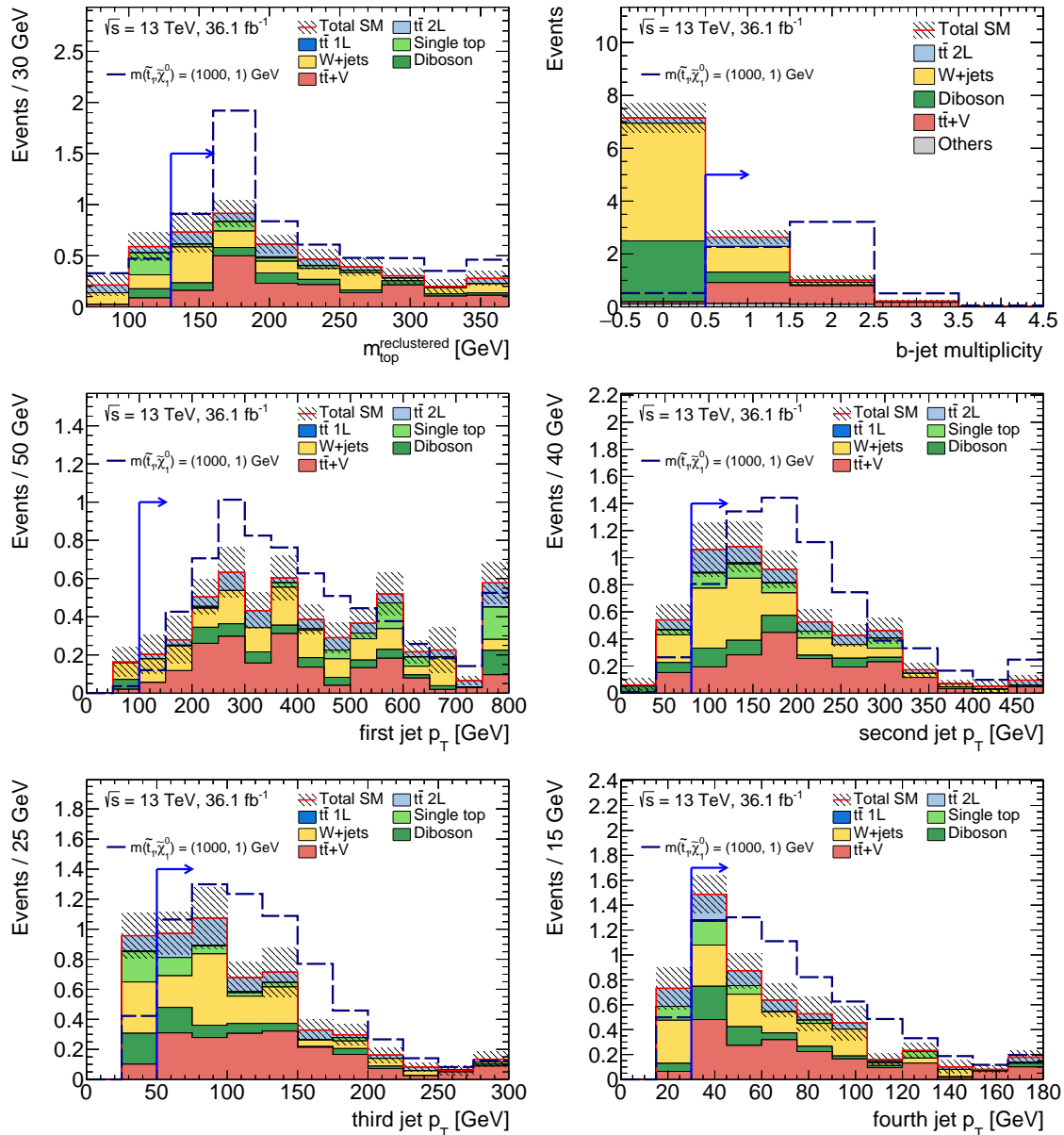
Figure 10.14: The mass of the hadronic top quark candidate, the *b*-jet multiplicity and the p_T of the leading jets in the signal region. The requirement on the displayed distribution, as indicated by the vertical line, is not applied.

10.3 Background estimation

As discussed in Section 8.1, the dominant backgrounds in the analysis are normalised in dedicated control regions. For the tN_high signal region, these are the $t\bar{t} + V$ and W+jets processes, as well as dileptonic $t\bar{t}$ events. The contributions of semi-leptonic and dileptonic $t\bar{t}$ events are treated independently in the analysis. Additionally, the single top background is also normalised in a control region. The diboson background is taken from simulation. Further processes and rare backgrounds, including Z+jets, $t\bar{t}WW$, tZ and tWZ events, contribute in total less than 0.1 events to the signal region and are therefore neglected.

In comparison to the search for vector-like quarks, the general control region selection has been redesigned. The $t\bar{t}$ background is normalised in a region defined by a veto on hadronic top candidates, in contrast to the $m_{\text{top}}^{\text{recl}} > 130$ GeV requirement in the signal region. This allows to require high m_{T} in the CR and enriching the events in dileptonic $t\bar{t}$ (T2LCR). With this selection, dileptonic $t\bar{t}$ events with an unidentified lepton can directly be normalised. This relaxes the need that the mechanisms through which a charged lepton is not identified in the reconstruction are well modelled in the simulation, as it was assumed and validated in the vector-like quark search.

The W+jets selection (WCR) is also defined with a hadronic top veto and an inverted m_{T} requirement, while keeping the b-jet multiplicity selection. With this, the analysis is unaffected by the uncertainty in the relative fraction of light and heavy flavour decays in W+jets events, as the flavour structure in the control and signal region is the same. In order to increase the purity of the selection, the charge asymmetry effect in W+jets production is exploited. Due to the higher parton density of u quarks, compared to d quarks in the proton, the production cross-section of W^++jets at the LHC is higher than for W^-+jets. This effect is enhanced by the high $E_{\text{T}}^{\text{miss}}$ requirement [162]. In general, the predominant W boson polarisation in W+jets events is left-handed. Due to the $V - A$ coupling, the lepton produced in the decay is boosted in the W boson flight direction, compared to the produced anti-lepton. By requiring high $E_{\text{T}}^{\text{miss}}$, $W^+ \to \ell^+ \nu_\ell$ events are favoured compared to

Table 10.4: Control region selection for the search for supersymmetric top quark partners. The same jet p_{T} requirements are set in each region. The veto on hadronic top candidates is fulfilled when either no candidate is found in the event, or if the mass is lower than 130 GeV.

Variable	SR	T1LCR	T2LCR	WCR	STCR
$E_{\text{T}}^{\text{miss}}$ [GeV]	> 550	> 400	> 350	> 350	> 350
m_{T} [GeV]	> 160	$\in [30, 90]$	> 120	$\in [30, 90]$	$\in [30, 120]$
am_{T2} [GeV]	> 175	< 200	< 200	> 200	> 200
m_{T2}^τ [GeV]	> 80	> 80	> 80	> 80	> 80
$H_{\text{T,sig}}^{\text{miss}}$	> 27	> 10	> 10	> 10	> 10
$|\Delta\phi(j_i, E_{\text{T}}^{\text{miss}})|, i = 1, 2$	> 0.4	> 0.4	> 0.4	> 0.4	> 0.4
# b-tagged jets	≥ 1	≥ 1	≥ 1	≥ 1	≥ 2
$\Delta R(b, \ell)$	< 2	–	–	–	–
top cand. mass	> 130 GeV	> 130 GeV	veto	veto	veto
$\Delta R(b_1, b_2)$	–	–	–	< 1.2	> 1.2
Lepton charge	–	–	–	= +1	–

Table 10.5: Background normalisation factors obtained in the simultaneous fit to all control regions.

Background	$t\bar{t}$ 2L	$t\bar{t}$ 1L	W+jets	Single top	$t\bar{t} + V$
Normalisation factor	1.01 ± 0.15	0.97 ± 0.08	0.82 ± 0.17	0.64 ± 0.37	1.11 ± 0.35

$W^- \to \ell^- \bar{\nu}_\ell$ events. To reduce the charge-symmetric contributions from other sources, a positively charged lepton is required in the WCR.

The single top control region (STCR) is defined similarly to the validation region in the search for vector-like quarks (see Section 9.4.3). In addition to the requirements of high am_{T2} and at least two b-jets with a minimal separation of $\Delta R(b_1, b_2) > 1.2$, also a veto on hadronic top candidates is used to suppress the $t\bar{t}$ contributions. The orthogonality between the STCR and the T2LCR is ensured by an inverted am_{T2} requirement in the latter region.

Due to the lowered m_T requirements in the WCR and the STCR, some contribution of semi-leptonic $t\bar{t}$ events is expected in these regions. Although it is small, mainly due to the veto on hadronic top candidates, a further control region is defined enriched in semi-leptonic $t\bar{t}$ events (T1LCR). This serves to normalise the semi-leptonic $t\bar{t}$ contributions to the other control regions, as the signal region contribution is negligible. It is defined similarly to the $t\bar{t}$ control region in the vector-like quark analysis, by inverting the m_T requirement with respect to the signal region.

Table 10.4 gives the full selection of these control regions, compared to the signal region requirements. An overview of the control regions setup is shown in Figure 10.15. The general control region strategy, building on a veto on hadronic top candidates in order to control dileptonic $t\bar{t}$ and W+heavy flavour events, is the basis for the background estimate for all signal regions in the analyses in Ref. [4] which include a hadronic top or W boson requirement.

The irreducible $t\bar{t} + Z(\to \nu\bar{\nu})$ background is estimated in a region selecting $t\bar{t} + Z(\to \ell^+\ell^-)$ events, defined in common for the analyses [4]. The control region (TTZCR) is defined requiring exactly three charged leptons, at least four jets and at least one b-tagged jet. Two leptons are required to have the same flavour and opposite charge, and the mass of the dilepton system, $m_{\ell\ell}$, is required to be in the range of $81\,\text{GeV} < m_{\ell\ell} < 101\,\text{GeV}$. The same jet p_T requirements as in the signal region are set.

The normalisation factors for the backgrounds obtained in the simultaneous fit to the control regions are shown in Table 10.5. All parameters agree with unity in the uncertainties. For the W+jets and single top processes, the best fit values are below one by 1σ. The W+jets normalisation is in agreement with the results seen in the search for vector-like top quarks. In the simultaneous fit, only the $t\bar{t} + V$ normalisation is shared between the TTZCR and the other regions. Due to the differences in the lepton multiplicity, all other contributions are treated as uncorrelated. Further details on the control regions are given in the following subsections.
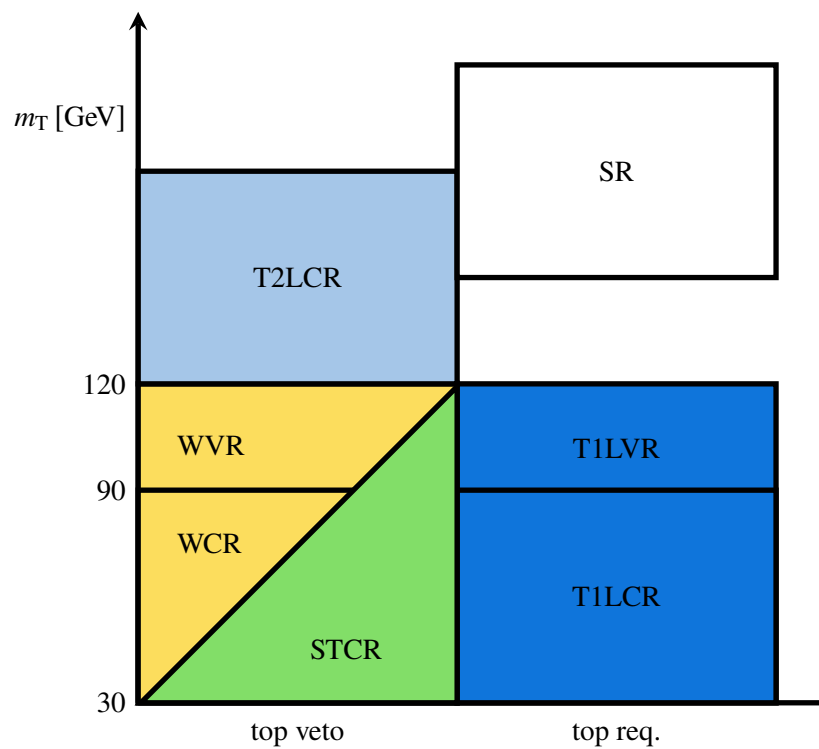
Figure 10.15: Sketch of the control region layout. The STCR and the WCR or WVR differ in the minimal *b*-jet multiplicity and the distance between the two leading *b*-jets.

10.3.1   Dileptonic $t\bar{t}$ control region

The expected and observed events in the T2LCR are shown in Table 10.6. Figure 10.16 shows the relative contributions of the SM events. The dileptonic $t\bar{t}$ process contributes more than 85% of the events, and less than 1% of the events are expected from the benchmark signal.

Figure 10.17 shows example distributions in the T2LCR after applying the normalisation factors obtained in the background only fit. Additional distributions are shown in Appendix C.1.1. The normalisation factor obtained in the fit is compatible with one and good agreement between the data and the prediction can be observed in the variables used in the analysis.

Table 10.6: Observed and expected events in the T2LCR. The individual uncertainties are correlated, and do not add up quadratically to the total uncertainty.

Region	T2LCR
Observed events	67
Total background events	67 ± 8
$t\bar{t}$ 2L events	59 ± 8
$t\bar{t}$ 1L events	2.3 ± 0.7
$t\bar{t} + V$ events	2.4 ± 0.7
W+jets events	1.25 ± 0.32
single top events	1.5 ± 1.2
diboson events	0.85 ± 0.31
MC exp. background events	67.5 ± 2.3
MC exp. $t\bar{t}$ 2L events	58.2 ± 1.8
MC exp. $t\bar{t}$ 1L events	2.4 ± 0.7
MC exp. $t\bar{t} + V$ events	2.15 ± 0.33
MC exp. W+jets events	1.52 ± 0.28
MC exp. single top events	2.4 ± 1.3
MC exp. diboson events	0.85 ± 0.31
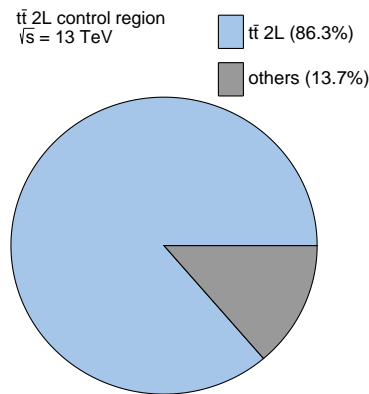
Figure 10.16: Breakdown of the individual SM contributions in the T2LCR.
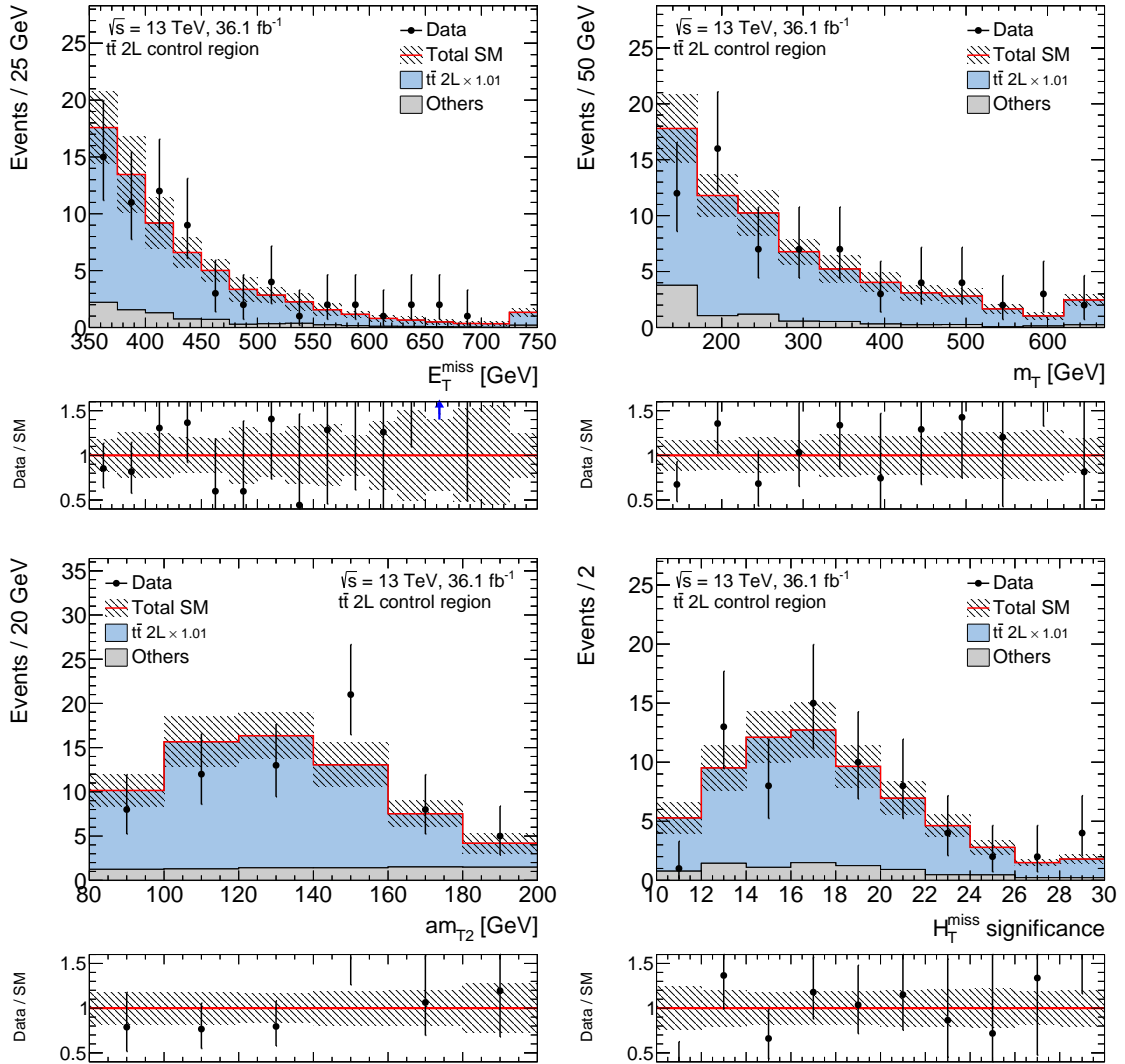
Figure 10.17: Distribution of E_T^{miss} (top left), m_T (top right), am_{T2} (bottom left) and $H_{T,sig}^{miss}$ (bottom right) in the dileptonic $t\bar{t}$ control region. The background normalisation factors are applied as indicated in the legend and the last bin contains overflow events. The lower panels show the ratio of the data to the prediction. The error bands include statistical and systematic uncertainties.

10.3.2 Semi-leptonic $t\bar{t}$ control region

Table 10.7 gives the expected events in the T1LCR, with the relative contributions visualised in Figure 10.18. In the control region, the semi-leptonic $t\bar{t}$ process makes up more than 75% of the expected events, and the contribution of the benchmark signal is below 0.1%.

Figure 10.19 shows illustrative distributions in the T1LCR after applying the normalisation factors obtained in the background only fit. Additional distributions are shown in Appendix C.1.2. Good agreement between the data and the prediction is observed, confirming the expected $t\bar{t}$ contribution in the other control regions. The normalisation factors for semi-leptonic and dileptonic $t\bar{t}$ are compatible, with a difference of less than 1σ.

Table 10.7: Observed and expected events in the T1LCR. The individual uncertainties are correlated, and do not add up quadratically to the total uncertainty.

Region	T1LCR
Observed events	411
Total background events	411 ± 20
$t\bar{t}$ 2L events	25 ± 7
$t\bar{t}$ 1L events	327 ± 25
$t\bar{t} + V$ events	5.7 ± 1.6
W+jets events	33 ± 9
single top events	15 ± 11
diboson events	5.0 ± 1.7
MC exp. background events	437 ± 18
MC exp. $t\bar{t}$ 2L events	24 ± 6
MC exp. $t\bar{t}$ 1L events	339 ± 8
MC exp. $t\bar{t} + V$ events	5.1 ± 0.8
MC exp. W+jets events	40 ± 8
MC exp. single top events	24 ± 11
MC exp. diboson events	4.9 ± 1.7
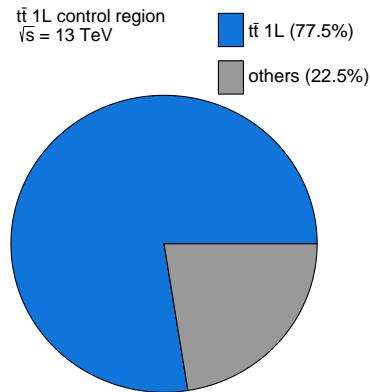
Figure 10.18: Breakdown of the individual SM contributions in the T1LCR.
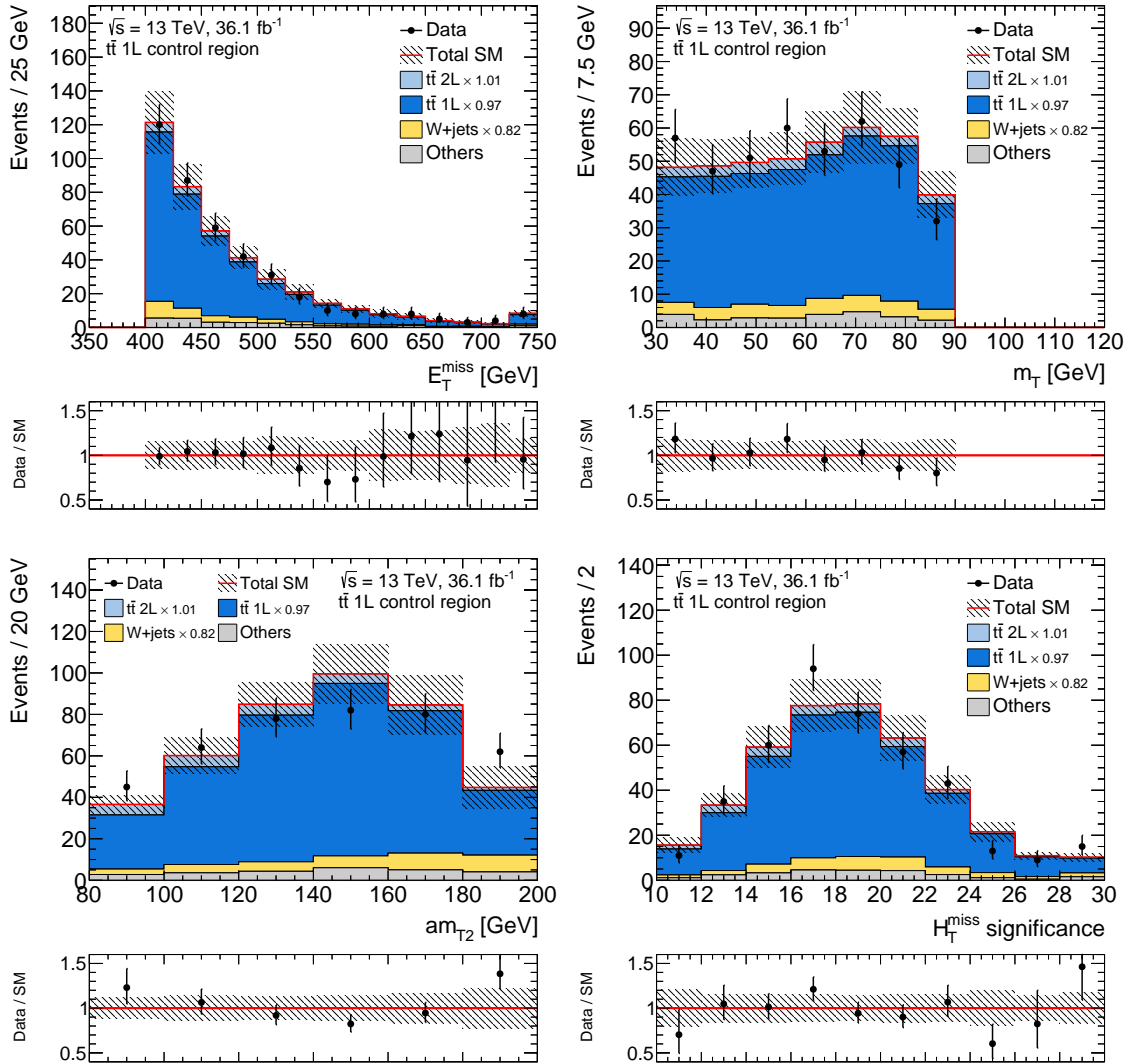
Figure 10.19: Distribution of E_T^{miss} (top left), m_T (top right), am_{T2} (bottom left) and $H_{T,sig}^{miss}$ (bottom right) in the semi-leptonic $t\bar{t}$ control region. The background normalisation factors are applied as indicated in the legend and the last bin contains overflow events. The lower panels show the ratio of the data to the prediction. The error bands include statistical and systematic uncertainties.

10.3.3   *W*+jets control region

The expected and observed events in the *W*+jets control region are shown in Table 10.8, and the relative contributions in Figure 10.20. The *W*+jets fraction is 68%, and less than 0.1% signal contribution is expected.

   The normalisation factor for *W*+jets is determined to 0.82 ± 0.17. While this is compatible with the prediction in the uncertainties, a similar downwards trend is observed as seen in other signal regions of the same publication, and in the search for vector-like quarks. In contrast to the *W*+jets control region in the search for vector-like top quarks, here at least one *b*-jet is required. The composition of heavy and light flavour jets in the control and signal region is the same, as shown in Figure 10.21.

   A comparison of data and simulation is shown in Figure 10.22 for some illustrative distributions, showing no significant deviations. Additional distributions are shown in Appendix C.1.3.

Table 10.8: Observed and expected events in the WCR. The individual uncertainties are correlated, and do not add up quadratically to the total uncertainty.

Region	WCR
Observed events	113
Total background events	113 ± 11
$t\bar{t}$ 2L events	2.6 ± 0.7
$t\bar{t}$ 1L events	18 ± 5
$t\bar{t} + V$ events	0.67 ± 0.33
W+jets events	76 ± 14
single top events	10 ± 7
diboson events	5.9 ± 1.7
MC exp. background events	136 ± 13
MC exp. $t\bar{t}$ 2L events	2.6 ± 0.6
MC exp. $t\bar{t}$ 1L events	19 ± 5
MC exp. $t\bar{t} + V$ events	0.60 ± 0.15
MC exp. *W*+jets events	92 ± 10
MC exp. single top events	16 ± 5
MC exp. diboson events	5.9 ± 1.7
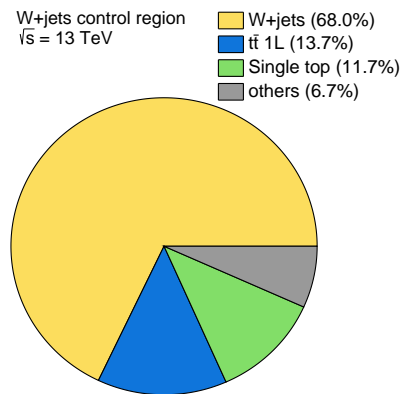
Figure 10.20: Breakdown of the individual SM contributions in the WCR.
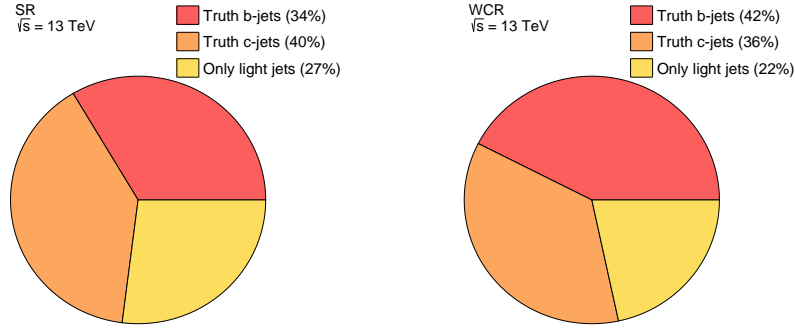
Figure 10.21: Breakdown of the flavour components of W+jets in the SR and the WCR.
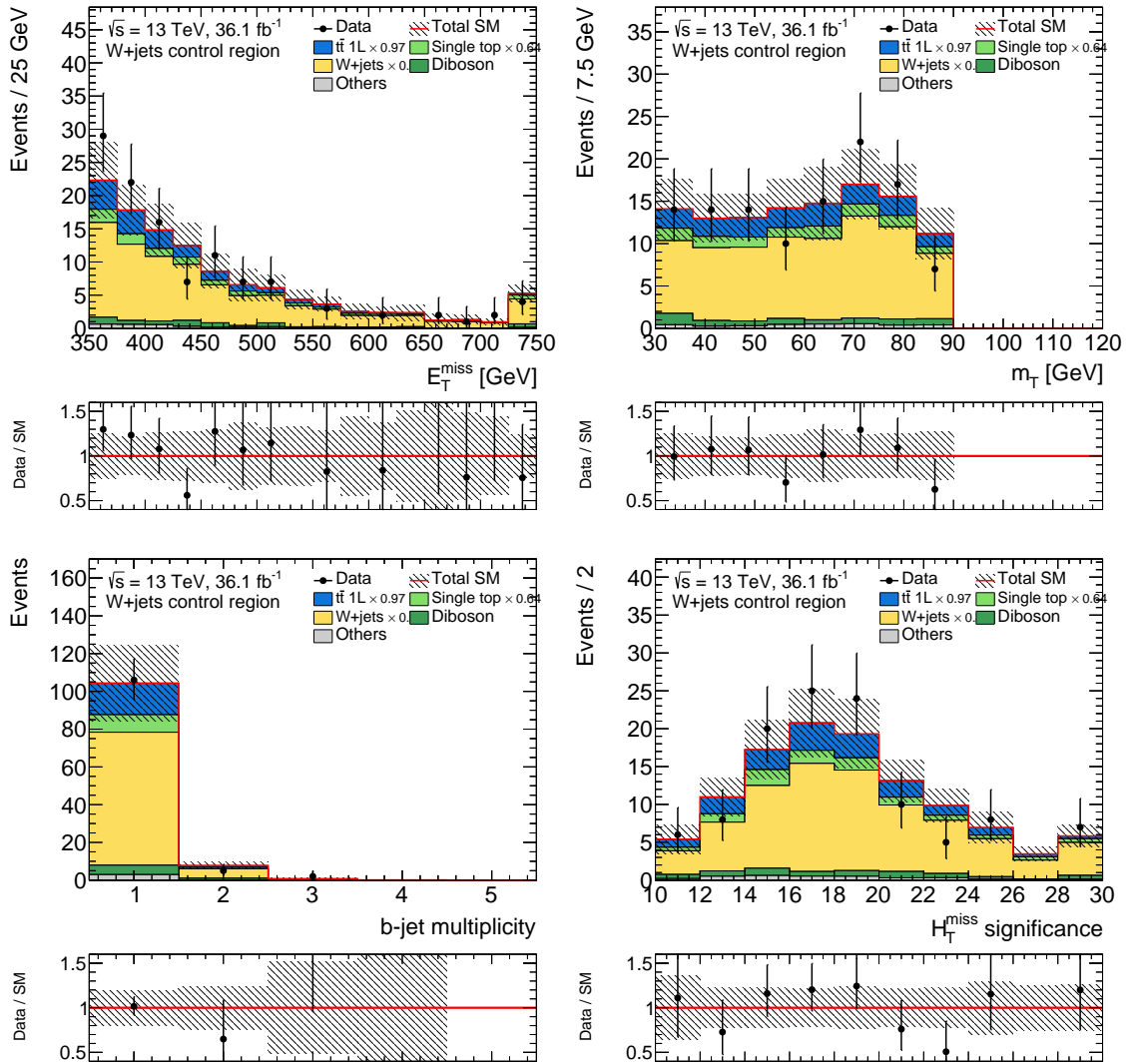
Figure 10.22: Distribution of E_T^{miss} (top left), m_T (top right), b-jet multiplicity (bottom left) and $H_{T,sig}^{miss}$ (bottom right) in the W+jets control region. The background normalisation factors are applied as indicated in the legend and the last bin contains overflow events. The lower panels show the ratio of the data to the prediction. The error bands include statistical and systematic uncertainties.

10.3.4 Single top control region

Table 10.9 shows the expected and observed events in the single top control region and the relative contributions are shown in Figure 10.23. The purity of the single top process reaches 45%, and less than 0.1% signal contribution is expected. In comparison to the single top validation region in the search for vector-like quarks (see Section 9.4.3), the single top purity is enhanced and the semi-leptonic $t\bar{t}$ contributions are reduced, due to the veto on hadronic top quarks.

Figure 10.24 shows a comparison of data and simulation with the normalisation applied. Good agreement between data and prediction can be observed. Additional distributions are shown in Appendix C.1.4. Even though the nominal normalisation factor is smaller than one, it is compatible with the prediction in the uncertainties.

Table 10.9: Observed and expected events in the STCR. The individual uncertainties are correlated, and do not add up quadratically to the total uncertainty.

Region	STCR
Observed events	40
Total background events	40 ± 6
$t\bar{t}$ 2L events	1.7 ± 0.5
$t\bar{t}$ 1L events	11.0 ± 3.1
$t\bar{t} + V$ events	0.49 ± 0.23
W+jets events	11.1 ± 2.5
single top events	15 ± 8
diboson events	0.72 ± 0.25
MC exp. background events	51 ± 6
MC exp. $t\bar{t}$ 2L events	1.7 ± 0.4
MC exp. $t\bar{t}$ 1L events	11.4 ± 2.9
MC exp. $t\bar{t} + V$ events	0.44 ± 0.15
MC exp. W+jets events	13.5 ± 2.6
MC exp. single top events	23.3 ± 1.9
MC exp. diboson events	0.72 ± 0.25

single top control region
$\sqrt{s}$ = 13 TeV
- Single top (45.6%)
- W+jets (26.5%)
- t$\bar{t}$ 1L (22.3%)
- others (5.6%)
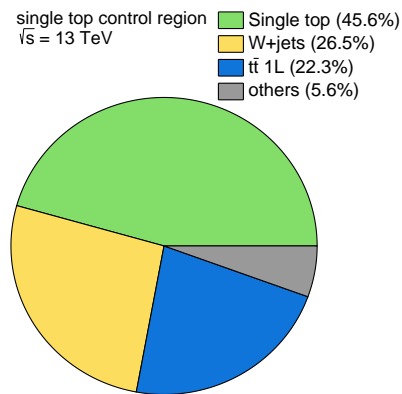
Figure 10.23: Breakdown of the individual SM contributions in the STCR.
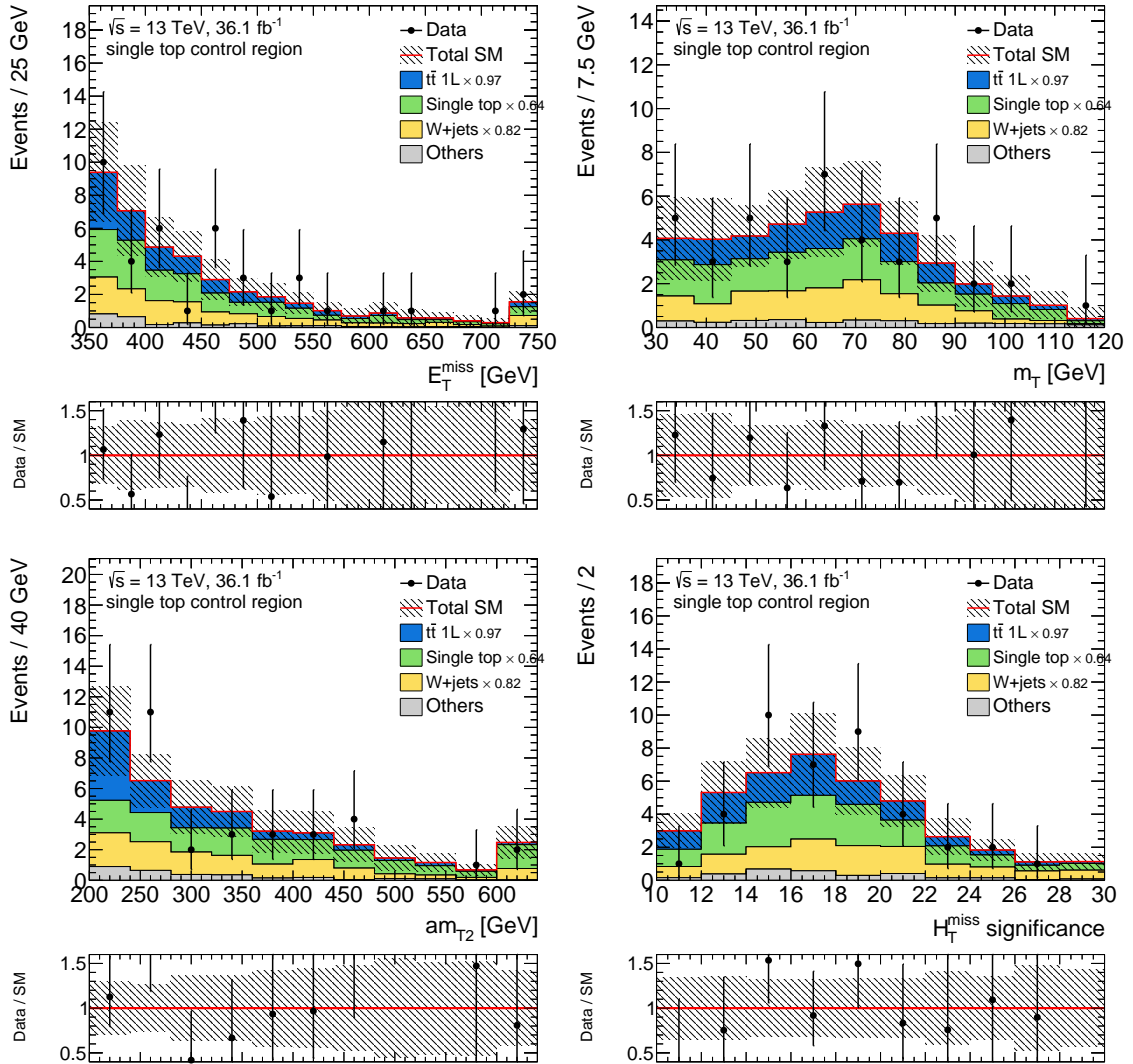
Figure 10.24: Distribution of $E_\mathrm{T}^\mathrm{miss}$ (top left), m_T (top right), am_T2 (bottom left) and $H_\mathrm{T,sig}^\mathrm{miss}$ (bottom right) in the single top control region. The background normalisation factors are applied as indicated in the legend and the last bin contains overflow events. The lower panels show the ratio of the data to the prediction. The error bands include statistical and systematic uncertainties.

10.3.5 $t\bar{t} + Z$ **control region**

The $t\bar{t} + Z$ control region is defined targeting $t\bar{t} + Z(\to \ell\ell)$ events. Figure 10.25 shows the $m_{\ell\ell}$ distribution in the control region. As can be seen, at the Z peak the dominant contribution comes from $t\bar{t} + V$ events, with diboson production being the next dominant process. A common normalisation factor of 80% was determined for the diboson process in all TTZCRs by inverting the b-jet requirement to a b-jet veto, leading to a diboson purity of more than 85%. Figure 10.25 shows the b-jet multiplicity with the normalisation factor applied.

Table 10.10 shows the expected and observed events in the TTZCR. The purity of the $t\bar{t} + V$ process is more than 65% (see Figure 10.26), and a normalisation factor of 1.11 ± 0.35 is determined.

Figure 10.27 shows the Z boson p_{T} and the equivalent $E_{\mathrm{T}}^{\mathrm{miss}}$, when treating the $Z \to \ell\ell$ decay as invisible and recalculating the $E_{\mathrm{T}}^{\mathrm{miss}}$ accordingly. This shows that the relevant features of the $t\bar{t} + V$ process are well modelled. The results of the TTZCR have been validated in a region selecting $t\bar{t} + \gamma$ events, and effectively treating the photon as an invisible particle [4].
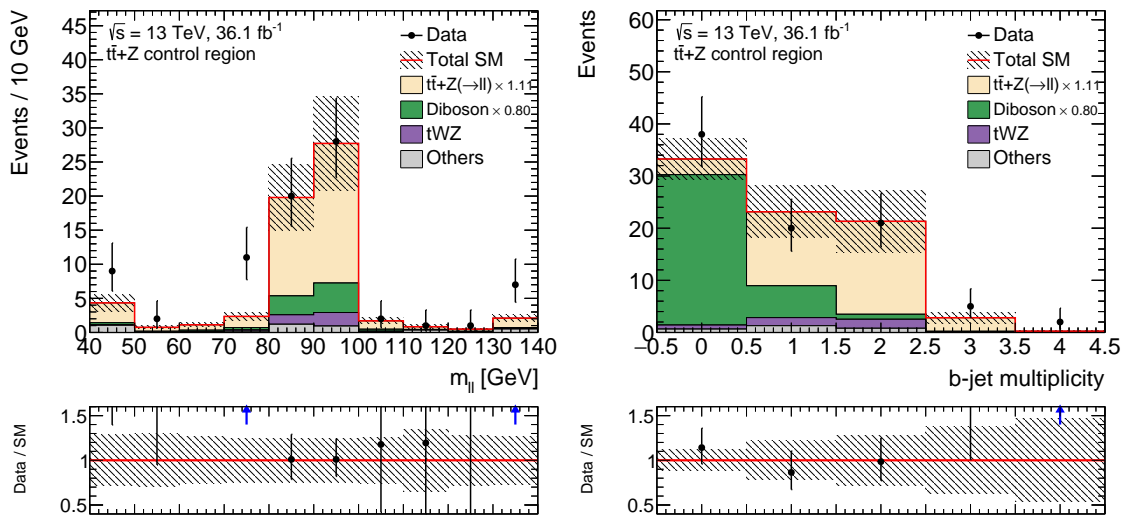
Figure 10.25: Distribution of the $m_{\ell\ell}$ (left) and the b-jet multiplicity in the $t\bar{t} + Z(\to \ell\ell)$ control region, without the requirement on the displayed variable. The $t\bar{t} + V$ and diboson normalisation factors are applied as indicated in the legend. The lower panels show the ratio of the data to the prediction. The errors bands include statistical and systematic uncertainties.

Table 10.10: Observed and expected events in the TTZCR. The individual uncertainties are correlated, and do not add up quadratically to the total uncertainty.

Region	**TTZCR**
Observed events	48
Total background events	48 ± 7
$t\bar{t} + V$ events	35 ± 11
diboson events	7.1 ± 1.1
tWZ events	3^{+6}_{-3}
tZ events	$1.3^{+2.3}_{-1.3}$
$t\bar{t}$ 2L events	0.59 ± 0.25
Z+jets events	0.142 ± 0.022
MC exp. background events	44 ± 9
MC exp. $t\bar{t} + V$ events	32.2 ± 2.2
MC exp. diboson events	7.1 ± 1.1
MC exp. tWZ events	3^{+6}_{-3}
MC exp. tZ events	$1.3^{+2.3}_{-1.3}$
MC exp. $t\bar{t}$ 2L events	0.59 ± 0.25
MC exp. Z+jets events	0.142 ± 0.021
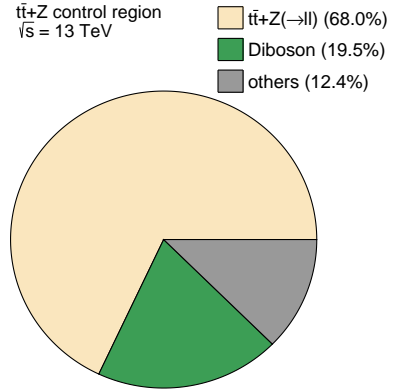
Figure 10.26: Breakdown of the individual SM contributions in the TTZCR.
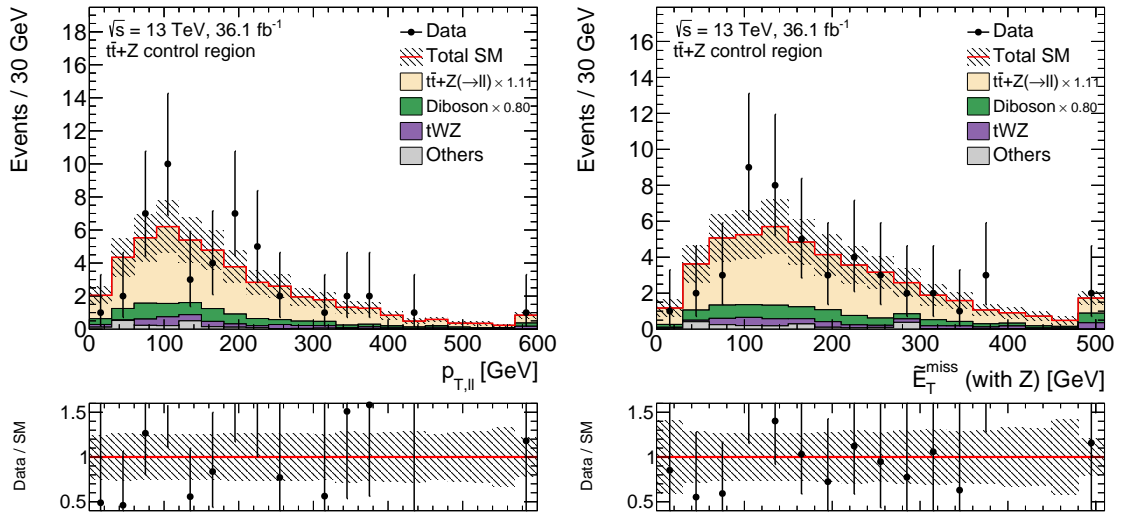
Figure 10.27: Distribution of $p_{T,\ell\ell}$ (left) and the recalculated E_T^{miss} including the Z boson (right) in the $t\bar{t} + Z$ control region. The background normalisation factors are applied as indicated in the legend and the last bin contains overflow events. The lower panels show the ratio of the data to the prediction. The error bands include statistical and systematic uncertainties.

10.4 Background validation

The background estimates are tested using validation regions. The background normalisation factors which are determined in the CRs are applied in the VRs and the predicted yields are compared with the data. Validation regions are defined for the dileptonic and semi-leptonic $t\bar{t}$ background (T2LVR, T1LVR) and for W+jets events (WVR). No single top validation region is defined, as the background is small in the signal region. The $t\bar{t} + V$ normalisation is tested in a $t\bar{t} + \gamma$ selection, as described in Section 10.3.5.

The dileptonic $t\bar{t}$ control region is defined by a veto on hadronic top candidates. In order to test the extrapolation to the signal region, in which a top candidate is required, the same requirement as in the SR is set in the T2LVR. To make the selection disjoint to the SR, and in order to reduce the signal contamination, a requirement of $am_{\mathrm{T2}} < 130\,\mathrm{GeV}$ is used. Due to this and the high m_{T} requirement the dileptonic $t\bar{t}$ is the dominant process in the T2LVR, even though a hadronic top candidate is required. The validation regions for semi-leptonic $t\bar{t}$ and W+jets events are defined by changing the m_{T} requirement. The full selection of the validation regions is listed in Table 10.11.

Figure 10.28 shows the composition of the expected events in the validation regions. The purity of the targeted processes is comparable to that achieved in the respective control regions. The observed events are compared in Table 10.12 with the expected events, including the normalisation obtained in the simultaneous fit to the control regions. The two $t\bar{t}$ validation regions show good agreement of observed and expected events. In the WVR, more events are observed than expected. The significance of the deviation, calculated as the difference in expected and observed events divided by the total uncertainty, is below 1.5σ.

Figure 10.29 shows distributions in the validation regions, after applying the normalisation factors. Additional distributions are shown in Appendix C.2.1, C.2.2 and C.2.3. No significant deviations are found and a good agreement of data and simulation can be observed.

Table 10.11: Validation region selection for the search for supersymmetric top quark partners. The same jet p_{T} requirements are set in each region. The veto on hadronic top candidates is fulfilled when either no candidate is found in the event, or if the mass is lower than $130\,\mathrm{GeV}$.

Variable	SR	T1LVR	T2LVR	WVR
$E_{\mathrm{T}}^{\mathrm{miss}}$	$> 550\,\mathrm{GeV}$	$> 400\,\mathrm{GeV}$	$> 350\,\mathrm{GeV}$	$> 350\,\mathrm{GeV}$
m_{T}	$> 160\,\mathrm{GeV}$	$\in [90, 120]\,\mathrm{GeV}$	$> 120\,\mathrm{GeV}$	$\in [90, 120]\,\mathrm{GeV}$
am_{T2}	$> 175\,\mathrm{GeV}$	$< 200\,\mathrm{GeV}$	$< 130\,\mathrm{GeV}$	$> 200\,\mathrm{GeV}$
m_{T2}^{τ}	$> 80\,\mathrm{GeV}$	$> 80\,\mathrm{GeV}$	$> 80\,\mathrm{GeV}$	$> 80\,\mathrm{GeV}$
$H_{\mathrm{T,sig}}^{\mathrm{miss}}$	> 27	> 10	> 10	> 10
$|\Delta\phi(j_i, E_{\mathrm{T}}^{\mathrm{miss}})|, i = 1, 2$	> 0.4	> 0.4	> 0.4	> 0.4
# b-tagged jets	≥ 1	≥ 1	≥ 1	≥ 1
$\Delta R(b, \ell)$	< 2	–	–	–
top cand. mass	$> 130\,\mathrm{GeV}$	$> 130\,\mathrm{GeV}$	$> 130\,\mathrm{GeV}$	veto
$\Delta R(b_1, b_2)$	–	–	–	< 1.2
Lepton charge	–	–	–	$= +1$
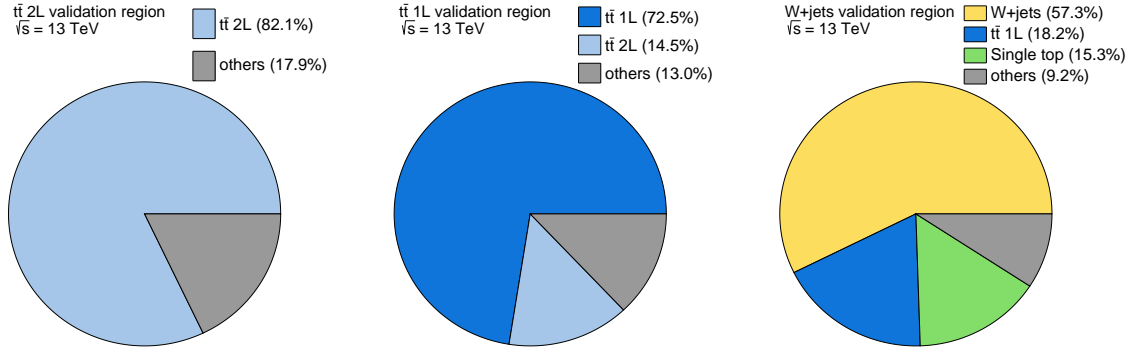
Figure 10.28: Breakdown of the individual SM contributions in the T2LVR (left), the T1LVR (middle) and the WVR (right).

Table 10.12: Observed and expected events in the validation regions. The individual uncertainties are correlated, and do not add up quadratically to the total uncertainty.

Region	T2LVR	T1LVR	WVR
Observed events	37	87	20
Total background events	38 ± 7	91 ± 22	13.1 ± 1.8
$t\bar{t}$ 2L events	31 ± 7	14 ± 4	0.77 ± 0.31
$t\bar{t}$ 1L events	2.1 ± 0.9	67 ± 21	2.7 ± 1.0
$t\bar{t} + V$ events	1.7 ± 0.5	1.9 ± 0.5	0.10 ± 0.05
W+jets events	1.2 ± 0.6	5.2 ± 1.7	7.3 ± 1.7
single top events	0.8 ± 0.7	2.5 ± 2.2	1.5 ± 1.1
diboson events	0.40 ± 0.14	0.5 ± 0.5	0.59 ± 0.23
MC exp. background events	38 ± 6	96 ± 23	15.6 ± 2.4
MC exp. $t\bar{t}$ 2L events	31 ± 6	14 ± 4	0.76 ± 0.29
MC exp. $t\bar{t}$ 1L events	2.2 ± 0.9	70 ± 21	2.8 ± 1.0
MC exp. $t\bar{t} + V$ events	1.49 ± 0.18	1.67 ± 0.22	0.09 ± 0.04
MC exp. W+jets events	1.5 ± 0.7	6.3 ± 1.7	8.9 ± 1.5
MC exp. single top events	1.3 ± 0.8	3.9 ± 2.5	2.4 ± 0.9
MC exp. diboson events	0.40 ± 0.15	0.5 ± 0.5	0.58 ± 0.24
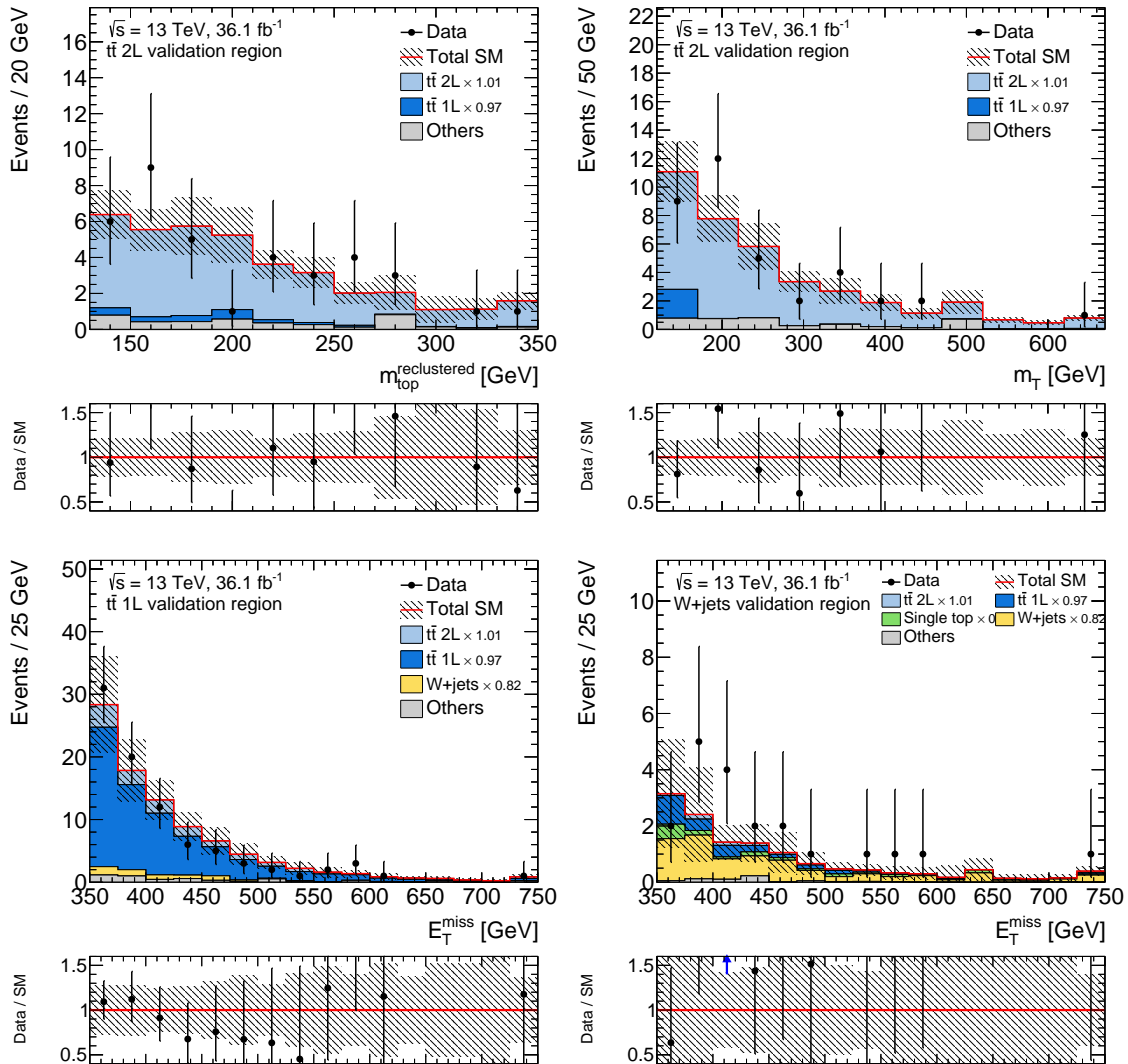
Figure 10.29: Distribution of the hadronic top mass (top left) and the m_T (top right) in the dileptonic $t\bar{t}$ VR, the E_T^{miss} (bottom left) in the semi-leptonic $t\bar{t}$ VR and the E_T^{miss} (bottom right) in the W+jets VR. The background normalisation factors are applied as indicated in the legend and the last bin contains overflow events. The lower panels show the ratio of the data to the prediction. The error bands include statistical and systematic uncertainties.

10.5   Impact of systematic uncertainties

The sources of systematic uncertainties affecting the analysis are detailed in Section 8.6. In comparison to the search for vector-like quarks, no uncertainty in the W+jets heavy flavour fraction affects the analysis, as the W+jets background is normalised in a control region with a requirement of at least one b-jet. The effect of the jet mass scale and resolution uncertainties was found to be negligible, as the hadronic top quark candidates contain more than one constituent in more than 95% of the cases.

In order to reduce the impact of the statistical uncertainty in the estimate of the background modelling uncertainties, a different approach for the evaluation was chosen compared to the vector-like quarks search. Starting with the preselection, the uncertainty is evaluated when only adding the requirement on one variable. This is repeated for all requirements forming a region and the systematic uncertainty is estimated as the quadratic sum of the effects on each individual variable. As the statistical precision is much better, the statistical uncertainty is not added to the estimate. This approach neglects any correlation between the variables, but was found to yield estimates comparable to using the full selection [2]. As discussed in Section 8.6, the uncertainties in the backgrounds that are normalised in control regions result from the relative difference of each systematic source in the SR to the respective CR. The semi-leptonic and dileptonic $t\bar{t}$ uncertainties are treated as fully uncorrelated. The former process is affected by uncertainties that change the m_T distribution, such as fragmentation effects or the jet energy resolution. In contrast, dileptonic $t\bar{t}$ events only enter the analysis when one charged lepton is not identified, and is therefore susceptible to effects that change the lepton kinematics.

The leading systematic uncertainties in the total background prediction are listed in Table 10.13. The dominant systematic effects are due to the modelling and the normalisation of the $t\bar{t} + V$ background, as this is the dominant background in the signal region. The leading experimental uncertainty is in the jet energy scale calibration, which also effects the hadronic top quark reconstruction. In general, the systematic uncertainties are smaller than the statistical uncertainty.

Table 10.13: Breakdown of the leading systematic uncertainties in the total background prediction in the signal region. The statistical precision is included in the uncertainties derived from the comparison of MC samples. The individual uncertainties are correlated, and do not necessarily add in quadrature to the total background uncertainty. Only uncertainties larger than 1% of the total background prediction are shown.

Uncertainty	**tN_high**
Total background expectation	3.82
Total statistical ($\sqrt{N_{\text{exp}}}$)	±1.95
Total background uncertainty	±1.00 [26.2%]
$t\bar{t} + V$ modelling	±0.69 [18.0%]
$\mu_{t\bar{t}+V}$	±0.59 [15.4%]
MC stat. (nominal samples)	±0.30 [7.8%]
Jet energy scale (1st component)	±0.23 [6.1%]
$\mu_{W+\text{jets}}$	±0.18 [4.8%]
Flavour-tagging c-jet mistag rate	±0.18 [4.8%]
$t\bar{t}$ MC generator	±0.10 [2.6%]
Jet energy resolution	±0.09 [2.5%]
Diboson cross section	±0.09 [2.3%]
Flavour-tagging light-jet mistag rate	±0.09 [2.3%]
$t\bar{t}$ radiation	±0.08 [2.1%]
$t\bar{t}$ fragmentation	±0.08 [2.1%]
Diboson modelling	±0.08 [2.1%]
$\mu_{t\bar{t}\,2\text{L}}$	±0.07 [1.9%]
$\mu_{\text{single top}}$	±0.07 [1.9%]
W+jets modeling	±0.06 [1.7%]
Flavour-tagging b-tagging efficiency	±0.05 [1.2%]
Single top radiation	±0.04 [1.0%]
$t\bar{t}$ single top interference	±0.04 [1.0%]
Jet energy scale (2nd component)	±0.04 [1.0%]

10.6 Results

The observed and expected number of events are summarised in Table 10.14. The agreement of the observed data and the expected events in the VRs and the SR is also visualised in Figure 10.30. No significant excess above the SM expectation is found in the signal region, with 8 observed and 3.8 ± 1.0 expected events. The compatibility of the background only prediction with the observed number of events corresponds to $p_0 = 0.05$ (1.6σ). The distributions of the E_T^{miss} and the hadronic top candidate mass in the signal region are shown in Figure 10.31. In general, the data follows the distribution of the SM prediction.

Table 10.14: Number of events observed in the signal region, together with the estimated SM backgrounds. The normalisation factors determined in the simultaneous fit are applied. The uncertainties include all statistical and systematic sources. The individual uncertainties are correlated, and do not necessarily add in quadrature to the total background uncertainty.

Region	tN_high
Observed events	8
Total background events	3.8 ± 1.0
$t\bar{t}$ 2L events	0.5 ± 0.2
$t\bar{t}$ 1L events	0.0 ± 0.0
$t\bar{t} + V$ events	1.9 ± 0.9
W+jets events	0.9 ± 0.2
single top events	0.1 ± 0.1
diboson events	0.4 ± 0.2
MC exp. background events	3.9
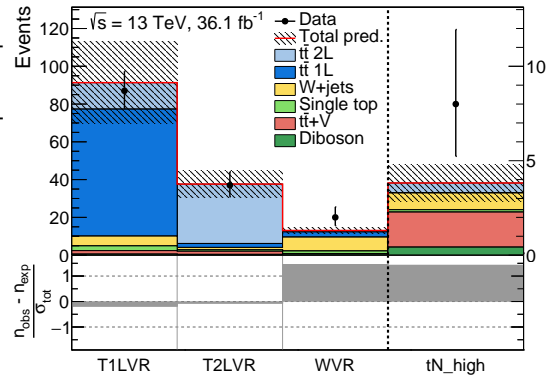
Figure 10.30: Comparison of the observed data (n_{obs}) with the predicted background (n_{exp}) in the VRs and the SR. The bottom panel shows the significance of the difference between data and predicted background, where the significance is based on the total uncertainty (σ_{tot}).

As no significant deviation of the SM prediction is found, limits on the direct top squark pair production are derived following the procedure outlined in Section 8.8. The observed upper limit on any non-SM events in the signal region is $N_{non-SM} < 10$, with an expected limit of 5.8 events.

Figure 10.32 shows the observed and expected exclusion contour in the $m_{\tilde{t}_1}$, $m_{\tilde{\chi}_1^0}$ plane. The $\pm 1\sigma_{exp}$ uncertainty band shows the impact of the systematic and statistical uncertainties on the expected limits. The $\pm 1\sigma_{th}$ uncertainty lines illustrate the change in the observed limit when scaling the signal cross-section by its theoretical uncertainty. Top squark masses below $900\,\text{GeV}$ can be excluded for scenarios with neutralino masses below $100\,\text{GeV}$ and $\mathcal{B}(\tilde{t}_1 \to t\tilde{\chi}_1^0) = 100\%$. Due to the slight excess of events in the signal region, the observed exclusion is lower than the expected sensitivity, which reaches top squark masses of above $1\,\text{TeV}$ for neutralino masses below $300\,\text{GeV}$. Figure 10.32 also shows the observed upper limit on the signal cross-section.
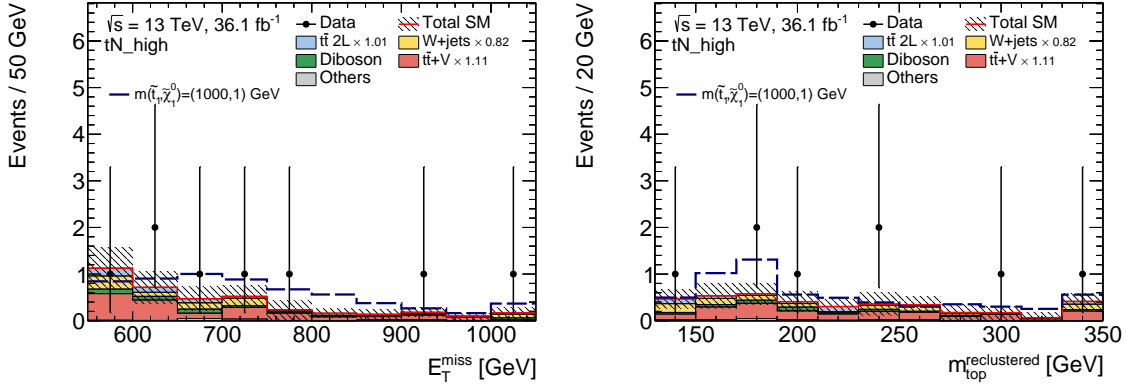
Figure 10.31: Comparison of data and prediction in the E_T^{miss} (left) and the m_{top}^{recl} (right) distribution in the SR. The error bands include statistical and systematic uncertainties. The expected shape for a signal with $m(\tilde{t}_1, \tilde{\chi}_1^0) = (1000, 1)\,$GeV is overlaid on the SM prediction.
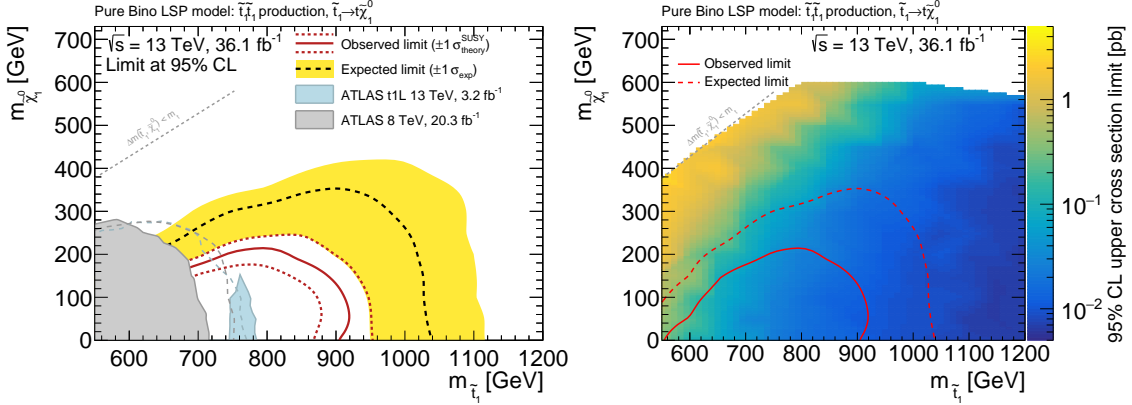
Figure 10.32: Expected and observed 95% CL excluded region (left) and upper cross-section limit (right) in the plane of $m_{\tilde{t}_1}$ versus $m_{\tilde{\chi}_1^0}$ for direct top squark pair production assuming a $\tilde{t}_1 \rightarrow t\tilde{\chi}_1^0$ decay with 100% branching ratio. The excluded regions from previous publications [2, 61] are shown with grey and blue shaded areas.

10.7 Comparison to similar searches

Direct top squark pair production is searched for also in other analyses at ATLAS and CMS. For comparison, the results of the ATLAS search in fully hadronic events [163] and the CMS search in the one lepton channel [164] are compared to the results presented here, focusing on the reach to high top squark masses. Figure 10.33 shows the 95% exclusion contours in the $m_{\tilde{t}_1}$ versus $m_{\tilde{\chi}_1^0}$ plane. The sensitivity of all three searches is very similar, resulting in an expected limit of $m_{\tilde{t}_1} \simeq 1$ TeV.

The fully hadronic search employs a similar strategy to the analysis discussed here. Several, overlapping signal regions are defined of which one (SRA) is optimised for the same benchmark signal as for tN_high. In contrast to tN_high, the SRA region is further split into three categories, according to the reconstruction quality of the second, hadronically decaying top quark. While the exact selection depends on the category, in general SRA has similar requirements on the E_T^{miss} and other kinematic variables as tN_high.
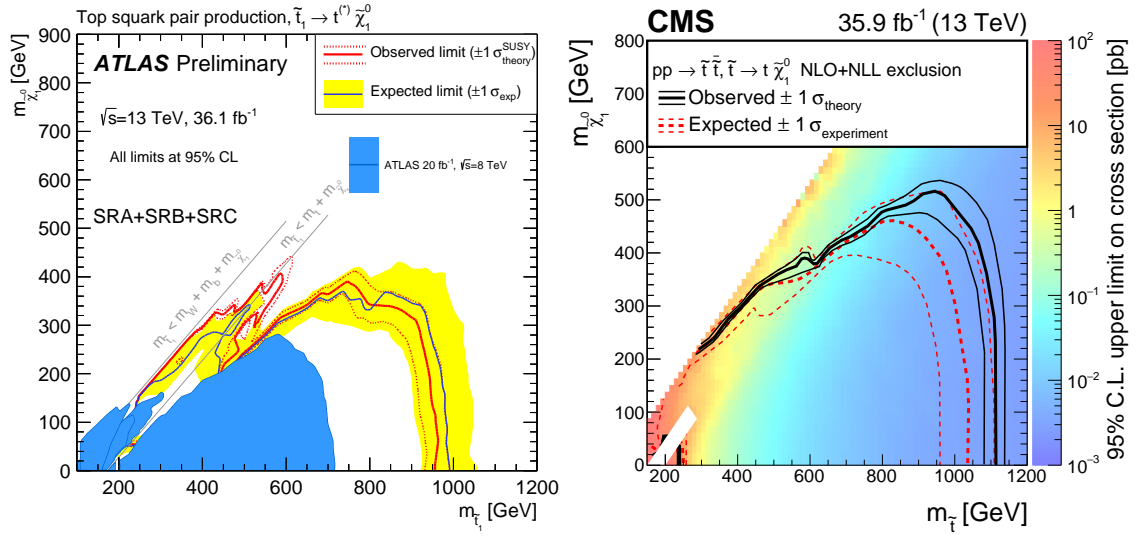
Figure 10.33: Expected and observed 95% CL excluded region in the plane of $m_{\tilde{t}_1}$ versus $m_{\tilde{\chi}_1^0}$ for direct top squark pair production assuming a $\tilde{t}_1 \to t\tilde{\chi}_1^0$ decay with 100% branching ratio for the ATLAS direct stop search in the fully hadronic channel [163] (left) and the CMS search in the 1 lepton channel [164] (right).

In the CMS analysis, 27 disjoint signal regions are defined by requirements on the jet multiplicity, the E_T^{miss}, the invariant mass of the required b-jet and the lepton, as well as the t_{mod} variable, which is the quality of a kinematic fit under the assumption of a dileptonic $t\bar{t}$ event in which one lepton is not reconstructed. While all signal regions are combined for the exclusion limits, the largest sensitivity to signals with large $m_{\tilde{t}_1}$ is found in bins with high E_T^{miss} and high t_{mod} requirements. The reach towards high $m_{\tilde{t}_1}$ is similar to the analysis presented here. In addition, the strategy employed by the CMS search enabled sensitivity towards higher neutralino masses.

10.8   Combination with a soft-lepton selection

The tN_high signal region is optimised for the $\tilde{t}_1 \rightarrow t\tilde{\chi}_1^0$ decay in a simplified model with a branching ratio of 100%. As discussed in Chapter 3, the neutralino in such models mainly consists of the bino. As discussed in Section 3.3.2 and 3.3.3, other scenarios with a high branching ratio for $\tilde{t}_1 \rightarrow t\tilde{\chi}_1^0$ exist, where the LSP is either a higgsino, or with a higgsino close in mass to the bino LSP. In such models the mass splitting between the lightest neutralinos and the lightest chargino is small and the decays $\tilde{t}_1 \rightarrow t\tilde{\chi}_2^0, \tilde{t}_1 \rightarrow b\tilde{\chi}_1^\pm$ and $\tilde{t}_1 \rightarrow t\tilde{\chi}_1^0$ are possible. The $\tilde{\chi}_1^\pm$ and $\tilde{\chi}_2^0$ further decay via the emission of an off-shell W, Z or Higgs boson into the LSP. The signatures of these decays are characterised by low-momentum ("soft") objects, which in the case of charged leptons can be reconstructed and used to reduce the background. In contrast to this, the minimal charged lepton p_T requirement of tN_high is 25 GeV, referred to as "hard" leptons. For the $t\tilde{\chi}_1^0$ decay, and for $t\tilde{\chi}_2^0$ with a hadronic decay of the Z or Higgs boson in $\tilde{\chi}_2^0 \rightarrow Z/H\tilde{\chi}_1^0$, or when $Z \rightarrow \nu\bar{\nu}$, the signatures of the alternative signal models resemble the simplified model targeted by the tN_high region.

The branching fractions of the different decay modes depend on the composition of the top squark. For top squarks mainly composed of $\tilde{t}_R$, the decay into $b\tilde{\chi}_1^\pm$ is dominant in the higgsino LSP model, while for high $\tilde{t}_L$ contents the $t\tilde{\chi}_2^0$ and $t\tilde{\chi}_1^0$ decay modes are more important. The $\tan\beta$ parameter also influences the branching fractions, with higher values leading to a higher branching ratio for the $b\tilde{\chi}_1^\pm$ decay.

In Ref. [4], where this analysis is a part of, three signal regions are optimised for the higgsino LSP scenario, targeting final states with a soft lepton: bCsoft_diag, bCsoft_med and bCsoft_high[1]. These regions require exactly one lepton with a minimal p_T of 4 GeV for muons and 5 GeV for electrons, respectively, in addition to high E_T^{miss} and high p_T^W. In order to keep the sensitivity to the $t\tilde{\chi}_1^0/\tilde{\chi}_2^0$ decays, the regions are later statistically combined with the tN_med region, which is similar to tN_high but optimised for intermediate top squark masses.

The results are also interpreted in the well-tempered neutralino model, in which the higgsino and the bino LSP are close in mass. Here, two cases are considered, in which the lightest top squark is either mostly left-handed or mostly right-handed. In the former case, the model also includes light bottom squarks, as discussed in Section 3.3.3.

The details of the combination are explained here on the basis of an additional combination of the bCsoft_high region with tN_high.

10.8.1   Soft-lepton signal region

The bCsoft_high signal region is optimised for high top squark masses, which makes it an ideal candidate for the combination with tN_high. In the target decay of $\tilde{t}_1 \rightarrow b\tilde{\chi}_1^\pm$ the $\tilde{\chi}_1^\pm$ is boosted due to the large mass difference between the top squark and the charged higgsino. The event signature is characterised by two high-p_T b-jets, large E_T^{miss} and a soft lepton. Table 10.15 lists the selection for the bCsoft_high signal region. The transverse momentum of the leptonically decaying W boson is calculated to $\vec{p}_T^W = \vec{p}_T^\ell + \vec{E}_T^{miss}$. As the W boson in the $\tilde{\chi}_1^\pm \rightarrow W\tilde{\chi}_1^0$ decay is highly off-shell, the bCsoft signal regions require low m_T. With the cut of $m_T < 160$ GeV, the bCsoft_high region is orthogonal to the tN_high region, where $m_T > 160$ GeV is required.

The targeted signal is characterised by low-p_T leptons and large E_T^{miss}, while the SM backgrounds are dominated by events with leptonic W boson decays. This makes the p_T^ℓ/E_T^{miss} a strong

---

[1]The names indicate the target of the $b\tilde{\chi}_1^\pm$ decay (bC) and the top squark mass range between low $\Delta m(\tilde{t}_1, \tilde{\chi}_1^\pm)$ (diag) and medium to high masses.

Table 10.15: Signal region selection for the bCsoft_high SR [4]. The jet p_T requirements refer to the objects ordered in p_T.

Variable	bCsoft_high
Lepton p_T	$> 5, 4\,\text{GeV for } e, \mu$
Number of jets, b-jets	$\geq 2, \geq 2$
Jet p_T	$> 100, 100\,\text{GeV}$
b-jet p_T	$> 100, 100\,\text{GeV}$
E_T^{miss}	$> 230\,\text{GeV}$
m_T	$< 160\,\text{GeV}$
p_T^W	$> 500\,\text{GeV}$
$p_T^\ell / E_T^{\text{miss}}$	< 0.03
am_{T2}	$> 300\,\text{GeV}$
$|\Delta\phi(b_i, E_T^{\text{miss}})|, i = 1, 2$	> 0.4
$\Delta R(b_1, b_2)$	> 0.8

discriminant, with very low values expected for the signal and a ratio of approximately one for the background. In order to fully use this variable, a shape-fit in the $p_T^\ell / E_T^{\text{miss}}$ is used for the signal-model dependent exclusion fits with the bCsoft signal regions. For bCsoft_high, three bins are used with borders at $[0, 0.015, 0.03, 0.1]$.

In total, about 12 SM events are expected in the bCsoft_high SR, with 2 events for $p_T^\ell / E_T^{\text{miss}} < 0.03$ and 10 events for $0.03 < p_T^\ell / E_T^{\text{miss}} < 0.1$, respectively. The dominant backgrounds are single top and W+jets events, followed by the semi-leptonic $t\bar{t}$ process. Three control regions are defined to normalise these processes, one for each of the listed backgrounds. The same p_T^W threshold is required in the CRs and the backgrounds are isolated by inverting the requirements on the am_{T2}, the $p_T^\ell / E_T^{\text{miss}}$ and the b-jet multiplicity.

10.8.2 Overlap between the soft and hard lepton selections

The statistical combination of the tN_high and the bCsoft_high signal region is based on a combined fit. It is therefore important that the event selections for the signal and control regions do not overlap. As discussed in the previous section, the signal region selections are disjunct due to the inverse m_T requirements. In order to assess the overlap between the control regions, the MC simulation of the backgrounds and several signals are used. For each simulated event all regions are determined for which the selection requirements are fulfilled. Figure 10.34 shows the number of overlapping simulated events in each region for the dominant backgrounds. In general, no overlapping events were found between the $t\bar{t}$ control regions of either selection and any of the other regions. The largest overlap is found between the W+jets and single top control regions. Up to 20% of the W+jets events are selected by the bCsoft_high_WCR and the tN_high_WCR, and a similar fraction is found for the respective STCR selections. Minor overlap is found between the bCsoft_high signal region and the tN_high WCR and STCR, with less than 10% shared events.

In order to reduce the overlap between the control regions, events that pass the tN_high WCR or STCR selections are removed from the bCsoft_high WCR or STCR, respectively. Such events have a high lepton p_T and therefore are less important for the determination of the background
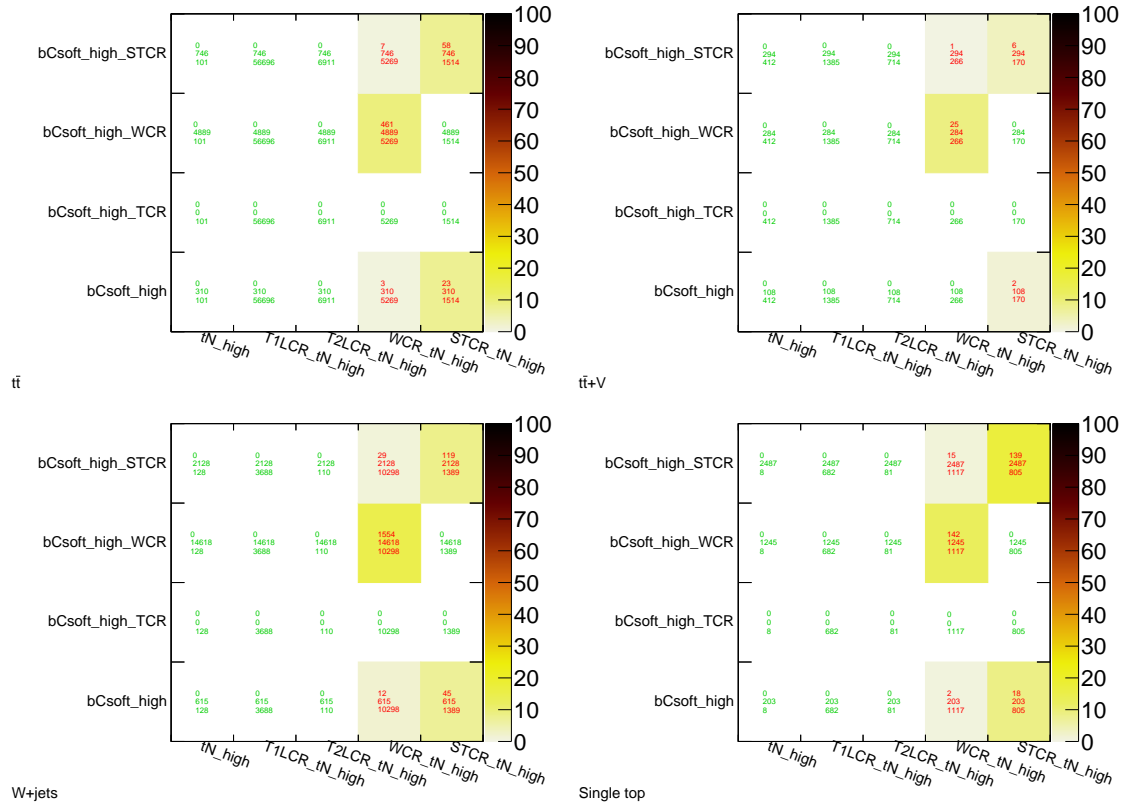
Figure 10.34: Number of simulated events selected by both a bCsoft_high and tN_high associated region for the $t\bar{t}$ (top left), $t\bar{t} + V$ (top right), W+jets (bottom left) and single top (bottom right) backgrounds. The numbers in each bin give the number of overlapping events and the number of events selected by the region indicated on the vertical axis and the horizontal axis, respectively, from top to bottom. The colour scale indicates the fraction of overlapping events in a bin.

Table 10.16: Number of observed and expected events in the bCsoft_high WCR and STCR before and after application of the overlap veto.

	no veto		with veto	
	WCR	STCR	WCR	STCR
Observed events	207	59	200	55
MC exp. SM events	216	101	202	94

normalisation in the soft-lepton signal region. The number of expected events in the control regions is reduced by about 7%, as detailed in Table 10.16. The remaining overlap, mainly between the bCsoft_high_STCR and the tN_high_WCR, as well as the bCsoft_high SR and the tN_high_STCR, is well below 10% for any of the signal or background processes and was deemed negligible, compared to the uncertainties in these regions. The overlap after the veto is shown in Appendix C.3.

10.8.3 Combined fit setup and validation

The control and signal regions for bCsoft_high and tN_high are included in a combined likelihood for the statistical evaluation. As the background processes differ and possible mismodelling effects depend strongly on the kinematic phase-space, the background normalisation factors for the soft- and hard-lepton selections are not shared. This means, taking as an example the single top background, that the single top contributions to the soft-lepton selections are scaled by a factor $\mu_{\text{single top}}^{\text{soft}}$ and the contributions to the hard-lepton selections by an uncorrelated factor $\mu_{\text{single top}}^{\text{hard}}$. Independent normalisation factors prevent mismodelling effects in one selection from affecting the other selection. Only the signal normalisation factor is shared, as there a fully correlated contribution to the two signal regions is expected.

The nuisance parameters for the experimental uncertainties are treated as fully correlated between the different selections. For the theory uncertainties, no correlation is assumed between the soft- and hard-lepton regions, as potentially different effects play a role there. Figure 10.35 shows the fitted results and uncertainties of the nuisance parameters. All Gaussian nuisance parameters have a best fit value of zero with an uncertainty of one, showing that no constraints are introduced by the correlation of the uncertainties between the regions. Additionally the correlations between the nuisance parameters were checked and found to agree well with the correlations observed in the standalone fits.

With this setup, identical background normalisation factors are expected for the tN_high backgrounds as from the standalone fit. For the soft-lepton selection small deviations are possible, due to the overlap removal in the control regions described in the previous section. The fitted values for the standalone and the combined fits are listed in Table 10.17. As can be seen, the normalisation factors for the soft-lepton selection agree well within the uncertainties, and no deviation is found for the hard-lepton fit results. The low values for the single top normalisation in the bCsoft_high region result from the strong interference effects between single top and $t\bar{t}$ which are not well modelled in the extreme phase-space targeted by this analysis.
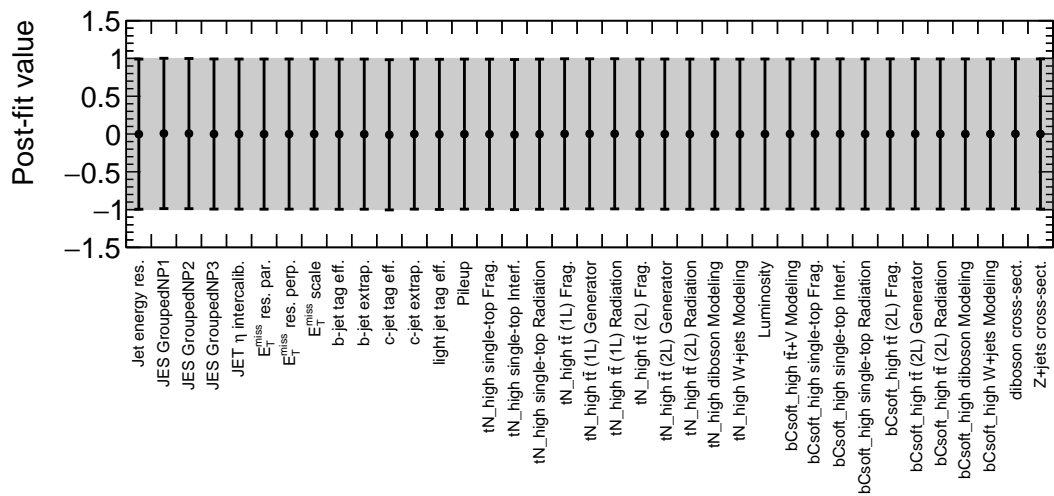
Figure 10.35: Fit values and errors of the Gaussian nuisance parameters in the combined background only fit to bCsoft_high and tN_high. The expected result is 0 with an uncertainty of ± 1.

Table 10.17: Summary of the background normalisation factors for the standalone regions and for the combined fit setup.

	$t\bar{t}$ (1L/2L)	W+jets	single top	$t\bar{t} + V$
bCsoft_high (standalone)	0.89 ± 0.14	1.18 ± 0.21	0.32 ± 0.13	–
bCsoft_high (combined)	0.93 ± 0.16	1.17 ± 0.21	0.35 ± 0.15	–
tN_high (standalone)	0.97 ± 0.08 / 1.01 ± 0.15	0.82 ± 0.17	0.64 ± 0.37	1.11 ± 0.25
tN_high (combined)	0.97 ± 0.08 / 1.01 ± 0.15	0.82 ± 0.17	0.64 ± 0.37	1.11 ± 0.25

10.8.4 Results

In Figure 10.36 the expected exclusion contours are shown for the individual tN_high and bC-soft_high regions and for the combination, comparing two cases in which the sensitivity is either improved by the combination, or dominated by the contributions of one signal region. For the $\tilde{t}_1 \sim \tilde{t}_L$ with large $\tan\beta$ signal model, resulting in equal branching ratios into all three decay modes, the standalone regions have a small sensitivity to the signal, as they are only sensitive to a part of the final states. The combination strongly increases the expected exclusion reach (left hand side). Even for the signal with $\tilde{t}_1 \sim \tilde{t}_R$, where the bCsoft_high has a good sensitivity but tN_high does not show an expected exclusion limit, an improvement can be seen with the combined results. In the third case, $\tilde{t}_1 \sim \tilde{t}_L$ with small $\tan\beta$, the sensitivity is dominated by tN_high, as shown in Appendix C.3.

The final, observed and expected exclusion contours are shown in Figure 10.37 for two signal grids with either $\Delta m(\tilde{\chi}_1^\pm, \tilde{\chi}_1^0) = 5$ GeV or with $m_{\tilde{\chi}_1^\pm} = 150$ GeV. These include the results for the combination of tN_med with the soft-lepton signal regions. For any signal point, the combination with the best expected significance is chosen. In comparison to the results without the addition of the bCsoft_high and tN_high combination [4], the expected significance towards larger masses is increased by about 50 GeV in the top squark mass. The combination involving tN_high provides better sensitivity for $m_{\tilde{t}_1} \gtrsim 900$ GeV. Due to the small excess in tN_high, and similar small excesses in tN_med and bCsoft_med, the observed exclusion is slightly weaker than the expected sensitivity.
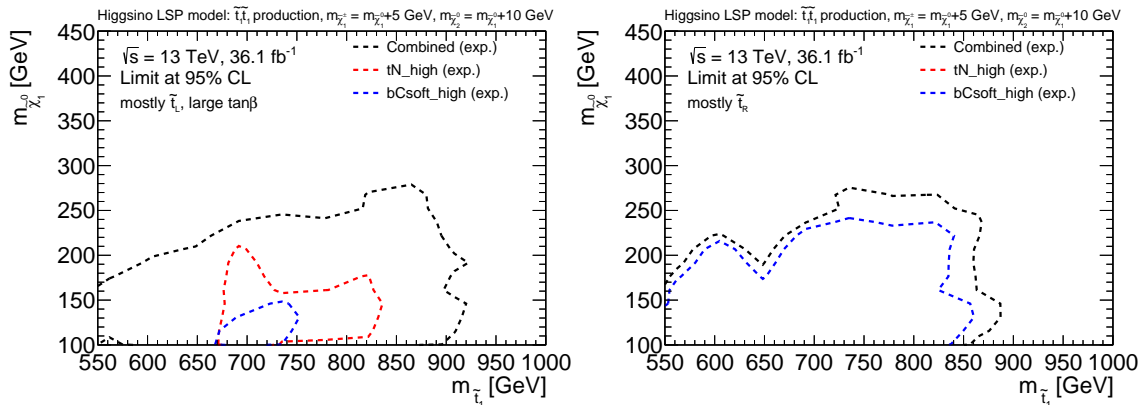
Figure 10.36: Expected 95% CL exclusion contour for the higgsino LSP signal with $\tilde{t}_1 \sim \tilde{t}_L$ and large $\tan\beta$ (left) and $\tilde{t}_1 \sim \tilde{t}_R$ (right) in the $m_{\tilde{t}_1}$ versus $m_{\tilde{\chi}_1^0}$ plane for the individual tN_high and bCsoft_high regions and for the combination.
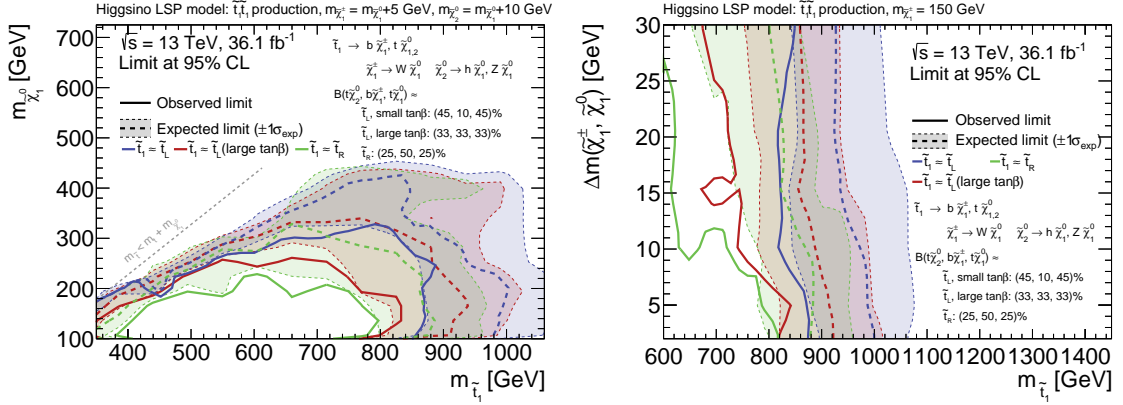
Figure 10.37: Expected and observed 95% excluded regions in the plane of $m_{\tilde{t}_1}$ versus $m_{\tilde{\chi}_1^0}$ (left) and of $m_{\tilde{t}_1}$ versus the higgsino mass splitting $\Delta m(\tilde{\chi}_1^\pm, \tilde{\chi}_1^0)$ (right) for direct stop pair production in the higgsino LSP model, including the results of the combination of the soft-lepton regions with tN_med [4] in addition to the combination with tN_high.
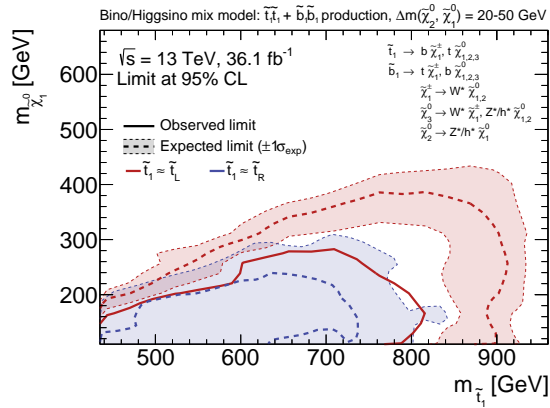
Figure 10.38: Expected and observed 95% excluded regions in the plane of $m_{\tilde{t}_1}$ versus $m_{\tilde{\chi}_1^0}$ for direct stop pair production in the bino/higgsino mix model, including the results of the combination of the soft-lepton regions with tN_med [4] in addition to the combination with tN_high.

As discussed above, the sensitivity to the $\tilde{t}_1 \sim \tilde{t}_R$ scenario is mainly driven by the soft-lepton regions, while for low $\tan\beta$ the hard-lepton selections dominate the reach. This can be seen in the dependence of the exclusion on the mass splitting $\Delta m(\tilde{\chi}_1^\pm, \tilde{\chi}_1^0)$. For low mass differences the soft-lepton regions are strongly sensitive, as the momentum of the charged lepton is directly correlated with the mass splitting. Larger mass differences decrease the sensitivity of the soft-lepton regions, as can be seen in the $\tilde{t}_1 \sim \tilde{t}_R$ scenario. The hard-lepton regions are nearly not affected.

The results are also interpreted in the well-tempered neutralino model. Figure 10.38 shows the exclusion contours for the two cases $\tilde{t}_1 \sim \tilde{t}_L$ and $\tilde{t}_1 \sim \tilde{t}_R$. In the former case, top squarks with masses below 800 GeV are excluded for neutralino masses below 200 GeV, with an expected range of 900 GeV and 400 GeV, respectively. The strong offset of the observed exclusion comes from the small excesses in the various signal regions in the combination. In the case of $\tilde{t}_1 \sim \tilde{t}_R$ the sensitivity is smaller with an expected limit of 720 GeV in the top squark mass. Due to the excess, no observed exclusion is found for this model.

Chapter 11 Comparison and outlook

Two searches for models predicting top quark partners are presented in this dissertation. The two models – vector-like top quarks and supersymmetric top quark partners – can lead to a similar final state characterised by a top quark pair and additional missing transverse momentum, $t\bar{t} + E_T^{\mathrm{miss}}$. Overall this prompts a similar search strategy, but differences in the models motivate an adaption to the specific signal process.

The underlying strategy for both searches is the same. Sensitivity to the signals is gained by comparing the observed events to the expected background, in a region constructed to maximise the significance. The background normalisation is constrained in control regions. The definition of the underlying physics objects is similar. For the vector-like quark search the definition is harmonised with other analyses. In the search for top squarks, especially the p_T requirements for the baseline electrons and muons is lowered. This helps to reduce the dileptonic $t\bar{t}$ background, by increasing the acceptance for the second lepton.

Due to their fermionic nature, the production cross-section for vector-like top quarks is higher than that for top squarks: $\sigma(pp \rightarrow T\bar{T}) = (43.8 \pm 4.8)\,\mathrm{fb}$ and $\sigma(pp \rightarrow \tilde{t}_1\tilde{t}_1) = (6.2 \pm 1.0)\,\mathrm{fb}$ for a mass of 1 TeV. The effective VLQ cross-section is reduced due to decay branching ratio considerations. Even for $\mathcal{B}(T \rightarrow Zt) = 100\%$ the requirement of a $Z \rightarrow \nu\bar{\nu}$ decay reduces the selectable signal to about 40%. Nonetheless, this difference in production cross-section necessitates a higher selection efficiency for the search for top squarks. In both analyses the semi-leptonic decay of the top quark pair is targeted. The reconstruction of the hadronic top quark decay provides a tool to suppress Standard Model backgrounds. In the search for vector-like top quarks, hadronic top quark decays are reconstructed using reclustered large-radius jets. In order to achieve a higher signal efficiency in the top squark search, a highly efficient reconstruction algorithm for hadronic top quark decays is developed.

The final state of vector-like quark decays include additional particles, with respect to that of the SUSY model. In the analysis, this feature is exploited by requiring a second hadronic resonance in addition to the top quark decay. With this requirement, the Standard Model backgrounds can be strongly reduced. The multitude of possible decay modes for vector-like quarks motivate a combination of several searches in different decay topologies. The basis of the analysis, the physics object definitions and general selection strategy, is therefore harmonised with other analyses, in view of a possible combination. In the SUSY search a combination of different signal regions within the same publication is made, in order to gain sensitivity to less simplified models that can feature more decay modes for the top squark.

While in the final states of the vector-like top quark signal an additional hadronic resonance is used to suppress the backgrounds, no such feature is expected for the SUSY signal. There, instead the E_T^{miss} requirement is increased. With this, the background composition changes and the Standard Model expectation in the signal region is dominated by $t\bar{t} + Z(\rightarrow \nu\bar{\nu})$ events. In order to constrain

the normalisation of this process, a dedicated control region based on $t\bar{t} + Z(\to \ell^+\ell^-)$ events is employed. Based on the experience gained in the vector-like quark search, the control regions in the SUSY analyses are constructed to directly target dileptonic $t\bar{t}$ decays and W + heavy flavour jet events. This is made possible by the highly efficient hadronic top quark reconstruction, which is used to suppress semi-leptonic $t\bar{t}$ events in the control regions. In the vector-like top quark search the control regions are dominated by semi-leptonic $t\bar{t}$ events and W+jets events with light flavour jets, and the extrapolation towards the background composition in the signal region is tested in validation regions.

In both searches no excess above the Standard Model prediction is found, and limits are set on models of top quark partners. Due to the higher cross-section, the vector-like quark search is sensitive to higher masses, excluding vector-like top quarks with $m_T < 1.16$ TeV for $\mathcal{B}(T \to Zt) = 100\%$ at 95% CL. For neutralino masses below 100 GeV, the limit on top squark masses is at $m_{\tilde{t}_1} < 900$ GeV with an expected limit of $m_{\tilde{t}_1} < 1040$ GeV.

Future analyses targeting these signal models can profit from the larger dataset, collected in the full LHC Run 2 and future LHC runs. In comparison to the pair production, the electroweak production of single vector-like top quarks can have a higher production cross-section at high masses. In the single production mode the production cross-section however depends also on the coupling to the W and Z bosons, making the exclusion limits more model dependent. The algorithm for reconstructing hadronic top quark decays could potentially increase the signal selection efficiency in the VLQ search. By additionally adapting the reconstruction to W or Z bosons, the reconstruction of the vector-like top quark mass in fully hadronic decays could be feasible. This opens the possibility of using the full distribution of the reconstructed mass in order to increase the sensitivity.

A further option, which also applies to the SUSY search, is to introduce categories according to the quality of the hadronic top quark reconstruction. Possible categorisation schemes would be the mass of the top quark candidate, the constituent jet multiplicity, as well as the existence of a b-jet in its constituents. Categories with a lower signal purity can help to constrain the background, when combined with high purity categories. A further categorisation in the E_T^{miss} could help to increase the sensitivity towards higher neutralino masses, for which the expected E_T^{miss} is lower. These improvements could help to exploit the possibilities enabled by larger, future datasets and potentially gain insights into theories beyond the Standard Model.

Conclusion

This dissertation presents searches in $t\bar{t} + E_T^{miss}$ final states using $36.1\,\text{fb}^{-1}$ of pp collision data at $\sqrt{s} = 13\,\text{TeV}$, recorded at the LHC by the ATLAS detector in 2015 and 2016. The searches target the pair production of top quark partners in models with vector-like quarks, as well as in models of Supersymmetry.

The first analysis searches for the pair production of vector-like top quarks with the decay mode $T \rightarrow Zt$ [3]. With the subsequent decay of the Z boson into neutrinos, this generates the targeted final state of $t\bar{t} + E_T^{miss}$. A signal region maximising the expected sensitivity is defined by using large-radius jets to reconstruct hadronic decays of the top quark and of massive bosons from vector-like top quark decays, as well as high thresholds on E_T^{miss} and related variables. The normalisation of the dominant Standard Model backgrounds is estimated in dedicated control regions. This data driven background normalisation estimate is validated in validation regions. No excess above the background estimate is found in the signal region and 95% CL limits are set on the vector-like top quark mass in dependence of the decay branching ratio. Assuming a branching ratio of $\mathcal{B}(T \rightarrow Zt) = 100\%$, masses below $1.16\,\text{TeV}$ are excluded, with an expected limit of $1.17\,\text{TeV}$. For vector-like top quark masses below $1\,\text{TeV}$, branching ratios $\mathcal{B}(T \rightarrow Ht) < 65\%$ are excluded for mixed $ZtHt$ decays, and branching ratios $\mathcal{B}(T \rightarrow Wb) < 45\%$ are excluded for mixed $ZtWb$ decays.

The second search targets a simplified model of Supersymmetry, with a light top squark decaying into a top quark and a neutralino as the lightest supersymmetric particle. For this analysis, the reconstruction of the hadronically decaying top quark is improved by a new iterative reclustering algorithm, compared to the previously used large-radius jets or χ^2 minimisation based techniques. In order to find and combine the decay products of the top quark, jets are iteratively reclustered, matching the radius of the combined object to its momentum. The algorithm is highly efficient in reconstructing hadronic top quark decays and is the basis for the definition of the signal region and the background estimate strategy. One of the dominant backgrounds are $t\bar{t}$ events in the dileptonic decay mode, in which one lepton cannot be reconstructed. The normalisation of this background is constrained in a selection vetoing events with hadronic top quark decays. In a similar fashion, control regions for the other backgrounds are constructed. The observed data in the signal region are compatible with the Standard Model prediction, and 95% CL limits are set on the masses of the top squark and the neutralino. For neutrino masses below $100\,\text{GeV}$, top squark masses up to $900\,\text{GeV}$ are excluded, with an expected limit on the mass of $1\,\text{TeV}$.

Combining this analysis with other analyses targeting low momentum leptons, sensitivity is achieved to additional models of Supersymmetry. In models with light higgsinos, and Dark-Matter-inspired models with a light mixture of the bino and higgsinos, top squark masses below $800\,\text{GeV}$ to $900\,\text{GeV}$ are excluded, depending on the model and the decay branching ratio of the top squark. The results of the tN_high analysis as well as the combination are part of the publication in Ref. [4].

The analyses presented in this dissertation are based on the first part of the dataset expected from the LHC Run 2, achieving for the first time sensitivity to top squark masses of $1\,\text{TeV}$ as well as vector-like top quarks with masses above $1\,\text{TeV}$. With the increase in luminosity and further data provided by the LHC, future searches can expand this sensitivity and challenge the common prediction of light top quark partners. Further improvements in the reconstruction of hadronic top quark decays, but also more complex analyses using multiple categories and the shape information of discriminating variables in the evaluation are needed to fully profit from the larger dataset.

Appendix

Appendix A b-tagging in dense environments

The efficiency and rejection of b-tagging algorithms are degraded in so-called *dense* environments, in which jets are close-by or even partially overlap [117]. This can be an important effect for analyses in final states with highly boosted top quarks, e.g. searches for a Z' boson. For high masses of the Z', the decay $Z' \to t\bar{t}$ produces boosted top quarks, with strongly collimated decay products. Important effects for the performance reduction are a shift of the jet axis with respect to the b-hadron flight direction, as well as the contamination of the tracks associated to the jet with tracks from nearby light-flavour jets.

In Ref. [117], several variables are identified which help to reduce the effects of dense environments on the b-tagging performance. These are used in Run 1 in order to train a multivariate classification algorithm called MVb, based on the MV1 algorithm, the predecessor of the MV2 algorithm used in Run 2. In the training, jets from simulated, high mass $Z' \to t\bar{t}$ events are included in addition to those from SM $t\bar{t}$ events, in order to incorporate jets in dense environments. The MVb algorithm shows an improved performance over MV1 in $Z' \to t\bar{t}$ events.

Here, the MVb algorithm is retrained for Run2, based on the MV2 tagger. In order to assess the impact of the different changes, each variable is added individually and the performance improvement is quantified. Furthermore, the effect of changing the training sample from pure SM $t\bar{t}$ events to additionally included high mass $Z' \to t\bar{t}$ events is analysed. Different hyperparameter settings for the BDT training are tested in order to reduce the effect of statistical fluctuations in the training samples.

A.1 Variables

The additional variables used to improve the sensitivity of the MVb algorithm in dense environments are shown in Figure A.1. The jet width is defined as the p_T weighted average of the distance of tracks to the jet axis,

$$w_{\text{jet}} = \frac{1}{\sum p_{T,i}} \sum_{i \in \text{tracks}} p_{T,i} \cdot \Delta R(i, \text{jet}) \;, \tag{A.1}$$

where $p_{T,i}$ refers to the p_T of track i, $\Delta R(i, \text{jet})$ is the distance between track i and the jet axis, and the sum goes over all tracks matched to the jet. A further track related quantity is the number of tracks with a high impact parameter significance, $|d_0/\sigma_{d_0}| > 1.8$. Due to the additional IP requirement, this quantity is less affected by the contamination of the tracks associated to the jet from nearby light flavour jets. In order to additionally reduce the effects of such contamination, the energy fractions of the secondary vertices found by the SV and JetFitter algorithms are scaled by the number of

tracks in the jet, relative to the number of tracks associated to the respective vertex. The d_0 and z_0 significances of the third track, ordered by the d_0 significance, are resilient against a shift in the jet axis and also provide good distinction between b and light jets.
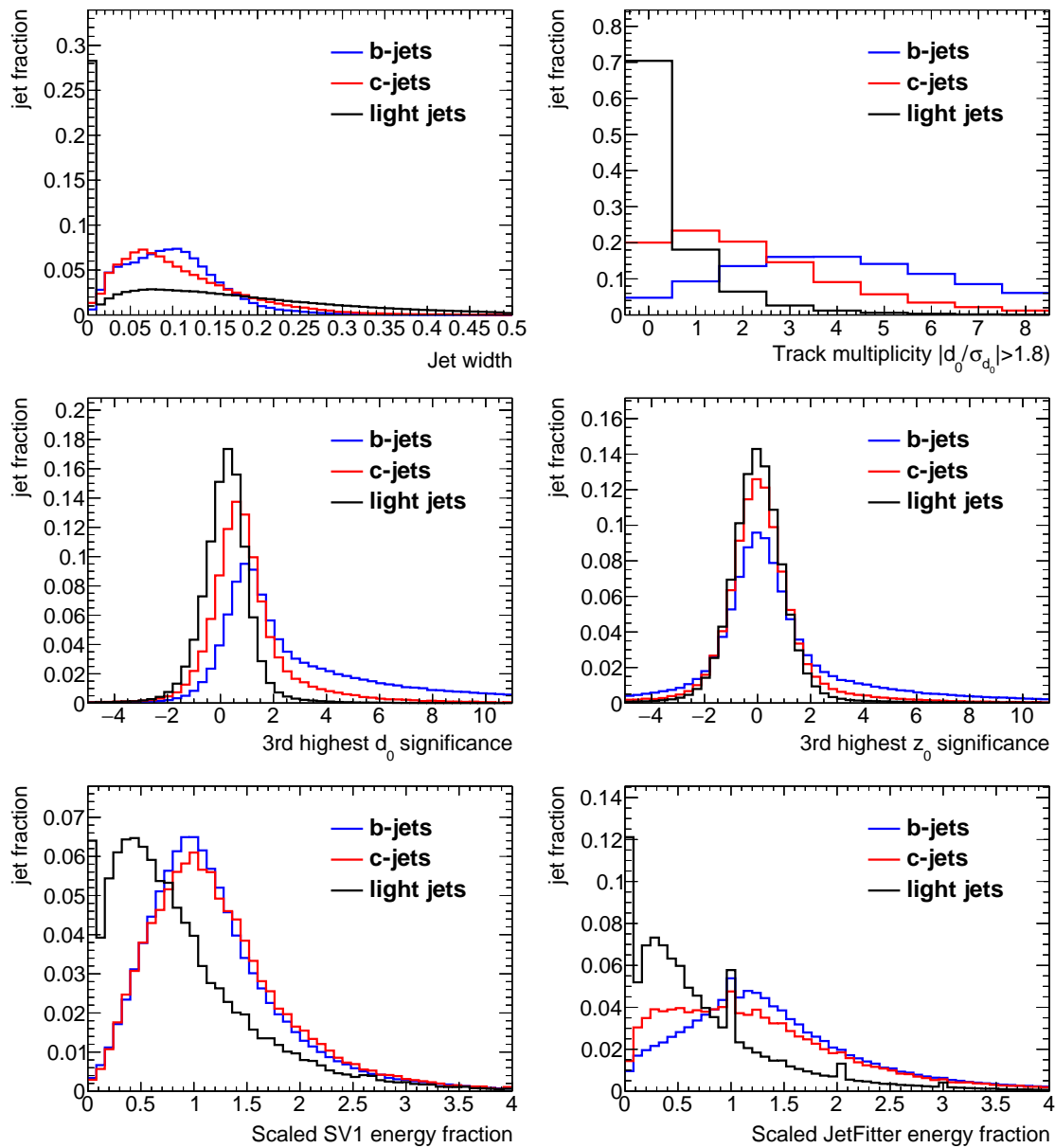
Figure A.1: Distribution of the additional variables for b-jets, c-jets and light jets in $t\bar{t}$ events.

A.2   Training

The training of the Run 2 MVb tagger is based on the MV2 configuration. Initially, only jets from an inclusive $t\bar{t}$ sample are used in the training. The training dataset is split into two parts, of which one is used in the actual training of the BDT and the other, statistically independent half is used to evaluate the performance of the trained classifier. This ensures that artificial differences between

b-jets and *c*- or light flavour jets in the training set due to statistical fluctuations do not bias the performance in the evaluation.

In the first step, the additional variables are added subsequently in the training:

1. the jet width,

2. the number of tracks with $|d_0/\sigma_{d_0}| > 1.8$,

3. the d_0 and z_0 significances of the third track, and

4. the scaled SV and JetFitter vertex energy fractions.

Figure A.2 shows the *b*-tagging efficiency versus the light jet rejection and the *c*-jet rejection, for the reference training with the MV2 configuration and for each step of the additional variables. The results are shown for the inclusive $t\bar{t}$ sample, as well as for $Z' \rightarrow t\bar{t}$ events with a mass of the Z' boson of $m_{Z'} = 3$ TeV, resulting in highly boosted top quark decays. The rejection is defined as the inverse tagging rate, e.g. $N(c-\text{jets})/N(c\text{-jets tagged as }b\text{-jets})$.

The inclusion of the jet width and the number of tracks with a high IP significance leads to an improvement in the performance in dense environments. The light jet rejection in inclusive $t\bar{t}$ events is slightly lowered in the region of $0.6 \lesssim \varepsilon_b \lesssim 0.8$. The addition of the IP significances of the third track leads to an improvement in the performance in both $t\bar{t}$ events and dense environments, bringing the $t\bar{t}$ performance back to the MV2 reference. The light jet rejection in $Z' \rightarrow t\bar{t}$ events is improved by a factor of up to 4, for $\varepsilon_b \simeq 77\%$. In general, the addition of the jet width brings an improvement of about 20% in the rejection, for $\varepsilon_b \lesssim 70\%$ in both resolved and dense environments. Further variables do not alter the performance of discriminating *b* and *c*-jets. The further addition of the scaled vertex energy fractions does not improve the performance, but instead leads to a light jet rejection decrease for SM $t\bar{t}$ as well as for dense environments. While this effect is not yet fully understood, the scaled energy fractions are not further used in the training.

Due to the increased number of variables, the BDT is more prone to training on statistical fluctuations. While this does not introduce a bias in the final results, as long as the events used in the training are not used in the evaluation, such overtraining indicates a loss of performance and generality. Several hyperparameters of the BDT influence the sensitivity to statistical fluctuations. Here, the maximal tree depth, is decreased from 10 to 5 in order to find settings with reduced overtraining. A lower maximal tree depth results in a lower probability of a split being taken due to a statistical fluctuation. In order to compensate for the lower depth, the number of trees in the BDT, `nTrees`, is increased from 400 to 500.

Figure A.3 shows the resulting BDT classifier distribution for signal and background, i.e. *b*-jets and *c* or light flavour jets, comparing the events used in the training and the statistically independent evaluation sample ("testing") for the two sets of hyperparameters. While the overall classifier output is similar for both configurations, the lower tree depth results in a lower difference between the training and the test dataset, i.e. a reduced overtraining. The reduced χ^2 for the signal distribution improves from 3.6 for a depth of 10 to 1.5 for a depth of 5. The improvement in the compatibility of the background distributions is similar. The tagging performance for the two configurations is compared in Figure A.4. A small performance decrease can be seen for $t\bar{t}$ events, while in dense environments the altered configuration shows a small performance gain.

In the next step, the training dataset is changed to additionally include $Z' \rightarrow t\bar{t}$ events with $m_{Z'} = 3$ TeV. Changing the training inputs requires a different reweighting of the p_T and η distributions of the jets. In the original configuration of the MV2 tagger, *b*- and *c*-jets in the training are reweighted to match the two dimensional $p_T \times \eta$ distribution of the light jets. The
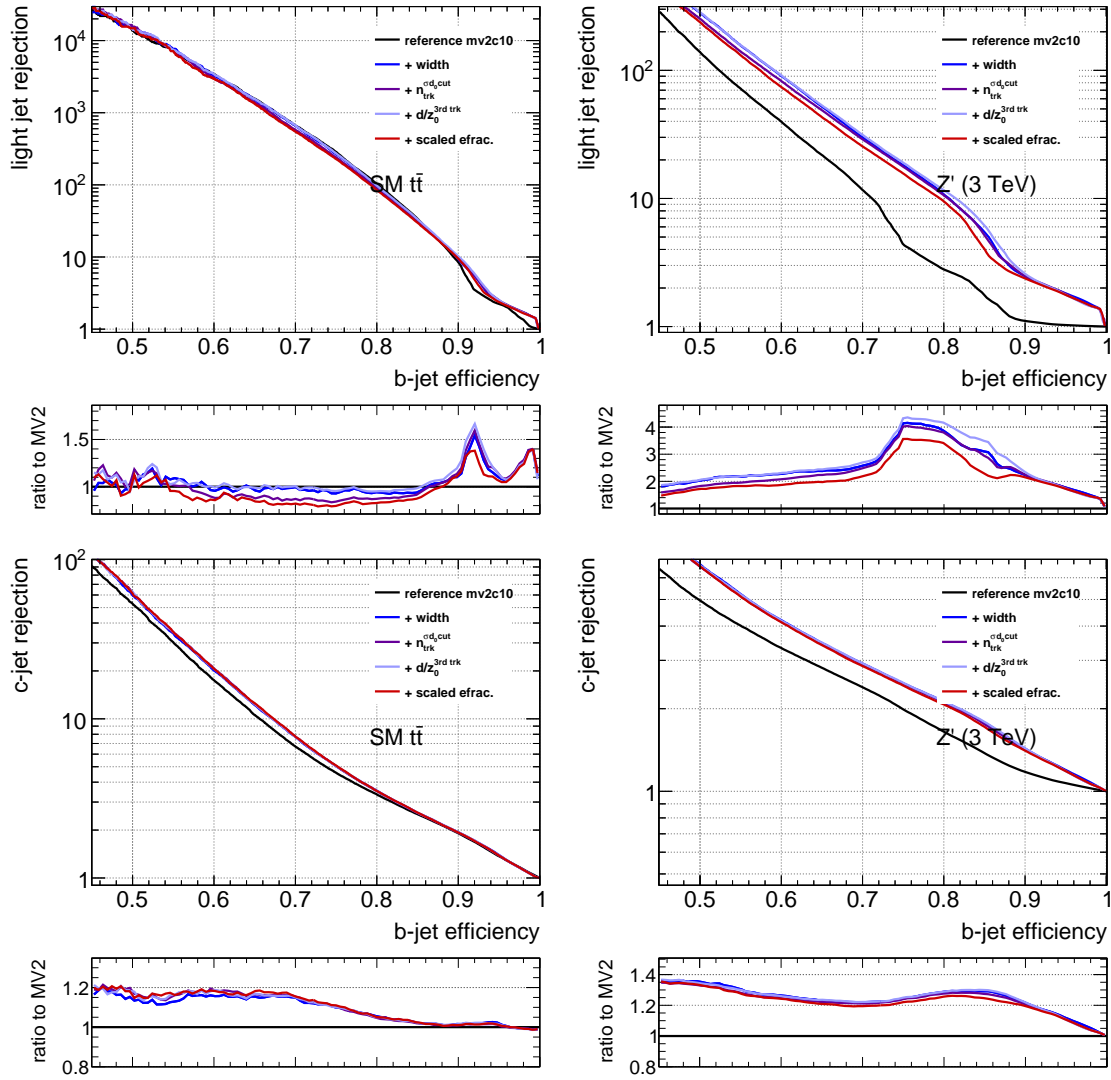
Figure A.2: Light flavour jet rejection (top) and *c*-jet rejection (bottom) as a function of the *b*-tagging efficiency for multiple training options based on MV2 and additional variables, evaluated on an inclusive $t\bar{t}$ sample (left) and on $Z' \to t\bar{t}$ events (right). The black line shows the reference MV2 training, the coloured lines show the results for subsequently adding additional variables.

correlation of the other variables to the p_T and η of the jet contain important information, and this procedure ensures that these correlations can be used in the training without a dependency on the actual p_T and η distributions of the jets in the training dataset. Due to the limited statistics in the dense environment training set, which contains only 15% of the inclusive events, this reweighting procedure results in strong fluctuations at high jet p_T. This effectively devalues the interesting *b*-jets in dense environments in the training, resulting in a poor performance. In order to resolve this issue, the reweighting procedure is changed to match the light and *c*-jet distributions to the *b*-jets as a reference. Figure A.5 shows the global performance for the reference tagger, the original reweighting procedure and the fixed version. As one can see, the original setting leads to a strong performance loss in dense environments, which is corrected when using the alternative version.
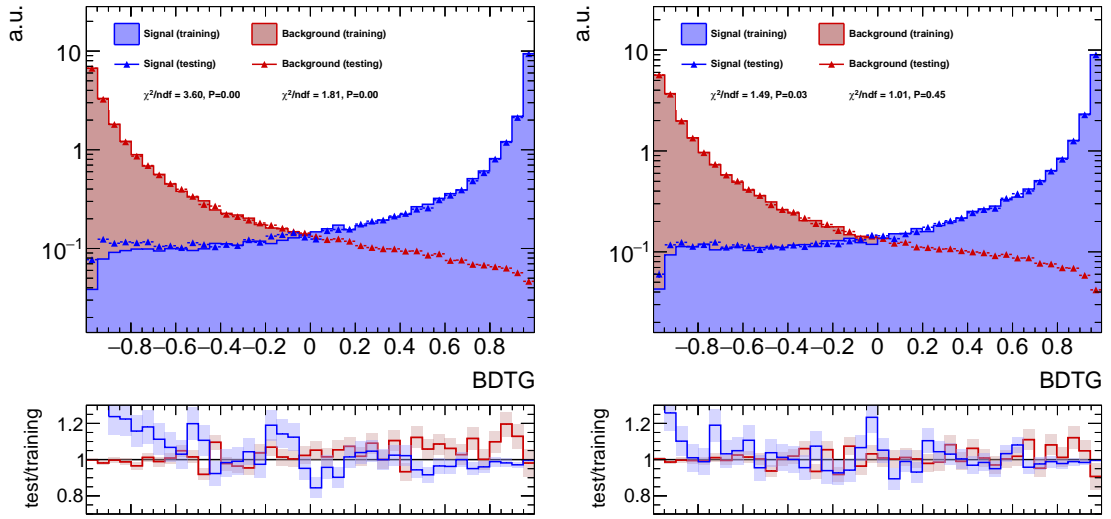
Figure A.3: Comparison of the BDT result for the training and the test samples, for two different sets of BDT settings. The left figure shows the training with `depth=10`, `nTrees=400` and the right figure shows the training with `depth=5`, `nTrees=500`. The reduced χ^2 and the χ^2-probability are given below the legends.

Overall, the inclusion of $Z' \to t\bar{t}$ events in the training strongly improves the performance in dense environments. For $\varepsilon_b \simeq 77\%$, the light jet rejection is increased by a factor of more than 4, and the c-jet rejection by about 35%. In SM $t\bar{t}$ events, the overall performance decreases, as the light jet rejection is decreased by about 40%. The c-jet rejection in resolved environments is not affected by the change in the training dataset.
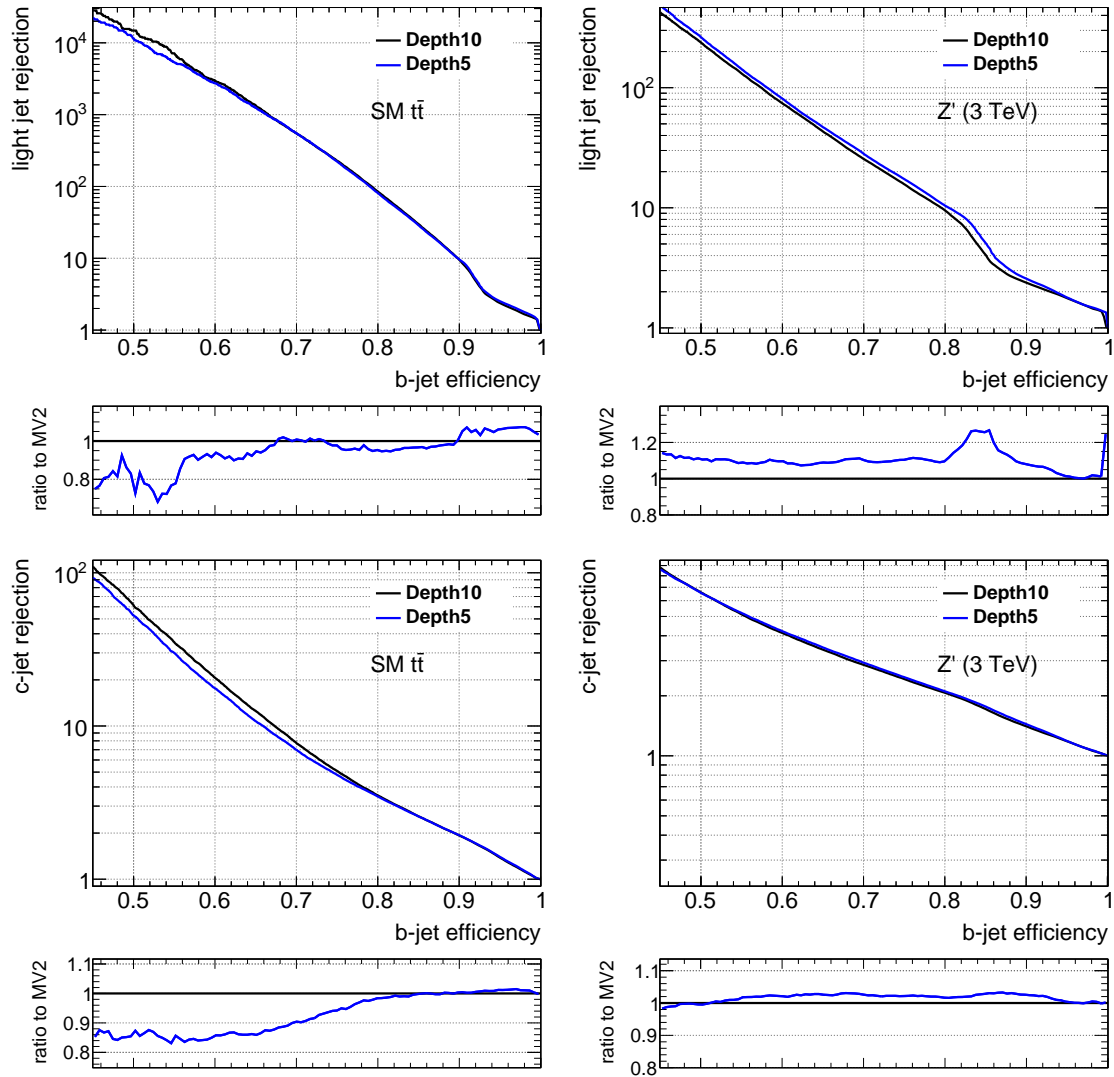
Figure A.4: Light flavour jet rejection (top) and *c*-jet rejection (bottom) as a function of the *b*-tagging efficiency for multiple training options based on MV2 and additional variables, evaluated on an inclusive $t\bar{t}$ sample (left) and on $Z' \to t\bar{t}$ events (right). The black line shows the training with `depth=10`, `nTrees=400` and the blue line shows the results for the training with `depth=5`, `nTrees=500`.
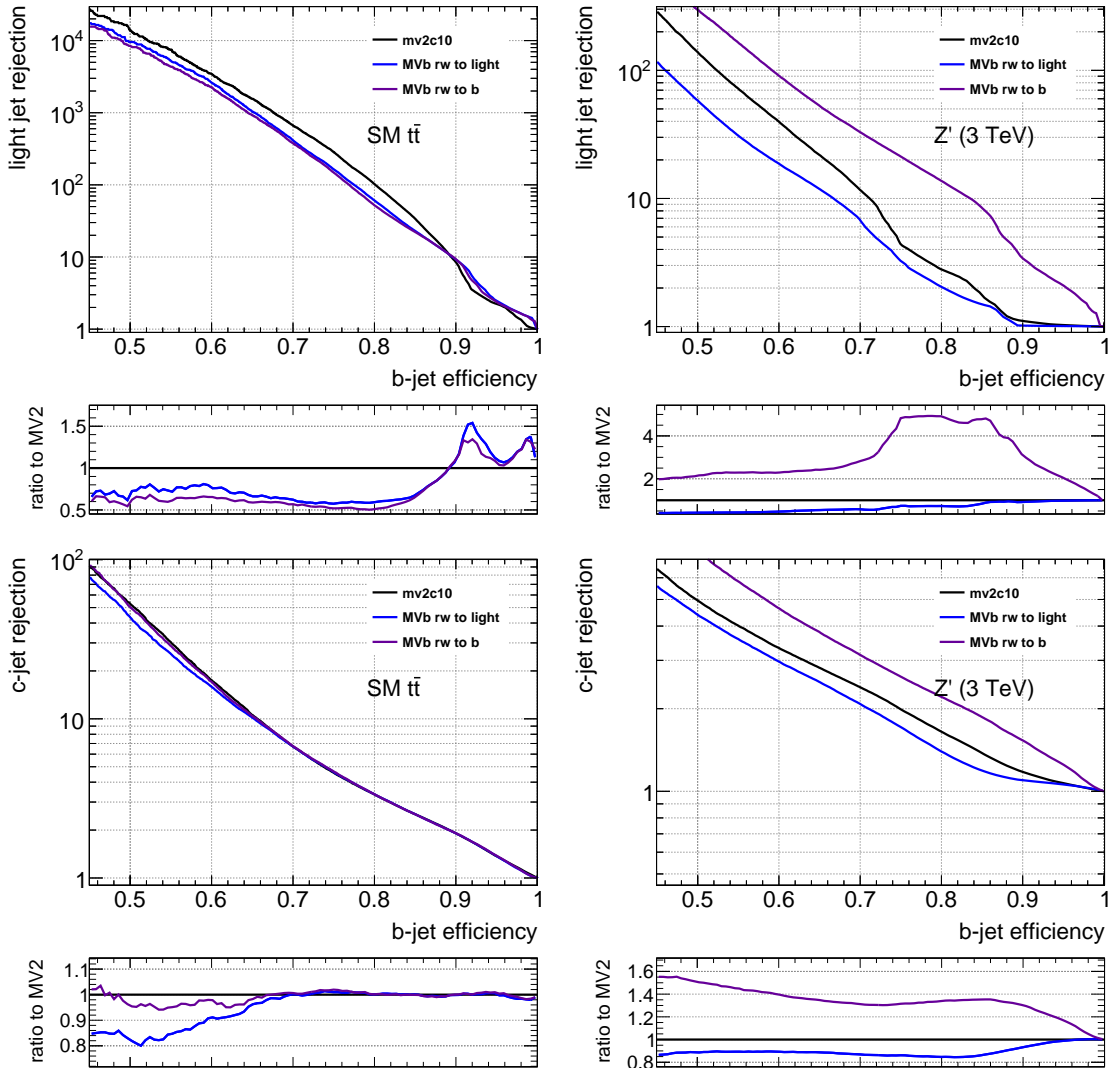
Figure A.5: Light flavour jet rejection (top) and *c*-jet rejection (bottom) as a function of the *b*-tagging efficiency for multiple training options based on MV2 and additional variables, evaluated on an inclusive $t\bar{t}$ sample (left) and on $Z' \rightarrow t\bar{t}$ events (right). The black line shows the MV2 tagger as the reference, the blue line shows the training with the original reweighting procedure and the purple line shows the results the reweighting to the *b*-jet distribution.

A.3 Conclusion

The MVb tagger is re-trained for Run 2 based on the MV2 configuration and including additional variables as well as $Z' \rightarrow t\bar{t}$ events in the training. Additionally, the hyperparameters of the BDT are optimised to reduce overtraining effects and increase the performance in dense environments. Both changes, the addition of information robust against dense environment effects as well as the specialised training including jets from highly boosted top quark decays, improve the performance in dense environments. This can be seen again in Figure A.6, where the performance of the changes is compared to the final MVb tagger and the MV2 algorithm. In dense environments, the MVb

tagger improves the light jet rejection for $\varepsilon_b \simeq 77\%$ by a factor of 5.8 compared to MV2, and the c-jet rejection is improved by 40%. In SM $t\bar{t}$ events the light jet rejection is decreased compared to the general algorithm, making MVb a specialised tool for dense environments. The c-jet rejection in SM $t\bar{t}$ events is not altered by the changes.
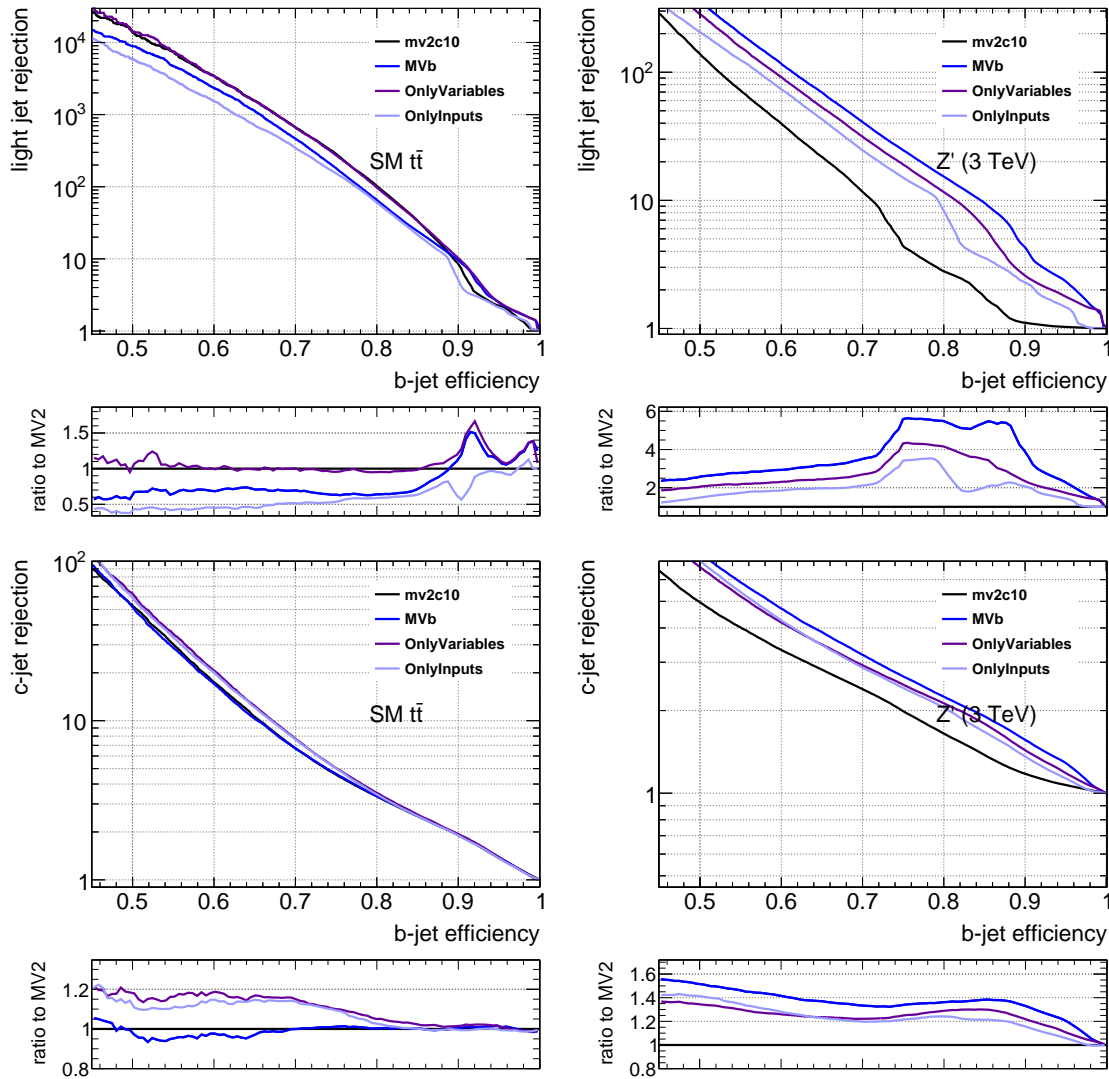
Figure A.6: Light flavour jet rejection (top) and c-jet rejection (bottom) as a function of the b-tagging efficiency for multiple training options based on MV2 and additional variables, evaluated on an inclusive $t\bar{t}$ sample (left) and on $Z' \to t\bar{t}$ events (right). The black line shows the MV2 tagger as the reference, the purple line the performance for MV2 with additional variables and the light blue line the performance for MV2 trained on the dense environment inputs. The blue line shows the performance of the full MVb training.

Appendix B Vector-like top quarks

B.1   Mass and decay mode dependency of the signal properties

B.1.1   Preselection
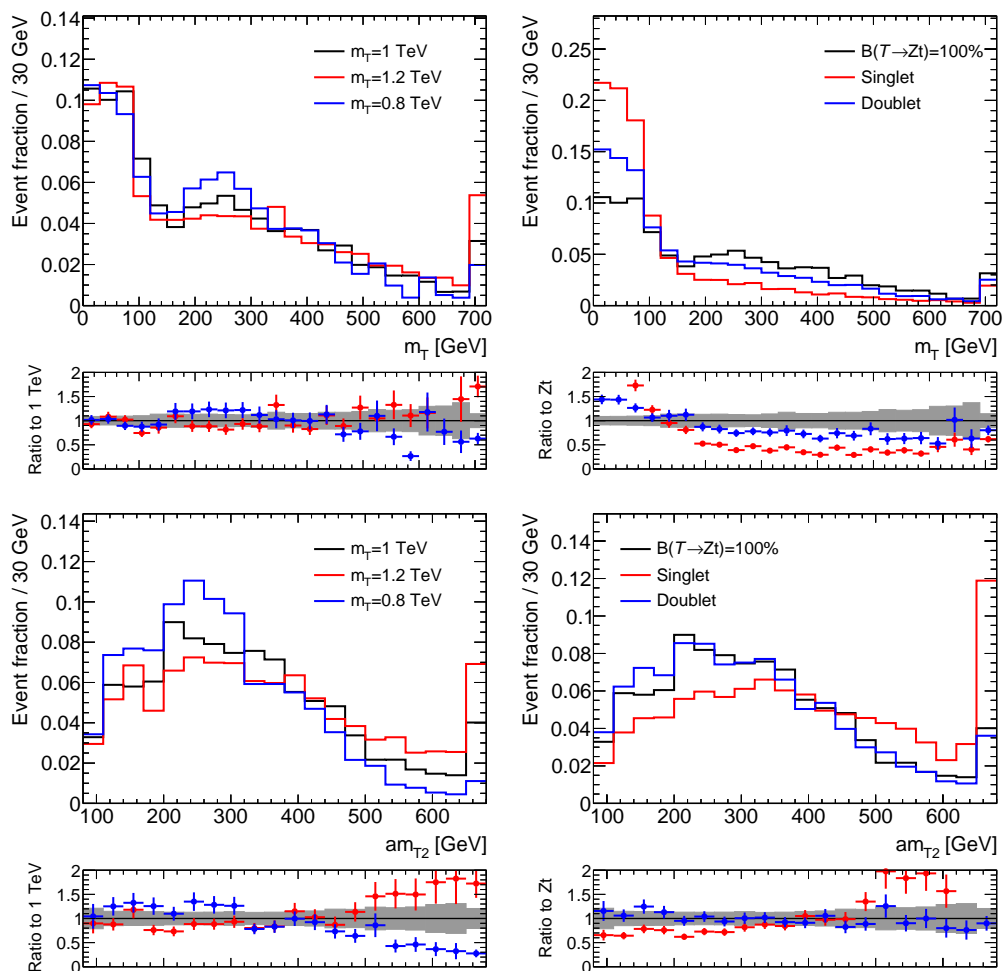
Figure B.1: Comparison of the m_T (top) and the am_{T2} (bottom) distribution for different signal masses for $\mathcal{B}(T \to Zt) = 100\%$ (left) and for different decay modes for $m_T = 1\,\text{TeV}$ (right) after the preselection.
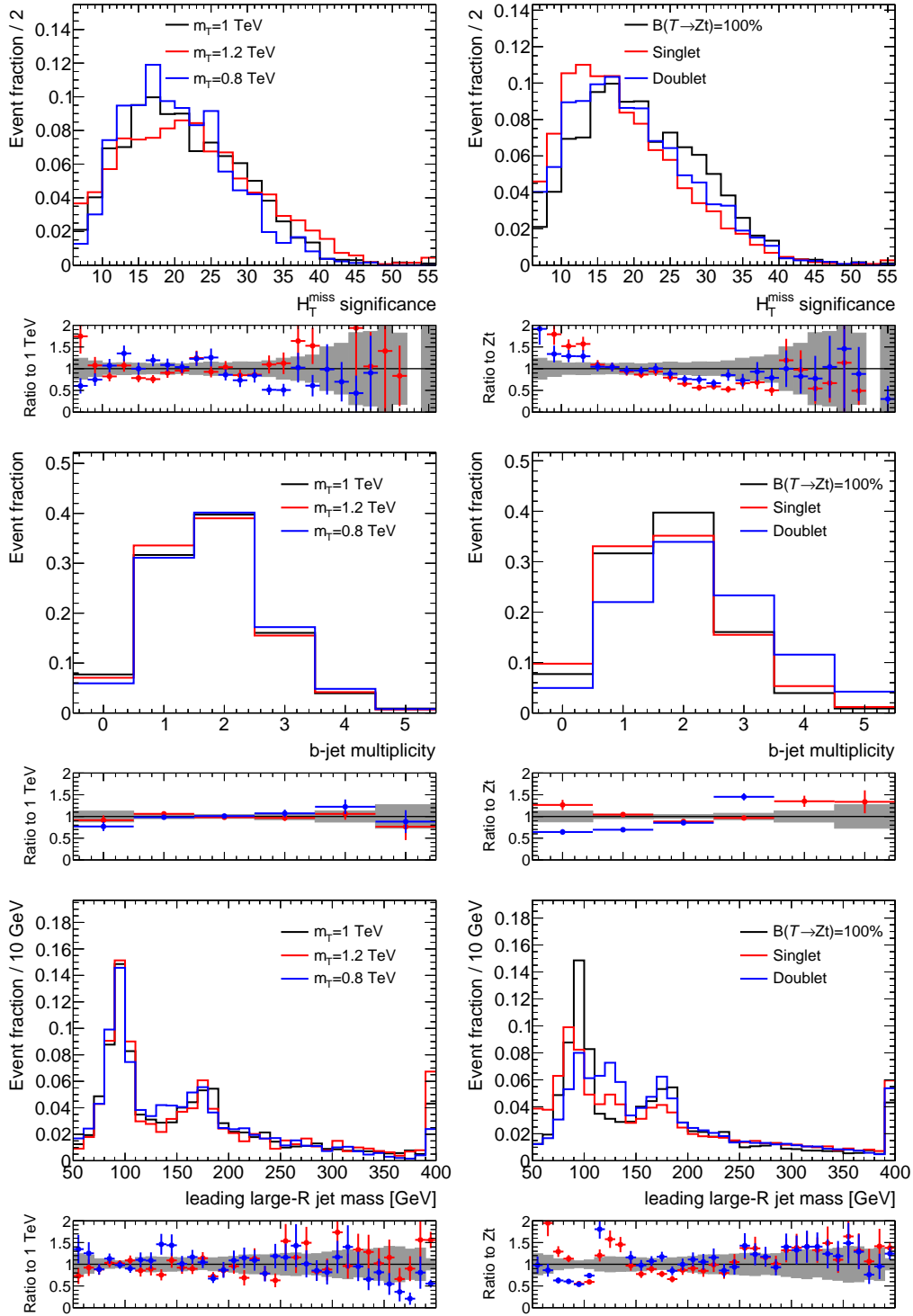
Figure B.2: Comparison of the $H_{\mathrm{T,sig}}^{\mathrm{miss}}$ distribution (top) the *b*-jet multiplicity (middle) and the mass of the leading large-*R* jet (bottom) for different signal masses for $\mathcal{B}(T \to Zt) = 100\%$ (left) and for different decay modes for $m_T = 1\,\mathrm{TeV}$ (right) after the preselection.
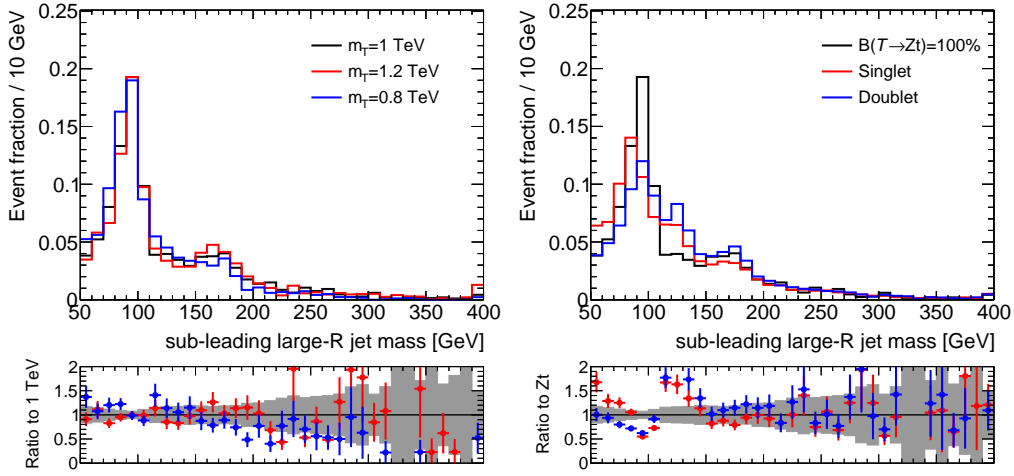
Figure B.3: Comparison of the mass of the sub-leading large-R jet for different signal masses for $\mathcal{B}(T \to Zt) = 100\%$ (left) and for different decay modes for $m_T = 1\,\text{TeV}$ (right) after the preselection.

B.1.2 Signal region
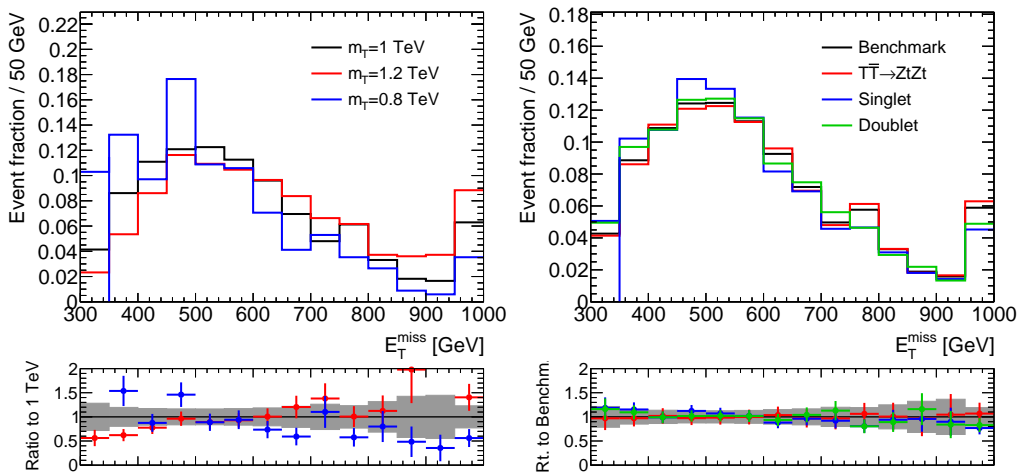
Figure B.4: Comparison of the E_T^{miss} distribution for different signal masses for $\mathcal{B}(T \to Zt) = 100\%$ (left) and for different decay modes for $m_T = 1\,\text{TeV}$ (right) in the signal region. The cut on the displayed variable is not applied, but indicated with a blue vertical line.
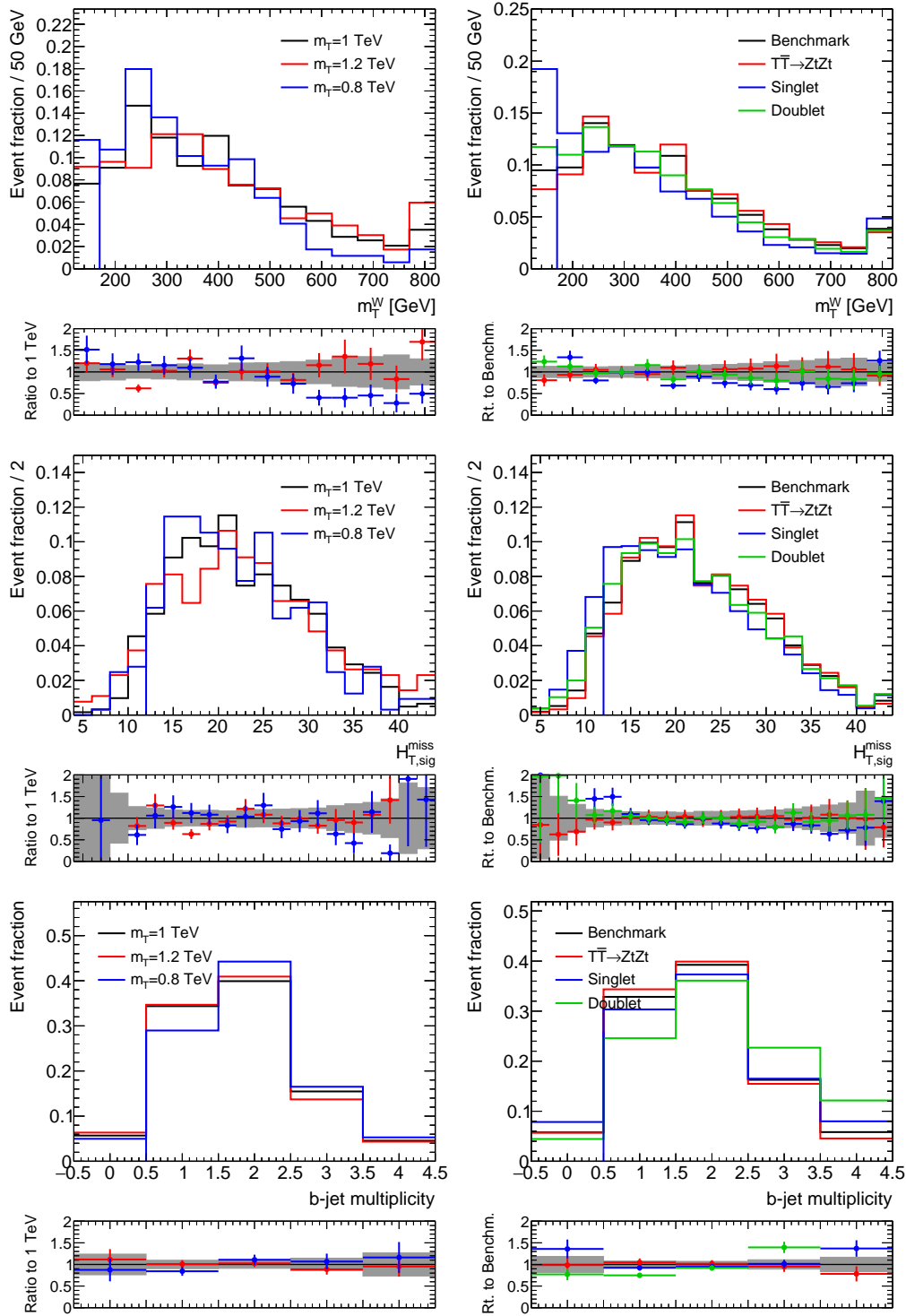
Figure B.5: Comparison of the m_T distribution (top), the $H_\mathrm{T,sig}^\mathrm{miss}$ distribution (middle) and the b-jet multiplicity (bottom) for different signal masses for $\mathcal{B}(T \to Zt) = 100\%$ (left) and for different decay modes for $m_T = 1\,\mathrm{TeV}$ (right) in the signal region. The cut on the displayed variable is not applied, but indicated with a blue vertical line.
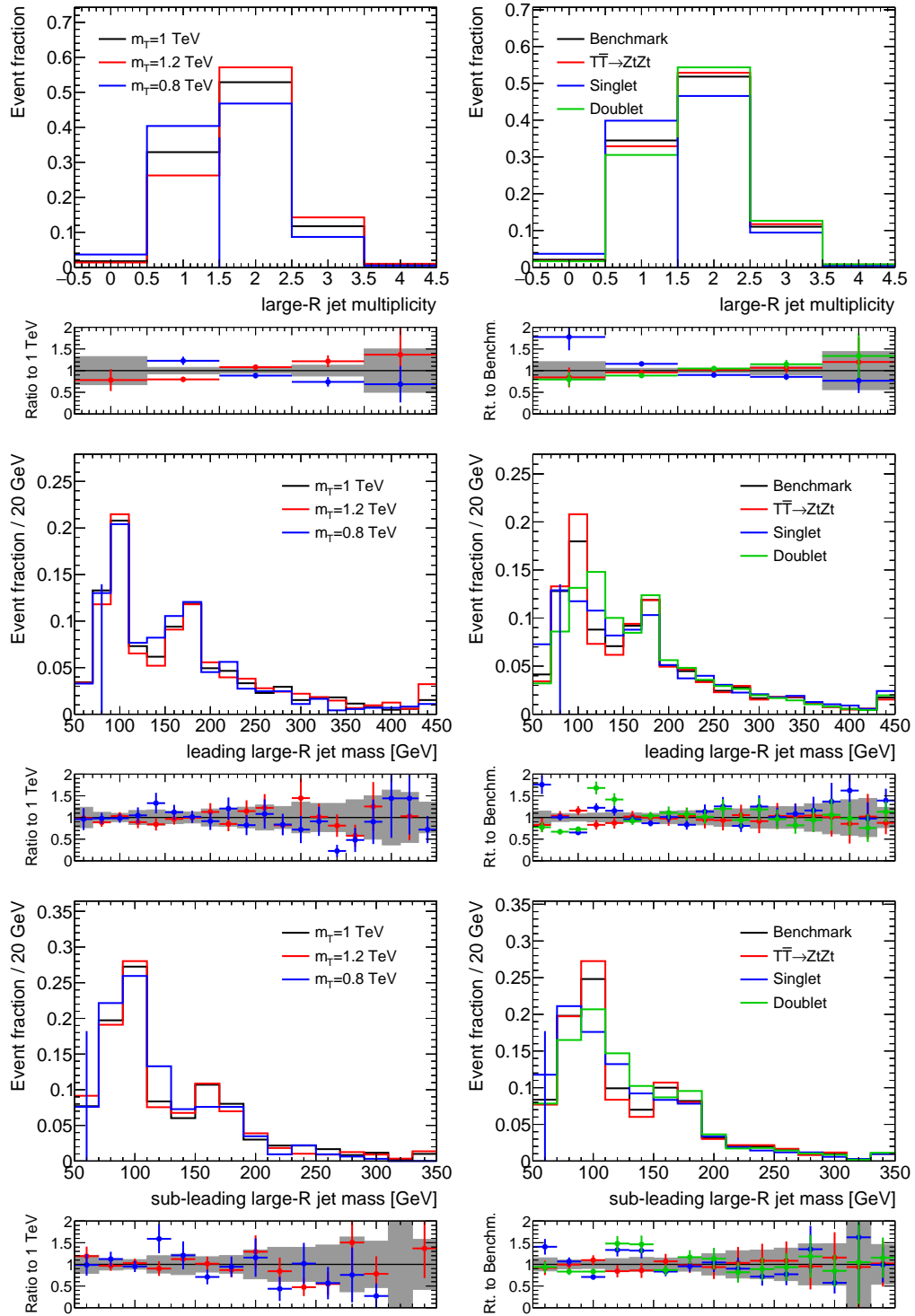
Figure B.6: Comparison of the large-*R* jet multiplicity (top) and the mass of the leading (middle) and sub-leading (bottom) large-*R* jet for different signal masses for $\mathcal{B}(T \to Zt) = 100\%$ (left) and for different decay modes for $m_T = 1$ TeV (right) in the signal region. The cut on the displayed variable is not applied, but indicated with a blue vertical line.

B.2 Additional control region distributions

B.2.1 $t\bar{t}$ control region
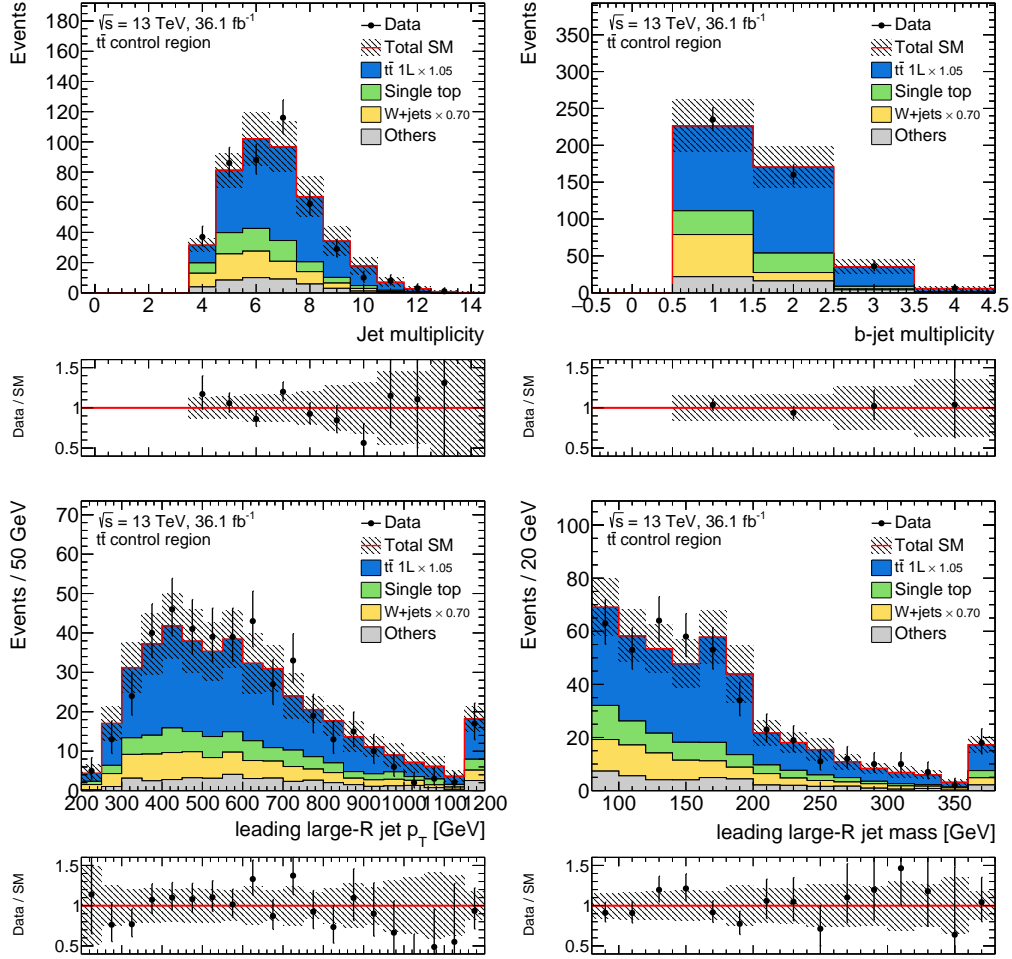
Figure B.7: Distribution of the jet and the *b*-jet multiplicity (top) and the p_T and the mass of the leading large-*R* jet (bottom) in the TCR. The $t\bar{t}$ and *W*+jets normalisation factors are applied as indicated in the legend. The lower panels show the ratio of the data to the prediction. The error bands include statistical and systematic uncertainties.
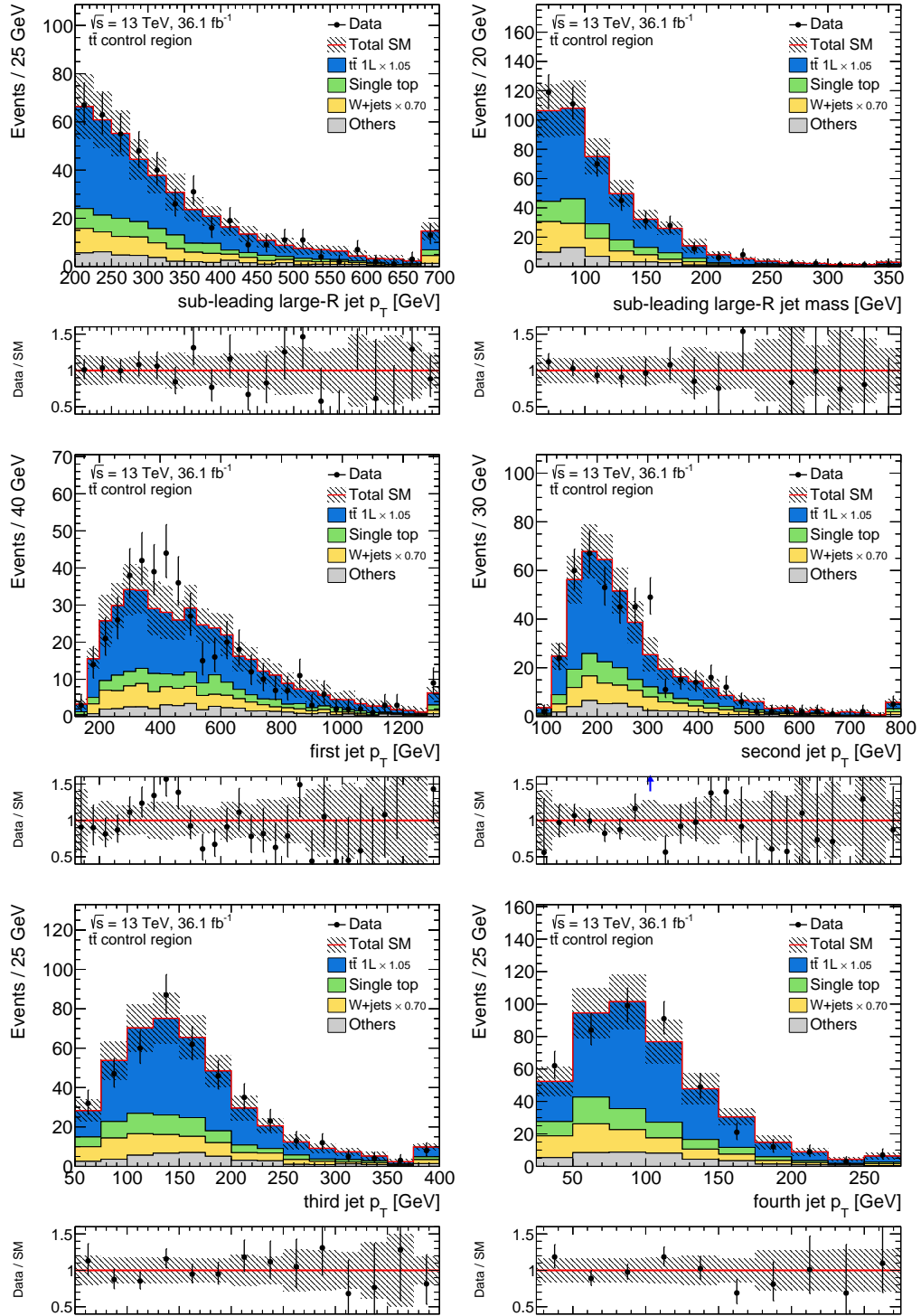
Figure B.8: Distribution of the p_T and the mass of the sub-leading large-*R* jet (top), the p_T of the leading and sub-leading jet (middle) and the p_T of the third and fourth leading jet (bottom) in the TCR. The $t\bar{t}$ and *W*+jets normalisation factors are applied as indicated in the legend. The lower panels show the ratio of the data to the prediction. The error bands include statistical and systematic uncertainties.
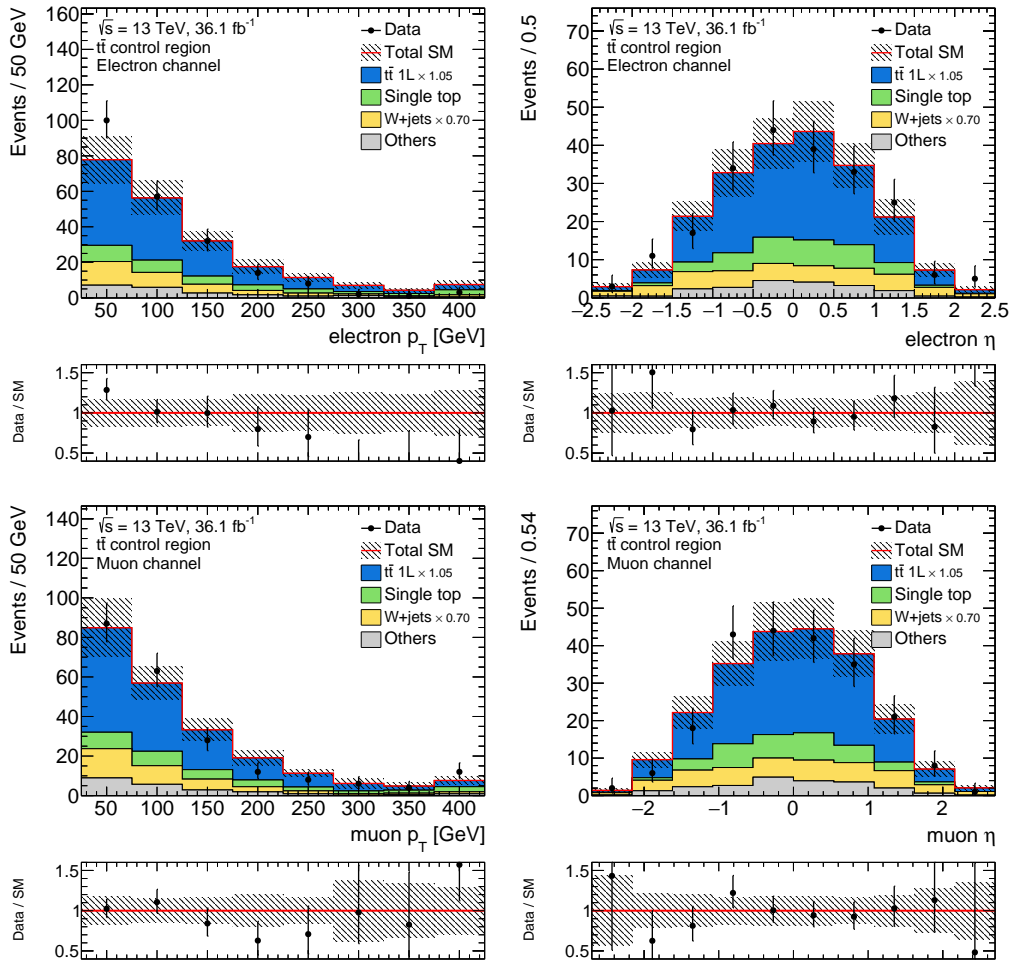
Figure B.9: Distribution of the p_T and the pseudo-rapidity of the signal electron (top) and muon (bottom) in the TCR. The $t\bar{t}$ and W+jets normalisation factors are applied as indicated in the legend. The lower panels show the ratio of the data to the prediction. The error bands include statistical and systematic uncertainties.

B.2.2 *W*+jets control region
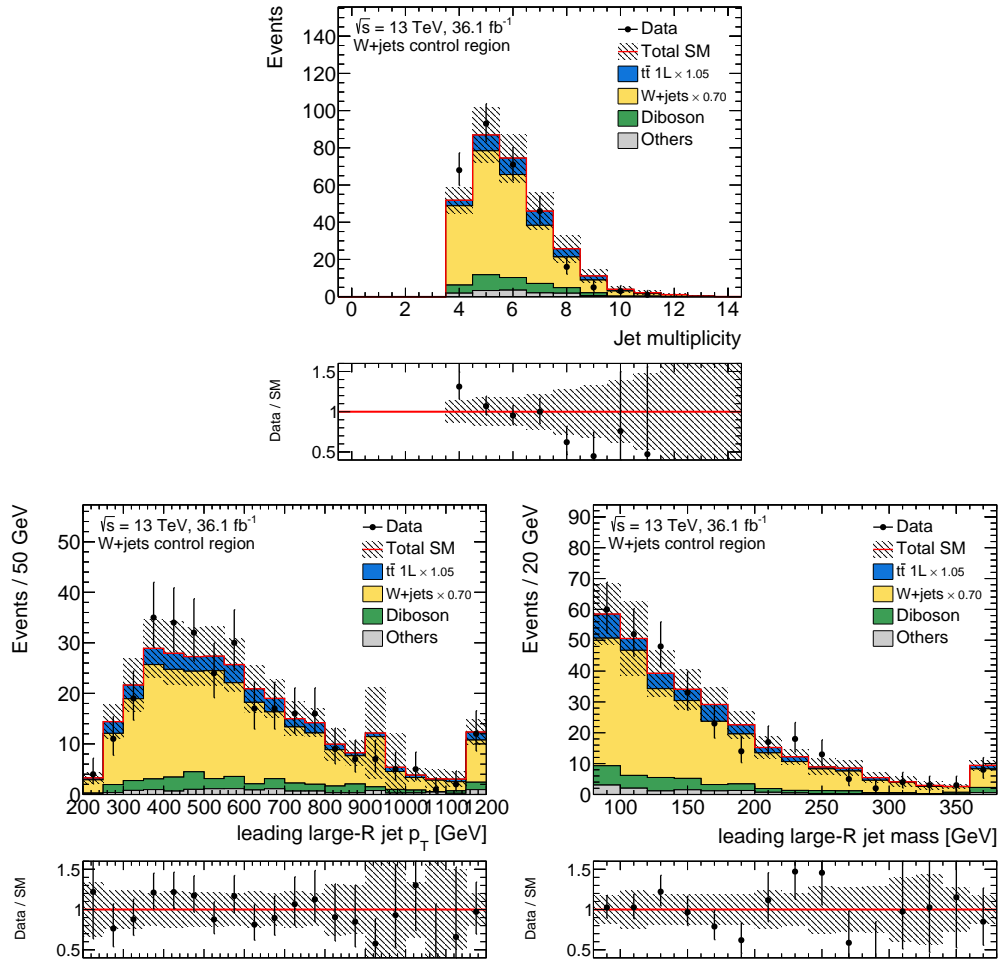
Figure B.10: Distribution of the jet multiplicity (top) and the p_T and the mass of the leading large-*R* jet (bottom) in the WCR. The $t\bar{t}$ and *W*+jets normalisation factors are applied as indicated in the legend. The lower panels show the ratio of the data to the prediction. The error bands include statistical and systematic uncertainties.
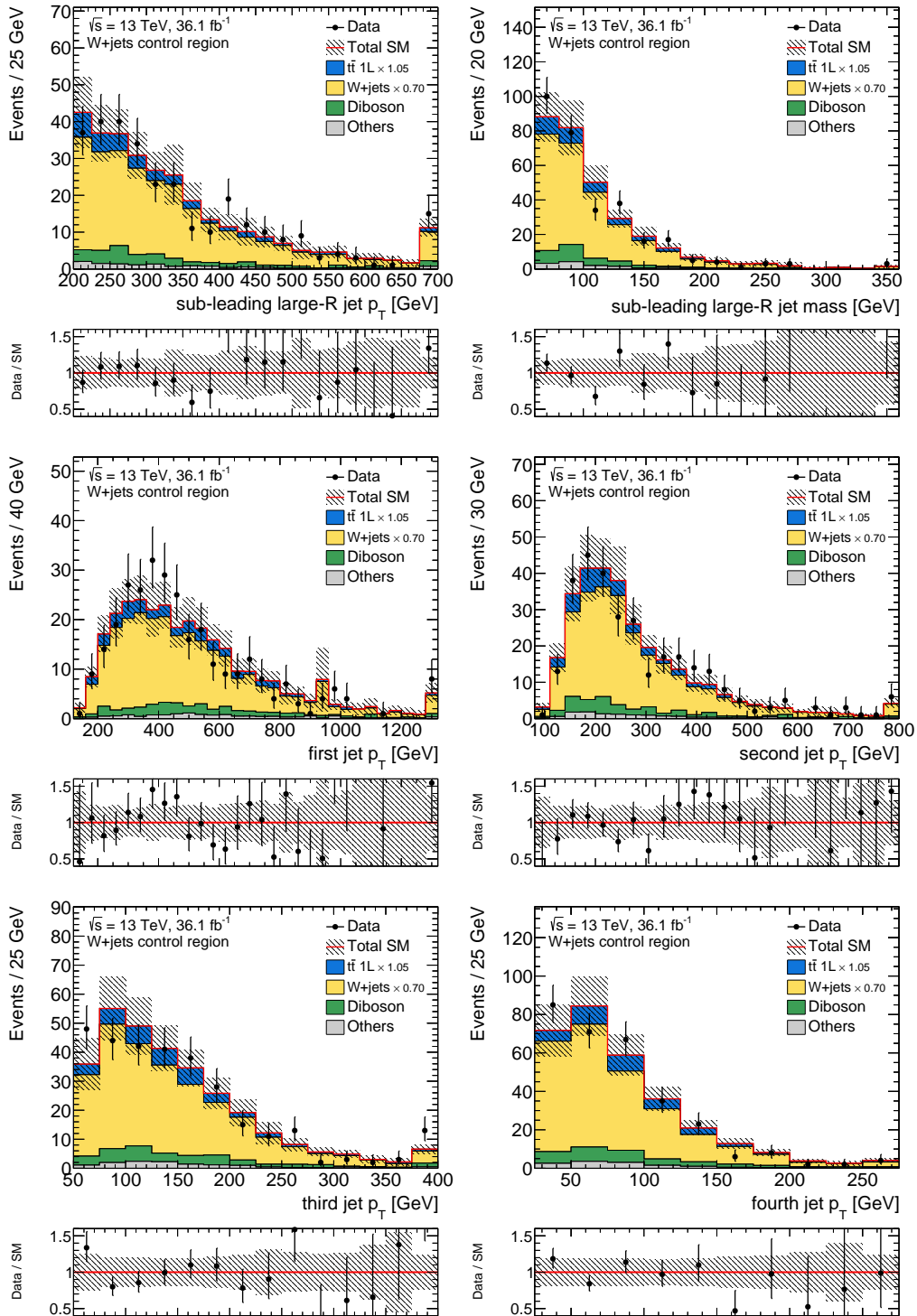
Figure B.11: Distribution of the p_T and the mass of the sub-leading large-R jet (top), the p_T of the leading and sub-leading jet (middle) and the p_T of the third and fourth leading jet (bottom) in the WCR. The $t\bar{t}$ and W+jets normalisation factors are applied as indicated in the legend. The lower panels show the ratio of the data to the prediction. The error bands include statistical and systematic uncertainties.
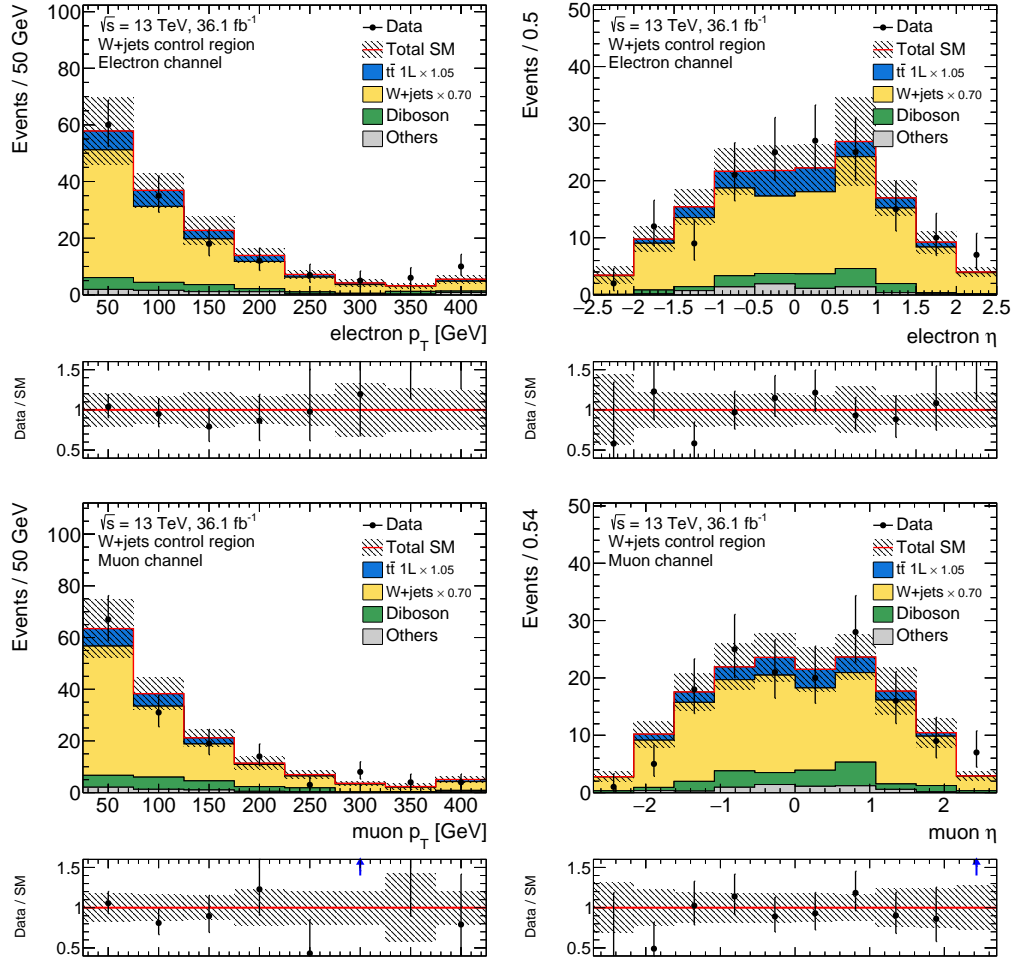
Figure B.12: Distribution of the p_T and the pseudo-rapidity of the signal electron (top) and muon (bottom) in the WCR. The $t\bar{t}$ and W+jets normalisation factors are applied as indicated in the legend. The lower panels show the ratio of the data to the prediction. The error bands include statistical and systematic uncertainties.

B.3 Additional validation region distributions

B.3.1 $t\bar{t}$ validation region
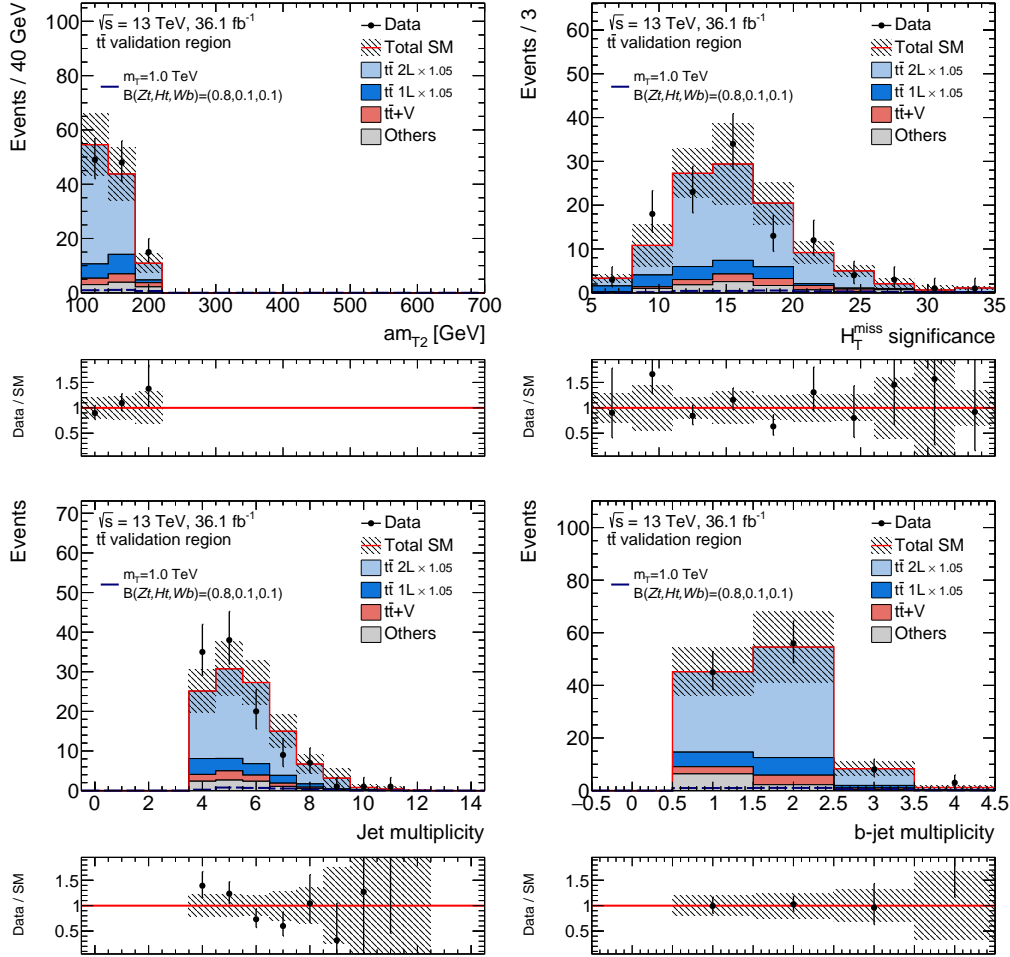
Figure B.13: Distribution of am_{T2} and $H_{T,\text{sig}}^{\text{miss}}$ (top) and the jet and the b-jet multiplicity (bottom) in the TVR. The $t\bar{t}$ and W+jets normalisation factors are applied as indicated in the legend. The lower panels show the ratio of the data to the prediction. The error bands include statistical and systematic uncertainties.
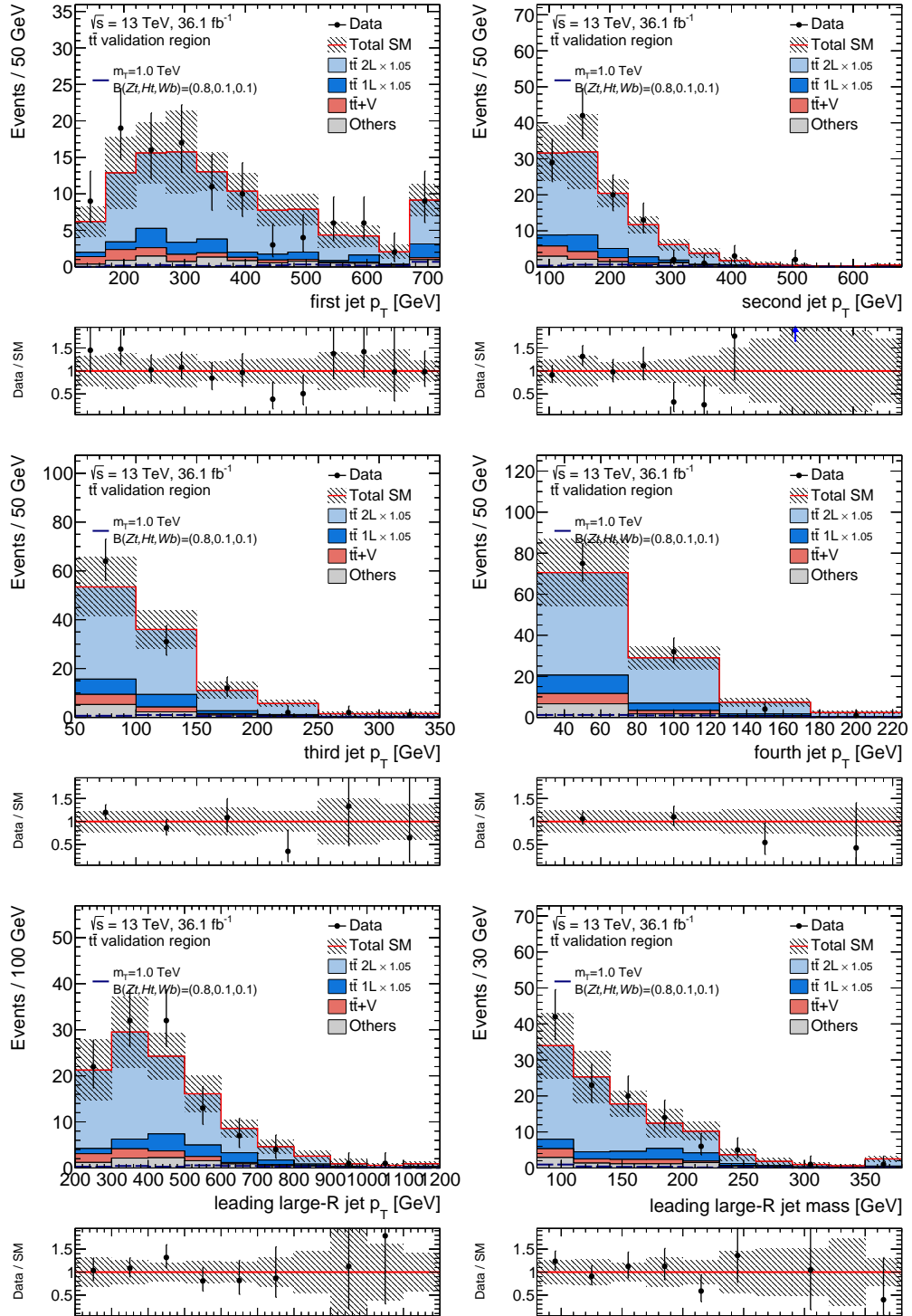
Figure B.14: Distribution of the jet p_T (top, middle) and the p_T and the mass of the leading large-R jet (bottom) in the TVR. The $t\bar{t}$ and W+jets normalisation factors are applied as indicated in the legend. The lower panels show the ratio of the data to the prediction. The error bands include statistical and systematic uncertainties.
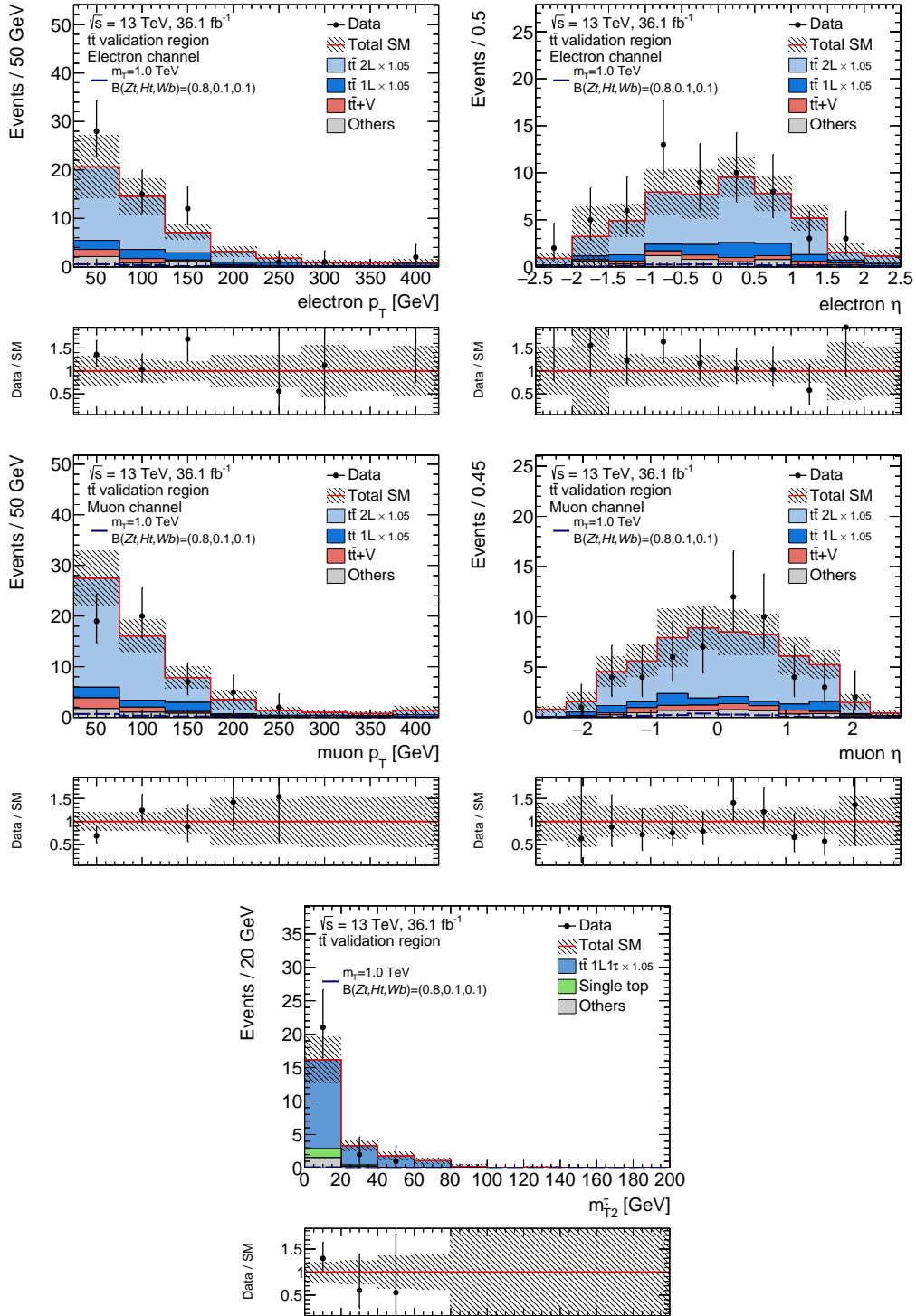
Figure B.15: Distribution of the p_T and the pseudo-rapidity of the signal electron (top) and muon (middle) and the m_{T2}^{τ} distribution (bottom, without the m_{T2}^{τ} requirement) in the TVR. The $t\bar{t}$ and W+jets normalisation factors are applied as indicated in the legend. The lower panels show the ratio of the data to the prediction. The error bands include statistical and systematic uncertainties.

B.3.2 *W*+jets validation region
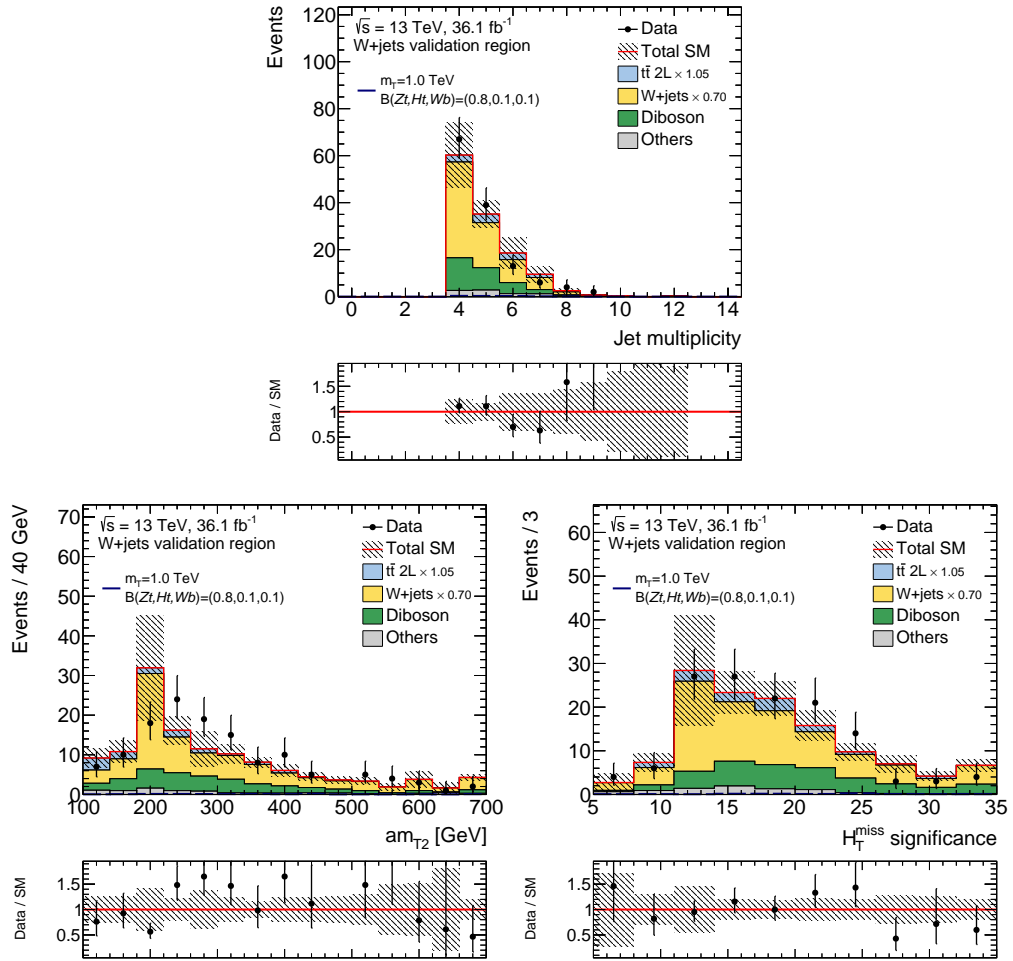
Figure B.16: Distribution of the jet multiplicity (top) and am_{T2} and $H_{T,sig}^{miss}$ (bottom) in the WVR. The $t\bar{t}$ and W+jets normalisation factors are applied as indicated in the legend. The lower panels show the ratio of the data to the prediction. The error bands include statistical and systematic uncertainties.
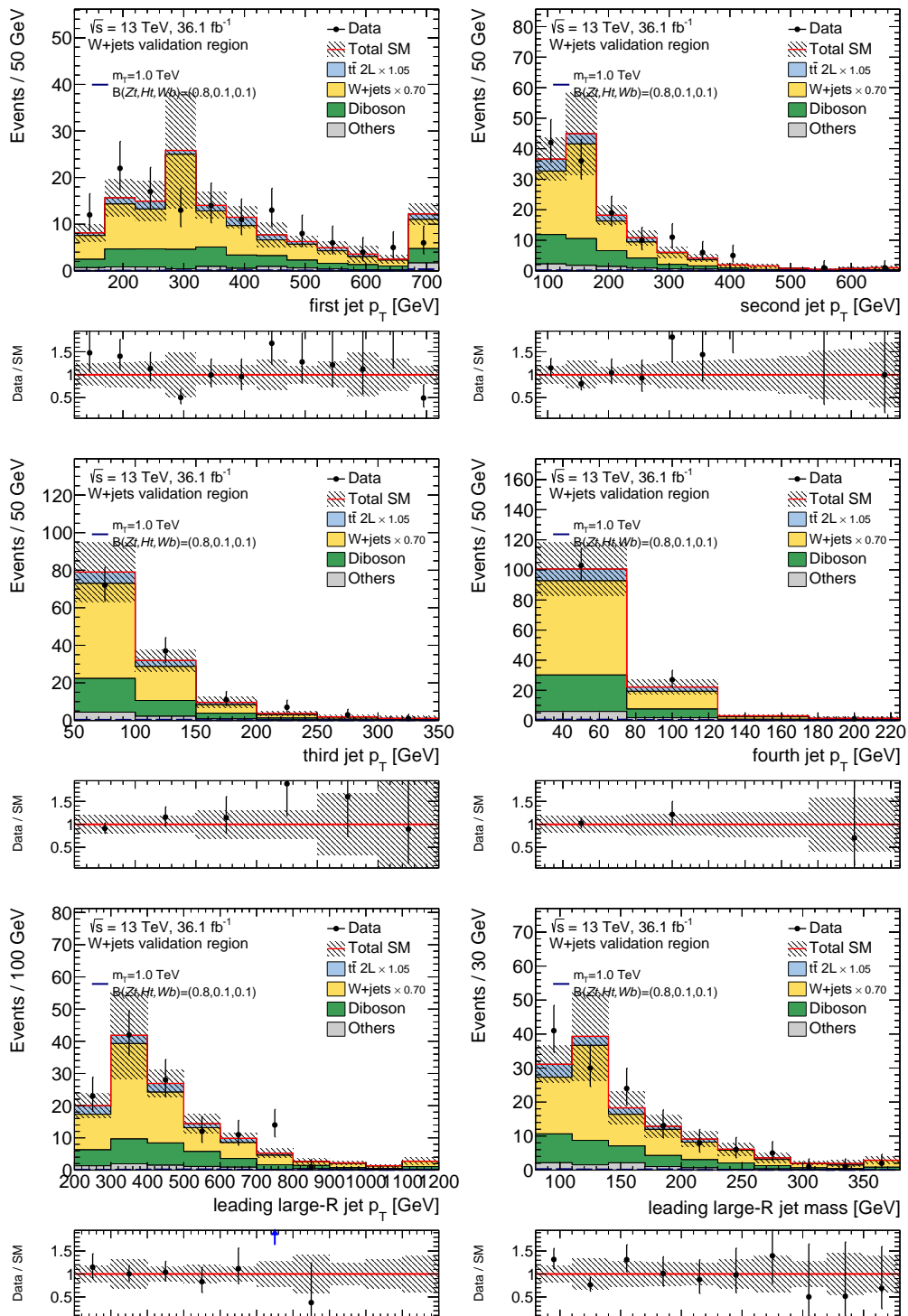
Figure B.17: Distribution of the jet p_T (top, middle) and the p_T and the mass of the leading large-R jet (bottom) in the WVR. The $t\bar{t}$ and W+jets normalisation factors are applied as indicated in the legend. The lower panels show the ratio of the data to the prediction. The error bands include statistical and systematic uncertainties.
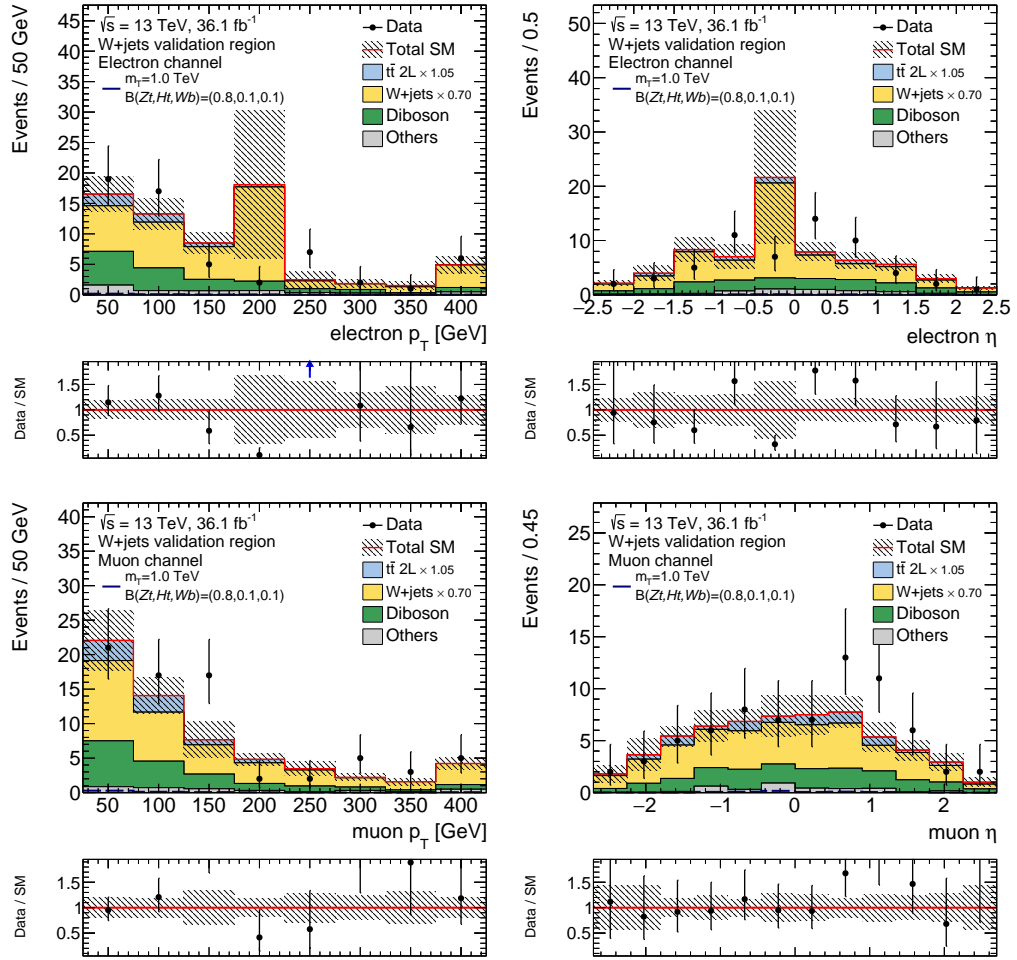
Figure B.18: Distribution of the p_T and the pseudo-rapidity of the signal electron (top) and muon (bottom) in the WVR. The $t\bar{t}$ and W+jets normalisation factors are applied as indicated in the legend. The lower panels show the ratio of the data to the prediction. The error bands include statistical and systematic uncertainties.

B.3.3 Single top validation region
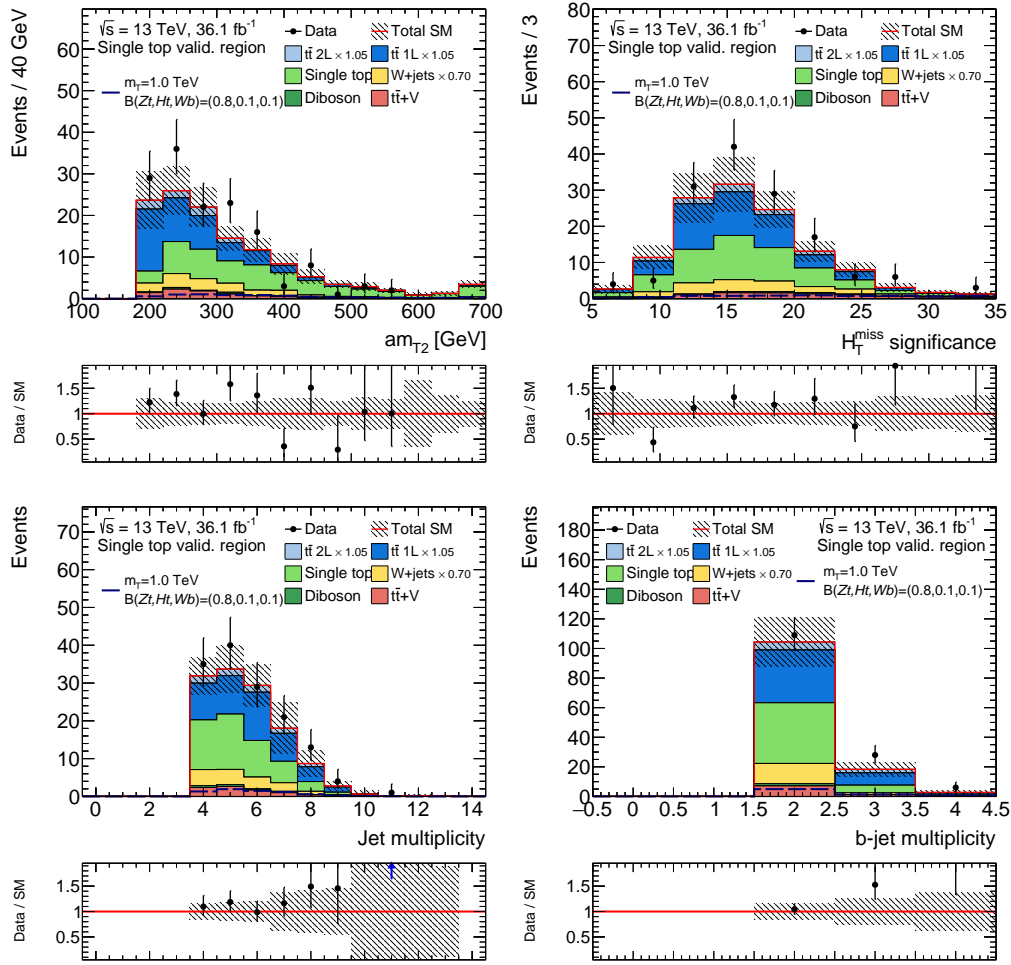
Figure B.19: Distribution of am_{T2} and $H_{T,sig}^{miss}$ (top) and the jet multiplicity and the *b*-jet multiplicity (bottom) in the STVR. The $t\bar{t}$ and *W*+jets normalisation factors are applied as indicated in the legend. The lower panels show the ratio of the data to the prediction. The error bands include statistical and systematic uncertainties.
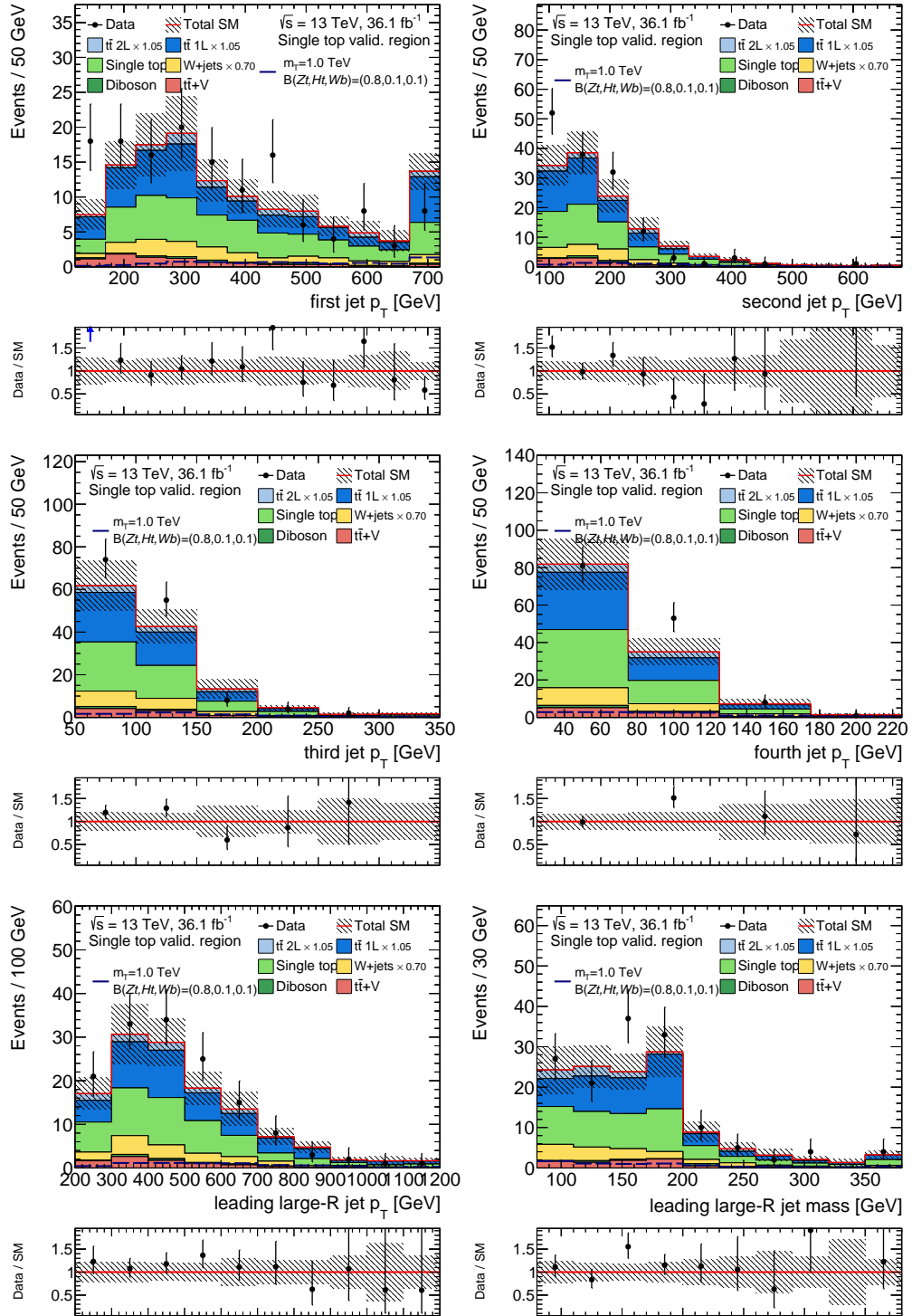
Figure B.20: Distribution of the jet p_T (top, middle) and the p_T and the mass of the leading large-R jet (bottom) in the STVR. The $t\bar{t}$ and W+jets normalisation factors are applied as indicated in the legend. The lower panels show the ratio of the data to the prediction. The error bands include statistical and systematic uncertainties.
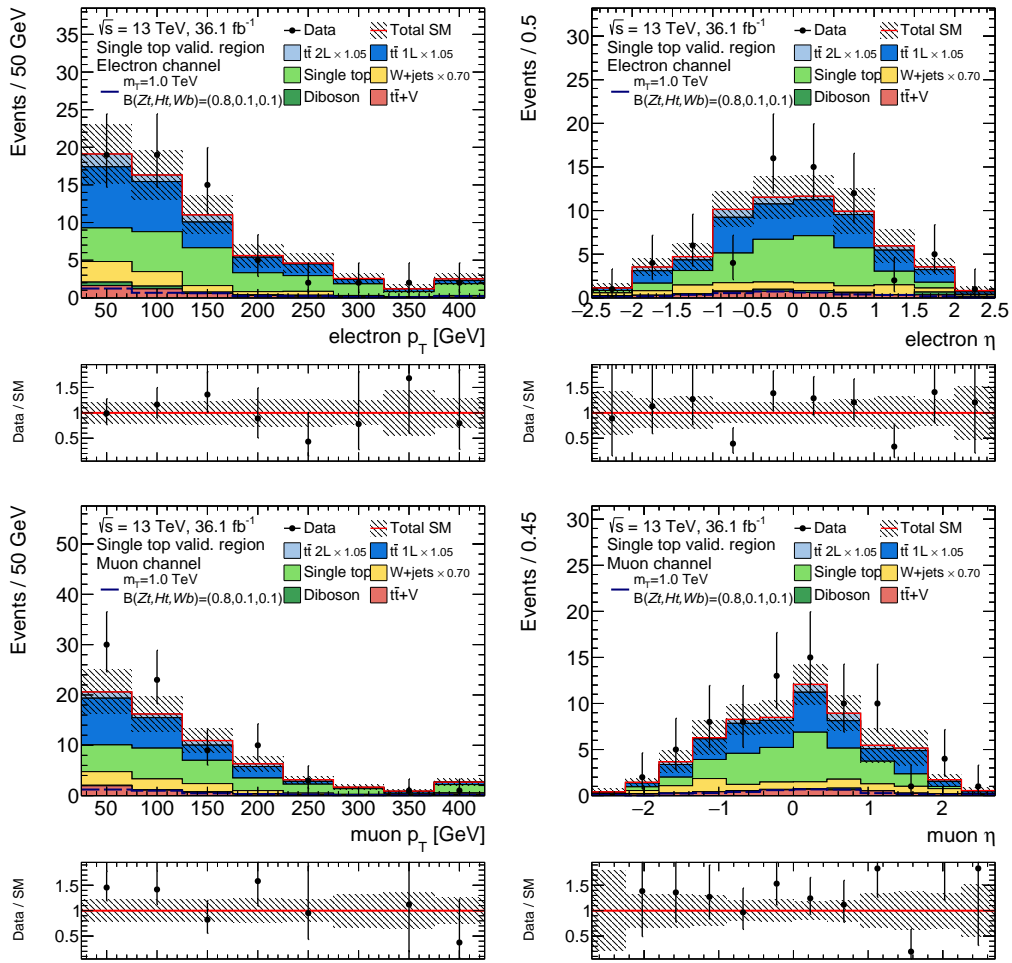
Figure B.21: Distribution of the p_T and the pseudo-rapidity of the signal electron (top) and muon (bottom) in the STVR. The $t\bar{t}$ and W+jets normalisation factors are applied as indicated in the legend. The lower panels show the ratio of the data to the prediction. The error bands include statistical and systematic uncertainties.

Appendix C Search for top squarks

C.1   Additional control region distributions

C.1.1   Dileptonic $t\bar{t}$ control region
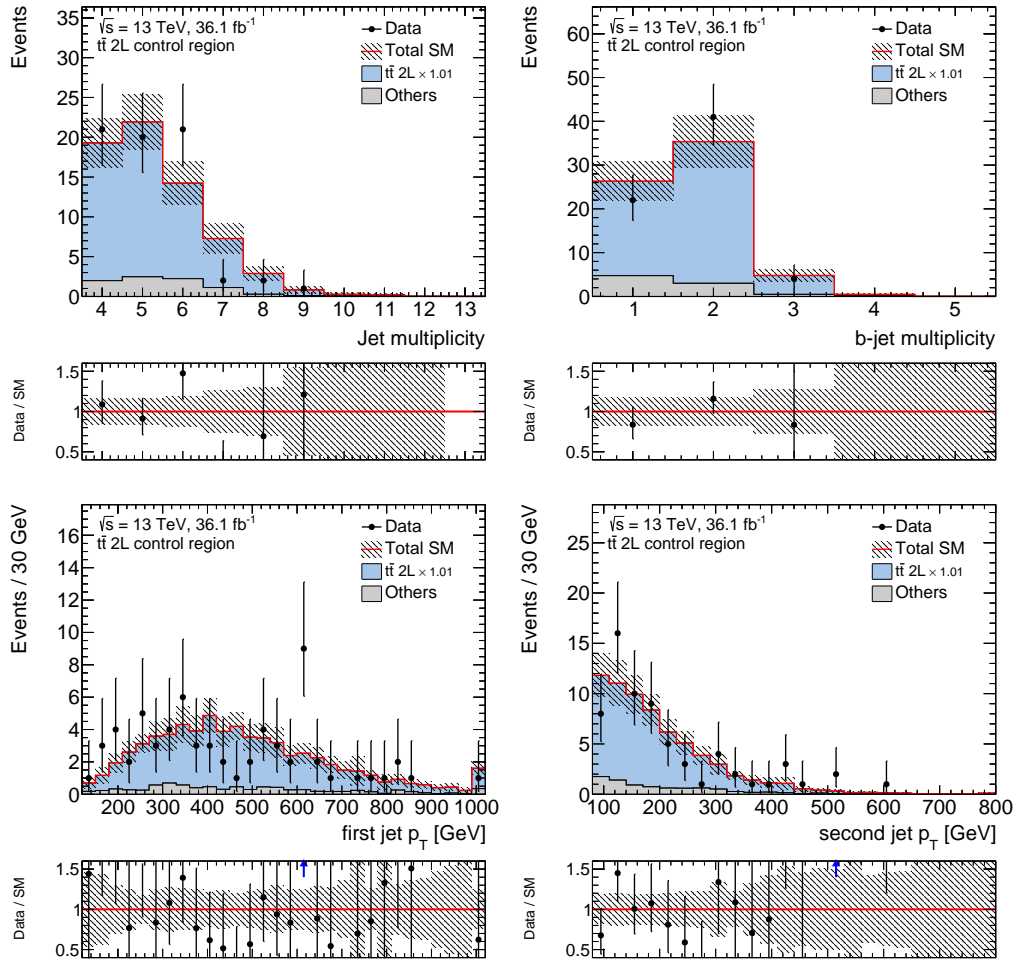
Figure C.1: Distribution of the jet and *b*-jet multiplicity, and the first and second jet p_T in the T2LCR. The background normalisation factors are applied as indicated in the legend. The lower panels show the ratio of the data to the prediction. The error bands include statistical and systematic uncertainties.
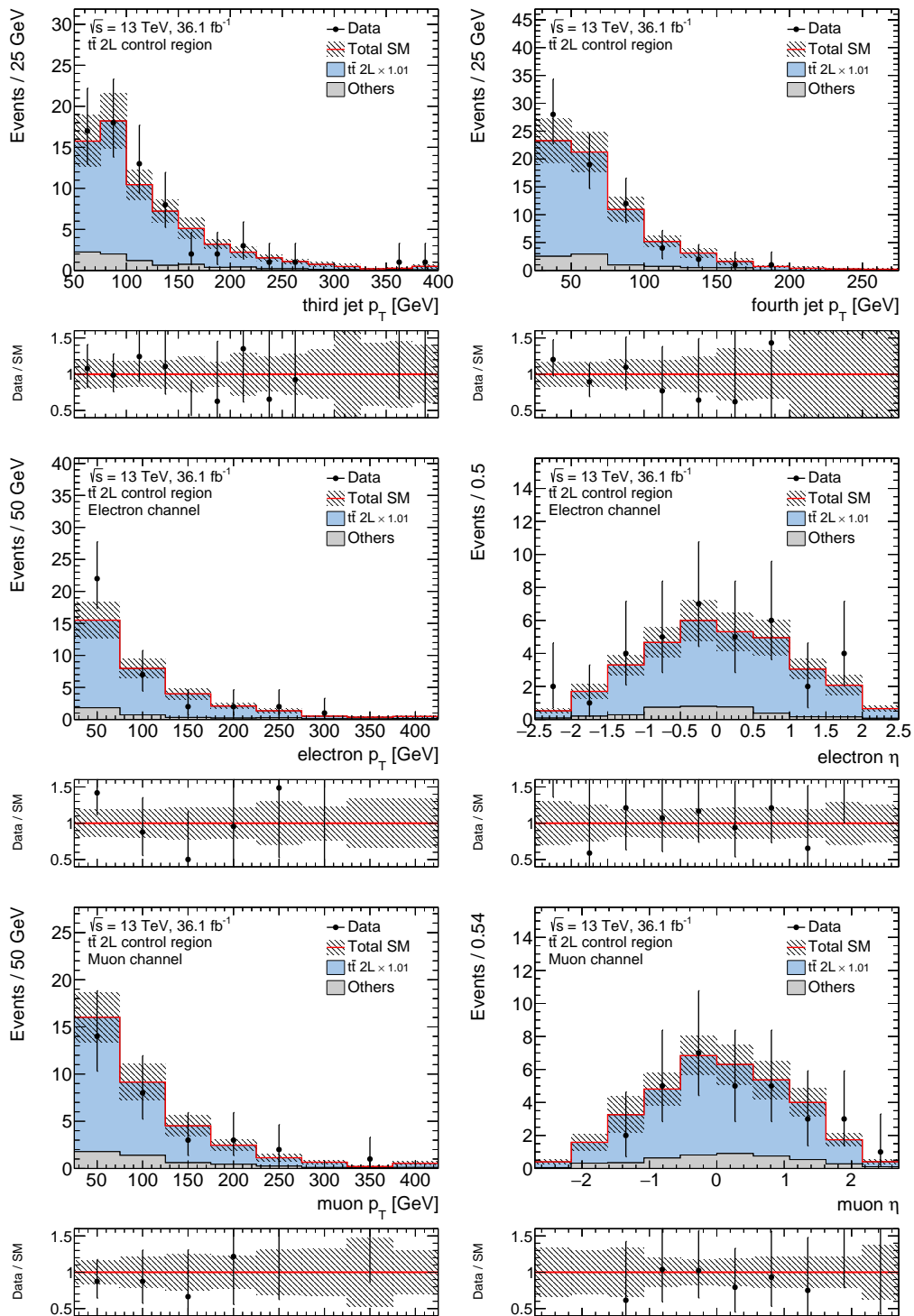
Figure C.2: Distribution of the third and fourth jet p_T (top) and the p_T and η of the electron (middle) and the muon (bottom) in the T2LCR. The background normalisation factors are applied as indicated in the legend. The lower panels show the ratio of the data to the prediction. The error bands include statistical and systematic uncertainties.
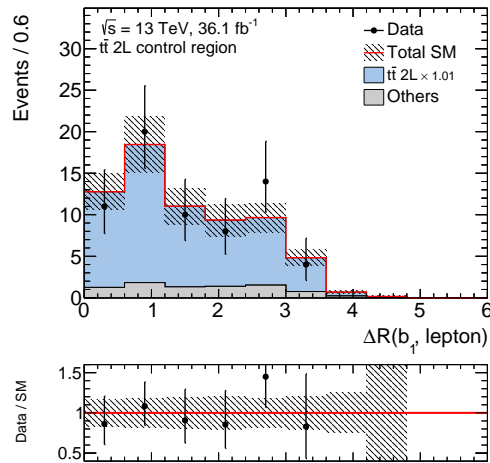
Figure C.3: Distribution of the $\Delta R(b, \ell)$ in the T2LCR. The background normalisation factors are applied as indicated in the legend. The lower panels show the ratio of the data to the prediction. The error bands include statistical and systematic uncertainties.

C.1.2 Semi-leptonic $t\bar{t}$ control region
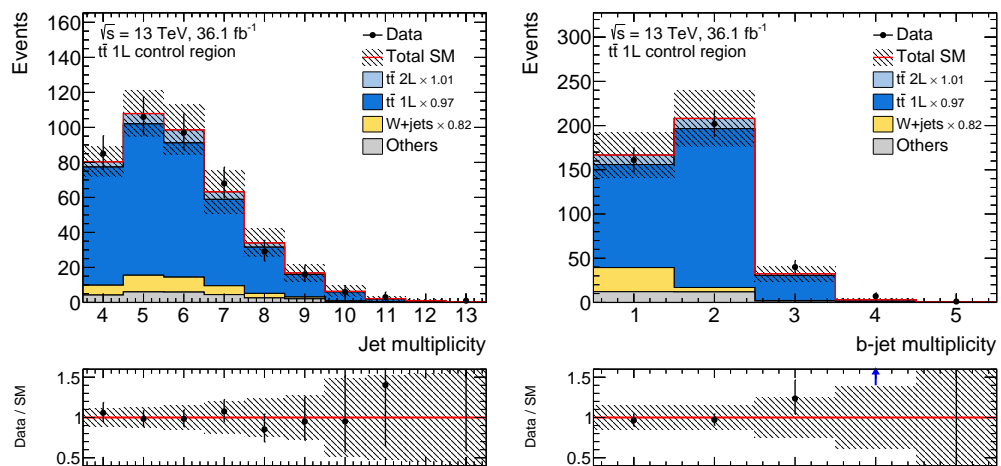
Figure C.4: Distribution of the jet and the b-jet multiplicity in the T1LCR. The background normalisation factors are applied as indicated in the legend. The lower panels show the ratio of the data to the prediction. The error bands include statistical and systematic uncertainties.
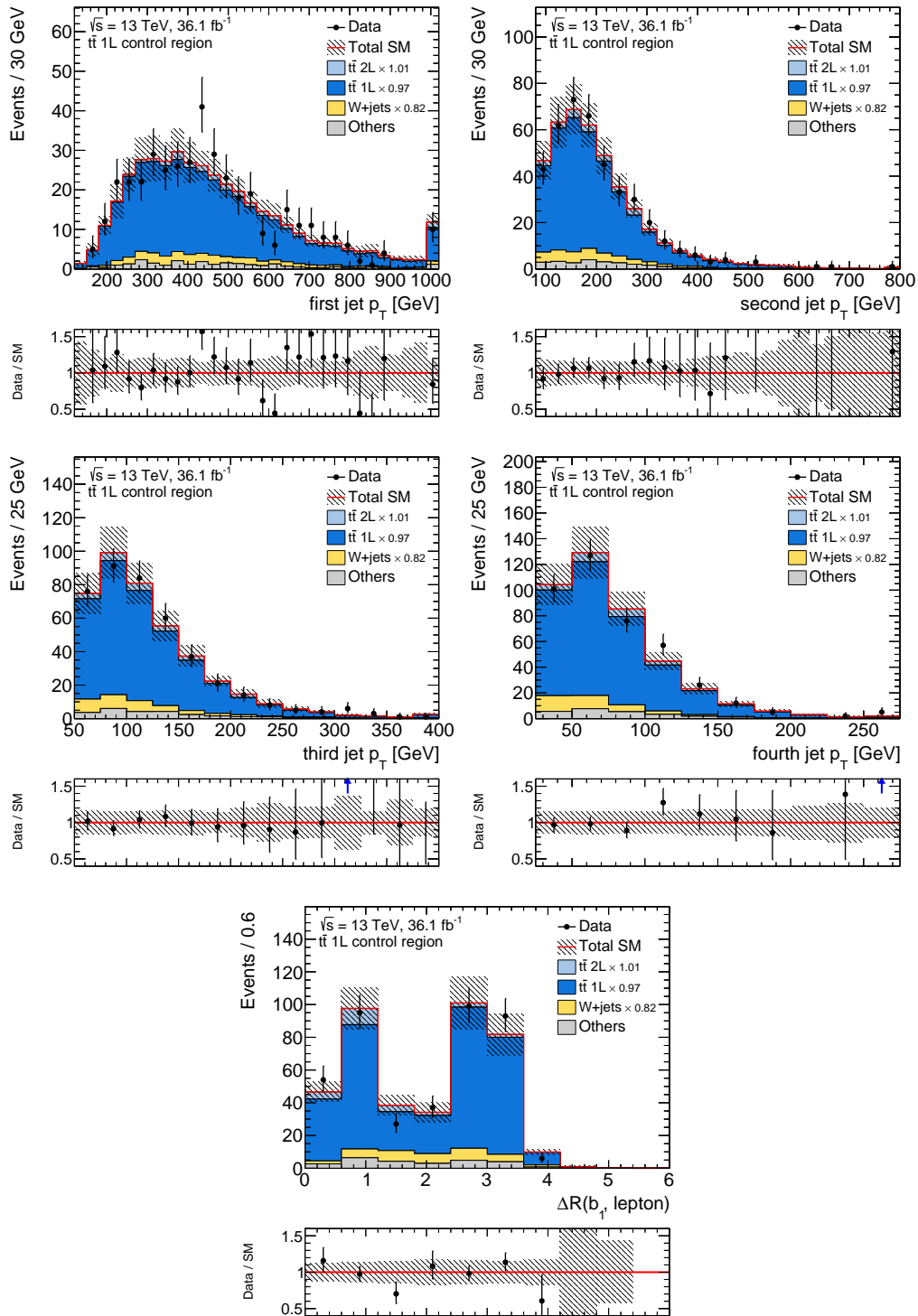
Figure C.5: Distribution of the jet p_T (top, middle) and the $\Delta R(b, \ell)$ (bottom) in the T1LCR. The background normalisation factors are applied as indicated in the legend. The lower panels show the ratio of the data to the prediction. The error bands include statistical and systematic uncertainties.
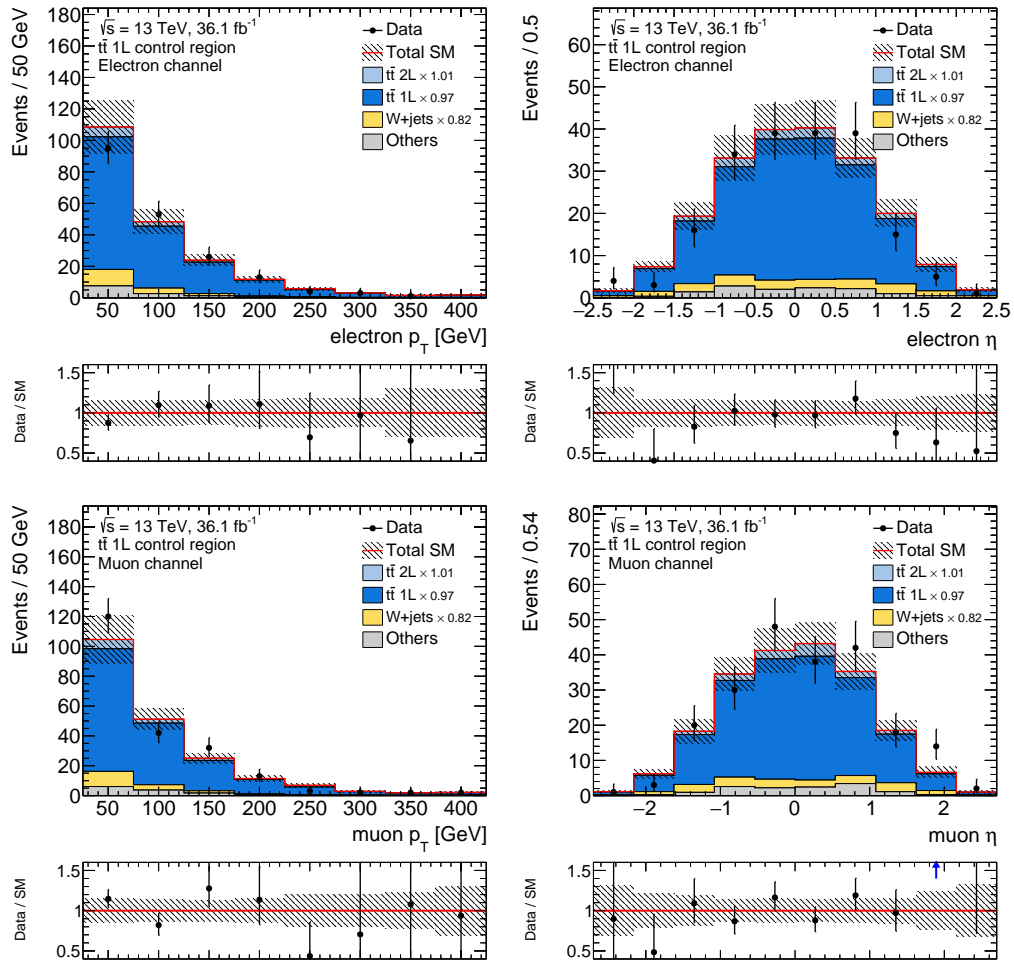
Figure C.6: Distribution of the electron (top) and muon (bottom) p_T and η in the T1LCR. The background normalisation factors are applied as indicated in the legend. The lower panels show the ratio of the data to the prediction. The error bands include statistical and systematic uncertainties.

C.1.3 *W+jets control region*
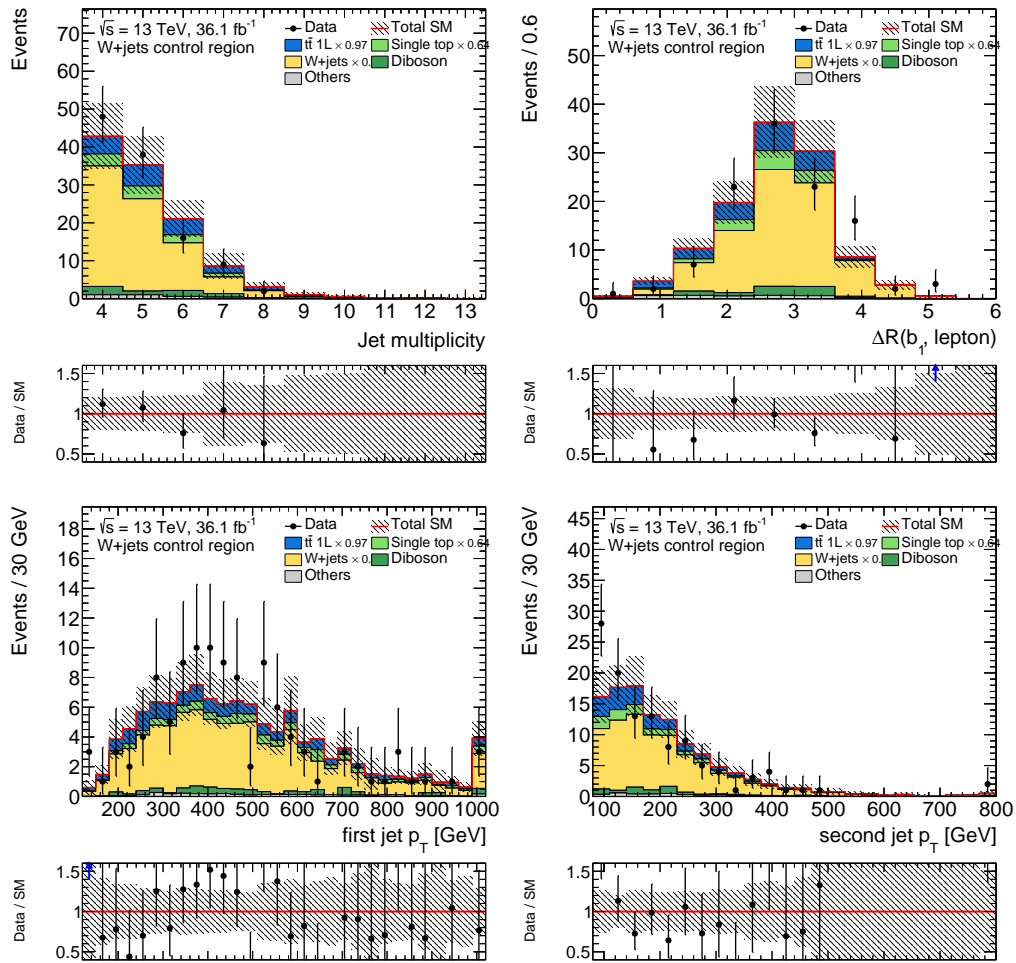
Figure C.7: Distribution of the jet multiplicity and the $\Delta R(b, \ell)$ (top) and the first and second jet p_T (bottom) in the WCR. The background normalisation factors are applied as indicated in the legend. The lower panels show the ratio of the data to the prediction. The error bands include statistical and systematic uncertainties.
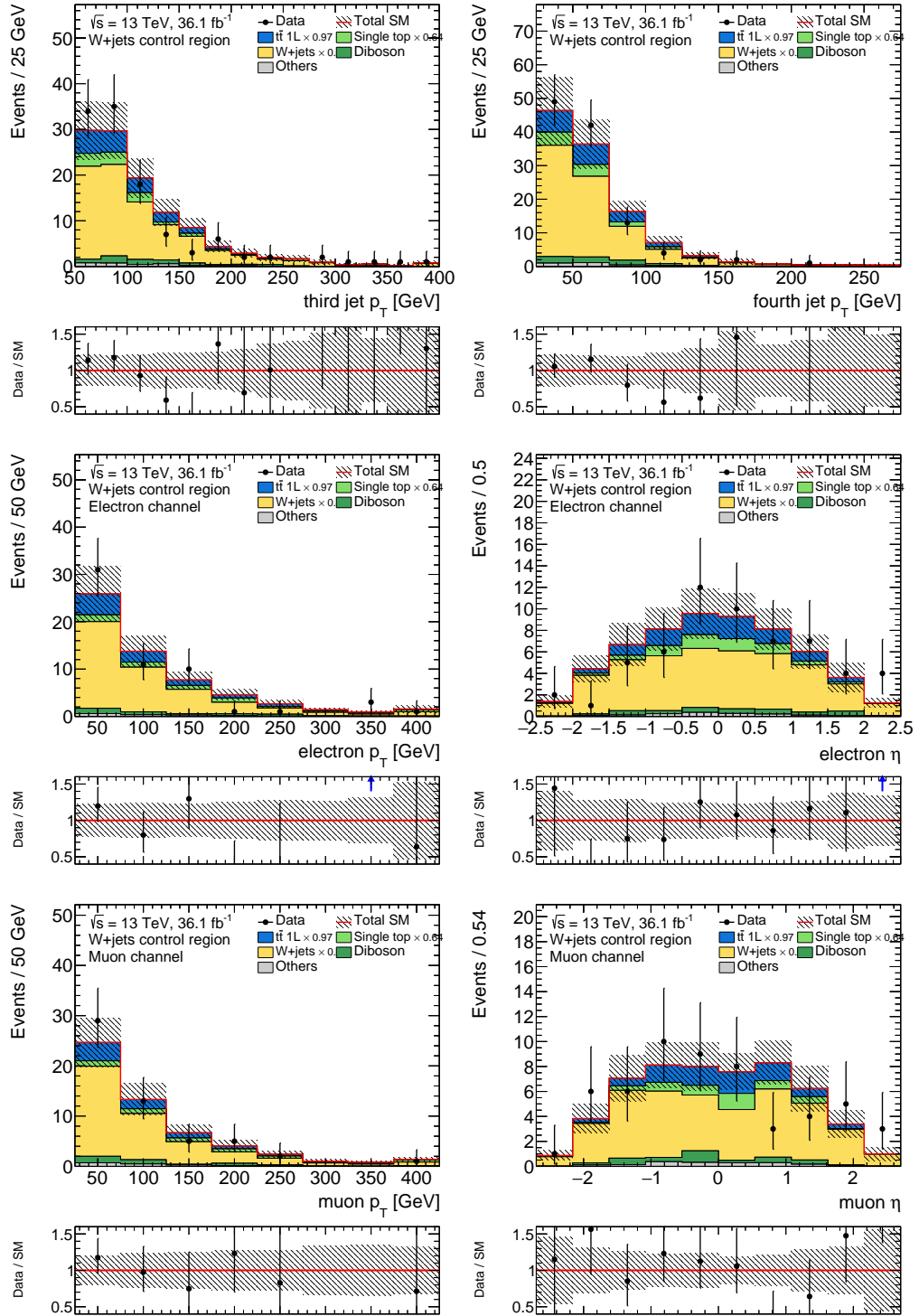
Figure C.8: Distribution of the third and fourth jet p_T (top) and the electron (middle) and muon (bottom) p_T and η in the WCR. The background normalisation factors are applied as indicated in the legend. The lower panels show the ratio of the data to the prediction. The error bands include statistical and systematic uncertainties.
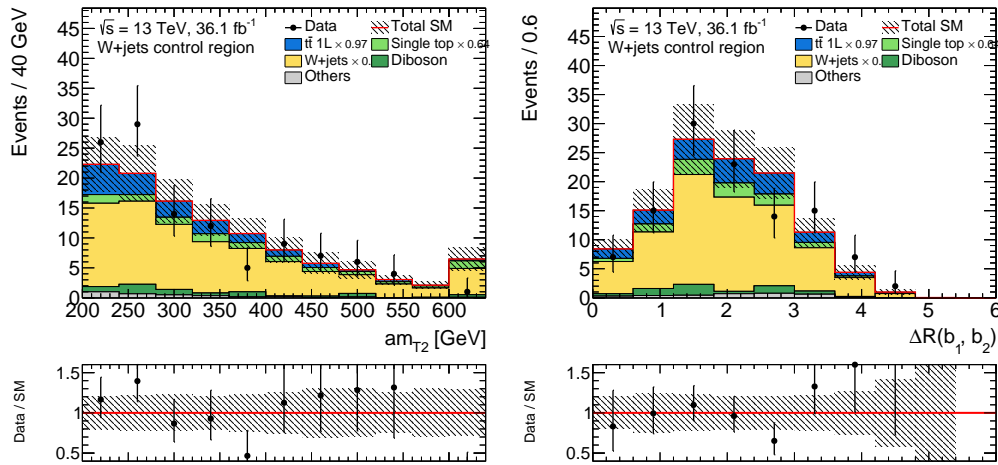
Figure C.9: Distribution of the am_{T2} and the $\Delta R(b, b)$ in the WCR. The background normalisation factors are applied as indicated in the legend. The lower panels show the ratio of the data to the prediction. The error bands include statistical and systematic uncertainties.

C.1.4 Single top control region
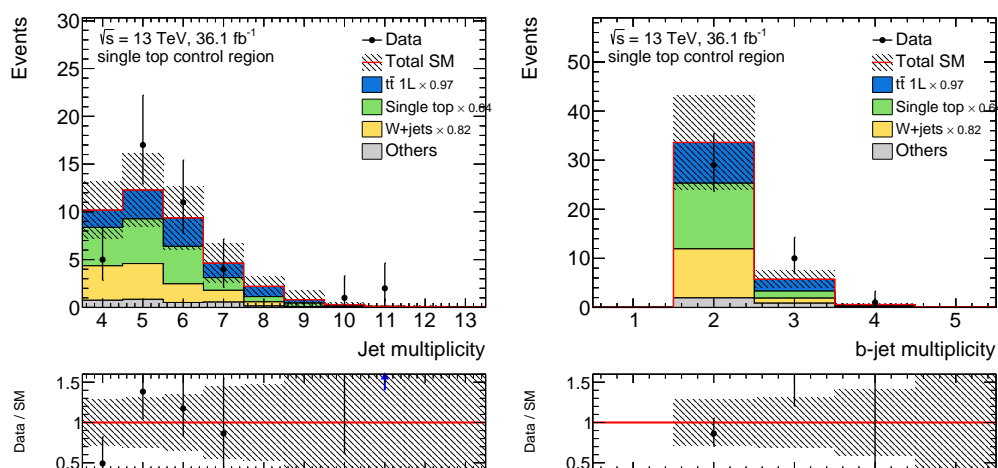
Figure C.10: Distribution of the jet and the *b*-jet multiplicity in the STCR. The background normalisation factors are applied as indicated in the legend. The lower panels show the ratio of the data to the prediction. The error bands include statistical and systematic uncertainties.
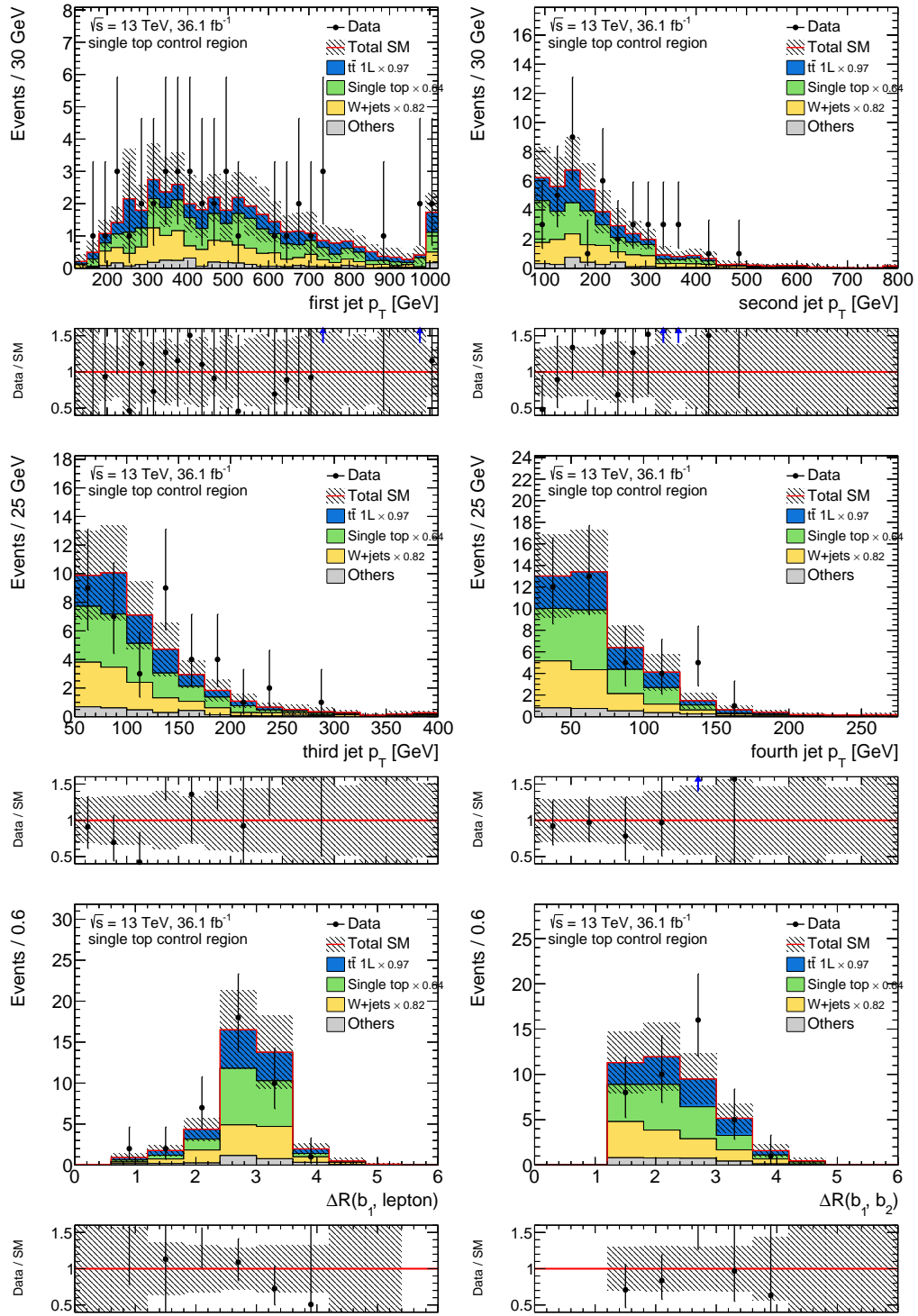
Figure C.11: Distribution of the jet p_T (top, middle) and the $\Delta R(b, \ell)$ and the $\Delta R(b, b)$ (bottom) in the STCR. The background normalisation factors are applied as indicated in the legend. The lower panels show the ratio of the data to the prediction. The error bands include statistical and systematic uncertainties.
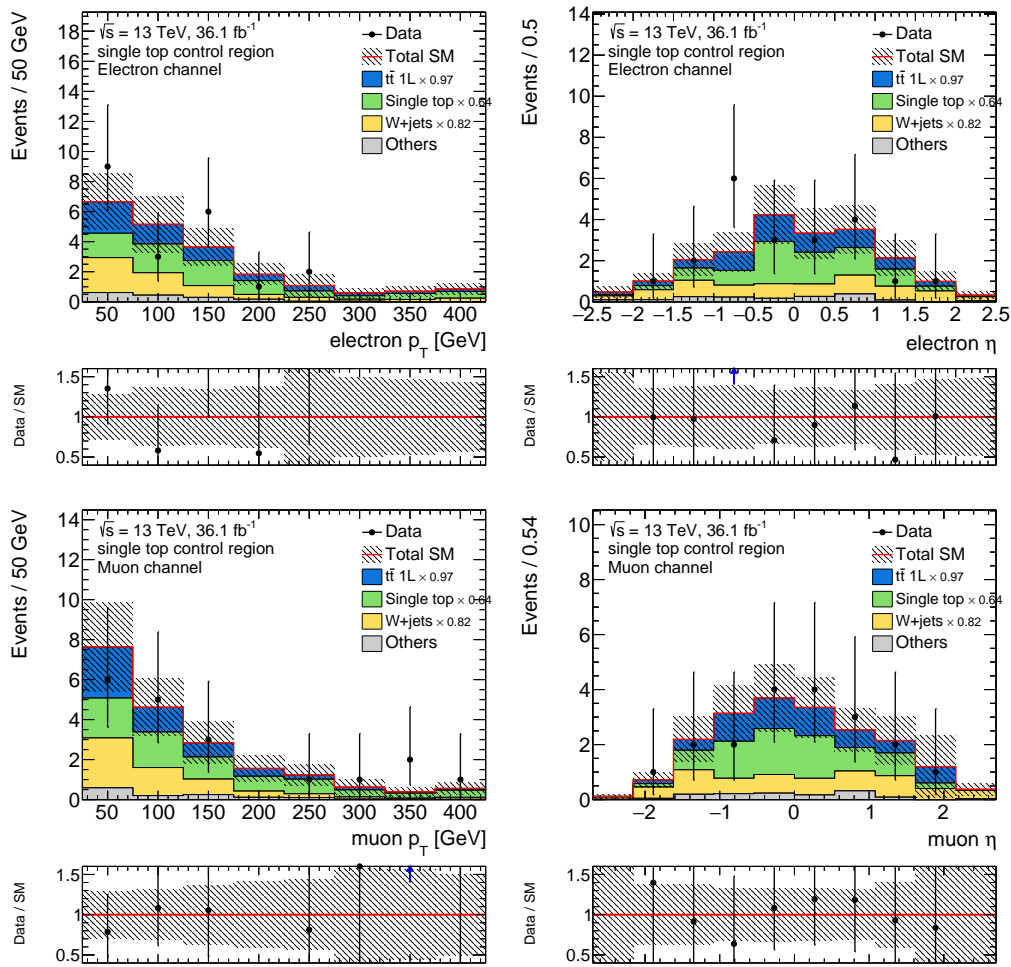
Figure C.12: Distribution of the electron (top) and muon (bottom) p_T and η in the STCR. The background normalisation factors are applied as indicated in the legend. The lower panels show the ratio of the data to the prediction. The error bands include statistical and systematic uncertainties.

C.2 Additional validation region distributions

C.2.1 Dileptonic $t\bar{t}$ validation region
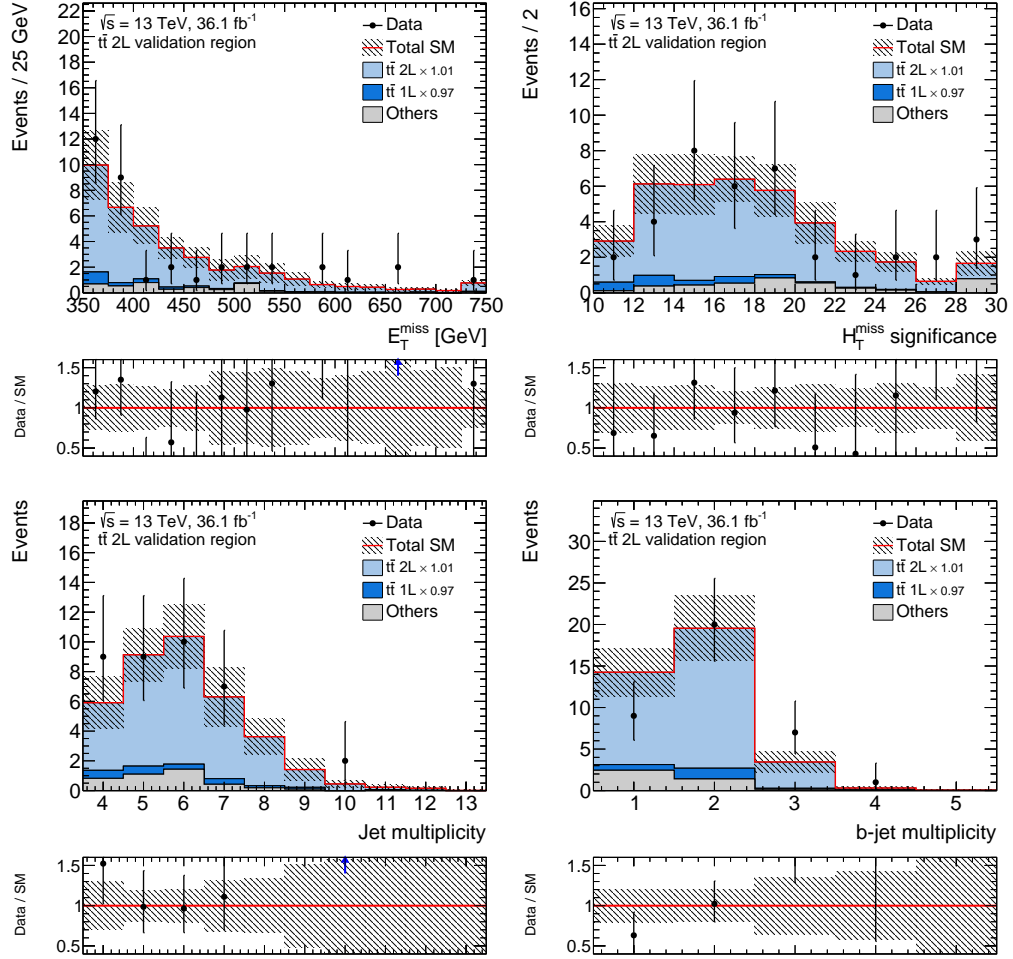
Figure C.13: Distribution of the E_T^{miss} and the $H_{T,sig}^{miss}$ (top) and the jet and b-jet multiplicity (bottom) in the T2LVR. The background normalisation factors are applied as indicated in the legend. The lower panels show the ratio of the data to the prediction. The error bands include statistical and systematic uncertainties.
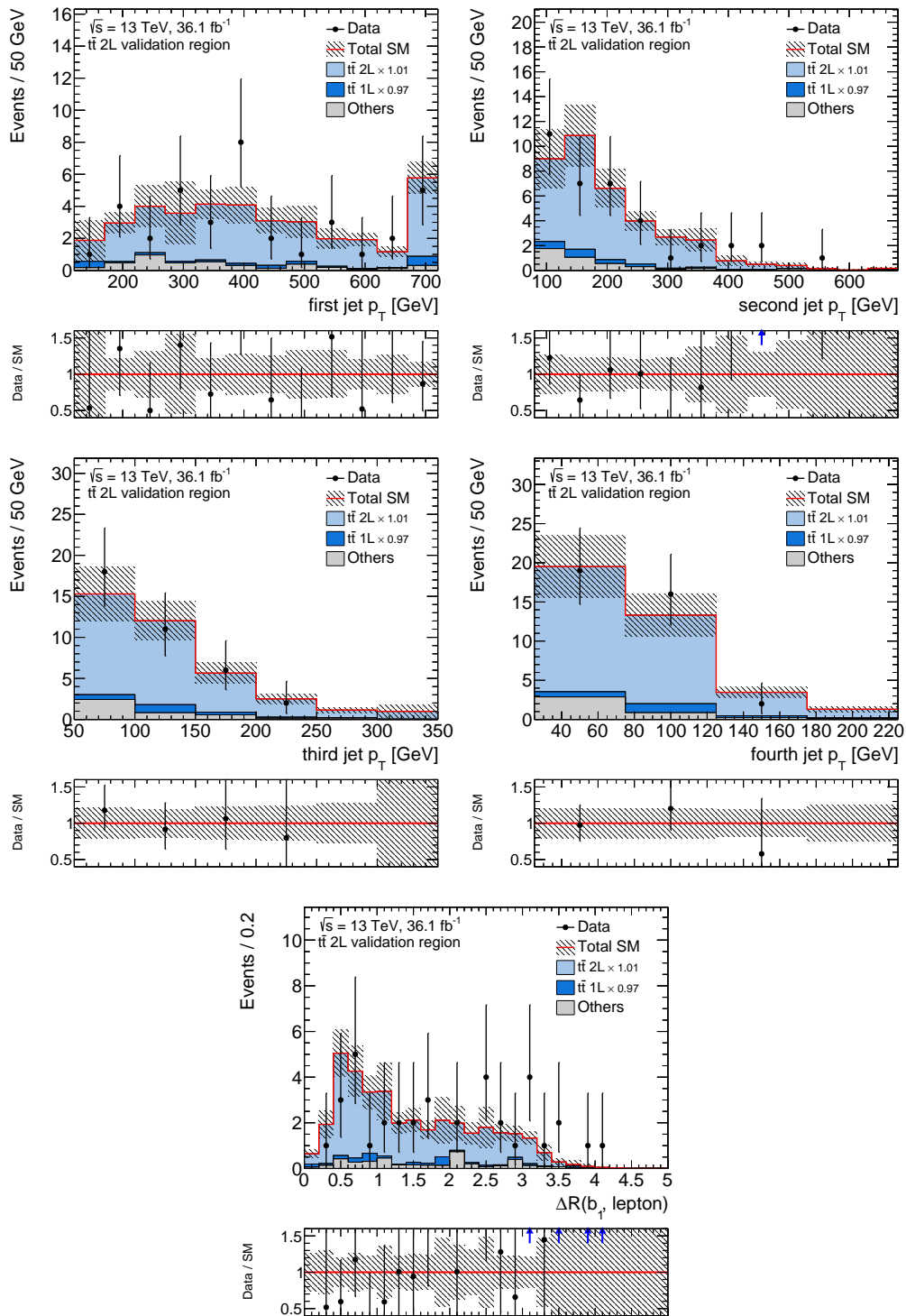
Figure C.14: Distribution of the jet p_T (top, middle) and the $\Delta R(b, \ell)$ (bottom) in the T2LVR. The background normalisation factors are applied as indicated in the legend. The lower panels show the ratio of the data to the prediction. The error bands include statistical and systematic uncertainties.
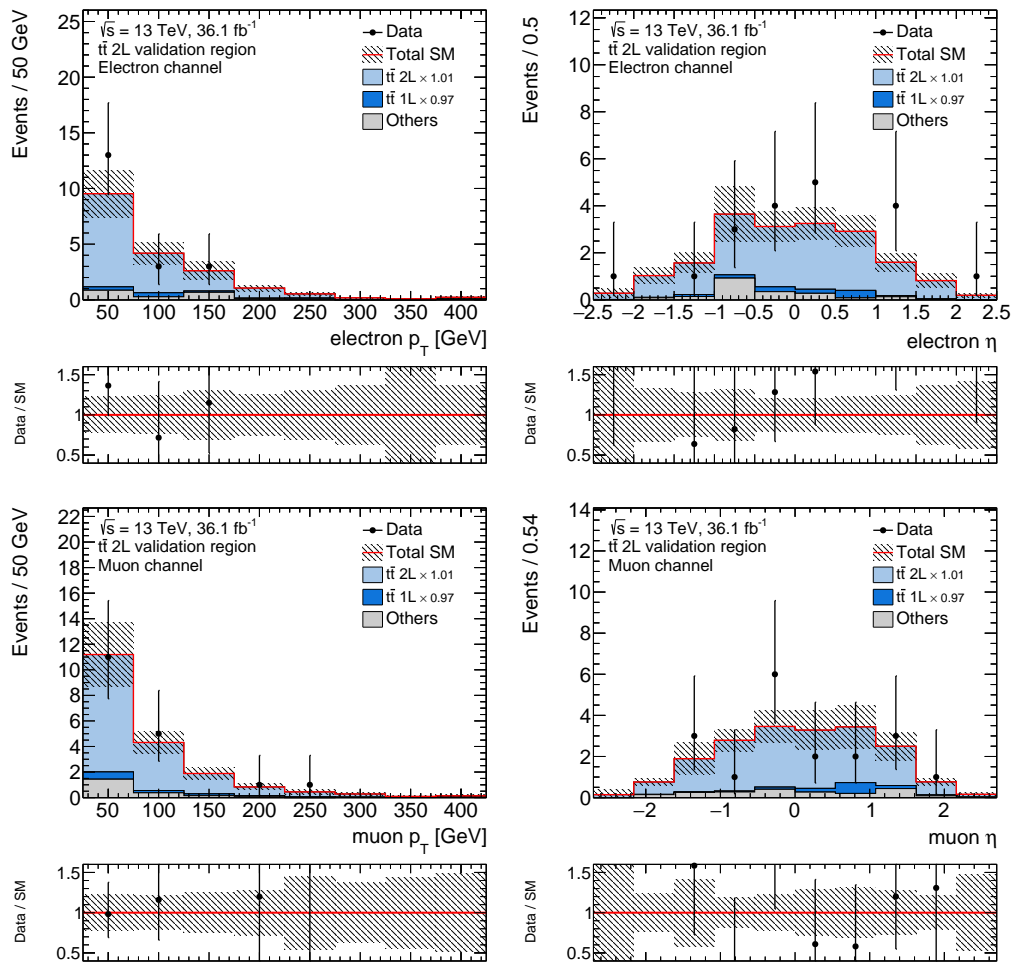
Figure C.15: Distribution of the electron (top) and muon (bottom) p_T and η in the T2LVR. The background normalisation factors are applied as indicated in the legend. The lower panels show the ratio of the data to the prediction. The error bands include statistical and systematic uncertainties.

C.2.2 Semi-leptonic $t\bar{t}$ validation region
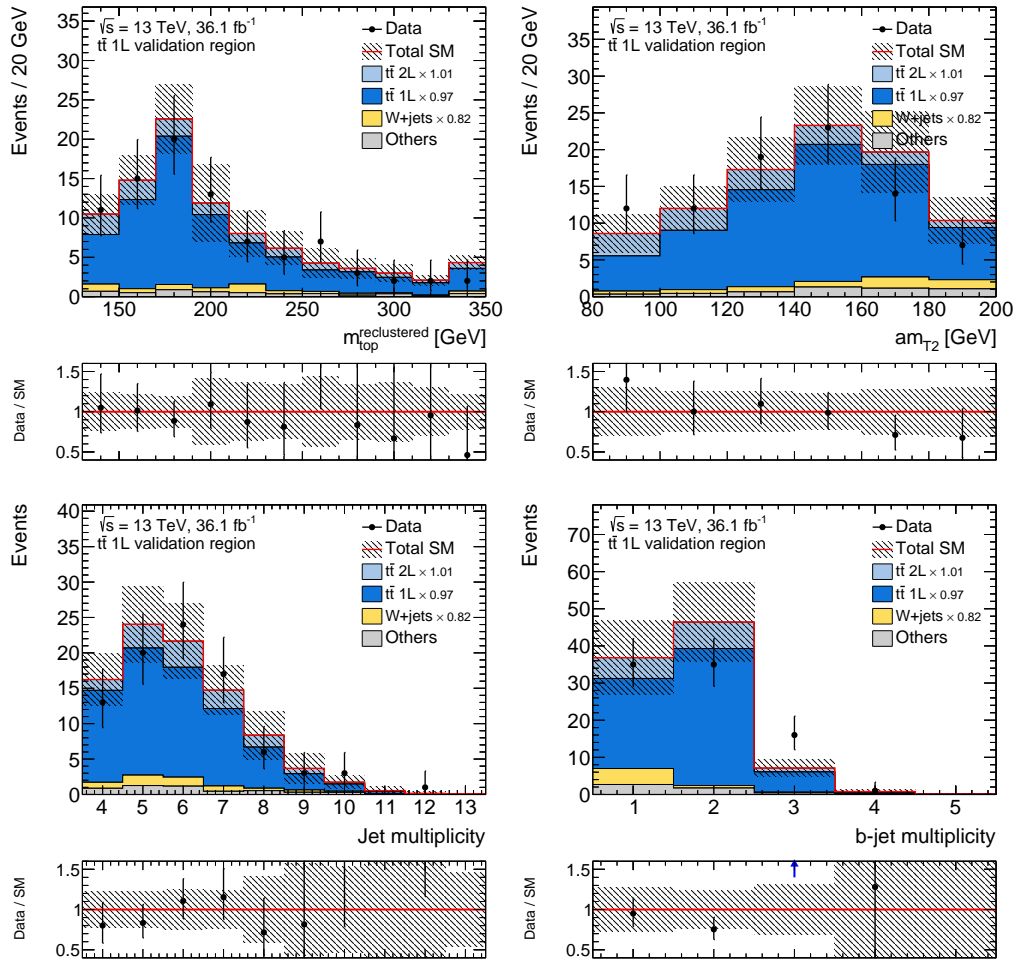
Figure C.16: Distribution of the hadronic top mass and the am_{T2} (top) and the jet and the b-jet multiplicity (bottom) in the T1LVR. The background normalisation factors are applied as indicated in the legend. The lower panels show the ratio of the data to the prediction. The error bands include statistical and systematic uncertainties.
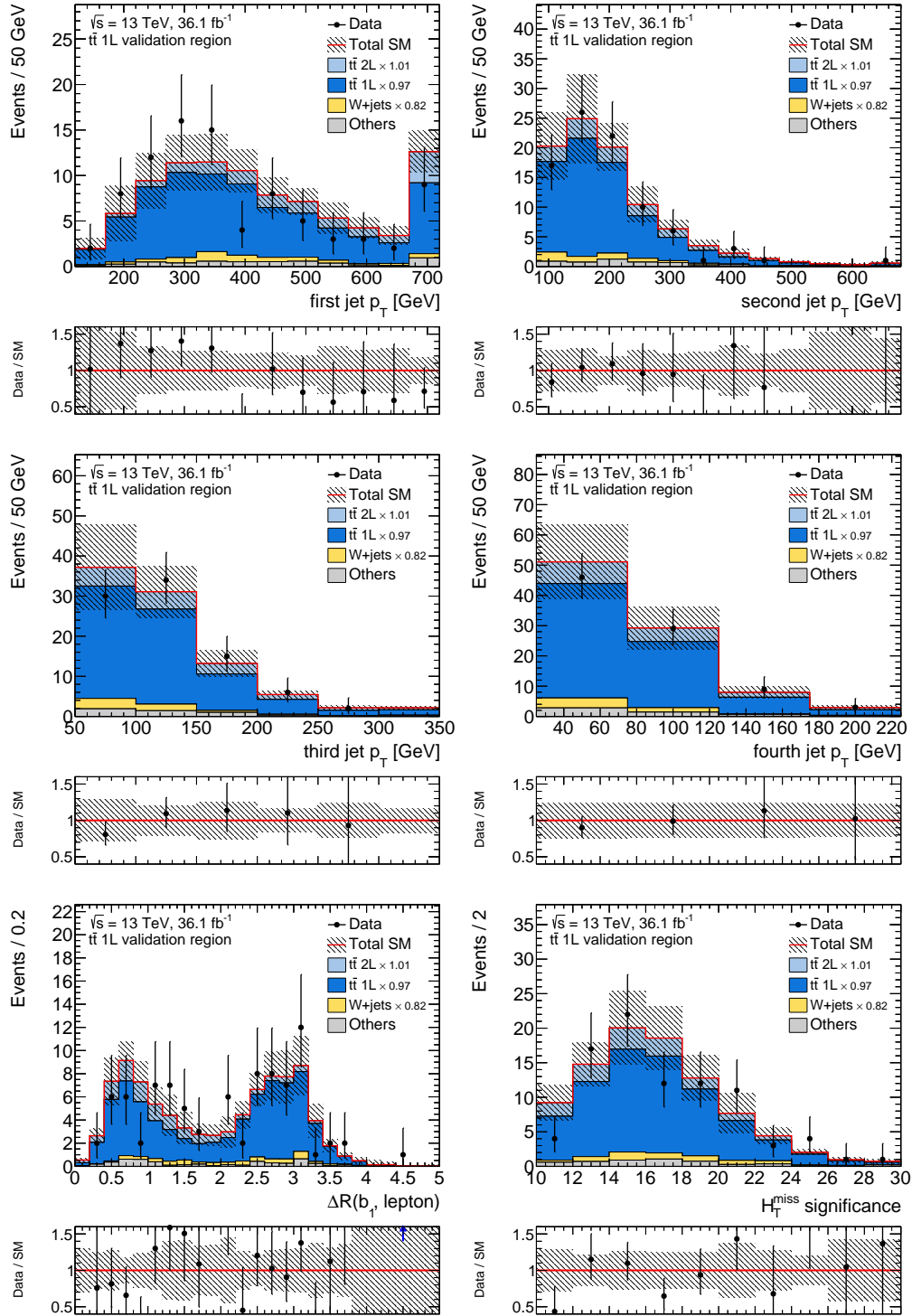
Figure C.17: Distribution of the jet p_T (top, middle) and the $\Delta R(b, \ell)$ and the $H_{T,\text{sig}}^{\text{miss}}$ (bottom) in the T1LVR. The background normalisation factors are applied as indicated in the legend. The lower panels show the ratio of the data to the prediction. The error bands include statistical and systematic uncertainties.
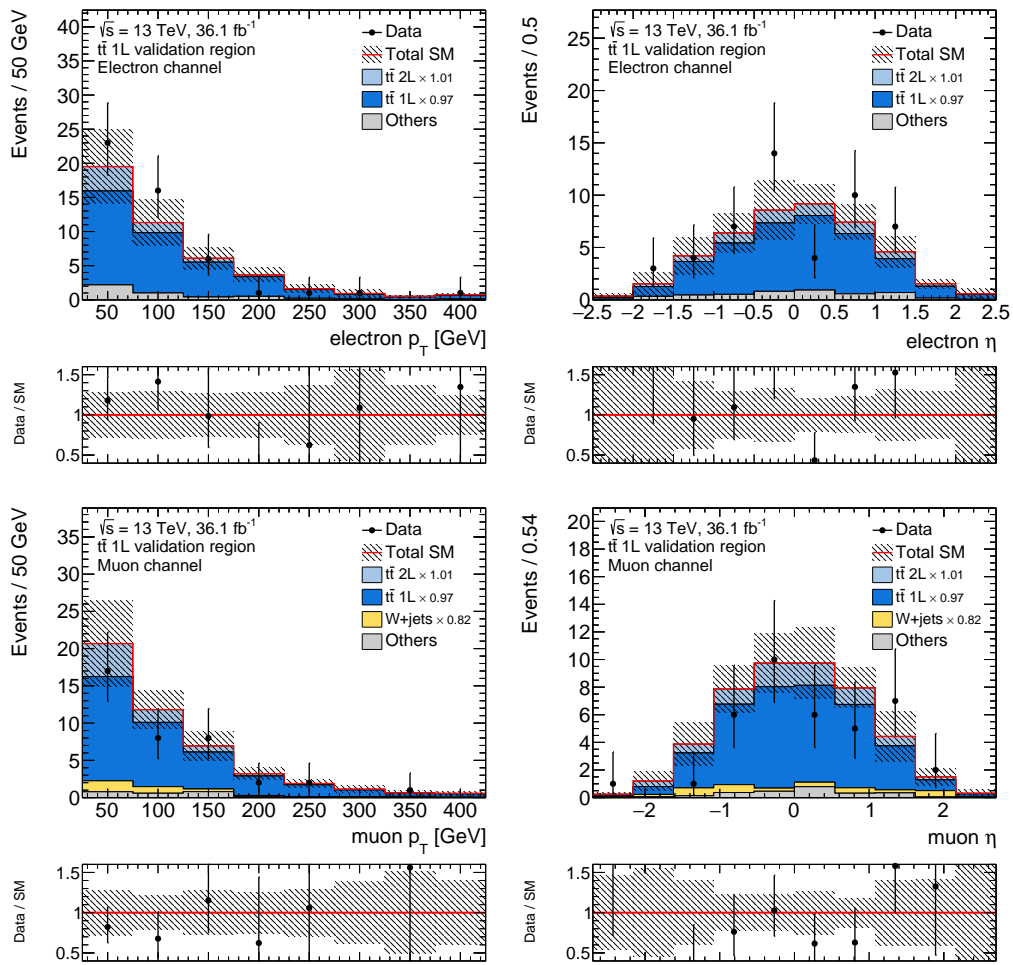
Figure C.18: Distribution of the electron (top) and muon (bottom) p_T and η in the T1LVR. The background normalisation factors are applied as indicated in the legend. The lower panels show the ratio of the data to the prediction. The error bands include statistical and systematic uncertainties.

C.2.3 *W*+jets validation region
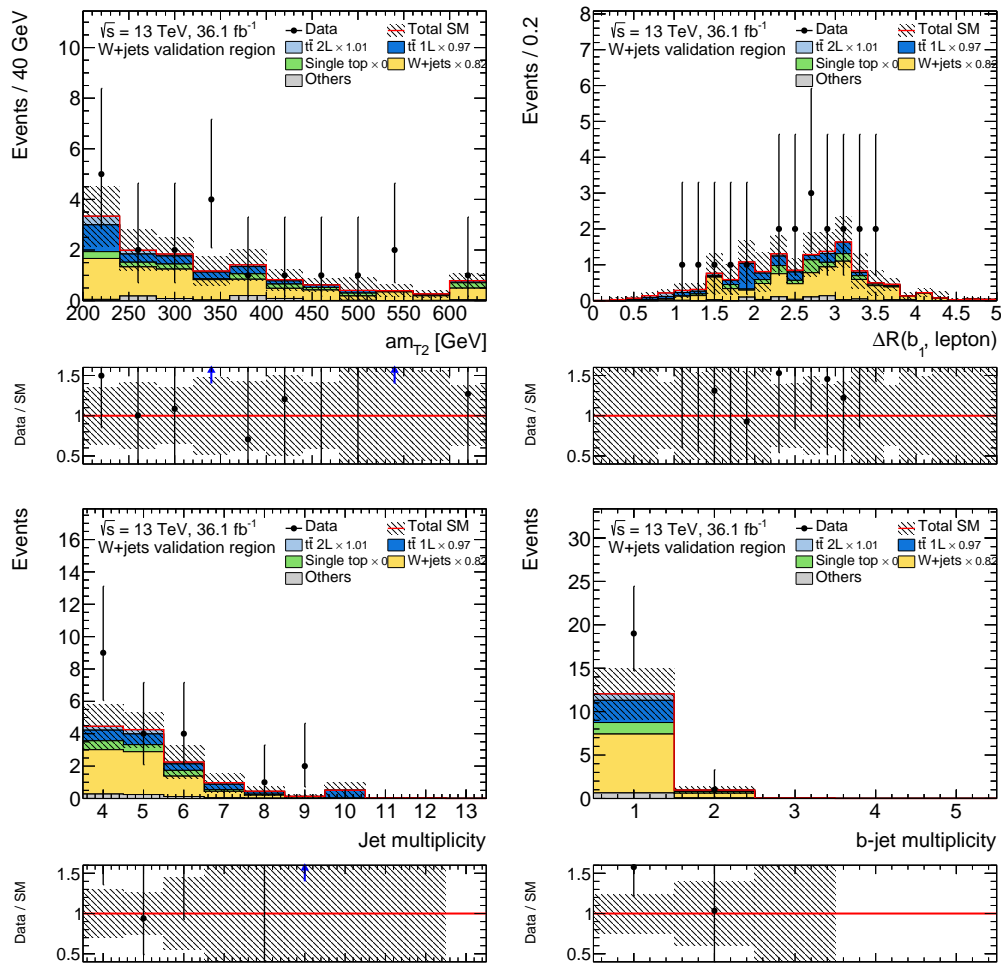
Figure C.19: Distribution of the *am*$_{T2}$ and the $\Delta R(b, \ell)$ (top) and the jet and the *b*-jet multiplicity (bottom) in the WVR. The background normalisation factors are applied as indicated in the legend. The lower panels show the ratio of the data to the prediction. The error bands include statistical and systematic uncertainties.
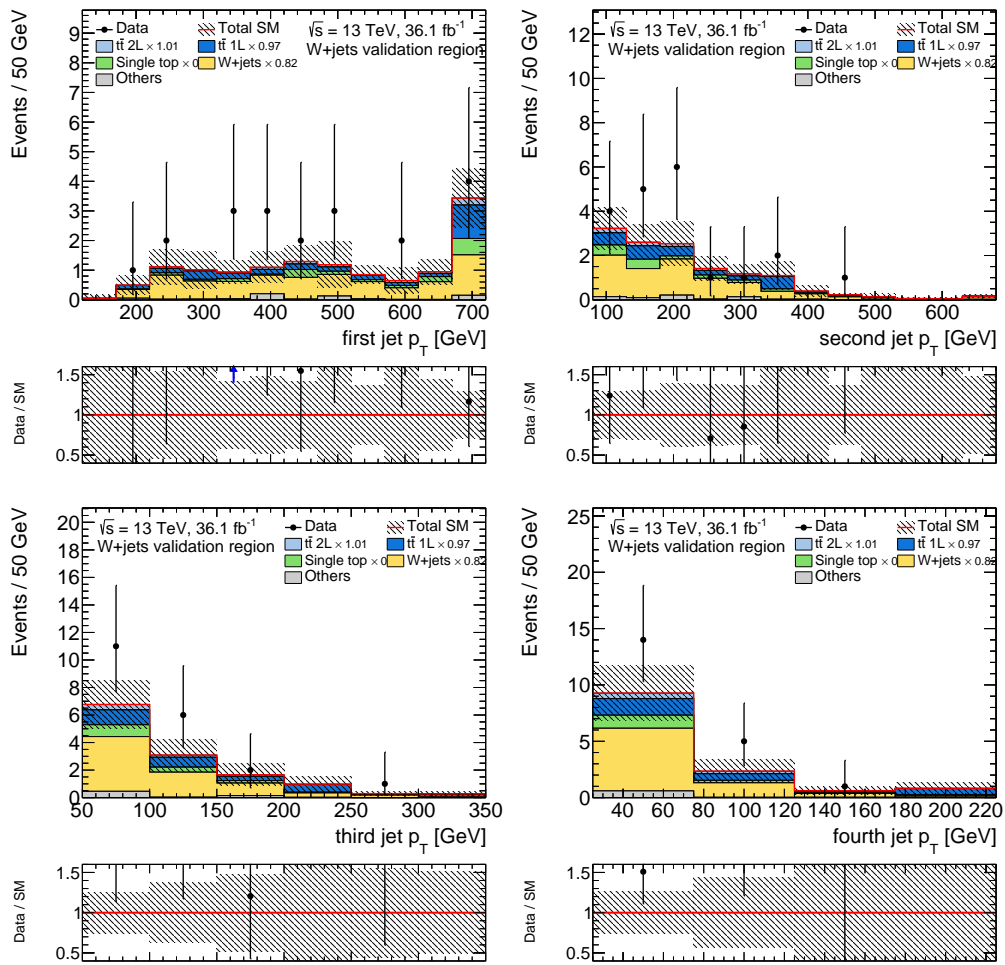
Figure C.20: Distribution of the jet p_T in the WVR. The background normalisation factors are applied as indicated in the legend. The lower panels show the ratio of the data to the prediction. The error bands include statistical and systematic uncertainties.
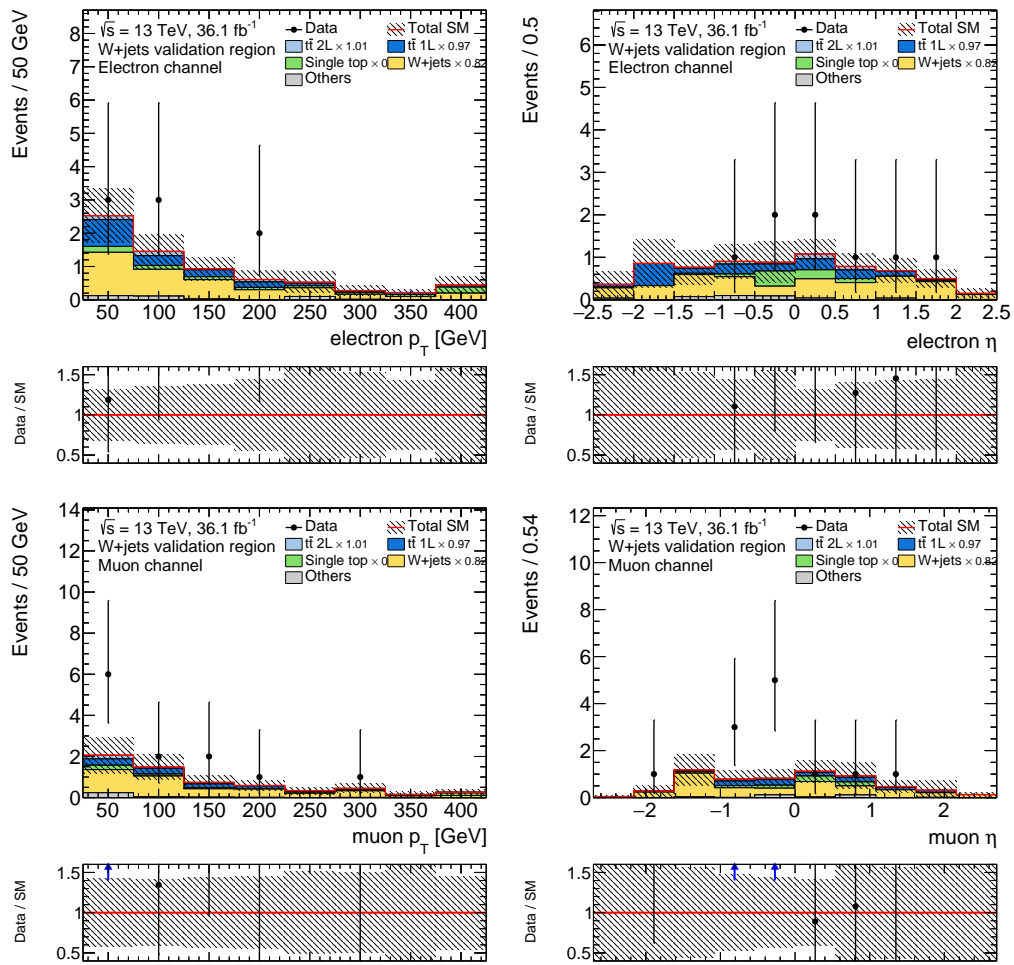
Figure C.21: Distribution of the electron (top) and muon (bottom) p_T and η in the WVR. The background normalisation factors are applied as indicated in the legend. The lower panels show the ratio of the data to the prediction. The error bands include statistical and systematic uncertainties.

C.3   Combination of tN_high and bCsoft_high
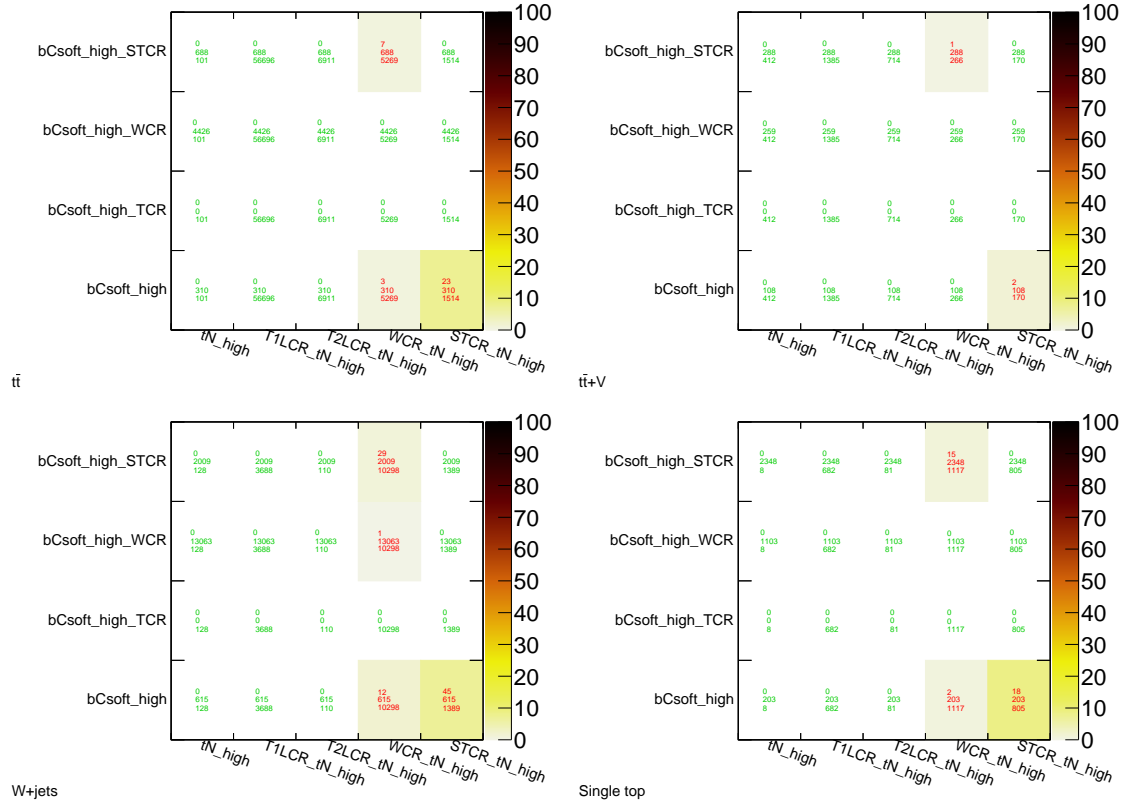
Figure C.22: Number of simulated events selected by both a bCsoft_high and tN_high associated region for the $t\bar{t}$ (top left), $t\bar{t} + V$ (top right), W+jets (bottom left) and single top (bottom right) backgrounds after the overlap veto. The numbers in each bin give the number of overlapping events and the number of events selected by the region indicated on the vertical axis and the horizontal axis, respectively, from top to bottom. The colour scale indicates the fraction of overlapping events.
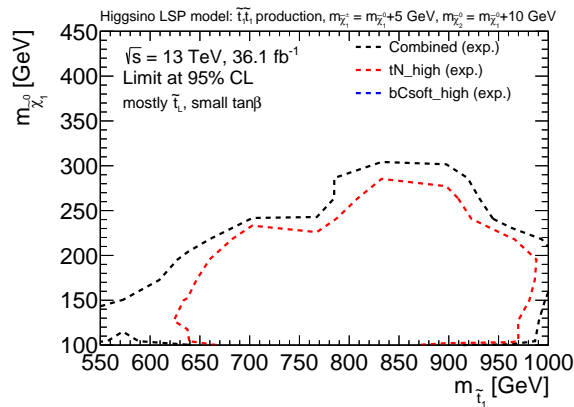
Figure C.23: Expected 95% CL exclusion contour for the higgsino LSP signal with $\tilde{t}_1 \sim \tilde{t}_L$ and small $\tan\beta$ in the $m_{\tilde{t}_1}$ versus $m_{\tilde{\chi}_1^0}$ plane for the individual tN_high and bCsoft_high regions and for the combination.

Bibliography

[1]   ATLAS Collaboration, *Charged-particle distributions in $\sqrt{s}$ = 13 TeV pp interactions measured with the ATLAS detector at the LHC*, Phys. Lett. B **758** (2016) p. 67, arXiv: 1602.01633 [hep-ex].

[2]   ATLAS Collaboration, *Search for top squarks in final states with one isolated lepton, jets, and missing transverse momentum in $\sqrt{s}$ = 13 TeV pp collisions with the ATLAS detector*, Phys. Rev. D **94** (2016) p. 052009, arXiv: 1606.03903 [hep-ex].

[3]   ATLAS Collaboration, *Search for pair production of vector-like top quarks in events with one lepton, jets, and missing transverse momentum in $\sqrt{s}$ = 13 TeV pp collisions with the ATLAS detector*, JHEP **08** (2017) p. 052, arXiv: 1705.10751 [hep-ex].

[4]   ATLAS Collaboration, *Search for top-squark pair production in final states with one lepton, jets, and missing transverse momentum using 36 fb^{-1} of $\sqrt{s}$ = 13 TeV pp collision data with the ATLAS detector*, JHEP **06** (2018) p. 108, arXiv: 1711.11520 [hep-ex].

[5]   ATLAS Collaboration, *Track Reconstruction Performance of the ATLAS Inner Detector at $\sqrt{s}$ = 13 TeV*, ATL-PHYS-PUB-2015-018, 2015, URL: https://cds.cern.ch/record/2037683.

[6]   S. L. Glashow, *Partial Symmetries of Weak Interactions*, Nucl. Phys. **22** (1961) p. 579.

[7]   S. Weinberg, *A Model of Leptons*, Phys. Rev. Lett. **19** (1967) p. 1264.

[8]   A. Salam, *Gauge Unification of Fundamental Forces*, Rev. Mod. Phys. **52** (1980) p. 525.

[9]   A. Salam and J. C. Ward, *Weak and electromagnetic interactions*, Nuovo Cim. **11** (1959) p. 568.

[10] ATLAS Collaboration, *Observation of a new particle in the search for the Standard Model Higgs boson with the ATLAS detector at the LHC*, Phys. Lett. B **716** (2012) p. 1, arXiv: 1207.7214 [hep-ex].

[11] CMS Collaboration, *Observation of a new boson at a mass of 125 GeV with the CMS experiment at the LHC*, Phys. Lett. B **716** (2012) p. 30, arXiv: 1207.7235 [hep-ex].

[12] C. Patrignani et al., *Review of Particle Physics*, Chin. Phys. C **40** (2016) p. 100001.

[13] M. E. Peskin and D. V. Schroeder, *An Introduction to quantum field theory*, Addison-Wesley, 1995, ISBN: 978-0201503975.

[14] A. Zee, *Quantum field theory in a nutshell*, 2003, ISBN: 978-0691140346.

[15] J. Goldstone, *Field Theories with Superconductor Solutions*,
      Nuovo Cim. **19** (1961) p. 154.

[16] J. Goldstone, A. Salam, and S. Weinberg, *Broken Symmetries*,
      Phys. Rev. **127** (1962) p. 965.

[17] M. Baak et al., *Results for the Global Electroweak Standard Model Fit*, 2017, URL:
      http://project-gfitter.web.cern.ch/project-gfitter/Standard_Model/.

[18] ATLAS Collaboration, *Summary plots from the ATLAS Standard Model physics group*,
      2017, URL: https:
      //atlas.web.cern.ch/Atlas/GROUPS/PHYSICS/CombinedSummaryPlots/SM/.

[19] ATLAS Collaboration,
      Measurement of the W-boson mass in pp collisions at $\sqrt{s}$ = 7 TeV with the ATLAS detector,
      (2017), arXiv: 1701.07240 [hep-ex].

[20] ATLAS Collaboration, *Measurements of the Higgs boson production and decay rates and
      coupling strengths using pp collision data at $\sqrt{s}$ = 7 and 8 TeV in the ATLAS experiment*,
      Eur. Phys. J. C **76** (2016) p. 6, arXiv: 1507.04548 [hep-ex].

[21] T. S. van Albada et al., *The Distribution of Dark Matter in the Spiral Galaxy NGC-3198*,
      Astrophys. J. **295** (1985) p. 305.

[22] Planck Collaboration, *Planck 2015 results. XIII. Cosmological parameters*,
      Astron. Astrophys. **594** (2016) A13, arXiv: 1502.01589 [astro-ph.CO].

[23] Y. Fukuda et al., *Evidence for oscillation of atmospheric neutrinos*,
      Phys. Rev. Lett. **81** (1998) p. 1562, arXiv: hep-ex/9807003 [hep-ex].

[24] M. Kobayashi and T. Maskawa,
      CP Violation in the Renormalizable Theory of Weak Interaction,
      Prog. Theor. Phys. **49** (1973) p. 652.

[25] A. Djouadi and A. Lenz, *Sealing the fate of a fourth generation of fermions*,
      Phys. Lett. B **715** (2012) p. 310, arXiv: 1204.1252 [hep-ph].

[26] J. A. Aguilar-Saavedra et al.,
      Handbook of vectorlike quarks: Mixing and single production,
      Phys. Rev. D **88** (2013) p. 094010, arXiv: 1306.0572 [hep-ph].

[27] N. Arkani-Hamed, A. G. Cohen, and H. Georgi,
      Electroweak symmetry breaking from dimensional deconstruction,
      Phys. Lett. B **513** (2001) p. 232, arXiv: hep-ph/0105239.

[28] M. Schmaltz and D. Tucker-Smith, *Little Higgs review*,
      Ann. Rev. Nucl. Part. Sci. **55** (2005) p. 229, arXiv: hep-ph/0502182.

[29] K. Agashe, R. Contino, and A. Pomarol, *The Minimal composite Higgs model*,
      Nucl. Phys. B **719** (2005) p. 165, arXiv: hep-ph/0412089.

[30] J. L. Hewett and T. G. Rizzo,
      Low-Energy Phenomenology of Superstring Inspired E(6) Models,
      Phys. Rept. **183** (1989) p. 193.

[31] M. Czakon, P. Fiedler, and A. Mitov,
      Total Top-Quark Pair-Production Cross Section at Hadron Colliders Through $O(\alpha_S^4)$,
      Phys. Rev. Lett. **110** (2013) p. 252004, arXiv: 1303.6254 [hep-ph].

[32] M. Czakon and A. Mitov,
NNLO corrections to top pair production at hadron colliders: the quark-gluon reaction,
JHEP **01** (2013) p. 080, arXiv: `1210.6832 [hep-ph]`.

[33] M. Czakon and A. Mitov, *NNLO corrections to top-pair production at hadron colliders:
the all-fermionic scattering channels*, JHEP **12** (2012) p. 054,
arXiv: `1207.0236 [hep-ph]`.

[34] P. Bärnreuther, M. Czakon, and A. Mitov, *Percent Level Precision Physics at the Tevatron:
First Genuine NNLO QCD Corrections to $q\bar{q} \rightarrow t\bar{t} + X$*,
Phys. Rev. Lett. **109** (2012) p. 132001, arXiv: `1204.5201 [hep-ph]`.

[35] M. Cacciari et al., *Top-pair production at hadron colliders with next-to-next-to-leading
logarithmic soft-gluon resummation*, Phys. Lett. B **710** (2012) p. 612,
arXiv: `1111.5869 [hep-ph]`.

[36] M. Czakon and A. Mitov,
Top++: A program for the calculation of the top-pair cross-section at hadron colliders,
Comput. Phys. Commun. **185** (2014) p. 2930, arXiv: `1112.5675 [hep-ph]`.

[37] S. L. Glashow, J. Iliopoulos, and L. Maiani,
Weak Interactions with Lepton-Hadron Symmetry, Phys. Rev. D **2** (1970) p. 1285.

[38] J. A. Aguilar-Saavedra, *Identifying top partners at LHC*, JHEP **11** (2009) p. 030,
arXiv: `0907.3155 [hep-ph]`.

[39] J. A. Aguilar-Saavedra, "Protos - PROgram for TOp Simulations",
URL: `https://jaguilar.web.cern.ch/jaguilar/protos/`.

[40] ATLAS Collaboration, *Analysis of events with b-jets and a pair of leptons of the same
charge in pp collisions at $\sqrt{s} = 8$ TeV with the ATLAS detector*, JHEP **10** (2015) p. 150,
arXiv: `1504.04605 [hep-ex]`.

[41] ATLAS Collaboration,
*Search for pair and single production of new heavy quarks that decay to a Z boson and a
third-generation quark in pp collisions at $\sqrt{s} = 8$ TeV with the ATLAS detector*,
JHEP **11** (2014) p. 104, arXiv: `1409.5500 [hep-ex]`.

[42] ATLAS Collaboration,
*Search for production of vector-like quark pairs and of four top quarks in the
lepton-plus-jets final state in pp collisions at $\sqrt{s} = 8$ TeV with the ATLAS detector*,
JHEP **08** (2015) p. 105, arXiv: `1505.04306 [hep-ex]`.

[43] ATLAS Collaboration, *Search for vectorlike B quarks in events with one isolated lepton,
missing transverse momentum, and jets at $\sqrt{s} = 8$ TeV with the ATLAS detector*,
Phys. Rev. D **91** (2015) p. 112011, arXiv: `1503.05425 [hep-ex]`.

[44] CMS Collaboration,
Inclusive search for a vector-like T quark with charge $\frac{2}{3}$ in pp collisions at $\sqrt{s} = 8$ TeV,
Phys. Lett. B **729** (2014) p. 149, arXiv: `1311.7667 [hep-ex]`.

[45] CMS Collaboration,
Search for pair-produced vectorlike B quarks in proton–proton collisions at $\sqrt{s} = 8$ TeV,
Phys. Rev. D **93** (2016) p. 112009, arXiv: `1507.07129 [hep-ex]`.

[46] CMS Collaboration,
Search for vectorlike charge 2/3 T quarks in proton–proton collisions at $\sqrt{(s)}$ = 8 TeV,
Phys. Rev. D **93** (2016) p. 012003, arXiv: 1509.04177 [hep-ex].

[47] CMS Collaboration, *Search for vector-like T quarks decaying to top quarks and Higgs bosons in the all-hadronic channel using jet substructure*, JHEP **06** (2015) p. 080,
arXiv: 1503.01952 [hep-ex].

[48] CMS Collaboration, *Search for single production of vector-like quarks decaying into a b quark and a W boson in proton–proton collisions at $\sqrt{s}$ = 13 TeV*, (2017),
arXiv: 1701.08328 [hep-ex].

[49] CMS Collaboration, *Search for pair production of vector-like T and B quarks in single-lepton final states using boosted jet substructure techniques at sqrt(s) = 13 TeV*,
(2017), arXiv: 1706.03408 [hep-ex].

[50] ATLAS Collaboration, *Summary plots from the ATLAS Exotic physics group*, 2015,
URL: https://atlas.web.cern.ch/Atlas/GROUPS/PHYSICS/
CombinedSummaryPlots/EXOTICS/ATLAS_VLQ_TT_step4/history.html.

[51] S. Coleman and J. Mandula, "All possible symmetries of the S matrix",
Dynamical Groups and Spectrum Generating Algebras, World Scientific, 1988 p. 469.

[52] R. Haag, J. T. Łopuszański, and M. Sohnius,
"All possible generators of supersymmetries of the S-matrix",
Dynamical Groups and Spectrum Generating Algebras, World Scientific, 1988 p. 987.

[53] S. Weinberg, *The Quantum Theory of Fields*, vol. 3, Cambridge University Press, 2005,
ISBN: 978-0-521-67055-5.

[54] S. P. Martin, *A Supersymmetry primer*,
(1997), [Adv. Ser. Direct. High Energy Phys.18,1(1998)],
arXiv: hep-ph/9709356 [hep-ph].

[55] B. de Carlos and J. A. Casas, *One loop analysis of the electroweak breaking in supersymmetric models and the fine tuning problem*, Phys. Lett. B **309** (1993) p. 320,
arXiv: hep-ph/9303291 [hep-ph].

[56] J. Alwall, P. Schuster, and N. Toro,
Simplified Models for a First Characterization of New Physics at the LHC,
Phys. Rev. D **79** (2009) p. 075020, arXiv: 0810.3921 [hep-ph].

[57] D. Alves, *Simplified Models for LHC New Physics Searches*,
J. Phys. G **39** (2012) p. 105005, ed. by N. Arkani-Hamed et al.,
arXiv: 1105.2838 [hep-ph].

[58] A. Djouadi et al., "The Minimal supersymmetric standard model: Group summary report",
GDR (Groupement De Recherche) - Supersymetrie Montpellier, France, April 15-17, 1998,
1998, arXiv: hep-ph/9901246 [hep-ph].

[59] C. F. Berger et al., *Supersymmetry Without Prejudice*, JHEP **02** (2009) p. 023,
arXiv: 0812.0980 [hep-ph].

[60] C. Borschensky et al., *Squark and gluino production cross sections in pp collisions at $\sqrt{s}$ = 13, 14, 33 and 100 TeV*, Eur. Phys. J. C **74** (2014) p. 3174,
arXiv: 1407.5066 [hep-ph].

[61] ATLAS Collaboration, *ATLAS Run 1 searches for direct pair production of third-generation squarks at the Large Hadron Collider*, Eur. Phys. J. C **75** (2015) p. 510, arXiv: 1506.08616 [hep-ex].

[62] CMS Collaboration, *Search for direct pair production of supersymmetric top quarks decaying to all-hadronic final states in pp collisions at $\sqrt{s}$ = 8 TeV*, Eur. Phys. J. C **76** (2016) p. 460, arXiv: 1603.00765 [hep-ex].

[63] CMS Collaboration, *Search for new physics with the M_{T2} variable in all-jets final states produced in pp collisions at $\sqrt{s}$ = 13 TeV*, JHEP **10** (2016) p. 006, arXiv: 1603.04053 [hep-ex].

[64] M. Papucci, J. T. Ruderman, and A. Weiler, *Natural SUSY Endures*, JHEP **09** (2012) p. 035, arXiv: 1110.6926 [hep-ph].

[65] N. Arkani-Hamed, A. Delgado, and G. F. Giudice, *The Well-tempered neutralino*, Nucl. Phys. B **741** (2006) p. 108, arXiv: hep-ph/0601041 [hep-ph].

[66] A. Buckley et al., *General-purpose event generators for LHC physics*, Phys. Rept. **504** (2011) p. 145, arXiv: 1101.2599 [hep-ph].

[67] J. C. Collins, D. E. Soper, and G. F. Sterman, *Factorization of Hard Processes in QCD*, Adv. Ser. Direct. High Energy Phys. **5** (1989) p. 1, arXiv: hep-ph/0409313 [hep-ph].

[68] Y. L. Dokshitzer, *Calculation of the Structure Functions for Deep Inelastic Scattering and e+ e- Annihilation by Perturbation Theory in Quantum Chromodynamics.*, Sov. Phys. JETP **46** (1977) p. 641, [Zh. Eksp. Teor. Fiz.73,1216(1977)].

[69] V. N. Gribov and L. N. Lipatov, *Deep inelastic electron scattering in perturbation theory*, Phys. Lett. B **37** (1971) p. 78.

[70] G. Altarelli and G. Parisi, *Asymptotic Freedom in Parton Language*, Nucl. Phys. B **126** (1977) p. 298.

[71] S. Dulat et al., *New parton distribution functions from a global analysis of quantum chromodynamics*, Phys. Rev. D **93** (2016) p. 033006, arXiv: 1506.07443 [hep-ph].

[72] A. Buckley et al., *LHAPDF6: parton density access in the LHC precision era*, Eur. Phys. J. C **75** (2015) p. 132, arXiv: 1412.7420 [hep-ph].

[73] T. Kinoshita, *Mass singularities of Feynman amplitudes*, J. Math. Phys. **3** (1962) p. 650.

[74] T. D. Lee and M. Nauenberg, *Degenerate Systems and Mass Singularities*, Phys. Rev. B **133** (1964) p. 1549, [,25(1964)].

[75] S. Catani et al., *QCD matrix elements + parton showers*, JHEP **11** (2001) p. 063, arXiv: hep-ph/0109231 [hep-ph].

[76] M. L. Mangano et al., *Matching matrix elements and shower evolution for top-quark production in hadronic collisions*, JHEP **01** (2007) p. 013, arXiv: hep-ph/0611129 [hep-ph].

[77] B. Andersson et al., *Parton Fragmentation and String Dynamics*, Phys. Rept. **97** (1983) p. 31.

[78] B. R. Webber, *A QCD Model for Jet Fragmentation Including Soft Gluon Interference*, Nucl. Phys. B **238** (1984) p. 492.

[79] S. Agostinelli et al., *GEANT4 – a simulation toolkit*,
      Nucl. Instrum. Meth. A **506** (2003) p. 250.

[80] ATLAS Collaboration, *The ATLAS Simulation Infrastructure*,
      Eur. Phys. J. C **70** (2010) p. 823, arXiv: `1005.4568 [physics.ins-det]`.

[81] L. Evans and P. Bryant, *LHC Machine*, JINST **3** (2008) S08001.

[82] K. Aamodt et al., *The ALICE experiment at the CERN LHC*, JINST **3** (2008) S08002.

[83] ATLAS Collaboration, *The ATLAS Experiment at the CERN Large Hadron Collider*,
      JINST **3** (2008) S08003.

[84] CMS Collaboration, *The CMS experiment at the CERN LHC*, JINST **3** (2008) S08004.

[85] A. A. Alves Jr. et al., *The LHCb Detector at the LHC*, JINST **3** (2008) S08005.

[86] C. Lefèvre, "The CERN accelerator complex. Complexe des accélérateurs du CERN",
      2008, URL: `http://cds.cern.ch/record/1260465`.

[87] D. Nisbet, "2016 operation: Operational efficiency and lessons learnt", 2017,
      URL: `https://indico.cern.ch/event/580313/contributions/2359285/`.

[88] ATLAS Collaboration, *Delivered Luminosity versus time for 2011-2017 (pp data only)*,
      2017, URL: `https://twiki.cern.ch/twiki/bin/view/AtlasPublic/`
      `LuminosityPublicResultsRun2`.

[89] ATLAS Collaboration, *Number of Interactions per Crossing*, 2017,
      URL: `https://twiki.cern.ch/twiki/bin/view/AtlasPublic/`
      `LuminosityPublicResultsRun2`.

[90] J. Pequenao, "Computer generated image of the whole ATLAS detector", 2008,
      URL: `http://cds.cern.ch/record/1095924`.

[91] ATLAS Collaboration, *ATLAS inner detector: Technical Design Report, 1*,
      ATLAS-TDR-4, 1997, URL: `https://cds.cern.ch/record/331063`.

[92] ATLAS Collaboration, *ATLAS inner detector: Technical Design Report, 2*,
      ATLAS-TDR-5, 1997, URL: `https://cds.cern.ch/record/331064`.

[93] ATLAS Collaboration, *Performance of the ATLAS track reconstruction algorithms in
      dense environments in LHC Run 2*, Eur. Phys. J. C **77** (2017) p. 673,
      arXiv: `1704.07983 [hep-ex]`.

[94] ATLAS IBL Collaboration, *Production and Integration of the ATLAS Insertable B-Layer*,
      JINST **13** (2018) T05008, arXiv: `1803.00844 [physics.ins-det]`.

[95] J. Pequenao, "Computer Generated image of the ATLAS calorimeter", 2008,
      URL: `http://cds.cern.ch/record/1095927`.

[96] ATLAS Collaboration, *ATLAS liquid-argon calorimeter: Technical Design Report*,
      ATLAS-TDR-2, 1996, URL: `https://cds.cern.ch/record/331061`.

[97] ATLAS Collaboration, *ATLAS tile calorimeter: Technical Design Report*, ATLAS-TDR-3,
      1996, URL: `https://cds.cern.ch/record/331062`.

[98] ATLAS Collaboration, *ATLAS muon spectrometer: Technical Design Report*,
      ATLAS-TDR-10, 1997, URL: `https://cds.cern.ch/record/331068`.

[99] J. Pequenao, "Computer generated image of the ATLAS Muons subsystem", 2008,
      URL: `http://cds.cern.ch/record/1095929`.

[100]   ATLAS Collaboration, *Performance of the ATLAS Trigger System in 2015*,
        Eur. Phys. J. C **77** (2017) p. 317, arXiv: 1611.09661 [hep-ex].

[101]   ATLAS Collaboration, *Luminosity determination in pp collisions at $\sqrt{s}$ = 8 TeV using the
        ATLAS detector at the LHC*, Eur. Phys. J. C **76** (2016) p. 653,
        arXiv: 1608.03953 [hep-ex].

[102]   S. van der Meer, *Calibration of the Effective Beam Height in the ISR*,
        CERN-ISR-PO-68-31, 1968, URL: http://cds.cern.ch/record/296752.

[103]   ATLAS Collaboration, *Performance of the ATLAS Inner Detector Track and Vertex
        Reconstruction in High Pile-Up LHC Environment*, ATLAS-CONF-2012-042, 2012,
        URL: https://cds.cern.ch/record/1435196.

[104]   T. Cornelissen et al., *The new ATLAS track reconstruction (NEWT)*,
        J. Phys. Conf. Ser. **119** (2008) p. 032014.

[105]   ATLAS Collaboration,
        Early Inner Detector Tracking Performance in the 2015 Data at $\sqrt{s}$ = 13 TeV,
        ATL-PHYS-PUB-2015-051, 2015, URL: https://cds.cern.ch/record/2110140.

[106]   ATLAS Collaboration, *Reconstruction of primary vertices at the ATLAS experiment in
        Run 1 proton–proton collisions at the LHC*, Eur. Phys. J. C **77** (2017) p. 332,
        arXiv: 1611.10235 [hep-ex].

[107]   ATLAS Collaboration, *Electron efficiency measurements with the ATLAS detector using
        the 2015 LHC proton–proton collision data*, ATLAS-CONF-2016-024, 2016,
        URL: https://cds.cern.ch/record/2157687.

[108]   ATLAS Collaboration,
        Electron and photon energy calibration with the ATLAS detector using LHC Run 1 data,
        Eur. Phys. J. C **74** (2014) p. 3071, arXiv: 1407.5063 [hep-ex].

[109]   ATLAS Collaboration, *Muon reconstruction performance of the ATLAS detector in
        proton–proton collision data at $\sqrt{s}$ = 13 TeV*, Eur. Phys. J. C **76** (2016) p. 292,
        arXiv: 1603.05598 [hep-ex].

[110]   ATLAS Collaboration,
        Topological cell clustering in the ATLAS calorimeters and its performance in LHC Run 1,
        Eur. Phys. J. C **77** (2017) p. 490, arXiv: 1603.02934 [hep-ex].

[111]   M. Cacciari, G. P. Salam, and G. Soyez, *The Anti-k(t) jet clustering algorithm*,
        JHEP **04** (2008) p. 063, arXiv: 0802.1189 [hep-ph].

[112]   ATLAS Collaboration, *Jet energy scale measurements and their systematic uncertainties
        in proton–proton collisions at $\sqrt{s}$ = 13 TeV with the ATLAS detector*,
        Phys. Rev. D **96** (2017) p. 072002, arXiv: 1703.09665 [hep-ex].

[113]   ATLAS Collaboration, *Performance of pile-up mitigation techniques for jets in pp
        collisions at $\sqrt{s}$ = 8 TeV using the ATLAS detector*, Eur. Phys. J. C **76** (2016) p. 581,
        arXiv: 1510.03823 [hep-ex].

[114]   ATLAS Collaboration, *Jet reclustering and close-by effects in ATLAS Run 2*,
        ATLAS-CONF-2017-062, 2017, URL: https://cds.cern.ch/record/2275649.

[115]   ATLAS Collaboration,
        Expected performance of the ATLAS b-tagging algorithms in Run-2,
        ATL-PHYS-PUB-2015-022, 2015, URL: https://cds.cern.ch/record/2037697.

[116] ATLAS Collaboration,
       Optimisation of the ATLAS b-tagging performance for the 2016 LHC Run,
       ATL-PHYS-PUB-2016-012, 2016, URL: https://cds.cern.ch/record/2160731.

[117] ATLAS Collaboration, *b-tagging in dense environments*, ATL-PHYS-PUB-2014-014,
       2014,
       URL: https://atlas.web.cern.ch/Atlas/GROUPS/PHYSICS/PUBNOTES/ATL-
       PHYS-PUB-2014-014.

[118] ATLAS Collaboration, *b-tagging calibration plots using dileptonic $t\bar{t}$ events produced in
       pp collisions at $\sqrt{s}$ = 13 TeV and a combinatorial likelihood approach*, 2016, URL:
       http://atlas.web.cern.ch/Atlas/GROUPS/PHYSICS/PLOTS/FTAG-2016-003/.

[119] ATLAS Collaboration, *Calibration of the performance of b-tagging for c and light-flavour
       jets in the 2012 ATLAS data*, ATLAS-CONF-2014-046, 2014,
       URL: https://cds.cern.ch/record/1741020.

[120] ATLAS Collaboration, *b-tagging calibration plots in light-flavour jets from 2015+2016
       data using the negative-tag method*, 2017, URL:
       http://atlas.web.cern.ch/Atlas/GROUPS/PHYSICS/PLOTS/FTAG-2017-002/.

[121] ATLAS Collaboration, *Reconstruction, Energy Calibration, and Identification of
       Hadronically Decaying Tau Leptons in the ATLAS Experiment for Run-2 of the LHC*,
       ATL-PHYS-PUB-2015-045, 2015,
       URL: https://atlas.web.cern.ch/Atlas/GROUPS/PHYSICS/PUBNOTES/ATL-
       PHYS-PUB-2015-045.

[122] ATLAS Collaboration, *Measurement of the tau lepton reconstruction and identification
       performance in the ATLAS experiment using pp collisions at $\sqrt{s}$ = 13 TeV*,
       ATLAS-CONF-2017-029, 2017, URL: https://cds.cern.ch/record/2261772.

[123] ATLAS Collaboration, *Expected performance of missing transverse momentum
       reconstruction for the ATLAS detector at $\sqrt{s}$ = 13 TeV*, ATL-PHYS-PUB-2015-023, 2015,
       URL: https://cds.cern.ch/record/2037700.

[124] ATLAS Collaboration, *Performance of missing transverse momentum reconstruction with
       the ATLAS detector in the first proton–proton collisions at $\sqrt{s}$ = 13 TeV*,
       ATL-PHYS-PUB-2015-027, 2015, URL: https://cds.cern.ch/record/2037904.

[125] S. Alioli et al., *A general framework for implementing NLO calculations in shower Monte
       Carlo programs: the POWHEG BOX*, JHEP **06** (2010) p. 043,
       arXiv: 1002.2581 [hep-ph].

[126] S. Frixione, P. Nason, and G. Ridolfi,
       A Positive-weight next-to-leading-order Monte Carlo for heavy flavour hadroproduction,
       JHEP **09** (2007) p. 126, arXiv: 0707.3088 [hep-ph].

[127] E. Re, *Single-top Wt-channel production matched with parton showers using the
       POWHEG method*, Eur. Phys. J. C **71** (2011) p. 1547, arXiv: 1009.2450 [hep-ph].

[128] S. Alioli et al., *NLO single-top production matched with shower in POWHEG: s- and
       t-channel contributions*, JHEP **09** (2009) p. 111, [Erratum: JHEP **02** (2010) 011],
       arXiv: 0907.4076 [hep-ph].

[129] T. Sjöstrand, S. Mrenna, and P. Z. Skands, *PYTHIA 6.4 physics and manual*,
       JHEP **05** (2006) p. 026, arXiv: hep-ph/0603175.

[130] T. Gleisberg et al., *Event generation with SHERPA 1.1*, JHEP **02** (2009) p. 007, arXiv: `0811.4622 [hep-ph]`.

[131] T. Gleisberg and S. Höche, *Comix, a new matrix element generator*, JHEP **12** (2008) p. 039, arXiv: `0808.3674 [hep-ph]`.

[132] F. Cascioli, P. Maierhofer, and S. Pozzorini, *Scattering Amplitudes with Open Loops*, Phys. Rev. Lett. **108** (2012) p. 111601, arXiv: `1111.5206 [hep-ph]`.

[133] J. Alwall et al., *The automated computation of tree-level and next-to-leading order differential cross sections, and their matching to parton shower simulations*, JHEP **07** (2014) p. 079, arXiv: `1405.0301 [hep-ph]`.

[134] H.-L. Lai et al., *New parton distributions for collider physics*, Phys. Rev. D **82** (2010) p. 074024, arXiv: `1007.2241 [hep-ph]`.

[135] R. D. Ball et al., *Parton distributions for the LHC Run II*, JHEP **04** (2015) p. 040, arXiv: `1410.8849 [hep-ph]`.

[136] R. D. Ball et al., *Parton distributions with LHC data*, Nucl. Phys. B **867** (2013) p. 244, arXiv: `1207.1303 [hep-ph]`.

[137] D. J. Lange, *The EvtGen particle decay simulation package*, Nucl. Instrum. Meth. A **462** (2001) p. 152.

[138] P. Konar et al., *Dark matter particle spectroscopy at the LHC: generalizing M_{T2} to asymmetric event topologies*, JHEP **04** (2010) p. 086, arXiv: `0911.4126 [hep-ph]`.

[139] A. J. Barr, B. Gripaios, and C. G. Lester, *Transverse masses and kinematic constraints: from the boundary to the crease*, JHEP **11** (2009) p. 096, arXiv: `0908.3779 [hep-ph]`.

[140] C. G. Lester and D. J. Summers, *Measuring masses of semi-invisibly decaying particles pair produced at hadron colliders*, Phys. Lett. B **463** (1999) p. 99, arXiv: `hep-ph/9906349`.

[141] C. G. Lester and B. Nachman, *Bisection-based asymmetric M_{T2} computation: a higher precision calculator than existing symmetric methods*, JHEP **03** (2015) p. 100, arXiv: `1411.4312 [hep-ph]`.

[142] B. Nachman and C. G. Lester, *Significance variables*, Phys. Rev. D **88** (2013) p. 075013, arXiv: `1303.7009 [hep-ph]`.

[143] ATLAS Collaboration, *Search for top squark pair production in final states with one isolated lepton, jets, and missing transverse momentum in $\sqrt{s}$ = 8 TeV pp collisions with the ATLAS detector*, JHEP **11** (2014) p. 118, arXiv: `1407.0583 [hep-ex]`.

[144] N. Kidonakis, *Two-loop soft anomalous dimensions for single top quark associated production with a W^- or H^-*, Phys. Rev. D **82** (2010) p. 054018, arXiv: `1005.4451 [hep-ph]`.

[145] S. Frixione et al., *Single-top hadroproduction in association with a W boson*, JHEP **07** (2008) p. 029, arXiv: `0805.3067 [hep-ph]`.

[146] J Butterworth et al., *Single Boson and Diboson Production Cross Sections in pp Collisions at $\sqrt{s}$ = 7 TeV*, 2010, URL: `https://cds.cern.ch/record/1287902`.

[147] ATLAS Collaboration, *A method for the construction of strongly reduced representations of ATLAS experimental uncertainties and the application thereof to the jet energy scale*, ATL-PHYS-PUB-2015-014, 2015, URL: https://cds.cern.ch/record/2037436.

[148] G. Cowan et al., *Asymptotic formulae for likelihood-based tests of new physics*, Eur. Phys. J. C **71** (2011) p. 1554, [Erratum: Eur. Phys. J. C **73** (2013) 2501], arXiv: 1007.1727 [physics.data-an].

[149] A. Wald, *Tests of statistical hypotheses concerning several parameters when the number of observations is large*, Transactions of the American Mathematical society **54** (1943) p. 426.

[150] A. L. Read, *Presentation of search results: The CL(s) technique*, J. Phys. G **28** (2002) p. 2693.

[151] M. Baak et al., *HistFitter software framework for statistical data analysis*, Eur. Phys. J. C **75** (2015) p. 153, arXiv: 1410.1280 [hep-ex].

[152] ATLAS Collaboration, *Search for new phenomena in $t\bar{t}$ final states with additional heavy-flavour jets in pp collisions at $\sqrt{s}$ = 13 TeV with the ATLAS detector*, ATLAS-CONF-2016-104, 2016, URL: https://cds.cern.ch/record/2220371.

[153] ATLAS Collaboration, *Search for pair production of heavy vector-like quarks decaying to high-p_{T} W bosons and b quarks in the lepton-plus-jets final state in pp collisions at $\sqrt{s}$ = 13 TeV with the ATLAS detector*, JHEP **10** (2017) p. 141, arXiv: 1707.03347 [hep-ex].

[154] B. Nachman et al., *Jets from Jets: Re-clustering as a tool for large radius jet reconstruction and grooming at the LHC*, JHEP **02** (2015) p. 075, arXiv: 1407.2922 [hep-ph].

[155] D. Krohn, J. Thaler, and L.-T. Wang, *Jet Trimming*, JHEP **02** (2010) p. 084, arXiv: 0912.1342 [hep-ph].

[156] R. D. Cousins, J. T. Linnemann, and J. Tucker, *Evaluation of three methods for calculating statistical significance when incorporating a systematic uncertainty into a test of the background-only hypothesis for a Poisson process*, Nucl. Instrum. Meth. A **595** (2008) p. 480, arXiv: physics/0702156 [physics.data-an].

[157] ATLAS Collaboration, *Measurement of the cross-section for W boson production in association with b-jets in pp collisions at $\sqrt{s}$ = 7 TeV with the ATLAS detector*, JHEP **06** (2013) p. 084, arXiv: 1302.2929 [hep-ex].

[158] J. A. Aguilar-Saavedra, D. E. López-Fogliani, and C. Muñoz, *Novel signatures for vector-like quarks*, JHEP **06** (2017) p. 095, arXiv: 1705.02526 [hep-ph].

[159] M. Chala, *Direct bounds on heavy toplike quarks with standard and exotic decays*, Phys. Rev. D **96** (2017) p. 015028, arXiv: 1705.03013 [hep-ph].

[160] ATLAS Collaboration, *Summary plots from the ATLAS Exotic physics group*, 2017, URL: https://atlas.web.cern.ch/Atlas/GROUPS/PHYSICS/CombinedSummaryPlots/EXOTICS/index.html#ATLAS_VLQ_BB_step4.

[161] ATLAS Collaboration, *Search for new phenomena using events with b-jets and a pair of same-charge leptons in 3.2 fb^{-1} of pp collisions at $\sqrt{s}$ = 13 TeV with the ATLAS detector*, ATLAS-CONF-2016-032, 2016, URL: https://cds.cern.ch/record/2161545.

[162] S. Chatrchyan et al., *Measurement of the Polarization of W Bosons with Large Transverse Momenta in W+Jets Events at the LHC*, Phys. Rev. Lett. **107** (2011) p. 021802, arXiv: 1104.3829 [hep-ex].

[163] ATLAS Collaboration, *Search for a Scalar Partner of the Top Quark in the Jets+ETmiss Final State at $\sqrt{s}$ = 13 TeV with the ATLAS detector*, 2017, URL: http://cds.cern.ch/record/2258142.

[164] CMS Collaboration, *Search for top squark pair production in pp collisions at sqrt(s)=13 TeV using single lepton events*, (2017), arXiv: 1706.04402 [hep-ex].

The images on the pages 5 and 33 have been adapted from:

CERN, *The decay of a lambda particle in the 32 cm hydrogen bubble chamber*, CERN-EX-11465, URL: https://cds.cern.ch/record/39474.

ATLAS Collaboration, *ATLAS: technical proposal for a general-purpose pp experiment at the Large Hadron Collider at CERN*, URL: https://cds.cern.ch/record/290968.

Acknowledgements

I want to thank my supervisor Peter Mättig for all the support and guidance in my years at Wuppertal university and especially for the nearly two years at CERN. This was a great opportunity and a wonderful time. I also want to thank Joseph Kroll and Erez Etzion for being referee for my dissertation.

During my time at CERN I met many great people. I want to thank all the (current and former) members of the stop 1-lepton analysis team for years of support, interesting discussions and giving me the opportunity to learn. This also goes to the members of the minimum bias team, in which I experienced a great atmosphere and also learned a lot about the fine nuances of creating a measurement. It was a great time at CERN, thank you for that!

Back in Wuppertal, I want to thank all the people in the particle physics group, and especially those in my office. You make the time at work enjoyable and helped a lot.

Many people have helped me creating this dissertation by reading and commenting. I want to thank Frank, Javier, Keisuke and Sophie for all the time and energy needed for that.

I want to thank my family and my friends for all the help during the last years (from spending free time and cooking to reading and commenting). I would not have been possible to complete this dissertation without so much support and encouragement from you!

Finally, I want to thank Daniela. I cannot express how much you mean to me or how much you have helped. Thank you for making our time the best I could ever wish for.